Solids Formation and Permeability Reduction in Zero-Valent Iron and Iron Sulfide Media for Permeable Reactive Barriers

by

Andrew Dalrymple Henderson

A dissertation submitted in partial fulfillment
of the requirements for the degree of
Doctor of Philosophy
(Environmental Engineering)
in The University of Michigan
2010

Doctoral Committee:

Associate Professor Avery H. Demond, Chair
Professor Rodney C. Ewing
Professor Kim F. Hayes
Associate Professor Terese M. Olson

... but you'll find the highest pH's underground.

-Ed Vizard and the Flatlanders, à la Dennis Norden and Frank Muir

Dedication

To Hannah Betty Henderson, for motivation
To Donald D. Dalrymple, for inspiration
To Ervin Leon Henderson, for smiles
To Elizabeth Phillips Dalrymple, for unknown gifts

Acknowledgements

I am tremendously grateful to friends and my family, both that with which I came to school and that which I found at school.

Linda, George, and Elizabeth enabled me to be here; they and Gwynne helped me to finish.

Table of Contents

List of Figures

List of Tables

List of Acronyms

Acronym	Meaning
AFB	Air Force Base
CGR	Carbonate green rust
DDI	Distilled, de-ionized water
DO	Dissolved oxygen
EDS	Electron dispersive spectroscopy
GC-RGA	Gas chromatograph – reduction gas analyzer
GC-TCD	Gas chromatograph – thermal conductivity detector
ICP-MS	Inductively coupled plasma – mass spectroscopy
IC	Ion chromatograph
ICH	Iron carbonate hydroxide
PSD	Pore size distribution
PTZ	Pre-treatment zone
PRB	Permeable reactive barrier
PV	Pore volume
PZC	Point of zero charge
SEM	Scanning electron microscopy
TDS	Total dissolved solids
TIC	Total inorganic carbon
TOC	Total organic carbon
UMTRA	Uranium mill tailings remedial action
XPS	X-ray photoelectron spectroscopy
XRD	X-ray diffraction
ZVI	Zero-valent iron

Abstract

Solids Formation and Permeability Reduction in Zero-Valent Iron
and Iron Sulfide Media for Permeable Reactive Barriers

by

Andrew Dalrymple Henderson

Chair: Avery H. Demond

Permeable reactive barriers (PRBs) are an in situ technology for remediation of contaminated groundwater. Most employ ZVI as the reactive medium, and although many achieve remediation goals, the performance of others is compromised by the precipitation of naturally-occurring solutes. With an interest in improving the understanding of the longevity of these systems, this research aimed to understand the precipitation of solids in these systems. Recent work has suggested the suitability of reduced iron sulfide (FeS) as a reactive material for PRB applications, so the work presented in this dissertation compared the solids production and hydraulic performance of pure ZVI and FeS-coated sands as the reactive media.

To better understand the factors associated with solids production and the potential for failure, a statistical analysis of data from field PRBs composed of ZVI was conducted. This analysis indicated that high nitrate (>20 mg/L), high alkalinity (>350 mg/L as $CaCO_3$), high chloride (>110 mg/L), and high internal E_H (>-200 mV) values were associated with PRBs that had failed or showed signs of failure.

Based on this statistical analysis, a series of column experiments was conducted utilizing a simulated groundwater with high calcium (280 mg/L), total carbonate (420 mg/L), and chloride (405 mg/L) as a base solution, to which oxidants were added. Oxidants added were either dissolved oxygen (0, 2, or 8 mg/L), nitrate (100 mg/L), or nitrate and sulfate (100 and 1170 mg/L, respectively).

Characterization of the aqueous phase in the ZVI column effluents indicated that ZVI created strongly reducing conditions, and that both calcium and carbonate were removed from solution. Production of gas bubbles was also observed. In the various ZVI column systems, increasing oxidant levels corresponded to higher hydraulic conductivity losses. Yet the spectroscopic analysis of solids produced and mass balances on the aqueous phase could not account for all of the hydraulic conductivity loss. Equilibrium geochemical modeling of the systems was also used to estimate the potential for solids formation and gas production. Results of this modeling were in agreement with the finding that solids alone were unable to account for the observed hydraulic conductivity losses in the ZVI systems. Therefore, it appears the hydraulic conductivity losses due to the gas phase that was produced in these systems may be a crucial component of permeability loss.

In the FeS columns, reducing conditions were also created. In contrast to the ZVI columns, no calcium or carbonate was removed in the columns, no hydraulic conductivity loss was measured, and no solids were detected on the surface of the solids. Modeling of the FeS and ZVI systems on an equal mass basis indicated the potential for solids formation with FeS is much less than that with ZVI. Based on these hydraulic considerations, FeS may have significant advantages over ZVI for PRB applications.

Chapter 1: Introduction

1.1 Groundwater contamination as a growing problem

Groundwater is a stressed resource in the United States and worldwide. Global water quality and quantity are being strained by population growth, land use changes, and climate change (Zimmerman et al. 2008). As the demand for water increases, reliance on groundwater is expected to increase as well (Ahlfeld and Dripps 2003). In the US, groundwater withdrawals have more than doubled since 1950, to the extent that groundwater is used by over half of the US population on a regular basis (Hutson et al. 2004), and many areas of the country are experiencing severe groundwater declines (Reilly et al. 2008). Furthermore, it is estimated there are 130,000 to 425,000 potential subsurface hazardous waste sites, many of which are expected to interact with and adversely affect groundwater (US General Accounting Office 1987). As groundwater is increasingly relied upon, its quality is clearly a concern.

Restoring the quality of contaminated groundwater has traditionally required active remediation: pump and treat systems have often been used to address groundwater pollution. These systems extract groundwater to the surface, treat it approaches such as air stripping or adsorption onto granular activated carbon, and either re-introduce the treated water to the subsurface or discharge it to a storm drain. Such approaches are energy-intensive and maintenance-intensive. More importantly, they are often ineffective: a National Research Council study found that 69 of 77 treatment sites using pump and treat had not met their cleanup goals (National Research Council 1994). Thus, while pump and treat may be an effective tool at some sites, other approaches are clearly necessary to effectively remediate a broader range of contaminated sites.

1.2 Permeable reactive barriers as a treatment alternative

Permeable reactive barriers (PRBs) are a promising groundwater remediation technology involving the emplacement of a hydraulically permeable reactive medium in the subsurface, downgradient of a contaminant source. As contaminated water flows through the barrier under its natural hydraulic gradient, the reactive medium degrades or traps the contaminants. Compared to alternative remediation technologies, PRBs may offer several advantages. First, subsurface, *in situ* treatment eliminates the need for above-ground management of both large volumes of water containing low concentrations of contaminants and the waste generated from the treatment of such water (Blowes et al. 1999). Secondly, because water flows under its natural gradient, there is no energy input required, so operational costs are low; furthermore, if the reactive media have a sufficient longevity and media rejuvenation or replacement is not required, the maintenance costs may also be low. Finally, if the reactive medium is appropriately chosen, a PRB can simultaneously treat multiple types of contaminants such as metals, organics and radionuclides.

PRBs are a relatively young technology; the oldest full-scale PRB has been in operation for less than fifteen years. This PRB was installed in 1995 at the Intersil Site in Sunnyvale, CA to treat chlorinated organics and Freon. It used 100% zero-valent iron (ZVI) in its reactive zone and was still meeting its cleanup goals as of 2004 (Warner et al. 2005; Sorel et al. 2003). With the initial success of PRBs, their use has become more widespread. Indeed, PRBs have been installed to treat organics, heavy metals, radionuclides, and nutrients (RTDF 2001), with nearly 50% treating organic contaminants and nearly 20% treating metals as of 2002 (EPA 2002). Typical reactive media used in the field include zero-valent iron (ZVI), cast iron, steel wool, amorphous ferric oxide, phosphate, zeolite, activated carbon, or limestone, among others (see Scherer et al. 2000); however, of the over 200 PRBs worldwide as of 2004, 120 are iron-based (90 in the US) (ITRC 2005).

1.3 Uncertainties about PRB performance

Despite numerous installations, PRBs are still considered an experimental technology (Warner and Sorel 2003), largely because their long-term performance is not well understood. While some PRBs have not achieved their cleanup goals because of design failure (poor hydraulic characterization and thus incomplete plume capture), operational failure – due to declining reactivity or loss of hydraulic conductivity – is rare (RTDF 2001). Only three PRBs seem to have suffered this sort of operational failure, one in Monticello, Utah, and two in Denmark.

Regarding the uncertainty about PRB longevity, Wilkin and Puls (2003) point out, "[f]ew case studies are available that evaluate the long-term performance of these *in situ* systems, especially with respect to the long-term efficiency of contaminant removal, the buildup of mineral precipitates, and the buildup of microbial biomass." Because their longevity is not understood, it has proven difficult to estimate their long-term cost effectiveness in relation to other treatment approaches.

With the lack of comprehensive retrospective studies, there is disagreement about what factors control PRB longevity, defined here as the length of time that a PRB continues to treat groundwater to design levels. Some have argued that PRB longevity is controlled by loss of reactivity (e.g., Vikesland et al. 2003; Roberts et al. 2002), whereas others assert that reduction in permeability is more important (e.g., Liang et al. 2003; Phillips et al. 2000). Depending on the assumptions about controlling factors, estimates of PRB longevity can vary by an order of magnitude (e.g., 10 to 117 years for Monticello, UT (Morrison et al. 2002)).

Solids accumulation in PRBs is of key concern, for solids will affect both of the factors noted above: hydraulic conductivity and reactivity. Indeed, the precipitation of solids has been observed in numerous ZVI PRBs (Henderson and Demond 2007). For example, commonly occurring groundwater constituents, such as calcium and carbonate – typically present in concentrations in the tens to hundreds of parts per million – often precipitate in PRBs. Given that contaminants are often present in the parts per *billion* range, quantities of these non-contaminant precipitates may greatly exceed the amount of any solids

formed by the contaminant itself. With this potential for solids production from dissolved non-contaminant species, it is not surprising that hydraulic changes seem to be at play when PRBs fail.

One option to limit solids buildup is to install a pretreatment zone upgradient of the reactive media zone, which could consist of a mixture of larger-grained non-reactive material and ZVI. The goal of such a zone would be to promote the precipitation of solids in a region where they would not have a large impact on hydraulic conductivity (Sarr 2001; Dwyer 2000b), but this approach has not been systematically studied. Another option to limit solids buildup is to consider the use of an alternative reactive material, one that may not accumulate as many solids as ZVI does.

1.4 Iron sulfide as an alternative reactive media

Iron monosulfide (FeS) may function well as a reactive media in PRB applications. Like ZVI, FeS may degrade chlorinated organic contaminants, effectively transforming them to non-hazardous organics (e.g., Butler and Hayes 1998). Indeed, FeS has been shown to be more reactive per unit surface area than ZVI towards trichloroethylene (Sivavec and Horney 1997).

In addition to treating chlorinated organics, FeS is an effective sequestration agent for heavy metals. Redox-active heavy metals such as chromium or metalloids such as arsenic may exist in different oxidation states; typically, the oxidized forms of these elements are more soluble and thus more difficult to sequester. FeS can reduce these heavy metals and metalloids to their reduced, less soluble forms (Boursiquot et al. 2002; Farquhar et al. 2002). In addition, FeS may act as a source of sulfide. Sulfide-bearing phases are typically quite insoluble; since FeS is slightly more soluble than other metal contaminant sulfide phases, contaminants may be favorably exchanged for iron, thus sequestering contaminants – both redox-active and non-redox-active – in an insoluble solid phase (Coles et al. 2000; Herbert et al. 2000). Even if such solids are not produced, contaminants may be removed via sorption to the FeS surface. For example, Gallegos

(2007) reported that As(III) forms inner-sphere complexes with mackinawite in alkaline solutions.

As an additional consideration, FeS may be regenerated through *in situ* microbial processes; ZVI, on the other hand, may not. Sulfate reducing bacteria, using organic material as a substrate, may use sulfate as an electron acceptor, reducing it to sulfide. If reduced iron is available (as often is the case in these subsurface systems), FeS may precipitate (Matsuo et al. 2000; Watson et al. 2000; Herbert et al. 1998). Sulfate-reducing bacteria (SRB) have been shown to be capable of producing FeS in the form of mackinawite (Vaughan and Lennie 1991), and such biogenically produced FeS has been shown to be reactive towards contaminants such as arsenic (Vannela et al. 2007).

The majority of field PRBs have used ZVI as a reactive media, and the author is not aware of any field PRBs in which FeS was purposely installed as the reactive media. However, iron sulfides have been identified in existing PRBS, and there is some evidence of FeS playing a role in the removal of contaminants. For example, mackinawite has been found in the 100% ZVI PRB at Elizabeth City, NC (Wilkin and Puls 2003). At the Nickel Rim, Ontario PRB, which is designed to removed sulfate, alkalinity, and amend the pH of drainage from an acid mine, FeS is formed in the PRB, but only removal of Mn by the FeS is mentioned (Benner et al. 1999). At the 100% ZVI PRB at Helena, MT, solids analysis of cores provided evidence of As(III) sorbed to FeS surfaces (Beak and Wilkin 2009).

1.5 Objectives

On the whole, PRBs, often composed of ZVI, have demonstrated an ability to degrade or trap a variety of contaminants in groundwater. However, a lack of understanding about their long-term performance, frequent field observations of precipitate accumulation and/or loss of reactivity, and the possibility of failure of ZVI PRBs due to precipitate accumulation, have hindered more widespread acceptance of this approach to groundwater remediation.

Iron sulfide has shown promise as an alternative reactive material for use in PRBs. Recent work has shown its ability to remove arsenic in column experiments (Han 2009). However, it is not yet known whether FeS is subject to the same permeability reduction as ZVI. In order to demonstrate the viability of FeS as a reactive medium for field-scale remediation projects, it is necessary to understand the potential for hydraulic conductivity loss in FeS-based PRBs. Therefore, this research aimed to evaluate the mechanism by which hydraulic conductivity is lost in PRBs and to assess whether FeS-based PRBs offer any advantages over ZVI PRBs in this regard. To achieve this goal, the following objectives were defined:

1. Determine the key geochemical parameters linked to hydraulic changes in ZVI PRBs,
2. Examine permeability loss in ZVI and FeS column experiments as a function of these geochemical parameters,
3. Assess the potential for permeability loss is FeS-based systems in column experiments representing a range of geochemical conditions, and
4. Characterize the precipitates formed in ZVI and FeS columns experiments representative of natural groundwater systems.

1.6 Document organization

There are eight chapters in this dissertation. The current chapter has provided the motivation for this work. Chapter 2 reviews the relevant literature, including a discussion of PRBs, the experience with their operation, and an overview of the geochemistry that governs ZVI and FeS systems. A statistical analysis of published data for ZVI PRBs is presented in Chapter 3. The findings from this work were used to inform the experimental matrix. The methodology and materials used in the column experiments are described in Chapter 4. Chapters 5 and 6 present experimental and modeling results for ZVI and FeS column experiments, respectively. Comparisons between the ZVI and FeS column experiment results are in Chapter 7, while Chapter 8 summarizes this work and its implications, as well as presents suggestions for future research in this area.

Chapter 2: Background

2.1 PRBs: Field and lab

Work in the 1970s investigated the destruction of chlorinated organic chemicals using reduced metals (Sweeny 1981a; Sweeny 1981b; Sweeny and Fischer 1973; Sweeny and Fischer 1972); this concept was revived by another research group in the late 1980s (Senzaki 1991; Senzaki and Kumagai 1989; Senzaki and Kumagai 1988), but without an *in situ* application in mind. This innovation can be attributed to the group that installed a pilot scale PRB in 1991 at the Borden AFB in Ontario, Canada (Morrison et al. 2002c; Gavaskar et al. 1997; O'Hannesin 1993; Gillham and O'Hannesin 1992; Reynolds et al. 1990). Although the PRB at Borden did not achieve its removal targets for TCE (trichloroethylene) and PCE (tetrachloroethylene), it was hypothesized that a higher ratio of zero-valent iron (ZVI) to sand (installed as 20:80) would have been adequate for complete contaminant removal (O'Hannesin and Gillham 1998). The first full-scale PRB – using 100% ZVI – was installed at the Intersil Site in Sunnyvale, CA in 1995. This is the oldest full-scale PRB, has been treating contaminants for nearly 15 years, and was continuing to perform well, meeting its cleanup goals as of 2004 (Warner et al. 2005; Sorel et al. 2003).

2.1.1 PRB configurations in the field

Field PRBs are often emplaced using excavation methods (e.g, backhoe, clamshell, or caisson) and backfilling with reactive material (Gavaskar 1999). Such trench-and-fill PRBs are placed so as to intercept a plume of contaminated groundwater that is relatively close to the ground surface, as shown in Figure 2.1.

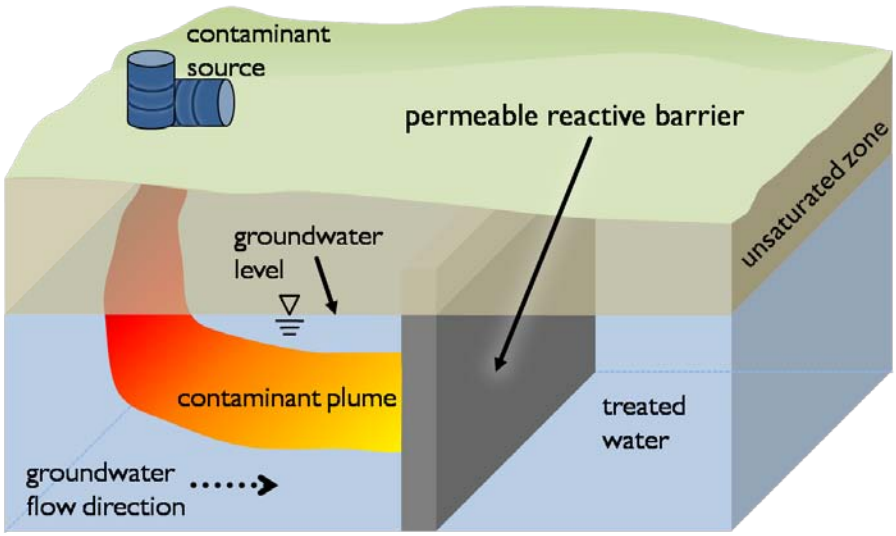

Figure 2.1: PRB schematic.

The PRB may be capped with native material or, commonly, a layer meant to prevent water intrusion from the surface, such as clay or clay and a geotextile (US DOE - Subsurface Contaminants Focus Area 2000; McMahon et al. 1999). Depending on the activities at the ground surface, the PRB installation may even be topped with pavement (Kiilerich et al. 2000). Typical dimensions of these PRBs are 2 to 50 m long (transverse to flow), <1 to 5 m wide (parallel to flow), and <1 to 10 m deep (RTDF 2001). PRBs have also been installed to greater depths using non-excavation techniques, such as hydraulic fracturing, deep soil mixing (Gavaskar 1999), or *in situ* redox manipulation (ISRM), which creates a reactive zone by reducing iron(III) oxides to iron(II) through the injection of a reducing agent such as sodium dithionate (Fruchter 2002).

PRB-like systems may also be installed above ground as *ex situ* systems, such as at the Portsmouth Groundwater Treatment Facility in Piketon, OH (Korte et al. 1997b) and the Uranium Mill Tailings Remedial Action Site in Durango, CO (Morrison et al. 2002b). At such installations, the flow of contaminated water is still natural: groundwater is collected in trenches and directed to above-ground containers filled with reactive material that are located below the hydraulic grade line. Although there is no pumping, and the system is thus not active, the fact that the reactive material is installed in a closed container makes these systems very different in practice. Indeed, the hydraulic conductivity loss observed

in these systems is often much greater than that seen in the field (Henderson and Demond 2007).

The design of PRBs usually involves bench scale tests to determine how the media, contaminants, and groundwater interact. To transfer the lab results to the field, safety factors are a key component of proper design (ESTCP 2003). Gavaskar (1999) cites the design of a PRB at the Dover Air Force Base (AFB), which used a safety factor of two in barrier width calculations. In addition, degradation rates increase with temperature (Senzaki and Kumagai 1989; Senzaki and Kumagai 1988); therefore a safety factor of 2 to 2.5 is recommended for changes in temperature of 10°C, while a safety factor of 1.5 is suggested to account for bulk compaction in the field (Gavaskar et al. 1998). Field heterogeneities and other uncertainties also point to the need for safety factors in design.

Some PRBs also have an upgradient section, or pre-treatment zone (PTZ). PTZs contain sand and gravel, usually with reactive media mixed in, although sometimes this is inadvertent (RTDF 2001; Blowes et al. 1999). The high permeability of this region has two presumed benefits: first, the high hydraulic conductivity is expected to improve the distribution of the incoming contaminant plume over the upgradient face of the PRB; second, precipitates that form in this region will not have the same effects as they would were they to form in the finer-grained pure media region (Sarr 2001; Dwyer 2000b). The jury is still out on the effects of mixtures of reactive and non-reactive media, be these mixtures in a PTZ or the reactive zone itself. Some research has indicated that mixtures do not affect the removal of contaminants (e.g., Kjeldsen and Locht 2000), but others have asserted that there is deleterious effect on contaminant treatment if the main section of a PRB contains such a mix (e.g., D'Andrea et al. 2005; Liang et al. 2000), whereas still others argue that mixtures of reactive and non-reactive media do, in fact, mitigate the hydraulic impact of precipitates (Furukawa et al. 2002).

2.1.2 Laboratory simulation of PRBs

Laboratory experiments to simulate PRBs or aid in PRB design are often run as columns. In this sense, they are not dissimilar to the *ex situ* reaction cells discussed above.

However, a survey of the literature identifies other complications that make a comparison of laboratory work to field PRBs difficult. Matching the flow rate, for example, is crucial. Short term column studies with high flow rates – intended to speed the aging of the reactive media and mimic long time scales – may not be representative of true media aging (Kamolpornwijit et al. 2003; Roberts et al. 2002; Sarr 2001; Farrell et al. 2000). Because kinetic factors may be more important in controlling a precipitation process than thermodynamic factors (Saripalli et al. 2001), the flow rate may be an important variable in PRB systems. Under the laminar flow conditions expected in most groundwaters, the growth rate of precipitates is diffusion limited, so the available surface area is a controlling property (Saripalli et al. 2001). Artificially high flow rates, however, may switch the control of precipitate growth from surface area to mass transport. The cutoff between "fast" and "acceptable" flow rates is not clearly demarcated, but a rate of 8 m/d has been identified as too high, because geochemical gradients in the column are unlikely to match those in the field, resulting in altered precipitation and reactive media surface chemistry (Roberts et al. 2002).

A further problem with laboratory column studies is that many have used feed water that is not representative of natural systems (Roberts et al. 2002; Liang et al. 2000). The use of buffering agents is also problematic, as some agents have been shown to alter iron corrosion rates (O'Hannesin and Gillham 1998; Uhlig and Revie 1985). Finally, studies utilizing high contaminant concentrations may not adequately represent long-term, low contaminant fluxes (Melitas et al. 2002).

2.1.3 PRB longevity and failure modes

Despite the growing evidence of PRB success, PRBs are still seen as a developing, experimental technology (Warner and Sorel 2003), largely because of the uncertainty surrounding their long-term performance. Wilkin and Puls (2003) note that "[f]ew case studies are available that evaluate the long-term performance of these *in situ* systems, especially with respect to the long-term efficiency of contaminant removal, the buildup of mineral precipitates, and the buildup of microbial biomass." Given the lack of

comprehensive, retrospective studies, it is not surprising that there are questions about what factors may control the longevity of PRBs. For the purposes of this discussion, the longevity of a PRB may be defined as the period of time that a PRB meets its design goals for contaminant removal. Some researchers argue that PRB longevity is controlled by losses in reactivity (e.g., Vikesland et al. 2003), while others argue that losses of hydraulic conductivity are more important (e.g., Liang et al. 2003; Phillips et al. 2000). Table 2.1 summarizes the variety of estimation methods in the literature for the longevity of ZVI PRBs, which underscores the still-developing nature of the understanding of PRB longevity.

Table 2.1: Selected longevity estimates for *in situ* PRBs

Site	Estimate	Basis of Estimate	Contaminant	Reference
Elizabeth City, NC	20 yrs	Oxidation of ZVI by all species in groundwater, based on laboratory studies.	Cr, TCE	Blowes et al. 2000
	750 yrs	Oxidation of all ZVI by Cr(VI) only (theoretical).		
Monticello, UT	10 yrs	Precipitation of calcite and resultant pore blockage, based on mass balance on Ca^{2+}.	U, As, Se, V, NO_3-	Morrison et al. 2002
	36 yrs	Passivation of iron surfaces (estimated by 35% loss of "reactivity efficiency" measured in PRB during 1st seven months of operation).		
	117 yrs	Dissolution of ZVI, based on effluent Fe^{2+} measured in column tests.		
Y-12 Plant (Pathway 2), Oak Ridge, TN	>15 yrs	Visual inspection of corrosion of ZVI.	U, NO_3^-	Phillips et al. 2000

Based on a literature review of published data for ZVI PRBs (Henderson and Demond 2007), three classes of possible failure modes of PRBs were identified: loss of reactivity, adverse hydraulic changes, and design flaws. Although the emphasis in the literature has been placed on loss of reactivity and adverse hydraulic changes, it is design flaws that have been the most common cause of PRB failure (Warner and Sorel 2003) and continue

to be one of the main challenges to successful groundwater remediation using PRBs (ESTCP 2003).

The failure of *in situ* PRBs due to the other two failure modes – loss of reactivity and loss of hydraulic conductivity – appears to be rare. The only *in situ* PRBs that have reported operational failures that are not solely due to design flaws (e.g., inadequate hydraulic characterization) are at Monticello (UT), the Copenhagen Freight Yard (Denmark), and Haardkrom (Denmark). The ZVI PRB at the Monticello site experienced a hydraulic conductivity loss of 2 orders of magnitude over 5.5 years, which, for this system, corresponds to approximately 120 pore volumes (Mushovic et al. 2006). The Copenhagen Freight Yard reported a loss of permeability in the ZVI barrier due to the precipitation of hydroxides and carbonates, but this PRB also suffered from incomplete plume capture due to poor hydraulic characterization (RTDF 2001; Kiilerich et al. 2000). The problems at the Haardkrom ZVI PRB, however, were attributed to "exhaustion of iron-chromate removal capacity," with little more specific detail given (Kjeldsen and Fulgsang 2000).

In contrast to the apparently robust performance of *in situ* PRBs, *ex situ* PRBs tend to clog and fail with regularity: every site where *ex situ* reaction cells have been installed has experienced clogging and failure of at least one of those cells, including the following: Hill AFB (UT), Portsmouth (Piketon, OR), UMTRA (Durango, CO), and Y-12 Pathway 1 (Oak Ridge, TN) (Morrison et al. 2002a; Ott 2000; Liang et al. 1997; Shoemaker et al. 1995). The *ex situ* PRB at Rocky Flats (Golden, CO) did not experience failure, but this is presumably because the crust forming on the reactive media was periodically broken up (Korte 2001; RTDF 2001).

Clogging, or loss of hydraulic conductivity, will decrease hydraulic residence times, decreasing the amount of time media is in contact with the contaminant, leading to less effective treatment (EPA 1999). In some cases, hydraulic short circuiting may occur, as preferential flow paths have been observed in some column studies, (Kamolpornwijit et al. 2003; Su and Puls 2003), and some evidence exists for their occurrence in the field (Liang et al. 2003). However, no performance changes have yet been attributed to

reduced residence time. Some sites did not reach treatment goals (e.g., Borden, Ontario, as described by O'Hannesin (1993)), and sometimes incomplete degradation occurred (e.g., the CSM site in Australia, as described by Duran et al. 2000), but these problems were design flaws (i.e., present at installation) and were not due to porosity reduction.

To further understand the potential for operational failure due to hydraulic conductivity loss or reactivity loss, it is important to consider the reactions in PRBs that drive treatment and interaction with naturally occurring solutes. The following section provides information about the aqueous chemistry, gas generation, and solids formation that may occur in reactive media in the subsurface.

2.2 Geochemistry of ZVI and FeS as PRB media

In this section, the properties of the two materials are described, and then their interaction with the aqueous phase is discussed.

2.2.1 Properties of ZVI

ZVI is a milled and sieved product created from waste iron from other iron milling processes. Often, producers of ZVI do not know the source of iron ore, nor do they characterize impurities in their feedstock. An example of this feedstock is shown in Figure 2.2.

Peerless Metal Powders and Abrasives (Detroit, MI), the source of ZVI for this study, has supplied the ZVI for several field PRBs (e.g., Former Naval Air Station Moffet Field in Mountain View, CA (FRTR 2002), Elizabeth City US Coast Guard Facility in Elizabeth City, NC, and the Denver Federal Center, CO (Wilkin and Puls 2003)). Peerless ZVI consists of irregularly-shaped rod-like and angular particles. It has a particle size range of 2.4 – 0.30 mm (-8 + 50 mesh sieve), a d_{50} of 0.72mm, a uniformity coefficient (d_{60}/d_{10}) of 3.77, and a concavity index ($d_{30}^2/d_{60}*d_{10}$) of 0.88.

Figure 2.2: Waste iron millings, before further milling to create ZVI.

Specific surface areas for ZVI from Peerless and other vendors are reported in Table 2.2. Most of the ZVI particles have specific surface areas between 1 and 2 m^2/g. Specific information about the bulk composition of Peerless ZVI is not available, but bulk analysis of another source of ZVI, Master Builders (Cleveland, OH), has indicated a composition of 90% Fe with smaller fractions of other metals, including < 3% copper, < 2% chromium, and 2.4% carbon (Hardy and Gillham 1996).

Table 2.2: Comparison of specific surface areas reported for ZVI

Site	Specific Surface Area (m^2/g)	ZVI Source[A]	Reference
Laboratory	1.9	Connelly-GPM	Lackovic et al. 2000
Laboratory	1.40-1.55	Connelly-GPM	Ritter et al. 2002
Vapokon Site, Denmark	1.8	Connelly-GPM	Lai et al. 2006
Laboratory	1	Master Builders	Roberts et al. 2002
Laboratory	1	Master Builders	Devlin et al. 1998
Laboratory	1.1	Master Builders	Hardy and Gillham 1996
USCG Support Center; Elizabeth City, NC	1.1	Master Builders	Puls et al. 1999b
Laboratory	2.53 ± 0.44	Peerless	Lien and Wilkin 2005
Moffett Field; Mountain View, CA	1.5	Peerless	Yabusaki et al. 2001
Laboratory	0.74	Unnamed iron foundry	O'Hannesin and Gillham 1998
Laboratory	0.98-1.75	VWR	Mackenzie et al. 1999

A: Sources: Connelly-GPM (Chicago, IL), Master Builders (Aurora, OH), VWR (West Chester, PA)

2.2.2 Properties of FeS

The microbial activity of sulfate-reducing bacteria, populating the anoxic regions of the subsurface and marine sediments, creates sulfide (Renock et al. 2009; Goldhaber and Kaplan 1974). Because of the relative abundance of iron, several iron sulfide minerals may form, including amorphous FeS, mackinawite (FeS), pyrrhotite (FeS), troilite (FeS), greigite (Fe_3S_4), marcasite (FeS_2), and pyrite (FeS_2) (Rickard 1969a). However, mackinawite is often one of the first iron sulfide phases to form in reduced iron and sulfur systems (Berner 1967); over time, it transforms to the more stable phases, such as ordered mackinawite (structure shown in Figure 2.3), then greigite, and finally pyrite and pyrrohtite (Wolthers et al. 2005a). However, before the bulk transformation of the iron monosulfide phase, there is evidence that the surface takes on a mixed iron (II) / iron (III) character, not unlike the greigite surface, in aqueous conditions, and even at low temperatures (Renock et al. 2009; Herbert et al. 1998). Unlike pyrite, mackinawite and

greigite can be dissolved in hydrochloric acid and are therefore termed “acid-volatile sulfides” (AVS) (Goldhaber and Kaplan 1975).

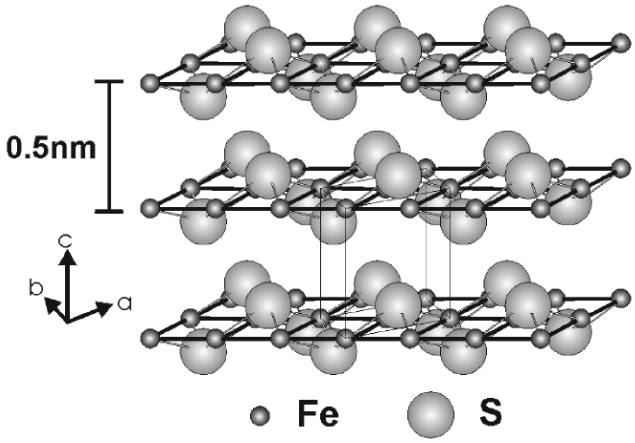

Figure 2.3: Structure of mackinawite (Wolthers et al. 2003).

A variety of methods have been used to synthesize FeS in the laboratory. Abiotic techniques include reacting sulfide with either metallic iron (Lennie et al. 1995; Berner 1964) or ferrous iron (Rickard 1969a), while the sulfate reducing species *Desulfovibrio desulfuricans* was shown to produce mackinawite after six months of being grown in an Fe^{2+}/Fe^{3+} media at pH 8 (Rickard 1969b).

A range of values has been reported for the surface area of synthetic FeS. Some estimates put the specific surface area at 350 m^2/g, although values reported in the literature are as low as 4 m^2/g (Wolthers et al. 2003). The point of zero charge (PZC) for disordered mackinawite is around pH 7.5 (Jeong et al. 2008; Wolthers et al. 2005a). Mackinawite produced through the reaction of sulfide with ferrous iron, the technique used in this research, has been shown to produce laminar prisms 2 to 5.7 nm thick, and 3 to 10.8 nm long, with a specific surface area of 380 ± 10 m^2/g (Ohfuji and Rickard 2006). This description matches that of the mackinawite produced by Gallegos et al. (2007).

2.2.3 Interactions between reactive media and the aqueous phase

Once installed in the subsurface, ZVI and FeS have the potential to remove contaminants because of their ability to change geochemical conditions in the groundwater and interact directly with contaminants. Both ZVI and FeS provide a reducing potential that can degrade some contaminants or change the solubility of others, possibly resulting in the precipitation of solid phases. In addition, the FeS itself, or the surface coating of ZVI may remove contaminants via sorption. Finally, FeS has the added advantage of providing a source of sulfide, which can couple with metal cations to form relatively insoluble metal sulfides.

Both ZVI and FeS may participate in electrochemical reactions, changing reduction-oxidation (redox) conditions in the groundwater. The degree to which species take part in such reactions is determined by the redox potential, E_H. The E_H (referenced to the standard hydrogen electrode) is related to pe, the negative log of the electron activity, by the following (Stumm and Morgan 1996):

$$E_H = 2.3\frac{RT}{F}pe \qquad \textbf{(2.1)}$$

where F is Faraday's constant (9.65 x 10^3 C/mol), T is the temperature in Kelvin, and R is the universal gas constant (8.314 J/mol-K) (Stumm and Morgan 1996).

Important elements in ZVI and FeS systems in groundwater are iron, sulfur, hydrogen, oxygen, and, for some contaminant sites, nitrogen. A summary of possible redox reactions for these species is shown in Table 2.3.

Table 2.3: Half-reactions for iron, sulfur, hydrogen, oxygen, and nitrogen (Stumm and Morgan 1996)

Reaction	Log K at 25° C	Standard Electrode Potential (V) at 25° C
$\frac{1}{2}Fe^{2+} + e^- = \frac{1}{2}Fe(s)$	-7.5	-0.44
$H^+ + e^- = \frac{1}{2}H_2(g)$	0.0	0.00
$\frac{1}{2}S(s) + H^+ + e^- = \frac{1}{2}H_2S(g)$	2.9	0.17
$\frac{1}{8}SO_4^{2-} + \frac{5}{4}H^+ + e^- = \frac{1}{8}H_2S + \frac{1}{2}H_2O$	5.3	0.31
$Fe^{3+} + e^- = Fe^{2+}$	13.0	0.77
$\frac{1}{8}NO_3^- + \frac{5}{4}H^+ + e^- = \frac{1}{8}NH_4^+ + \frac{3}{8}H_2O$	14.9	0.88
$\frac{1}{6}NO_2^- + \frac{4}{3}H^+ + e^- = \frac{1}{6}NH_4^+ + \frac{1}{3}H_2O$	15.1	0.90
$Fe(OH)_3(s) + 3H^+ + e^- = Fe^{2+} + 3H_2O$	16.0	0.95
$\frac{1}{5}NO_3^- + \frac{6}{5}H^+ + e^- = \frac{1}{10}N_2 + \frac{3}{5}H_2O$	21.6	1.25
$\frac{1}{4}O_2(g) + H^+ + e^- = \frac{1}{2}H_2O$	20.8	1.23

In addition to redox chemistry, changes in pH will affect the speciation of solutes in the aqueous phase, which in turn affects the potential for solids precipitation as shown in the aqueous-phase reactions specific to each reactive material considered below.

2.2.3.1 ZVI chemistry

As noted above, ZVI is the most commonly used reactive material in existing PRBs. It can treat contaminated groundwater through a combination of processes, including redox reactions, precipitation reactions, and sorption. ZVI has been shown to be an effective agent to remove organics, heavy metals, radionuclides, and nutrients, among other contaminants (RTDF 2001). Although the specific reaction is clearly a function of the

contaminant and may be affected by the constituents in the groundwater, the reaction is often a surface reaction, and thus requires contact between the contaminant and a reactive surface site (Weber 1996).

In the following discussion of PRB geochemistry, reactions for the removal of chlorinated organics and metals are presented, as they are the dominant contaminants treated in field PRBs. In the case of chlorinated organics, the contaminant is degraded as the oxidation of ZVI is coupled with the reductive dechlorination of the organic, RCl (Powell et al. 1998):

$$Fe^0 + RCl + H^+ = Fe^{2+} + RH + Cl^- \quad \textbf{(2.2)}$$

In Equation 2.2, the contaminant has been reductively dechlorinated. While the contaminant may require further dechlorination (e.g. reductive dechlorination of PCE produces TCE), this reaction shows a degradation pathway that, when repeated, may entirely degrade daughter products.

The sequestration of metals or metalloids may occur via a variety of mechanisms, including surface adsorption, surface complexation or (co)precipitation, which may be coupled to redox reactions if the element in question is redox-active, as are arsenic and chromium (Scherer et al. 2000, Lien and Wilkin 2005, and references therein), as shown below for chromium:

$$CrO_4^{2-} + \frac{3}{2} Fe^0(s) + 4\,H_2O = Cr^{3+} + \frac{3}{2} Fe^{2+} + 8\,OH^- \quad \textbf{(2.3)}$$

Note that this reduction has not sequestered the contaminant; rather it is now in a reduced form. This, however, is an important step: for both arsenic and chromium, as reduction from the more oxidized species (As(V) and Cr(VI) to As(III) and Cr(III)) ultimately results in a less mobile species. For example, following the reduction of chromium, the contaminant may be removed via the precipitation of a mixed Fe/Cr solid, as shown below (Powell et al. 1998). It should be reinforced that these equations demonstrate only one possible removal route for chromium: i.e., it may be removed in a variety of solids,

not just as an iron (oxyhydr)oxide. Field data, however, confirm that chromium sequestered in the reactive material is in the trivalent state (Wilkin et al. 2005):

$$(1-x)\,Fe^{3+} + (x)\,Cr^{3+} + 2\,H_2O = Fe_{(1-x)}Cr_xOOH(s) + 3\,H^+ \qquad \textbf{(2.4)}$$

A key feature of ZVI geochemistry is the fact that water itself, as well as non-contaminant solutes that naturally occur in groundwater, also interact with ZVI. Because they are often present in vastly greater stoichiometric abundance than the contaminant(s), water or those other solutes may dominate the reactions of the reactive material by controlling its oxidation (Gillham and O'Hannesin 1994). For example, at the PRB in Elizabeth City, NC, the influent concentration of chromium was approximately 3 mg/L, and the influent concentration of sulfate was about 50 mg/L. In this PRB, Mayer (1999) estimated that biologically-mediated reduction of sulfate to sulfide would consume 50 times more ZVI than reducing Cr(VI) to Cr(III).

Water is clearly ubiquitous in groundwater systems, and oxygen is also often present, albeit at low levels. ZVI is thermodynamically unstable in water (e.g., Table 2.3) and may therefore be oxidized by water. When this occurs, the pH increases and hydrogen gas is produced, as shown below:

$$Fe^0(s) + 2\,H_2O = Fe^{2+} + H_2(g) + 2\,OH^- \qquad \textbf{(2.5)}$$

When dissolved oxygen is the oxidant, ZVI may be oxidized to the ferrous or the ferric state. This oxidation produces an increase in pH, although hydrogen gas is not produced. The oxidation to ferrous iron is shown below:

$$2\,Fe^0(s) + O_2 + 2\,H_2O = 2\,Fe^{2+} + 4\,OH^- \qquad \textbf{(2.6)}$$

Other possible redox-active species commonly found in groundwaters include nitrate and sulfate; the reductions of these species are shown in Table 2.3. Therefore, ZVI may also be oxidized by nitrate, which may be reduced to ammonia or nitrogen gas (Kielemoes et al. 2000) and sulfate, which may be reduced to sulfide, provided that the reaction is biologically-mediated (Al-Agha et al. 1995). According to Table 2.3, the coupling of the

oxidation of ZVI with reduction of nitrate or sulfate will also increase the pH. Therefore, the reactions shown above indicate that the oxidation of ZVI by contaminants, water, or native groundwater constituents is accompanied by an increase in pH and a decrease in the E_H of the aqueous system, as electrons from the ZVI are released. For example, Wilkin and Puls (2003) show that for a ferrous/ferric iron redox couple, a pH increase is tied to an E_H decrease. This E_H reduction is often seen in the field (Powell et al. 1998). The E_H changes in a system will, in turn, affect the speciation of potential solids, which has implications for the suite of solids – and gases – that may be formed in a porous matrix.

Table 2.4 shows average values and standard deviations for pH and E_H, as well as other parameters, from a selection of ZVI PRBs. Data from the groundwater influent to the PRBs and inside the PRBs are presented, which illustrates changes in the geochemistry as the groundwater flows into these ZVI barriers. The increase in pH and decrease in E_H discussed above are evident, as is the stoichiometric abundance of naturally-occurring solutes relative to typical contaminant concentrations.

Table 2.4: Statistics for groundwater constituents from selected ZVI PRBs (after Henderson and Demond 2007). Values are concentrations in mg/L (with mmol/L in parenthesis) unless otherwise noted. pe values are calculated from reported field measurements of E_H.

Constituent	influent		internal	
	mean	st. dev.	mean	st. dev.
pH (-)	6.9	0.9	9.4	1.1
E_H (mV)	175	175	-341	131
pe (-)	3.0	3.0	-5.8	2.2
alkalinity (mg/L as $CaCO_3$ (meq/L))	239 (11.9)	168 (8.4)	214 (10.7)	237 (11.8)
calcium	229 (5.7)	202 (5.0)	111 (2.8)	173 (4.3)
chloride	75 (2.1)	48 (1.3)	83 (2.3)	57 (1.6)
total carbonate	381 (6.4)	183 (3.1)	393 (6.6)	354 (5.9)
oxygen	1.7 (0.05)	1.7 (0.05)	0.4 (0.01)	0.6 (0.02)
magnesium	41 (1.7)	31 (1.3)	27 (1.1)	31 (1.3)
nitrate	17 (0.3)	35 (0.6)	2 (0.03)	5 (0.1)
sulfate	562 (5.8)	728 (7.6)	338 (3.5)	531 (5.5)

2.2.3.2 FeS chemistry

The removal of heavy metals by iron sulfides may occur via adsorption, precipitation, or co-precipitation. In general, a heavy metal that forms a sulfide phase that is more soluble than iron sulfide is expected to primarily adsorb to the iron sulfide; conversely, less soluble metal sulfides are expected to precipitate, either as discrete metal sulfide phases or as co-precipitates with iron sulfide (Coles et al. 2000). In either case, iron sulfides have been demonstrated to be effective scavengers (either via adsorption or precipitation) of heavy metals. Laboratory work has shown that pyrrhotite and pyrite have removed Zn^{2+}, Cd^{2+}, Pb^{2+}, and Hg^{2+} (Hyland et al. 1990; Jean and Bancroft 1986; Brown et al. 1979), and mackinawite has removed Mn^{2+}, Co^{2+}, Ni^{2+} (Arakaki and Morse 1993; Morse and Arakaki 1993) , Pb^{2+} and Cd^{2+} (Coles et al. 2000), and Hg2+ (Jeong et al. 2007). These laboratory findings have been corroborated in the field, as the presence of iron sulfides in anoxic sediments is correlated to the removal of heavy metals (Wolthers et al. 2003; Morse and Luther 1999; Huerta-Diaz et al. 1998).

Like ZVI, FeS can remove chlorinated organics, also through reductive dechlorination (Butler and Hayes 2001; Butler and Hayes 2000; Butler and Hayes 1999; Butler and

Hayes 1998). Also like ZVI, FeS can remove both redox active and non redox active metals, although there is evidence that FeS may be more effective than ZVI at removing certain metals. Because they are in a reduced form, the iron and sulfide in FeS have the ability to reduce redox-active metals like chromium (Boursiquot et al. 2002; Patterson et al. 1997) or arsenic (Farquhar et al. 2002). Chromium reduced by mackinawite can then be precipitated as a mixed Fe(III)/Cr(III)phase (Mullet et al. 2004). The presence of sulfide allows for the formation of insoluble metal sulfides (Billon et al. 2001; Herbert et al. 2000; Rochette et al. 2000), or mixtures of solid phases within FeS (Coles et al. 2000). Mackinawite can also bind materials through sorption (Wolthers et al. 2005a; Wolthers et al. 2005b).

As with ZVI, the interaction of FeS with non-contaminant species, rather than contaminant species, is perhaps of greater importance in assessing subsurface behavior and longevity, due to the relative stoichiometric abundance of the former. Like ZVI, FeS may be oxidized by oxygen. Unlike FeS, FeS may be stable in water, depending on the prevailing E_H conditions and aqueous concentrations of ferrous iron and sulfide. If the solid is stable in water, it is still subject to maintaining equilibrium with respect to dissolution of ferrous iron and bisulfide, as governed by the following equation:

$$FeS(s) + H^+ = Fe^{2+} + HS^- \qquad \textbf{(2.7)}$$

which has a solubility constant $K_s = 10^{-3.5\pm0.25}$ (Rickard 2006). Note that this dissolution increases the pH, a phenomenon also observed with ZVI systems. Although FeS has not been used in field installations, an increase in pH caused by the addition of FeS to water has been observed by (Lee 2009). Because both iron and sulfur are present in a reduced state in Equation 2.7, these elements may be oxidized if they are paired with a reduction reaction, thus decreasing the system E_H. For example, manganese dioxide, MnO_2, and oxygen can both abiotically oxidize FeS (Schippers and Jørgensen 2002). Whether the iron, sulfide, or both elements in FeS are oxidized depends on the prevailing E_H conditions (Table 2.3).

However, the pairing of the oxidation and reduction reaction may require biological mediation. For example, has been shown that nitrate and Fe(III) oxides do not abiotically oxidize FeS (Schippers and Jørgensen 2001). However, nitrate-reducing sulfide-oxidizing bacteria can mediate the oxidation of iron sulfides by nitrate (Lin et al. 2009). A slightly more reduced form of nitrogen, nitrite, may chemically oxidize FeS to greigite, Fe_3S_4, via intermediate reactions with HS^- to form sulfur (Lin et al. 2009). A reduction reaction for nitrite is shown in Table 2.3.

Another feature of the FeS system is the possibility of surface complexation reactions such as the following:

$$FeS(s) + H^+ = FeSH^+ \quad \textbf{(2.8)}$$

$$FeS(s) + H_2S(aq) = Fe(SH)_2^0 \quad \textbf{(2.9)}$$

There is still uncertainty about equilibrium constants for the iron sulfide system (Davison et al. 1999), in part because the reactivity of FeS is very sensitive to preparation method (Davison 1991). Wolthers et al. (2005a) and Rickard (2006) concluded that the solubility of FeS is not controlled by any one reaction; rather, the controlling reaction is a function of pH.

Rickard (2006) presents evidence that FeS dissolution has two regions. The first is an acidic region in which dissolution is pH-dependent, as shown by Equation 2.7; in the second region, dissolution is independent of pH and is governed by Equation 2.10.

$$FeS(s) = FeS^0(aq) \quad \textbf{(2.10)}$$

where FeS^0 is a monomer of the aqueous species $Fe_nS_n(aq)$. The transition between these regions depends on the sulfide concentration. Rickard (2006) adjusted total sulfide by equilibrating solutions with $H_2S(g)$, as shown in Figure 2.4.

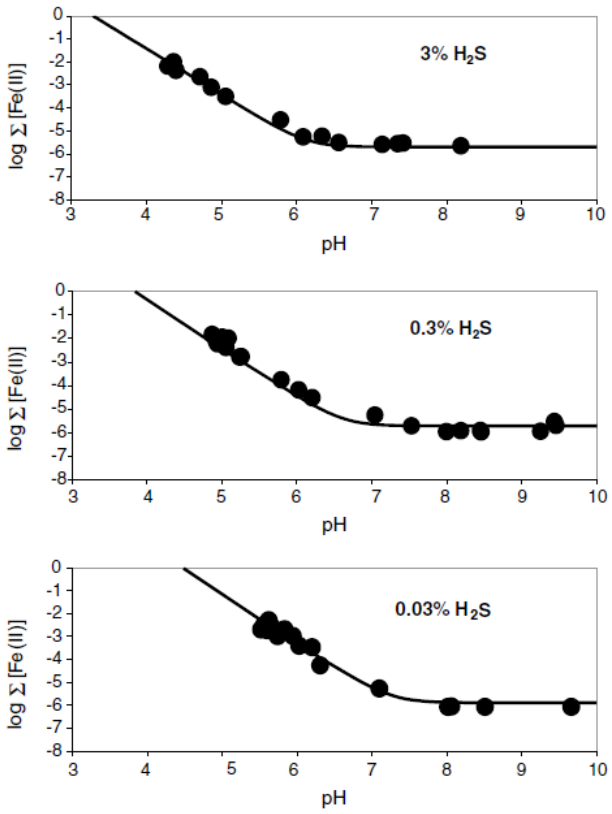

Figure 2.4: Plots from Rickard 2006 showing the total aqueous Fe(II) concentration as a function of pH and the H_2S(g) concentration, which controlled the total sulfide in the system.

Figure 2.4 shows that for a batch system with a headspace H_2S gas concentration of 3%, the transition between the pH-dependent regime and the pH-independent regime occurs at approximately pH 6.5. With less total sulfide, the transition point occurs at higher pH values. At 100% H_2S(g), the sum of the sulfide species in the system is 10^{-1} M.

Whether the reactive material is FeS or ZVI, equilibrium chemistry indicates that pH and E_H changes are expected. The following section considers how these changes may affect the reactive media itself.

2.2.4 Media corrosion and aging

Many mechanisms for the removal of contaminants are coupled, either directly or indirectly, to changes in the reactive media. For ZVI, Equations 2.2 and 2.3 show this

direct linkage as corrosion of the reactive material, while the sorption of a contaminant to a hydroxide phase is coupled indirectly, for the hydroxide would not be produced without the corrosion of ZVI. For FeS, Equation 2.7 shows that the dissolution of FeS may produce the sulfide necessary to precipitate metal-sulfide phases. If FeS is oxidized, it may form mixed and higher-valence iron oxides, such as goethite, or it may transform to the more oxidized iron sulfide forms such as greigite (a mixed Fe(II)/Fe(III) phase) or pyrite (Lennie et al. 1997). However, the aging of iron sulfide from mackinawite to other phases such as greigite or pyrite may decrease reactivity towards some compounds (Jeong and Hayes 2003; Butler and Hayes 2001).

It is important to note, then, that even if reduced iron PRB materials are oxidized, the resulting solid phases can still provide a certain level of protection from contaminants. The corrosion products of zero-valent or ferrous iron are, themselves, capable of sequestering contaminants, both cations and species like arsenic that are complexed as oxyacids (Furukawa et al. 2002; Su and Puls 2001b; Hingston 1981; Kinniburgh and Jackson 1981). For arsenic, As(V) and As(III) were shown to be taken up as inner-sphere complexes by the ZVI corrosion products lepidocrocite and magnetite (Manning et al. 2002), and the dissolution (some of which is catalyzed by Fe^{2+}) and recrystallization of iron oxides can result in arsenic being more strongly bound to the iron phases (Pedersen et al. 2006). However, changes in the oxidation rate of the reactive media will affect the removal mechanisms and removal capacity. Furthermore, since contaminant removal mechanisms vary from contaminant to contaminant, changes in the reactive material are expected to affect different contaminants in different ways (Devlin and Allin 2005).

It is expected that with continuing treatment, and thus continuing exposure to the aqueous phase, that the rate of corrosion of the reactive media will change with time. Therefore, it is not surprising that time-dependent reaction rates for organic contaminant removal are often noted in batch and column work with ZVI (e.g., Klausen et al. 2003; Devlin et al. 1998; Agrawal and Tratnyek 1996; Gillham and O'Hannesin 1994). For example, Farrell (2000) investigated the degradation half-life of TCE with ZVI in solutions of chloride/sulfate and nitrate. Over a time frame of nearly two years, the half-life with chloride and sulfate increased from 6.7 to 42 hours, while the half-life in the nitrate

solution increased from 25 to 58 hours. Evidence for the time-dependent behavior of the removal of metals is more sparse; but it may not be as strongly dependent on aging. For example, work with a mixed contaminant solution of 1,2-dichloroethylene and arsenic showed a decrease in the removal rate of the organic, but not of arsenic (Köber et al. 2005).

As a general rule, increasing concentrations of anions correspond to higher corrosion rates, which, in turn, increases the reactivity of iron (Devlin and Allin 2005; Liang et al. 2003). However, increased corrosion does not always correspond to increased reactivity. As discussed above, corrosion may lead to the precipitation of solids, which may reduce permeability and/or passivate the reactive material by preventing further access of the aqueous phase to reactive sites. Some research suggests that chloride and sulfate do destabilize passivating films and promote corrosion (Devlin and Allin 2005; Johnson et al. 1998). However, sulfate has also been shown to inhibit arsenic removal by ZVI, as have phosphate, molybdate, chromate, and silicate (Melitas et al. 2002; Su and Puls 2001a; Lackovic et al. 2000). Silicate has also been shown to inhibit the degradation of TCE (D'Andrea et al. 2005; Klausen et al. 2001). Nitrate has been shown to inhibit corrosion, passivating the iron surface (D'Andrea et al. 2005; Devlin and Allin 2005; Farrell et al. 2000; Schlicker et al. 2000), but it has also been shown to promote corrosion (Liang et al. 2000). Carbonate also cuts both ways: initially, it may increase corrosion of ZVI, but with time, the precipitation of carbonate solids passivates the reactive media surface (Devlin and Allin 2005; Klausen et al. 2003; Köber et al. 2002; Gu et al. 1999; Wieckowski et al. 1983). Higher-valency iron (hydr)oxides are also expected to passivate the reactive media (Ritter et al. 2002).

While the specific effects of groundwater constituents on reactivity are temporally complex and matrix-dependent, there is evidence that corrosion products may continue to treat contaminants. However, one of the major concerns – from a perspective of PRB longevity – is the formation of solid phases, for these phases will impact the permeability of the barrier. The following section discusses solid phases that have been observed in field installations of ZVI PRBs.

2.2.5 PRB mineralogy

Given the nature of the reactive media, iron is readily available in ZVI or FeS PRBs. As common groundwater constituents, so too are calcium and carbonate: in a literature review of PRBs, it was found that typical calcium and carbonate levels in groundwater may range from the tens to hundreds of mg/L; Table 2.4 summarizes these findings for several constituents (Henderson and Demond 2007). In the aqueous phase, carbonate is a diprotic acid, moving between $H_2CO_3^*$ (carbonic acid), HCO_3^- (bicarbonate), and CO_3^{2-} (carbonate) as the pH changes. This equilibrium chemistry is shown in the following equations (Stumm and Morgan 1996) :

$$H_2CO_3^* = HCO_3^- + H^+ \quad (\log K = -6.35) \qquad \textbf{(2.11)}$$

$$HCO_3^- = CO_3^{2-} + H^+ \quad (\log K = -10.33) \qquad \textbf{(2.12)}$$

According to the above, when pH is greater than 8.3, carbonate becomes the dominant species.

The pH increases and redox changes expected in ZVI and FeS PRBs alter the speciation of groundwater constituents and create conditions favorable for the precipitation of carbonate and iron solids, among others. Precipitation of solids is indeed commonplace in most PRBs constructed of ZVI. Some commonly observed solid phases include iron hydroxides and oxyhydroxides, carbonates, and sulfides, which are summarized in Table 2.5. Note that the prevailing redox conditions will influence the redox state of iron and sulfur, thus dictating which solids – assuming equilibrium with the solution redox state – may be allowed to form. Although these are species that have been observed in ZVI PRBs, they are possible precipitates in FeS systems as well.

Table 2.5: Formation reactions for solids found in PRBs (Jambor et al. 2005; Liang et al. 2003; Wilkin and Puls 2003).

Solid name	Reaction	Average oxidation state of iron
Iron (hydr)oxides		
Ferrous Hydroxide	$2H_2O + Fe^{2+} = 2H^+ + Fe(OH)_2$	2
Magnetite	$4H_2O + Fe^{2+} + 2Fe^{3+} = 8H^+ + Fe_3O_4$	8/3
Ferrihydrite	$3H_2O + Fe^{3+} = 3H^+ + Fe(OH)_3$	3
Hematite	$3H_2O + 2Fe^{3+} = 6H^+ + Fe_2O_3$	3
Goethite (α-FeOOH)	$2H_2O + Fe^{3+} = 3H^+ + FeOOH$	3
Carbonate-bearing		
Aragonite / Calcite	$Ca^{2+} + CO_3^{2-} = CaCO_3(s)$	n/a
Siderite	$Fe^{2+} + CO_3^{2-} = FeCO_3(s)$	2
Carbonate Green Rust (CGR)	$4Fe^{2+} + 2Fe^{3+} + 14H_2O + CO_3^{2-} = [Fe^{II}_4Fe^{III}_2(OH)_{12}][CO_3 \cdot 2H_2O] + 12H^+$	7/3
Iron Sulfides		
Mackinawite	$Fe^{2+} + HS^- = FeS + H^+$	2
Pyrite	$Fe^{2+} + 2HS^- = FeS_2 + 2H^+$	2
Greigite	$2Fe^{3+} + Fe^{2+} + 4HS^- = Fe_3S_4 + 4H+$	8/3
Sulfate-bearing		
Sulfate Green Rust	$4Fe^{2+} + 2Fe^{3+} + 14H_2O + SO_4^{2-} = [Fe^{II}_4Fe^{III}_2(OH)_{12}][SO_4 \cdot 2H_2O] + 12H^+$	7/3

The following figures are reproductions of SEM micrographs of some of these solids. These images provide a reference point for comparison of some of the SEM results presented in Chapter 5. Figure 2.5 shows green rust, siderite, goethite, and aragonite from the Y-12 ZVI PRB in Oak Ridge, TN (Phillips et al. 2003). Figure 2.6 also shows carbonate green rust from a ZVI column experiment (Gu et al. 1999); its morphology is different than the green rust obtained from a field site (Figure 2.5a).

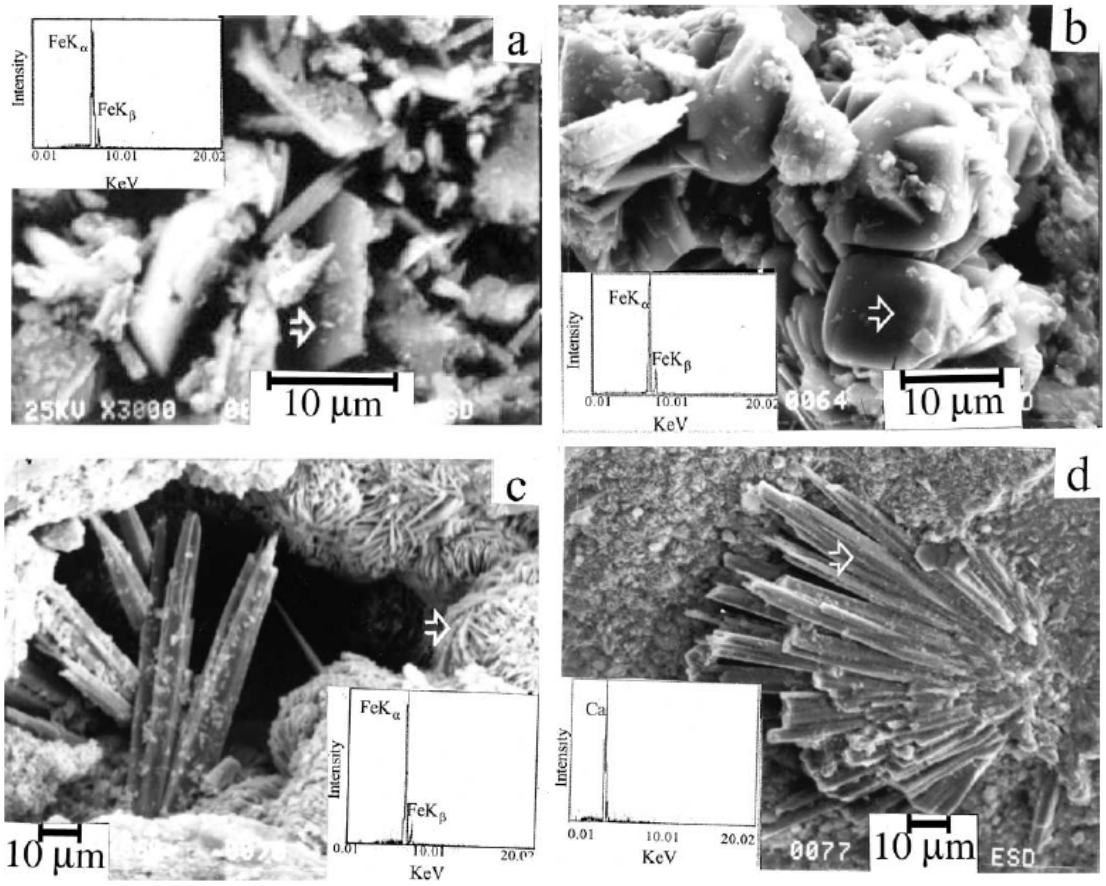

Figure 2.5: SEM micrographs and EDS spectra of (a) green rust, (b) siderite, (c) goethite, and (d) aragonite observed at the Y-12 Pathway 2 PRB in Oak Ridge, TN (Phillips et al. 2003).

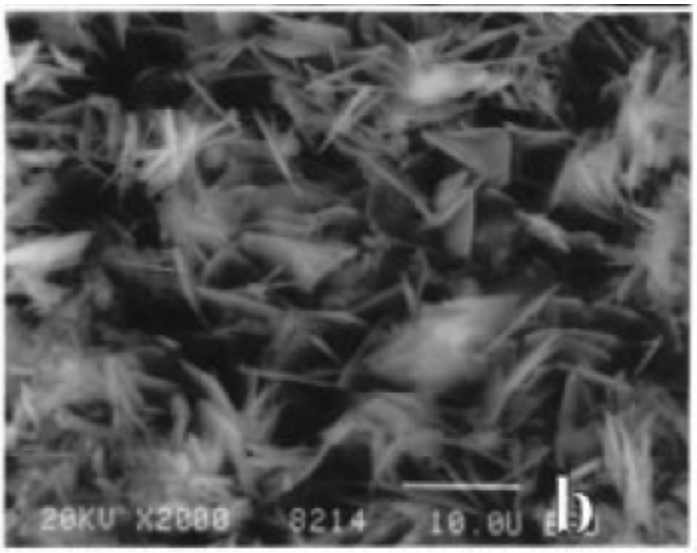

Figure 2.6: SEM micrograph of carbonate green rust from a ZVI column receiving 32 mM HCO_3^- and 7.3 mM SO42- (Gu et al. 1999).

Redox conditions will influence the oxidation state of iron (shown in the last column of Table 2.5) and other species with multiple oxidation states, such as sulfur. The oxidation state of constituent elements will determine which solids may form in a given system; the densities of these solids will, in turn, have an impact on the permeability of a porous matrix, as less dense solids will occupy a larger volume per mass, thus reducing the permeability to a greater degree than a denser solid. Figure 2.7 shows, as an example, the effect of prevailing pH and pe conditions on solid speciation in the iron-carbonate system. Solids lines indicate dominance regions for solids (sulfide species not shown), while dashed lines indicate the dominance regions for aqueous phase species. The activities of the Fe, CO_2, and S species are 10^{-5}, 10^{-2}, and 10^{-3} M, respectively (Wilkin and Puls 2003).

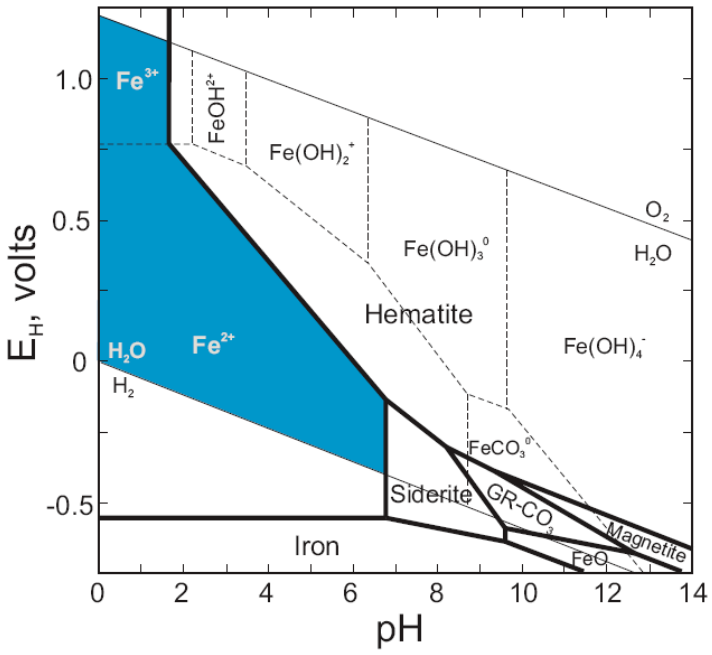

Figure 2.7: Stability diagrams for the aqueous iron-carbonate system (top), and iron-sulfur-carbonate system (bottom) (from Wilkin and Puls 2003).

In Figure 2.7, it is seen that siderite ($FeCO_3$) and carbonate green rusts (labeled GR-CO_3 in this diagram), which have been observed in PRBs, occur at pH values between 7 and 12 and E_H values between, approximately, 0 and -500 mV, but are not expected to form in other conditions.

The precipitates observed in PRBs are of great concern, for they may affect the performance of the barrier either by changing the hydraulic conductivity or by changing the reactivity. The effect of non-contaminant precipitates is non-negligible, for such precipitates dominate any solids containing the contaminant(s) of interest. For example, at the UMTRA site (Durango, CO), uranium made up only 0.2% (by weight) of the precipitates (Matheson et al. 2002) and solid-phase uranium was below the detection limit at the Y-12 site (Oak Ridge, TN), although it was being removed in the barrier (Phillips et al. 2000).

Identifying the exact nature and distribution of solids in the field is quite challenging, for many species are metastable, and the measurement techniques may change the solids themselves (Phillips et al. 2003). In the field, it is thought that the oxidation of ZVI first produces $Fe(OH)_2$ (Farrell et al. 2000). As oxidation continues, ferrous hydroxide may transform to magnetite (Fe_3O_4), which is electrically conductive, or to green rusts, which are also reactive (Su and Puls 2004; Phillips et al. 2003; Melitas et al. 2002; Ritter et al. 2002). Further oxidation of these species may produce entirely ferric solids, which may age from the poorly crystalline ferrihydrite to the more crystalline goethite (α-FeOOH) and lepidocrocite (γ-FeOOH) (Abdelmoula et al. 1996). However, the transformation of ferrihydrite into more crystalline iron oxides is strongly environment dependent; hematite is favored at pH 7 and 8, while goethite is favored at pH 12 (Schwertmann and Murad 1983).

Of particular concern are the carbonate and iron (hydr)oxide solids that may form. First, these solids have been observed to dominate precipitates in many PRBs (Gillham 1999). Secondly, carbonate solids (Devlin and Allin 2005; Klausen et al. 2003; Köber et al. 2002; Roberts et al. 2002) and iron (hydr)oxides (Ritter et al. 2002) have been shown to passivate iron surfaces. Of these two types of solids, carbonate solids are often the major cause of passivation (Jeen et al. 2006; Zhang and Gillham 2005). In addition to potentially reducing the reactivity of the iron surface, all solids will reduce the hydraulic conductivity of the reactive media to some degree.

The temporal and spatial behavior of precipitates is also complex. Zhang and Gillham (2005) have suggested a degree of self-regulation of precipitates in a ZVI column: in a region of the column, oxidation of ZVI will increase the pH and make precipitation of $CaCO_3$(s) favorable, the precipitation of which will passivate the ZVI, limiting further reaction in that region of the column. Subsequent precipitation may occur further downstream of the column. Zhang and Gillham found that in ZVI columns treating TCE, at a flow rate of 0.95 m/d, and an influent concentration of 100 mg/L $CaCO_3$(aq), precipitation reached a maximum value of about 30 mg/g ZVI, and then progressed through the column as a front. A moving front was also observed by Jeen et al. (2006) in ZVI columns also receiving TCE and 100 mg/L of $CaCO_3$ in the influent, at flow rates of 2.3 m/d. These columns lost about an order of magnitude of hydraulic conductivity over the course of 2000 pore volumes.

2.3 Hydraulic considerations

As discussed above, the precipitation of solids has been observed in numerous PRBs. Relating this solids accumulation to the hydraulic properties of a PRB is therefore critical to an understanding of PRB behavior.

2.3.1 Permeability and porosity

The hydraulic conductivity of a saturated porous medium is defined by Darcy's Law (Jury and Horton 2004), which states that the volumetric flow rate per unit area is proportional to the gradient of the hydraulic head:

$$q = -K\nabla\psi_T \qquad \textbf{(2.13)}$$

In this equation, q is the Darcy velocity, the volumetric flux Q/A_{bulk}; it is also known as the specific discharge or superficial velocity. The proportionality constant in Equation 2.13 is the hydraulic conductivity, K, and ψ_T is the total head, the energy per unit weight of water relative to the reference state. Note that the Darcy velocity is a not a true

velocity, for the actual average water velocity, $\bar{v}$, is higher because the area for flow is less than the bulk area, as described by the porosity, n (i.e., $\bar{v} = q/n$) (Charbeneau 2000). In a one-dimensional vertical column, Darcy's Law may be written as

$$q = -K\frac{\partial \psi_T}{\partial z} = -K\frac{\partial(\psi_P + \psi_z)}{\partial z} = -K\left(\frac{\partial \psi_P}{\partial z} + 1\right) \quad \textbf{(2.14)}$$

where ψ_P and ψ_Z are the heads due to the pressure and the gravitational potential, respectively. Separating variables and integrating yields

$$\psi_P = -\left(1 + \frac{q}{K}\right)z - C \quad \textbf{(2.15)}$$

where C is a constant of integration. Using the above, a change in hydraulic conductivity may be calculated from a change in pressure head.

The hydraulic conductivity, K, is related to the intrinsic permeability of a porous matrix as follows (Nutting 1930):

$$K = \frac{k\rho g}{\mu} \quad \textbf{(2.16)}$$

where k is the intrinsic permeability of the porous medium, ρ is the density, g is the gravitational constant, and μ is the dynamic viscosity of the liquid. This relationship divides the hydraulic conductivity into a portion that is attributable to liquid phase properties $(\rho g/\mu)$ and a portion attributable to properties of the porous medium properties (k), such as the porosity and tortuosity.

One of the most well-known and successful models to define the intrinsic permeability is the Kozeny-Carman equation. This equation is built upon the hydraulic radius approach to fluid flow, in which the velocity in a capillary, u, is given by (after Charbeneau 2000):

$$u = \frac{\rho g R_h^2}{c\mu}\frac{\Delta\psi}{\Delta L_e} \quad \textbf{(2.17)}$$

where R_h is the hydraulic radius (the flow cross section divided by the wetted perimeter), ΔL_e is the effective length of the capillary (i.e., accounting for tortuosity), $\Delta\psi$ is the difference in total head along the capillary, and c is a shape coefficient that varies between 2 (for flow in a circular capillary) and 3 (for flow between flat plates). Some formulations of the Kozeny-Carman equation show specific surface area as a parameter, which was recognized by Kozeny (1928) and others as important for describing the shape and size of particles (Carman 1939). Assuming the porous medium is composed of spherical particles, the actual flow is on average 45° from the mean flow direction (due to tortuosity), and that a shape factor of 2.5 is appropriate, Equation 2.17 may be transformed to the following:

$$q = -\frac{d_e^2}{180}\frac{n^3}{(1-n)^2}\left(\frac{\rho g}{\mu}\right)\nabla\psi_T \qquad \textbf{(2.18)}$$

where n is the porosity, and d_e is the effective grain diameter, and may be either the d_{50} or d_{10}. Based on Equation 2.18, the intrinsic permeability is given by the following:

$$k = \frac{d_e^2}{180}\frac{n^3}{(1-n)^2} \qquad \textbf{(2.19)}$$

The Kozeny-Carman equation is limited to conditions in which the flow is laminar, and it does not work well for irregular particles, in which the measured and calculated specific surface areas are not similar. However, the Kozeny-Carman equation has been shown to predict, within a factor of 3, the hydraulic conductivity of homogenized soils with $10^{-1} < K < 10^{-11}$ m/s (Chapuis and Aubertin 2003).

Based on Equation 2.19, a loss of porosity – due to precipitation – can be equated with a loss of permeability. Figure 2.8 shows this reduction in permeability as a function of the fractional porosity reduction.

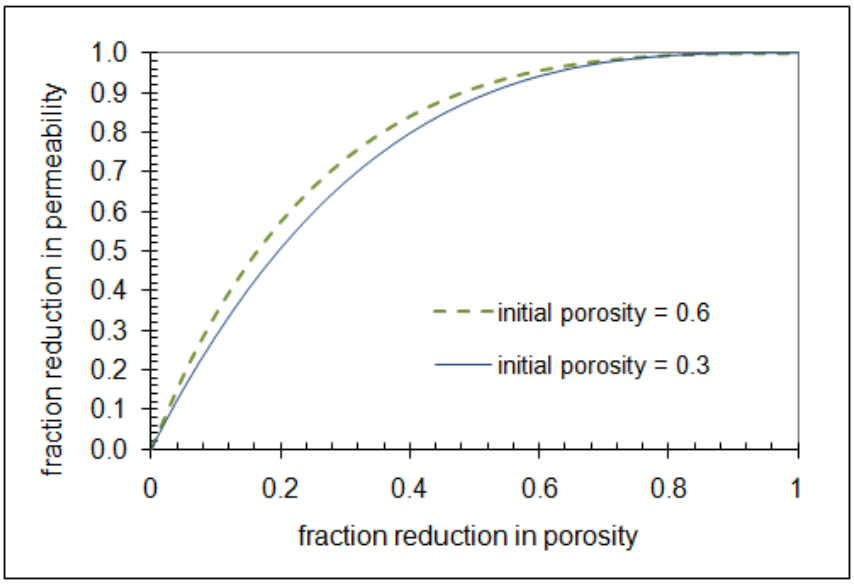

Figure 2.8: Relationship between porosity reduction and permeability loss as predicted by the Kozeny-Carman equation.

If a porous matrix is not saturated, the void space is no longer occupied by only the water phase. In this case, the porosity, n, includes both the water content, θ (volume of water / total volume), and the gas content, a (volume of gas / total volume). One possible approach to estimate the unsaturated hydraulic conductivity of a porous matrix is an empirical power law function, such as that proposed by Wyllie (1962):

$$k_{rw} = S_e^{\,3} \tag{2.20}$$

where k_{rw} is the relative permeability to the wetting phase, (such that hydraulic conductivity to the wetting phase is $K_H = k_{rw} * K_{H,sat}$), and S_e is the effective saturation, which is related to the wetting phase saturation, $S_w = \theta/n$, and the residual wetting phase saturation, S_{wr}, as follows:

$$S_e = \frac{S_w - S_{wr}}{1 - S_{wr}} \tag{2.21}$$

Demond et al. (1996) describes other methods for estimating unsaturated hydraulic conductivity. In the absence of capillary pressure measurements of ZVI, the empirical power law approach is used in this research, since Demond et al. (1996) show that the

power law equation of Wyllie (1962) is a satisfactory model of the unsaturated hydraulic conductivity

2.3.2 Hydraulic conductivity in PRBs

A PRB must balance the needs for high hydraulic conductivity and for high reactivity. The first consideration suggests the use of large-grained media, while the second suggests smaller media with a high specific surface area. However, numerical simulations of PRBs indicate that such a balance may not be impossible to achieve. Simulations by Starr and Cherry (1994) and Smyth (1997) show that while the discharge through the PRB increases as the hydraulic conductivity of the PRB increases, the increase was minimal once the hydraulic conductivity of the PRB was 10 times that of the aquifer.

In a literature review (Henderson and Demond 2007), information was collected for 16 ZVI PRBs operating in the field. Hydraulic information from these PRBs is summarized in the following tables and figures: Table 2.6 provides an overview of the hydraulic conductivities of the PRBs and aquifers, while Table 2.7 summarizes flow rates reported from field ZVI PRBs. Figure 2.9 shows the distribution of reported hydraulic conductivities for aquifers and PRBs, and Figure 2.10 shows the ratio of PRB to aquifer hydraulic conductivity (this ratio could only be calculated for those four sites which reported the hydraulic conductivities of both the PRB and the surrounding aquifer).

Table 2.6: Statistics for reported hydraulic conductivities (m/d) of field ZVI PRBs and aquifers.

Hydraulic conductivity statistic	PRB n=7	Aquifer n=10
mean	34.6	5.4
standard deviation	27.2	4.4
median	30.9	6.0
max	86.0	11.7
min	2.4	0.1

Table 2.7: Summary of linear flow velocity from PRB statistical analysis.

Statistic (n=17)	Flow velocity (m/d)
mean	1.1
standard deviation	1.7
median	0.25
min	0.01
max	5.7

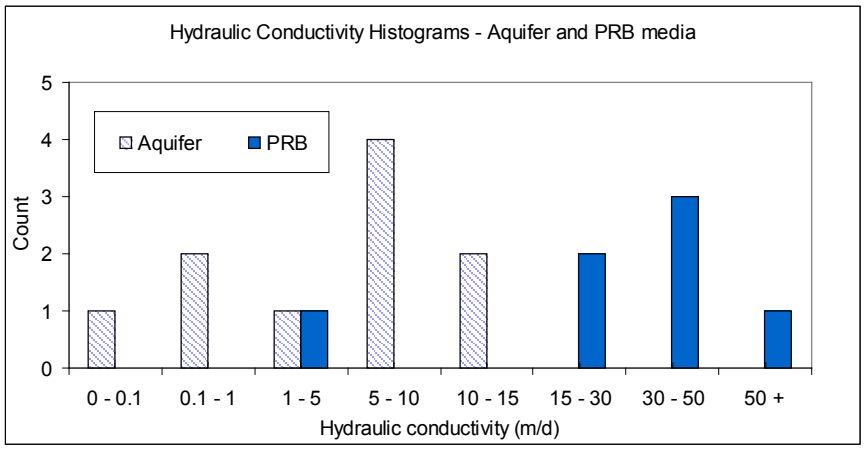

Figure 2.9: Distribution of measured hydraulic conductivity for aquifers and ZVI reactive media.

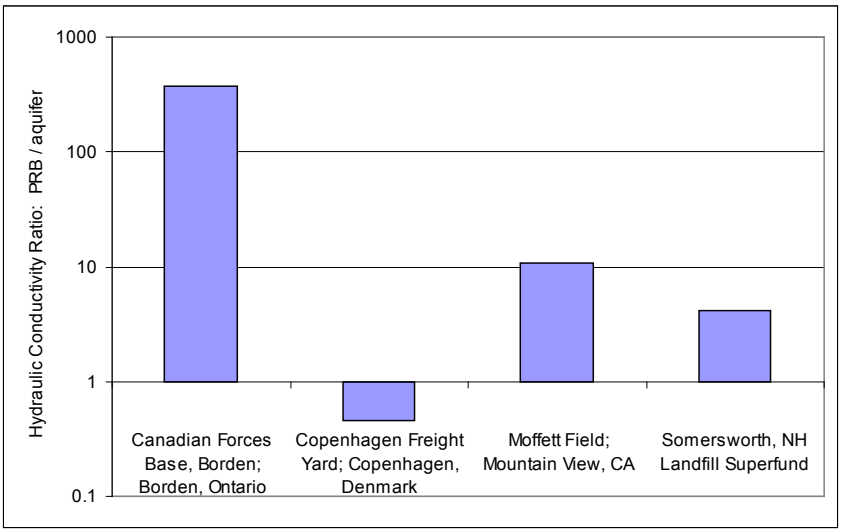

Figure 2.10: Ratio of PRB to aquifer hydraulic conductivity for four PRB sites.

Of the four PRBs shown in Figure 2.10, only the Copenhagen Freight Yard had a lower hydraulic conductivity than the surrounding aquifer. As noted in Section 2.1.3, this PRB experienced operational difficulties. Whether the reported hydraulic conductivity at the

Copenhagen Freight Yard was for fresh or reacted ZVI is not clear, but it is clear that a range of hydraulic conductivities have been used in the field. Again, with only sporadic reporting of PRB and aquifer hydraulic conductivities, there is not enough field evidence to suggest a permissible lower limit for the ratio between the two.

Attempts to mitigate the hydraulic effects of precipitation in ZVI have largely been ad hoc. Typically, a pretreatment zone (PTZ) is placed immediately upgradient of a PRB and contains gravel or sand – possibly with reactive media mixed in. It has been suggested in the literature, that such a zone allows for precipitate formation with minimal permeability reduction, and can therefore reduce potential clogging at the upgradient of a PRB (Sarr 2001; Dwyer 2000b).

Measurable porosity losses are often concentrated at the upgradient aquifer/PRB interface (Kamolpornwijit et al. 2003; Liang et al. 2003; FRTR 2002; Naftz et al. 2000; Vogan et al. 1998). For example, at the PRB at the US Coast Guard Facility in Elizabeth City, after 4 years of operation, the thickness of precipitates at the upgradient section (<8 cm into the PRB, which is 60 cm long in the direction of flow) was 10-50 μm; further into the PRB, the precipitation wass discontinuous and <5 μm thick (Wilkin et al. 2003). However, at this PRB, there was an "indication that a precipitation front is progressively moving through the PRB" (Wilkin and Puls 2003). At the PRB in upstate New York, the maximum $CaCO_3$(s) mass fraction, 6%, was observed within the first 15 cm of the upgradient interface; this fraction was less than 1% at distances greater than 15 cm into 90 cm barrier (Vogan et al. 1999). Similarly, at the PRB at the Denver Federal Center in Lakewood, CO, precipitation thicknesses of 10-50 μm are reported for samples within the first 20 cm of the upgradient interface (the length of this PRB in the direction of flow is 1.2m) (FRTR 2002).

Overall, porosity losses for the Denver Federal Center were estimated to be 0.35-0.5% per year due to calcite and siderite precipitation (McMahon et al. 1999). Other PRBs have reported larger estimated values. For example, a 9.7% porosity loss over 18 months was estimated for the PRB at Lowry Air Force Base, CO (RTDF 2001; EPA 1999).

Based on the Kozeny-Carman equation (Figure 2.8), a 10% porosity loss could correspond to a 40% reduction in permeability.

Although *qualitative* hydraulic conductivity losses are reported in the field (e.g., Vapokon, Denmark (Lai et al. 2006), Y-12, Oak Ridge, TN (Phillips et al. 2003; Gu et al. 2002)), *quantified* permeability losses are not often reported. Of the 16 PRBs investigated by Henderson and Demond (2007), only the PRB at Copenhagen Freight Yard, Denmark reported the actual loss of conductivity. In that PRB, precipitates reduced the hydraulic conductivity from 5.2 m/d to 0.7 m/d, an 87% decrease, during the first year of operation (RTDF 2001; Kiilerich et al. 2000; Kjeldsen and Fulgsang 2000).

Adverse hydraulic changes may also be caused by gas formation or biomass accumulation. When ZVI reacts with water, hydrogen gas may be produced (Equation 2.5), and hydrogen gas has been observed at several field PRBs, including the Denver Federal Center, CO (McMahon et al. 1999) and the Industrial Facility, NY (Vogan et al. 1999), the Elizabeth City, NC PRB (Blowes et al. 1999), and the Intersil Site in California, where $H_2(g)$ was near saturation values (RTDF 2001; Warner et al. 1998). At the Copenhagen Freight Yard, it was estimated, based on Reardon's (1995) estimate of anaerobic corrosion rates and $H_2(g)$ production, this PRB could produce enough H_2 to fill 5% of the void space on a daily basis (RTDF 2001).

The production of other gases is also possible, especially as microbial activity comes into play. For example, methane was reported in the *in situ* PRB at the Copenhagen Freight Yard (Denmark) (Kiilerich et al. 2000) and in the *ex situ* Cell C at the UMTRA site (Durango, CO) (Morrison et al. 2002a), presumably from the activity of methanogenic bacteria. *Ex situ* PRBs, which are confined systems, frequently report plugging due to gas production (e.g., Portsmouth, OR and UMTRA, Durango, CO) (Morrison et al. 2002a; Mackenzie et al. 1999; Korte et al. 1997a). However, porosity reduction due to gas production has not been reported for *in situ* PRBs, perhaps suggesting that any gas that is formed is able to migrate out of the barrier.

However, the assumption that gas may be able to diffuse out of the PRB may not always be appropriate. As PRBs are often capped with materials such as clays, geotextiles,

pavement, or some combination thereof, diffusion may be limited. For example, the Denver Federal Center PRB in Lakewood, CO was constructed with a bentonite cap (McMahon et al. 1999), the PRB at Monticello, UT, had a a geotextile used to cap the ZVI in the vadose zone (US DOE - Subsurface Contaminants Focus Area 2000). The Copenhagen Freight Yard PRB – which, as noted above – was estimated to produce enough hydrogen gas to fill 5% of its void space every day (RTDF 2001), was capped with geotextile, clay, and pavement (Kiilerich et al. 2000).

The produced gas may also be consumed by bacteria. In Gate 2 of the Denver Federal Center PRB, it was hypothesized that the H_2 (g) produced was utilized by sulfate-reducing bacteria as an electron donor, thus keeping the H_2(g) concentration low (Wilkin and Puls 2003). The provision of substrate for bacterial communities raises concerns about hydraulic conductivity loss due to biofouling, and biomass-related hydraulic changes have been observed in some laboratory studies (e.g., Vandevivere and Baveye 1992; Taylor et al. 1990). However, they have not been identified as an issue in the field. Microbial growth was minimal at Intersil (Sunnyvale, CA), Moffett Field (Mountain View, CA), Industrial Site (NY), Lowry AFB (CO) and Somersworth (NH) (Gu et al. 1999). Although observed at locations like USCG (Elizabeth City, NC) and Denver Federal Center (CO) (Wilkin et al. 2003), it did not measurably impact performance perhaps because biofouling is unlikely at the high pH and low E_H values often observed in ZVI PRBs (Liang et al. 2000).

In the laboratory, the evolution of hydrogen gas in ZVI columns has been observed to affect permeability, as the gas phase occupies large pores and reduces the permeability of the media. However, running columns in an upflow mode has been shown to reduce entrapment of evolved gases (Kamolpornwijit and Liang 2006; Vikesland et al. 2003). This gas production tends to make permeability measurements of ZVI, both in the field and in the lab, inherently noisy. For example, Jeen et al. (2006) show hydraulic conductivity data in which sequential measurements may vary by a factor of 5.

Nonetheless, ZVI columns with an influent solution containing 300 mg/L $CaCO_3$ have shown $CaCO_3$(s) occupying 7% of the initial porosity, and gas occupying about 10%, the

latter creating a hydraulic conductivity loss from 50 to 80% (Zhang and Gillham 2005). Mackenzie et al. (1999) used ZVI columns with deaerated water and concluded that the observed 5-10% porosity loss was due to solids formation resulting from the oxidation of ZVI by oxygen, since distinct gas bubbles were not observed. Using the anaerobic corrosion rate of iron reported by Reardon (1995), it was concluded that $Fe(OH)_2$ precipitation, and possibly a film of hydrogen gas, was likely to be the cause of the initial observed porosity losses. However, at later times in the experiment, the precipitation of $Fe(OH)_2$, $FeCO_3$, and $CaCO_3$ was argued to be responsible for the majority of porosity losses the longer a column was run (Mackenzie et al. 1999).

2.4 Modeling of PRB systems

Because the actual PRB system involves the interaction of multiple aqueous and solid species in a porous matrix with spatial and kinetic limitations, models of PRB performance represent simplifications of the system. In order to model the hydraulic behavior of a PRB, it is, for example, difficult to predict permeability from porosity, because grain size, non-contributing porosity, pore jamming, and pore cementation also have strong effects on permeability (Civan 2001).

For the hydraulic behavior of PRBs, several models have assumed equilibrium conditions. With assumptions of equilibrium, the saturation index, defined as the difference between the actual pH and the pH at which solution ions would be in equilibrium with a solid phase (SI = pHactual – pHequilib) (Köber et al. 2002), provides an indication of whether solids will precipitate. Liang (2003) used the saturation index as a tool by which to compare field data to the equilibrium state of that system; calculations of oversaturation were indications that a solid would be likely to precipitate. Using this approach, severe clogging over a 10-year period was predicted at the Monticello (UT) PRB, and, indeed, this PRB experienced a hydraulic conductivity loss of two orders of magnitude over 5.5 years of operation (Mushovic et al. 2006). Clearly, assumptions of equilibrium can only capture certain aspects of a system. For example, the groundwater entering a PRB may itself not be in equilibrium with respect to the solids in the

surrounding aquifer (Lindberg and Runnells 1984). Therefore, it is expected that kinetic limitations may prevent the aqueous phase from reaching equilibrium with the solid phase in a PRB.

Models that have taken kinetics into account have made other simplifying assumptions. For example, Mayer et al. (2001) did not model the loss of permeability due to a loss of porosity, and Li et al. (2006) assumed that the specific surface area of iron particles was constant (Li et al. 2006). Also of note, the models of Jeen et al. (2007), Li et al. (2006), and Mayer et al. (2001) did not account for the effects of hydrogen gas on permeability, if they accounted for its production at all. The latter model assumed that generated gas bubbles could exit to the atmosphere immediately, which may be a reasonable assumption, given that no field PRBs have reported losses of hydraulic conductivity due to gas buildup. However, the hydraulic importance of hydrogen gas in a field site, as noted in Section 2.3.2, may depend on the establishment of H_2-utilizing sulfate-reducing bacteria and the use of materials such as clay or geomembranes that affect the ability of gas to diffuse out of a PRB.

Nonetheless, numerical modeling using the Kozeny-Carman equation and assumption of uniform precipitation has qualitatively captured features of ZVI in the field and in columns. A model of the PRB at Elizabeth City allowed the supersaturation of minerals and simulated 20 years of operation, during which time the porosity decreased from 0.5 to 0.36 (Mayer et al. 2001). Mayer et al. (2001) note that this decrease matched the prediction of 10% porosity loss over 5 years (Blowes et al. 1999). For laboratory columns, phenomena such as moving fronts of precipitation (discussed in Section 2.2.5) have been captured in models. Jeen et al. (2007) used the Kozeny-Carman equation and allowed the reactive surface area to change. With a linear flow velocity of 0.1 m/d in a ZVI barrier, and an influent $CaCO_3$ concentration of 200 mg/L, the simulated porosity loss, due to precipitation of aragonite, $CaCO_3$(s), ranged from 0.55 to 0.38 over the column.

2.5 Summary

ZVI PRBs have been installed in numerous sites to treat a variety of groundwater contaminants; these PRBs have, for the most part, performed well. However, the very properties that make ZVI and FeS proven (and potential) candidates for PRBs are the properties that may cause operational problems. In particular, the interaction of these media with naturally occurring oxidants, such as water, oxygen, or nitrate, is expected to produce a pH increase, an E_H decrease, and, in the case of ZVI, hydrogen gas. The pH increase is problematic because of the potential for solids to precipitate. These solid and gas phases, in turn, are expected to impact the performance of the PRB by reducing the hydraulic conductivity or the reactivity of the media. Because a variety of factors have been postulated to control PRB longevity, it was necessary to investigate which of these factors may be critical in determining solids production. Therefore, an analysis of data from field PRBs available in the literature was conducted; this study is described in the next chapter.

Chapter 3: Statistical Analysis of ZVI Field PRBs

3.1 Introduction

The complexity of PRB systems, along with challenges inherent in characterizing subsurface systems that may take years to achieve steady-state – or quasi-steady-state, has made it difficult for engineers to fully characterize these systems. Since few *in situ* PRBs have failed due to other than design flaws, it is difficult to determine factors controlling longevity by looking at failure rates. Rather, the existing information must be analyzed for factors that place a PRB "at-risk," defined as an increased likelihood of compromised performance, based on reports of a decrease in permeability or in contaminant removal. In ZVI PRBs, high concentrations of dissolved solids, dissolved oxygen, carbonate, nitrate, and/or sulfate are expected to favor media corrosion and solids precipitation. This tendency would be exacerbated at high pH or low E_H.

The objective of the work presented in this chapter is to analyze the geochemical and performance data from existing *in situ* ZVI PRBs and determine whether certain geochemical parameters can indeed indicate a potential for reduced PRB longevity. In particular, three categories of parameters were considered: 1) master variables like pH and E_H, 2) parameters related to the quantity of precipitation (these precipitation parameters include total dissolved solids, dissolved oxygen and the concentrations, mass fluxes and cumulative fluxes of individual solutes [e.g., CO_3^{2-}, Ca^{2+}], and saturation indices); and 3) parameters relating to reactivity promotion or inhibition that are not expected to precipitate (e.g., anions like NO_3^- and Cl^-). It is recognized that these categories of parameters are not mutually exclusive: pH affects carbonate speciation, carbonate affects iron reactivity, etc.

3.2 Data collection and statistical methods

Because of the limited comprehensive geochemical data available in the literature, the quantitative analysis was, of necessity confined to 16 ZVI *in situ* field PRBs treating organics and/or metals for which extensive information was available (Table 3.1). *Ex situ* barriers were not included in the analysis for they clearly operate under different conditions than *in situ* barriers, rendering them more prone to failure. Based on information provided in the literature and geochemical principles, 37 parameters were selected for consideration (Tables 3.2 and 3.3). Frequently, ranges of values, or values from several sampling events, or values from different monitoring wells were reported for a given parameter at a particular PRB. To distill this information to a single data point for the analysis, an arithmetic mean was used for all parameters except hydraulic conductivity, hydraulic gradient, and flow rate. Reported values of these parameters frequently ranged over several orders of magnitude, so a geometric mean was used. In some cases, geochemical parameters such as total dissolved solids and alkalinity were not reported and were calculated from the available information. Sites were assigned a 0 or 1 indicating failure, or 0 or 1 indicating at-risk if a loss in permeability, a loss in reactivity, or some other indication of compromised performance was reported. The collated data are presented in Table 4 and the calculated parameters in Table 5.

Table 3.1: Summary of PRBs analyzed.

Name & Location	Contaminants	Performance Notes	Reference
Beka Site; Tubingen, Germany	TCE; cDCE; VC	Despite the precipitation of calcium, iron, and magnesium carbonates, no changes in hydraulics were observed	(Klein and Schad 2000)
Canadian Forces Base, Borden; Borden, Ontario	TCE; PCE	Lower contaminant concentrations could have been achieved with higher Fe : sand ratio, or a more reactive Fe. Observed half-lives were ~6 times larger than those in bench tests, and rate constants decreased over time. Observations with time: 1 yr - no visual or microbial fouling; 2 yrs - no precipitates or cementation; 4 yrs - precipitates observed; 5 yrs - no decline in performance.	(RTDF 2001; O'Hannesin and Gillham 1998; O'Hannesin 1993; Nicholson et al. 1983)
Chlorinated Solvent Manufacturing; Sydney, Australia	PCE; CTET	Estimated 1.3% porosity loss/yr (based only on precipitation of FeS)	(Duran et al. 2000)
Denver Federal Center; Denver (Lakewood), CO	TCE; cDCE; 1,1-DCA; 1,1,1-TCA; 1,1-DCE	Hydraulic mounding and bypassing observed. Estimates of 0.35% - 0.5% porosity loss/yr due to calcite and siderite -- most at upgradient interface. Some cemented areas after 5 years; effects on K_H are expected. After 4 years, 10-50 µm layer of precipitates. at the upgradient interface (<20 cm into barrier). After 5 years, 50% of upgradient interface pore space is lost. $H_2(g)$ production decreases with time in Gate 2.	(Wilkin and Puls 2003; Wilkin et al. 2003; FRTR 2002; RTDF 2001; McMahon et al. 1999)
Dover Air Force Base, Area 5; Dover, DE	PCE; TCE; DCE	Little precipitation observed after 18 months; no conclusions about long-term performance drawn. pH increases were not controlled by the pyrite-Fe mix, and the pyrite-Fe mix was not as effective at removing DO as was pure Fe.	(FRTR 2002; Liang et al. 2001; RTDF 2001; Gavaskar et al. 2000; Yoon et al. 2000)
Haardkrom Site; Kolding, Denmark	Cr	Failure attributed to heterogeneous loading of PRB, which has created "exhaustion of iron-chromate removal capacity in the wall" (RTDF 2001).	(RTDF 2001; Kjeldsen and Fulgsang 2000)
Industrial Facility; Upstate New York	TCE; cDCE; VC	Expect 10% porosity loss over 2 years. 6% (wt) $CaCO_3$ at upgradient interface; < 1% 15 cm into barrier. Calcite & aragonite dominate at upgradient interface. No adverse effects of precipitates noted: VOC removal constant; hydraulic conductivity close to fresh iron; water velocity constant. Expect H_2-utilizing and sulfate-reducing bacteria, but no microbial films observed. Suggest periodic scarification of upgradient face if necessary.	(Vogan et al. 1999; Vogan et al. 1998)
Intersil Semiconductor Site; Sunnyvale, CA	TCE; cDCE; VC	Pea gravel PTZ has resulted in precipitation of minerals and pretreatment of contaminants, and is therefore expected to increase life. Production of $H_2(g)$ (to near saturation) taken as indication of continued PRB operation (i.e., Fe corrosion continues).	(Sorel et al. 2003; RTDF 2001; Warner et al. 1998)

Table 3.1: Summary of PRBs analyzed (continued).

Name & Location	Contaminants	Performance Notes	Reference
Lowry Air Force Base; CO	TCE	Estimate 9.7% porosity loss over 18 months. Groundwater flow has probably not been affected by porosity changes. "During a clogging study performed in May 1997, 18 months after installation, calcite, aragonite, "green rusts", amorphous iron hydroxides, and magnetite were observed. A porosity loss of 9.7% for the 18-month operational period was estimated from the investigation" (RTDF 2001).	(ESTCP 2003; FRTR 2002; RTDF 2001; EPA 1999; Jain et al. 1999; Vogan et al. 1998)
Moffett Field; Mountain View, CA	TCE; cDCE; PCE	Aragonite, calcite, iron carbonate hydroxide found at upgradient interface. Some precipitates found in well silt traps.	(Gavaskar et al. 2005; FRTR 2002; RTDF 2001; Yabusaki et al. 2001; EPA 1999; Sass et al. 1998)
Monticello Mill Tailing Site; Monticello, Utah	U; Mn; Mo; NO_3^-; As; Se; V	Postulated that PTZ of gravel mix allows precipitation to occur upgradient of the reactive media. In contrast to column tests, effluent Fe concentrations are kept low by precipitation of $Fe(OH)_2$. 1 foot of upgradient mounding caused by 3 orders of magnitude hydraulic conductivity loss in pure ZVI; PTZ hydraulic conductivity remains unchanged.	(Mushovic et al. 2006; Morrison et al. 2002; Purdy et al. 2002; Morrison et al. 2001; RTDF 2001; Ott 2000; US DOE - Subsurface Contaminants Focus Area 2000)
Somersworth, NH Landfill Superfund	PCE; TCE; 1,2-DCE; VC	Initial decrease in hydraulic conductivity due to settling.	(O'Hara 2006; Sivavec et al. 2003)
USCG Support Center; Elizabeth City, NC	Cr; TCE	Estimate 1-2% porosity loss per year, but this should not affect the PRB permeability for 10 years. No hydraulic performance changes observed over 5 years.	(Wilkin et al. 2003; FRTR 2002; RTDF 2001; Puls et al. 1999a)
Vapokon Site, Denmark	PCE, TCE, cis-DCE, VC, other chlorinated organics	No "pronounced" deterioration of chlorinated organic removal. Expect hydraulics change in future - limiting lifespan to 10 years. Tracer study reveals zones of low permeability and clogging that change flow path. 0.88% porosity loss per year between March 2000 and August 2003	(Lai et al. 2006; Lai et al. 2005)
Y-12 Plant; Pathway 2; Oak Ridge, TN	U, NO_3^-	Oxidation, precipitation, and cementation increased from 15 to 30 months (depends on depth). Akagenite transforms to goethite, and amorphous FeS into mackinawite. Fe oxy(hydr)oxides dominate precipitates; calcite not observed until 30 months. 30-80% of Fe filings are replaced by FeOOH corrosion rinds in cemented zones; Fe reactivity decreases. Based on corrosion, estimate lifespan of 5-10 years.	(Gu 2005a; Gu 2005b; Phillips et al. 2003; FRTR 2002; Gu et al. 2002; Korte 2001; Liang et al. 2001; Ott 2000; Phillips et al. 2000)

In Table 3.1, "PTZ" stands for pre-treatment zone

Table 3.2: Reported geochemical data for PRBs.

Name	Run Time (yr)	Flow Rate (m/d)	pH in	pH int	E_H int (mV)	TDS in (mg/L)	DO in (mg/L)	Ca in (mg/L)	Ca int (mg/L)	Alk in (mg/L as $CaCO_3$)	Alk int (mg/L as $CaCO_3$)	CT in (mg/L as CO_3)	Fe(T) int (mg/L)	SO_4 in (mg/L)	NO_3 in (mg/L)	Cl in (mg/L)	PTZ	Δ hydr.	Δ perf.	failure	at-risk
Beka Site, Germany	2	0.01	7.1	10.1	-310	800	1	150	20.0	338	711	464	0.25	88	7	75	1	0	0	0	0
Canadian Forces Base, Borden, Canada	10	0.08	8.1	8.7	-330	1065	3.4	278	102	140	82.0	170	7.5	609	0.6	2	0	0	0	0	0
Chlorinated Solvent Manufacturing, Australia	1	0.60	4.6	7.0	-217	1907	0	-	-	15.3	185	941	201	159	-	-	0	0	0	0	0
Copenhagen Freight Yard, Denmark	3	0.11	7.7	9.4	-	1222	0.2	130	3.6	503	299	625	0.2	110	0.2	180	1	1	0	0	1
Denver Federal Center, CO	7	0.07	7.5	9.7	-190	1100	0.61	107	2.7	440	350	560	0.04	260	2	64.5	1	1	0	0	1
Dover Air Force Base, Area 5, DE	4	2.45	5.1	10.8	-320	106	4.2	4.5	7.0	6	41.9	129	0.06	19.5	8	30	1	0	0	0	0
Haardkrom Site, Denmark	2	0.06	8.7	10.5	-	322	5.2	53.5	5.0	121	188	143	0.2	85.5	34.4	-	0	0	1	1	1
Industrial Facility, NY	4	0.45	7.4	9.5	-459	489	-	90.6	9.6	239	61.1	310	0.16	17.2	0.31	47.4	1	0	0	0	0
Intersil Semiconductor Site, CA	8	0.23	7.8	10.5	-350	686	2	-	-	235	7.4	291	0.05	400	-	-	1	0	0	0	0
Lowry Air Force Base, CO	8	0.30	6.9	10.0	-725	2900	0.66	290	-	530	-	795	-	1000	4	100	0	0	0	0	0

Table 3.2: Reported geochemical data for PRBs (continued).

Name	Run Time (yr)	Flow Rate (m/d)	pH in	pH int	E_H int (mV)	TDS in (mg/L)	DO in (mg/L)	Ca in (mg/L)	Ca int (mg/L)	Alk in (mg/L as $CaCO_3$)	Alk int (mg/L as $CaCO_3$)	CT in (mg/L as CO_3)	Fe(T) int (mg/L)	SO_4 in (mg/L)	NO_3 in (mg/L)	Cl in (mg/L)	PTZ	Δ hydr.	Δ perf.	failure	at-risk
Moffett Field, CA	9	0.05	7.1	10.5	-372	820	0.1	158	10.9	288	20.2	400	0.02	350	2.4	40.9	1	0	0	0	0
Monticello Mill Tailing Site, UT	3	5.70	6.5	9.0	-388	1300	0.44	339	211	237	22	460	0.17	1170	118	123	1	1	1	1	1
Somersworth Landfill, NH	4	0.09	6.5	10.0	-750	400	2.0	82.7	37.5	338	175	660	0	13.7	0.5	84.3	0	0	0	0	0
USCG Support Center, NC	7	4.45	6.1	9.8	-400	290	1.1	12.5	5.3	50	38	155	0.05	49	1.1	40	0	0	0	0	0
Vapokon Petrochem. Works, Denmark	7	0.27	7.2	9.8	-133	754	3.4	179	42.7	314	64.5	422	2.5	120	-	46.0	1	1	0	0	1
Y-12 Plant; Pathway 2, TN	6	2.20	6.7	9.0	-166	887	2.8	190	93.0	360	868	604	14.9	92.5	85	50.5	1	1	1	0	1

In Table 3.2, “in” and “int” indicate influent and internal values, respectively; “Run Time” is the time from a PRB’s construction to the most recently published information regarding that PRB; “PTZ” stands for Pre-Treatment Zone; “Δ hydr.” and “Δ perf.” indicate reported changes in hydraulics and performance, respectively; “at-risk” indicates a PRB for which either a hydraulic change, a performance change, or failure has been reported.

Table 3.3: Calculated geochemical data for PRBs.

Name	Legend	Ca Flux Rate ($g\ m^{-2}\ d^{-1}$)	Alk flux rate ($g\ m^{-2}\ d^{-1}$)	CT flux rate ($g\ m^{-2}\ d^{-1}$)	SO_4 flux rate ($g\ m^{-2}\ d^{-1}$)	NO_3 flux rate ($g\ m^{-2}\ d^{-1}$)	Cl flux rate ($g\ m^{-2}\ d^{-1}$)	Ca Flux ($kg\ m^{-2}$)	Alk flux ($kg\ m^{-2}$)	CT Flux ($kg\ m^{-2}$)	SO_4 Flux ($kg\ m^{-2}$)	NO_3 Flux ($kg\ m^{-2}$)	Cl Flux ($kg\ m^{-2}$)	SI Calcite	SI Aragonite	SI Siderite	SI Fe(OH)2	SI Magnetite	SI Hematite	SI Ferrihydrite	SI Goethite	at-risk
Beka Site, Germany	Beka	2.2	5.0	6.8	1.3	0.10	1.1	1.6	3.6	5.0	0.94	0.075	0.80	2.8	2.6	1.1	0.23	2.5	2.0	0.66	1.7	0
Canadian Forces Base, Borden, Canada	Borden	22.8	11.5	13.9	49.9	0.049	0.16	83.2	42.0	50.9	182	0.18	0.60	1.5	1.3	1.9	0.27	2.1	1.4	0.11	1.2	0
Chlorinated Solvent Manufacturing, Australia	CSM	-	9.2	564	95.4	-	-	-	3.4	206	34.8	-	-	-	-	2.1	-0.72	1.4	0.80	-0.50	0.57	0
Copenhagen Freight Yard, Denmark	Copen	14.3	55.3	68.8	12.1	0.022	19.8	15.7	60.5	75.3	13.2	0.024	21.7	1.2	1.1	-	-	-	-	-	-	1
Denver Federal Center, CO	DFC	7.5	30.8	39.2	18.2	0.14	4.5	19.1	78.7	100	46.5	0.36	11.5	1.4	1.2	0.03	-0.42	2.5	2.1	0.78	1.8	1
Dover Air Force Base, Area 5, DE	Dover	11.0	14.7	317	47.8	19.6	73.5	16.1	21.5	463	69.8	28.6	107	1.3	1.1	-2.6	-0.42	2.2	1.7	0.40	1.5	0
Haardkrom Site, Denmark	Haard	3.3	7.4	8.7	5.2	2.1	-	2.4	5.4	6.4	3.8	1.5	-	1.7	1.6	-	-	-	-	-	-	1
Industrial Facility, NY	IF_NY	40.8	108	139	7.7	0.14	21.3	59.5	157	204	11.3	0.20	31.1	1.00	0.85	0.50	0.04	1.6	0.78	-0.52	0.55	0
Intersil Semiconductor Site, CA	Inter	-	52.8	65.4	90.0	-	-	-	154	191	263	-	-	-	-	-2.6	-0.26	2.1	1.5	0.24	1.3	0

Table 3.3: Calculated geochemical data for PRBs (continued).

Name	Legend	Ca Flux Rate ($g\ m^{-2}\ d^{-1}$)	Alk flux rate ($g\ m^{-2}\ d^{-1}$)	CT flux rate ($g\ m^{-2}\ d^{-1}$)	SO_4 flux rate ($g\ m^{-2}\ d^{-1}$)	NO_3 flux rate ($g\ m^{-2}\ d^{-1}$)	Cl flux rate ($g\ m^{-2}\ d^{-1}$)	Ca Flux ($kg\ m^{-2}$)	Alk flux ($kg\ m^{-2}$)	CT Flux ($kg\ m^{-2}$)	SO_4 Flux ($kg\ m^{-2}$)	NO_3 Flux ($kg\ m^{-2}$)	Cl Flux ($kg\ m^{-2}$)	SI Calcite	SI Aragonite	SI Siderite	SI Fe(OH)2	SI Magnetite	SI Hematite	SI Ferrihydrite	SI Goethite	at-risk
Lowry Air Force Base, CO	Lowry	87.0	159	239	300	1.2	30.0	254	464	697	876	3.5	87.6	-	-	-	-	-	-	-	-	0
Moffett Field, CA	Moffett	8.5	15.6	21.6	18.9	0.13	2.2	28.0	51.1	71.0	62.1	0.43	7.3	1.1	0.95	-2.5	-0.45	1.9	1.3	-0.01	1.1	0
Monticello Mill Tailing Site, UT	Mont	1932	1351	2620	6670	673	701	2116	1479	2869	7303	736	768	1.5	1.4	-0.07	-0.28	1.5	0.81	-0.49	0.58	1
Somersworth Landfill, NH	Somer	7.4	30.4	59.4	1.2	0.045	7.6	10.9	44.4	86.8	1.8	0.07	11.1	2.4	2.2	-	-	-	-	-	-	0
USCG Support Center, NC	USCG	55.6	223	690	218	4.7	178	142	568	1763	557	11.9	455	0.77	0.62	-0.37	-0.07	1.9	1.2	-0.15	0.92	0
Vapokon Petrochem. Works, Denmark	Vapok	48.9	85.7	115	32.8	-	12.5	125	219	294	83.9	-	32.0	1.9	1.8	-0.12	-0.05	3.0	2.7	1.4	2.4	1
Y-12 Plant; Pathway 2, TN	Y-12	418	792	1328	204	187	111	915	1735	2909	446	410	243	2.7	2.6	3.1	0.53	3.4	3.0	1.7	2.8	1

In Table 3.3, SI stands for saturation index. The 'Legend' column indicates the site names used in Figures 3.1 - 3.4 and 3.6.

Both graphical and statistical analyses were conducted to determine which geochemical parameters are correlated with potential decreased longevity. As a first cut, the data were plotted to give a rough indication as to whether the particular parameter had any relation to classifying PRBs as at-risk. Statistical analyses included an assessment for collinearity, univariate and multivariate logistic regression, and maximization of odds ratios. The degree of linear correlation for all parameter combinations was calculated using the SPSS statistical software package (SPSS Inc., Chicago, IL). The sample correlation coefficient, also known as Pearson's correlation, is defined as (Myers 1990)

$$r = \frac{S_{xy}}{\sqrt{S_{xx} S_{yy}}} \tag{3.1}$$

where S is the residual sum of squares (either for the interaction of 2 variables or each variable singly). Variables found to be correlated at the 95% confidence level were discarded. Then, univariate logistic regression was carried out, following the approach outlined in Hosmer and Lemeshow (1989), using the SPSS software package. For the vector **x**, a set of independent, predictor variables (the geochemical parameters), the conditional probability, $\pi(\mathbf{x})$, of a dependent variable outcome of "at-risk" can be calculated from:

$$\pi(\mathbf{x}) = \frac{\exp(g(\mathbf{x}))}{1 + \exp(g(\mathbf{x}))} \tag{3.2}$$

using a linear predictor, $g(\mathbf{x})$, with coefficients β_i:

$$g(\mathbf{x}) = \beta_0 + \beta_1 x_1 + \beta_2 x_2 + \cdots + \beta_p x_p + \beta_{12} x_1 x_2 + \cdots + \varepsilon \tag{3.3}$$

where ε accounts for variations that are not covered by terms in the model. If the logistic regression considers only one variable, then this linear predictor reduces to $g(\mathbf{x}) = \beta_0 + \beta_1 x_1 + \varepsilon$. Continuously scaled variables (such as influent alkalinity), binary variables (such as the use of a pre-treatment zone), and combinations of variables may all be included in $g(\mathbf{x})$. The coefficients β_i are calculated through regression between the independent predictor variable vector **x** and $g(\mathbf{x})$. $g(\mathbf{x})$ is determined using Equation 3.2, assuming that $\pi(\mathbf{x})$ may be calculated as:

$$\pi(\mathbf{x}) = P(\text{"at\_risk"} \mid \mathbf{x}) \tag{3.4}$$

where an estimate of P("at_risk"|**x**) is based on counts of PRBs that are at-risk and those which are not (Faraway 2006; Hosmer and Lemeshow 1989).

In estimating each value of β_i, a standard error (S.E.) is estimated, and thus the Wald statistic ($\text{Wald}_i = \beta_i / \text{S.E.}(\beta_i)$) may be calculated. The Wald statistic tests the null hypothesis that $\beta_i = 0$; if the significance (or p-value) associated with the regression is acceptably small (e.g., ≤ 0.25), it may be assumed with the associated confidence level (for $p \leq 0.25$, this confidence level is 75%) that the null hypothesis may be rejected, and thus the estimate of β_i is equivalent to β_i. Based on the recommendation of Hosmer and Lemeshow (1989), variables with significance ≤ 0.25 were considered further.

In addition to logistic regression, odds ratio maximization was used to identify geochemical parameters with a strong relationship to "at-risk" PRBs. The odds ratio estimates how much more likely it is for a certain outcome (e.g., "at-risk") given an input (e.g., influent alkalinity concentration above a specified value). The odds ratio can be expressed as (Hosmer and Lemeshow 1989):

$$\psi = \frac{\pi(1)/(1-\pi(1))}{\pi(0)/(1-\pi(0))} \tag{3.5}$$

where $\pi(1)$ is the probability of being at-risk, and $\pi(0)$ is the probability of being not-at-risk.

If $\pi(\mathbf{x})$ is not known, the probabilities may be estimated with a contingency table, a 2 x 2 matrix that shows, for each possible outcome, the number of cases with each independent variable. For example, consider the parameter influent alkalinity concentration or Alk_inf (Table 3.2). If 300 mg/L is defined as the cutoff value, then of the PRB sites with Alk_inf $\geq$ 300 mg/L, 4 are at-risk, and 3 are not-at-risk. Similarly, the cases with Alk_inf < 300 mg/L are divided into 2 at-risk and 7 not-at-risk, yielding the contingency table shown in Table 3.3. The estimated odds ratio is then (4/3) / (2/7), or 4.67. This result indicates that, for this dataset, sites with Alk_inf $\geq$ 300 mg/L are 4.67 times more likely to be at-risk than those with lower Alk_inf.

Table 3.3: Example of contingency table using a cutoff value for influent concentration of alkalinity of 300 mg/L

Total n = 16	Alk_inf >= 300 mg/L	Alk_inf < 300 mg/L
at-risk	4	2
not-at-risk	3	7

Clearly, the selection of a cutoff value is integral to the calculation of an odds ratio. In this study, the odds ratio for each parameter was maximized. Cutoff values for each parameter were systematically varied over 100 steps between the minimum and maximum values for that parameter, and the maximum odds ratio was recorded. A perfect predictor, a cutoff below which all sites were not-at-risk and above which all sites were at-risk, would lead to the recording of zero values in the off-diagonal in the contingency table and thus a value of zero in the denominator of Equation 3.5. In those cases, the zero value was replaced with 0.5, as recommended by Hosmer and Lemeshow (1989). To evaluate the importance of the calculated odds ratios, significance values were computed using the two-sided Fisher Exact Test. This test, a form of the Chi-square evaluation, is appropriate for sparse datasets and evaluates whether the tested variables are independent or associated (Faraway 2006). In the current study, a significance (p-value) of 0.05 was used as the criterion for inclusion of variables for further consideration.

Finally, those parameters selected by the univariate logistic regression based on a significance ≤ 0.25 or an odds ratio Fisher Exact Test significance ≤ 0.10 were incorporated into a multivariate logistic regression model. These variables were then used together in logistic regression (Equations 3.2 - 3.4) in an attempt to judge the relative significance of the variables in determining longevity potential.

3.3 Results and discussion

3.3.1 Graphical analysis

To determine which geochemical parameters correlated with compromised PRB performance, matrix plots of all the variables were constructed, an example of which is shown in Figure 3.1.

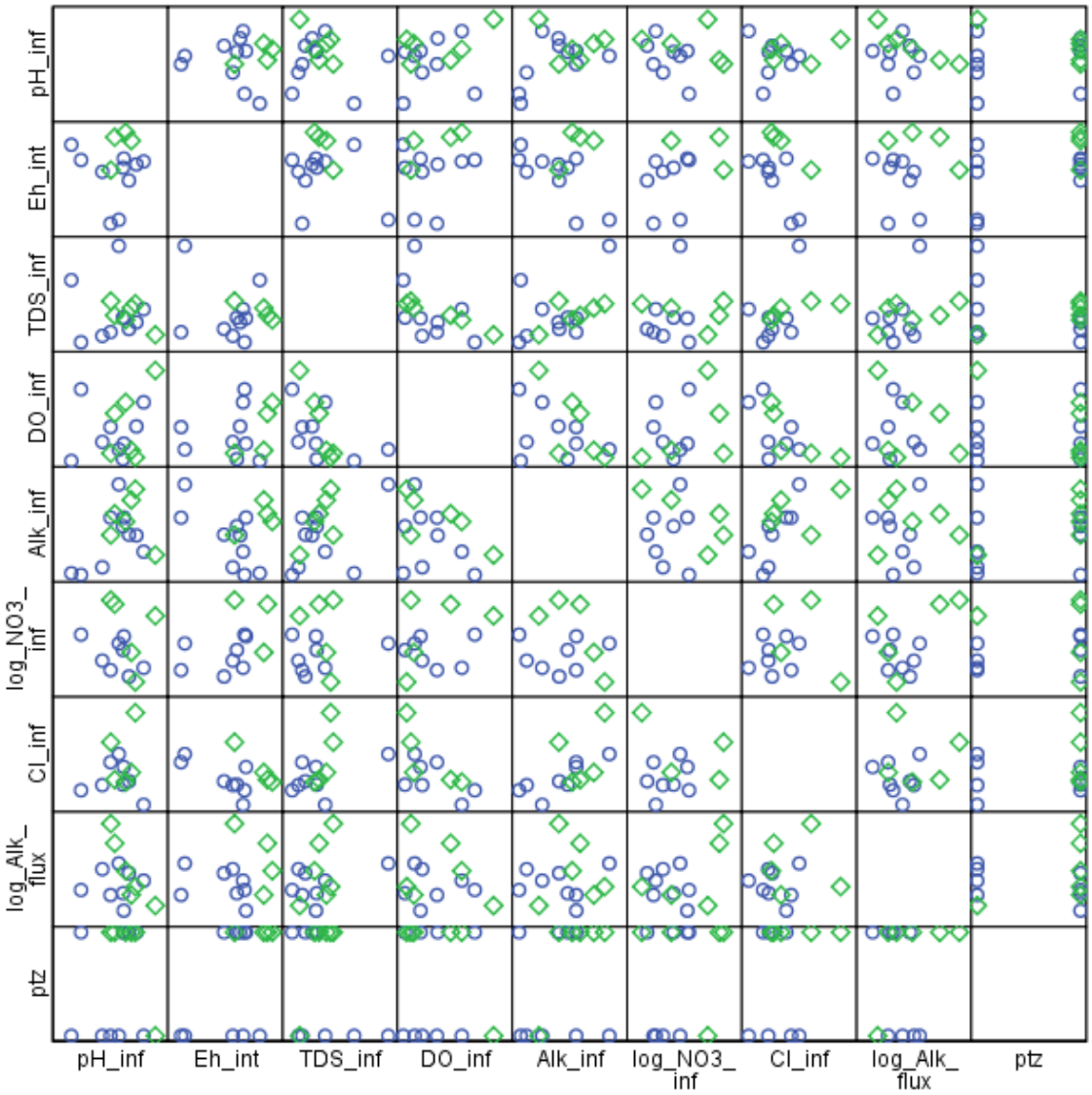

Figure 3.1: Matrix plot of selected geochemical parameters. At-risk PRBs are indicated by diamond markers, not-at-risk by circles. Units are (mg/L) except for E_H (mV) and ptz (1 indicates use of a pre-treatment zone).

In Figure 3.1, PRBs classified as at-risk are indicated by diamonds, while those PRBSs classified as not-at-risk are indicated by circles. Regions in these two-dimensional geochemical spaces where PRBs at-risk and those not-at-risk tend to group may be indicative of important geochemical parameters; lack of grouping is suggestive of little correlation. For example, this figure suggests that DO and TDS (shown enlarged in Figure 3.2), although expected to strongly influence PRB performance based on the literature, do not do so. Column studies and theoretical calculations have clearly shown the possibility of deleterious effects of DO on barrier hydraulics (Morrison et al. 2002a; Simon et al. 2001; Kjeldsen and Fulgsang 2000; Ott 2000; Mackenzie et al. 1999; Liang et al. 1997). DO is expected to corrode iron, increase pH, and promote the formation of (oxyhydr)oxide solids. If influent DO were a controlling factor, at-risk PRBs should be grouped above some cutoff DO value. Yet Figure 3.2(a) shows at-risk PRBs at extremely low DO values, suggesting that DO is not well correlated with PRB longevity.

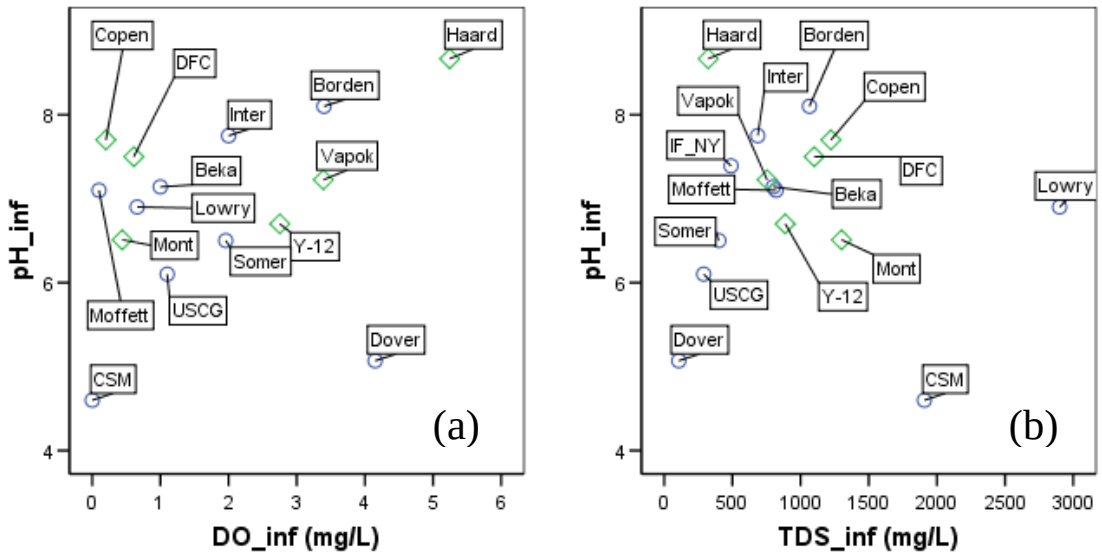

Figure 3.2: Plot of at-risk and not-at-risk PRBs with respect to influent pH and (left) influent DO, (right) influent TDS. At-risk PRBs are indicated by diamond markers, not-at-risk by circles.

Similarly, based on the literature, it seems likely that TDS is a good estimator of potential failure: high influent TDS concentrations generally lead to high quantities of mineral precipitation (ESTCP 2003; Wilkin and Puls 2003; Gu et al. 1999; Gillham et al. 1993). However, as seen in Figure 3.2(b), there are several PRB sites with high TDS that are

not-at-risk. If solutes such as Na^+ account for a large portion of the dissolved solids, TDS may not be a reliable indicator of the potential for precipitation.

Besides suggesting parameters that may not correlate with the potential for reduced longevity, these matrix plots indicated other parameters that might be related to at-risk PRBs. Perhaps most evident were very high fluxes and cumulative fluxes of influent alkalinity, as well as influent concentrations and cumulative fluxes of nitrate (Figure 3.3).

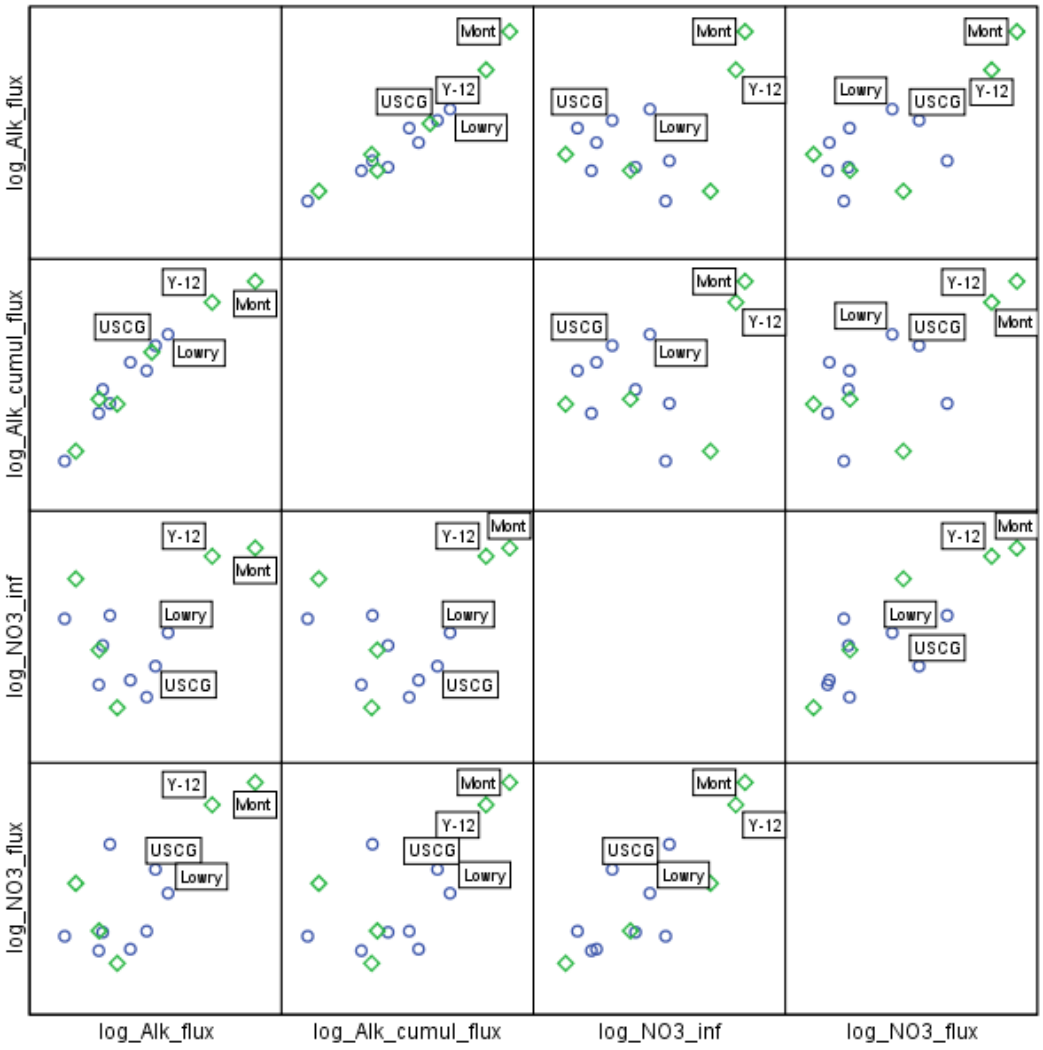

Figure 3.3: Significance of very high alkalinity and nitrate for prediction of at-risk PRBs. At-risk PRBs are indicated by diamond markers, not-at-risk by circles.

Although these outliers were few in number, the extreme values appear to be strongly correlated with at-risk PRBs. Monticello (UT) and Y-12 (Oak Ridge, TN) PRBs have very high mass fluxes and cumulative fluxes for alkalinity and nitrate (as well as total

carbonate and calcium); these PRBs are also classified as at-risk. This finding makes conceptual sense, as exceptionally high mass loadings increase the possibility of high levels of precipitation (Wilkin and Puls 2003). In most PRBs, nitrate values are generally quite low; only Monticello, Y-12, and Haardkrom (Denmark) have values above 10 mg/L, and of these three, two, Monticello and Haardkrom, have actually failed.

This analysis of the matrix plots also indicated some combinations of parameters that may be correlated with at-risk PRBs, including internal E_H, influent alkalinity, influent chloride concentrations, and the saturation indices of iron(III) solids. Two example plots are shown in Figure 3.4. Figure 3.4(a) shows a complete separation of at-risk and not-at-risk PRBs using internal E_H and influent chloride concentration. In the upper right section of the graph, the at-risk PRBs are found, while the not-at-risk PRBs lie below and to the left. This PRB grouping makes sense: higher E_H values may lead to more oxidation and thus more potential passivation of iron (Wilkin and Puls 2003; Johnson et al. 1998; Stumm and Morgan 1996). Chloride has been shown to increase the corrosion of iron (Devlin and Allin 2005; Johnson et al. 1998), which would be expected to improve PRB performance; however, Klausen et al. (2001) showed that the reactivity-diminishing effects of nitrate may outweigh the corrosion-promoting effects of chloride. Figure 3.4(b) shows the data set plotted as a function of influent alkalinity and nitrate. Although the separation of at-risk and not-at-risk PRBs is not as definitive as in Figure 3.4(a), Figure 3.4(b) still suggests that higher alkalinity and higher NO_3^- correlate with being at-risk. The PRB at Lowry AFB (CO), with low nitrate and high alkalinity, is an exception to this trend, but considering Figure 3.4(a), this may be attributable to its very low E_H value.

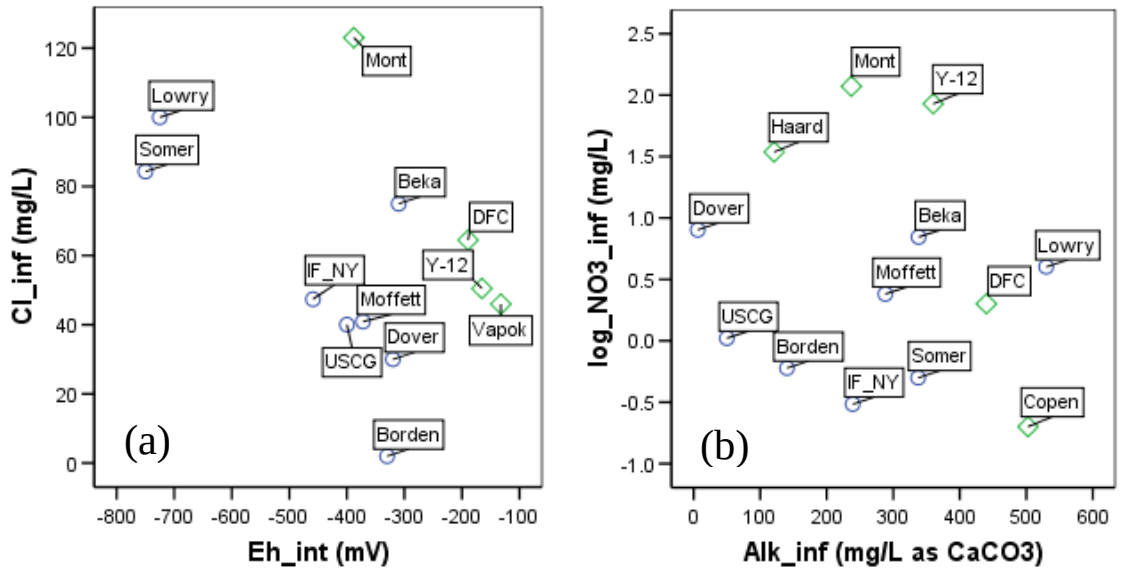

Figure 3.4: Geochemical parameters with relationship to at-risk and not-at-risk PRBs: (a) Influence chloride vs. internal E_H; (b) influent nitrate vs. influent alkalinity. At-risk PRBs are indicated by diamond markers, not-at-risk by circles.

Finally, the matrix plots of the data indicated that many of the parameters, especially mass fluxes, cumulative fluxes, and saturation indices are strongly correlated with one another. The high degree of collinearity between mass fluxes (g m^{-2} d^{-1}) and cumulative fluxes (kg m^{-2}) (Figure 3.5) suggests that variation in the flow rate dominates the parameter value rather than the variation in concentration.

Similarly, the saturation indices of hematite, ferrihydrite, and goethite, all iron(III) species, and magnetite, an iron(II)/iron(III) solid, are collinear. This relationship stems from the fact that at the E_H values in the PRBs in this data set, aqueous iron(III) concentrations are negligible. Iron (III) may be calculated from the reported values of iron (II), but it will be directly proportional to the reported E_H values. Because the saturation indices of these solids vary with the aqueous iron(III) concentrations, all are collinear.

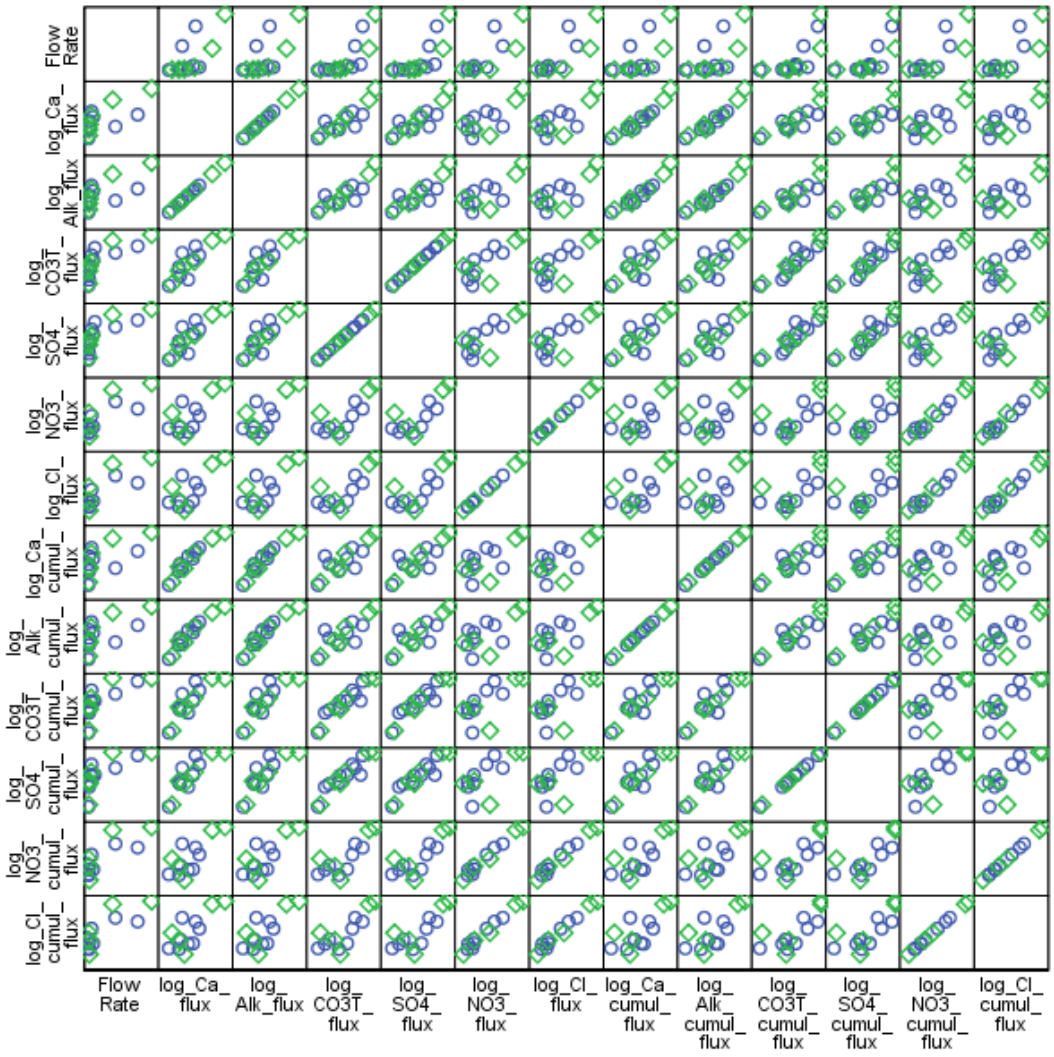

Figure 3.5: Matrix plot of fluxes, cumulative fluxes, and flow rate showing high degree of collinearity. At-risk PRBs are indicated by diamond markers, not-at-risk by circles.

3.3.2 Statistical analysis

To assess the degree of collinearity in the data, a Pearson correlation test was conducted. The results showed that three sets of variables had correlations significant at the 95% confidence level: 1) flow rate, mass fluxes, and cumulative fluxes, 2) the saturation indices of calcite and aragonite, and 3) E_H with saturation indices of iron(III) solids. Based on this analysis, it was deemed necessary to include only one flux, one calcium carbonate solid, and one member of the third set. Based on its potential to diminish the hydraulic conductivity and reactivity of ZVI PRBs, the mass flux of alkalinity was

chosen in the first category, calcite was chosen as the calcium carbonate solid, and E_H, as a master variable, was chosen over the iron(III) solid saturation indices. In addition, it was found that influent alkalinity and chloride were linearly correlated at a 95% confidence level; however, both parameters were retained because they were not expected to be mechanistically related, as were the parameters in the other categories.

Univariate logistic regression was carried out for each of the reported and calculated geochemical parameters in Tables 3.2 and 3.3, with the exception of those parameters eliminated due to high collinearity, reducing the total number of parameters considered from 37 to 21. The results, presented in Table 3.4, include β_1 (Equation 3.2) values, the standard error (S.E.), the Wald value (β_1/S.E.), and the p-value, or significance. Variables with a p-value ≤ 0.25 were considered to be significant: influent pH, internal E_H, influent alkalinity, mass flux of alkalinity, influent chloride, and the use of a pre-treatment zone (ptz). Influent nitrate, with a significance of 0.258, is on the cusp of inclusion. These results agree well with the qualitative graphical analysis. With the exception of influent pH and ptz, the variables with p-values ≤ 0.25 were also those identified in the graphical presentation.

Table 3.4: Univariate logistic regression analysis and maximized odds ratio results.

		Logistic Regression				Odds Ratio		
Parameter	Legend	β	Standard Error	Wald	Significance	Max. Odds Ratio	Cutoff Value	Fisher Exact Test Significance
Run Time (yr)	RunTime	-0.1470	0.200	0.54	0.461	1.33	2.5	1.000
Flow Rate (m/d)	FlowRate	0.1806	0.302	0.36	0.550	2	1	0.604
pH in	pH_in	0.8910	0.700	1.62	0.203	4.5	7.4-8	0.518
pH internal	pH_int	-0.1315	0.564	0.05	0.816	20	8.9-9.9	0.035
E_H internal (mV)	EH_int	0.0161	0.009	3.32	0.069	60	-200	0.011
TDS in (mg/L)	TDS_in	0.0000	0.001	0.00	0.965	5	700	0.307
DO in (mg/L)	DO_in	0.2015	0.334	0.36	0.547	3.6	5	0.400
Ca in (mg/L)	Ca_in	0.0035	0.006	0.39	0.534	5	100	0.301
Ca internal (mg/L)	Ca_int	0.0106	0.012	0.84	0.359	6	40	0.266
Alk in (mg/L as $CaCO_3$)	Alk_in	0.0050	0.004	1.70	0.192	9	350	0.118
Alk internal (mg/L as $CaCO_3$)	Alk_int	0.0025	0.002	1.15	0.284	8	200	0.235
CT in (mg/L as CO_3)	CT_in	0.0007	0.002	0.09	0.759	7.5	410	0.145
Fe internal (mg/L)	Fe_int	-0.0180	0.035	0.26	0.610	1.75	1.3	1.000
SO_4 in (mg/L)	SO4_in	0.0003	0.001	0.04	0.840	8	75	0.234
NO_3 in (mg/L)	NO3_in	0.1005	0.089	1.28	0.258	24	20	0.035
Cl in (mg/L)	Cl_in	0.0246	0.018	1.93	0.165	10.67	110	0.128
Ca Flux Rate (g/d)	Ca_flux_rate	0.0071	0.008	0.80	0.371	8	100	0.165
Alk flux rate (g/d)	Alk_flux_rate	0.0040	0.003	1.37	0.242	5	25	0.307
CT flux rate (g/d)	CT_flux_rate	0.0013	0.001	1.36	0.243	2.14	30	1.000
SO_4 flux rate (g/d)	SO4_flux_rate	0.0007	0.001	0.39	0.530	3	4	0.500
NO_3 flux rate (g/d)	NO3_flux_rate	0.0227	0.028	0.67	0.412	10.67	25	0.128
Cl flux rate (g/d)	Cl_flux_rate	0.0050	0.005	0.86	0.353	6	3	0.231
Ca Flux (kg)	Ca_flux	0.0029	0.003	0.99	0.320	3	100	0.580
Alk flux (kg)	Alk_flux	0.0019	0.001	1.89	0.170	7.5	55	0.145
CT Flux (kg)	Ct_flux	0.0008	0.001	1.56	0.211	2.14	72	1.000
SO_4 Flux (kg)	SO_4_flux	0.0005	0.001	0.69	0.407	3	3	0.500
NO_3 Flux (kg)	NO_3_flux	0.0110	0.014	0.64	0.425	10.67	50	0.128

Table 3.4: Univariate logistic regression analysis and maximized odds ratio results.

		Logistic Regression				Odds Ratio		
Parameter	Legend	β	Standard Error	Wald	Significance	Max. Odds Ratio	Cutoff Value	Fisher Exact Test Significance
Cl Flux (kg)	Cl_flux	0.0027	0.003	0.89	0.346	10	9	0.231
SI Calcite	SI_calcite	0.5300	0.911	0.34	0.561	9	1.15	0.192
SI Aragonite	SI_aragonite	0.5300	0.911	0.34	0.561	9	1	0.192
SI Siderite	SI_siderite	0.3483	0.377	0.85	0.356	8	-0.2	0.208
SI Fe(OH)2	SI_feoh2	0.9669	1.806	0.29	0.592	5.33	0.35	0.333
SI Magnetite	SI_magnetite	2.3404	1.493	2.46	0.117	21	2.3	0.067
SI Hematite	SI_hematite	2.0237	1.243	2.65	0.104	48	2.05	0.018
SI Ferrihydrite	SI_ferrihydrite	2.0237	1.243	2.65	0.104	48	0.7	0.018
SI Goethite	SI_goethite	2.0237	1.243	2.65	0.104	48	1.75	0.018
PTZ	ptz	1.6094	1.265	1.62	0.203	5	1	0.307
media mix	zvi_mix	-20.9	28420	0.00	0.999	3	1	0.500

A reexamination of the data indicates why influent pH and ptz were not identified graphically. The influent pH data reveals that, while the pH data are tightly clustered relative to other variables, most at-risk PRBs have influent pH values greater than 7; on the other hand, there are several not-at-risk PRBs with lower influent pH values, while one - the PRB at Borden, Ontario - has an influent pH greater than 8. Secondly, the probability of a PRB being at-risk increases with the use of a pre-treatment zone. Though counterintuitive, this appears to be a case of correlation, rather than causation. In cases where performance problems are anticipated, a PTZ is installed, which while undoubtedly useful, does not preclude loss of reactivity or permeability in the reactive zone.

To further corroborate the results of the graphical analysis and the univariate logistic regression, an odds ratio analysis was conducted using the same parameters as for the logistic regression. The results of this analysis are also shown in Table 3.4, which lists the maximum odds ratio achieved and the cutoff value corresponding to the maximum odds ratio. The two-sided Fisher Exact Test was used to evaluate whether the tested variables are independent or associated, with a cutoff significance of $p \leq 0.10$. Therefore,

the geochemical parameters deemed to be most correlated with being at-risk via odds ratio maximization were internal E_H and influent nitrate. While internal E_H was deemed highly significant by logistic regression, influent nitrate was on the borderline. Nitrate (Figure 3.3) has outlying points; when fitting these data to the linear regressor equation $g(\mathbf{x})$ (Equation 3.2), it is difficult to estimate an accurate β for this parameter, since there are outlying points and each point weighs heavily in the small data set. In contrast, when calculating the odds ratio, there is no weight associated with the extent that a point is an outlier (e.g., with an influent nitrate cutoff of 20 mg/L, the odds ratio treats values of 20.1 and 200 identically). Therefore, outliers do not affect the odds ratio in the same manner they do the logistic regression.

Had a less stringent cutoff of, for example, p-value ≤ 0.15 been chosen, the list of relevant parameters selected via odds ratio maximization would have included influent alkalinity, influent total carbonate, and influent chloride. With the exception of total carbonate, these additional parameters are a subset of those selected via logistic regression. Like influent nitrate, discussed above, the significance of total carbonate is very different when evaluated by logistic regression (significance = 0.76) and by odds ratio maximization (Fisher's exact significance = 0.145). An inspection of the data, illustrated in Figure 3.6, reveals that, although influent alkalinity and total carbonate are generally well correlated, there is one outlying point – that of the CSM PRB (Australia). This site has an unusually low pH, and hence its low alkalinity does not correspond to low total carbonate. As in the case of nitrate, this outlier affects the fit such that the logistic regression using total carbonate predicts no at-risk PRBs for any of the total carbonate values in the data set. In contrast, the alkalinity values lack outliers and hence the estimated β value is more meaningful.

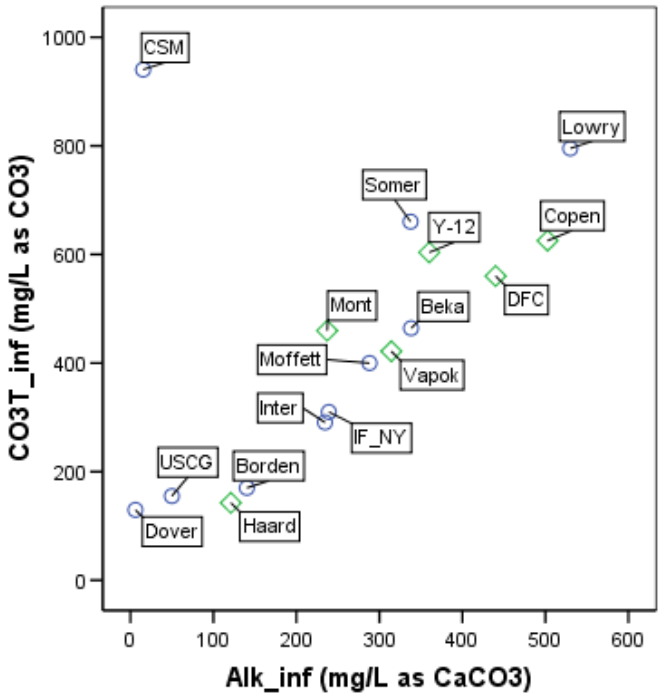

Figure 3.6: Differences between influent alkalinity and influent total carbonate; the CSM (Australia) PRB has unusually low influent pH. At-risk PRBs are indicated by diamond markers, not-at-risk by circles.

Both of the statistical approaches utilized here corroborated the qualitative graphical observations. TDS and DO are not major parameters in determining at-risk PRBs. However, influent pH, internal E_H, influent alkalinity, influent chloride, influent nitrate, mass flux of alkalinity, and use of a pre-treatment zone are significant for describing at-risk PRBs. Despite the problems inherent with measuring E_H in the field (Sposito 1989), both statistical approaches showed that this parameter has strong predictive power. While both approaches agreed on the significance of some parameters, influent nitrate was found to be more significant in the odds ratio analysis than in the logistic regression.

To better assess the relative significance and potential interaction of terms, multivariate logistic regression was performed with the combination of the parameters selected using the univariate logistic regression (p-value ≤ 0.25) and the maximization of the odds ratio (p-value ≤ 0.10): pH_inf, EH_int, Alk_inf, NO_3_inf, Cl_inf, Alk_flux, and ptz. Yet for this limited data set, internal E_H and influent chloride are "perfect predictors," separating the data set completely into at-risk and not-at-risk groupings (Figure 3.4(a)). Furthermore, the parameter subset influent alkalinity (or influent chloride, which is

linearly correlated at the 95% confidence level), alkalinity mass flux, and influent nitrate perfectly predicted the data. Including perfect predictors into multivariate regression results in unstable parameter estimates (Faraway 2006). Because of the limitations of the size of the data set, the best multivariate logistic regression that could be achieved included no interaction terms and only the parameters pH_inf, Alk_inf, and Alk_flux. Even so, this model predicted at-risk PRBs with an 87.5 % success rate, with Alk_flux significant at a 90% confidence level and the other two at an 80% confidence level.

3.4 Summary

The quantitative analyses performed here suggest that high influent pH, internal E_H, high influent concentrations of nitrate, chloride, and alkalinity, are problematic for PRBs. Other parameters such as total dissolved solids, dissolved oxygen and the saturation indices of carbonate solids that have been suggested in the literature as controlling PRB longevity did not appear to have much predictive ability for classifying a PRB as at-risk. Ideally, the parameters selected by univariate regression should be utilized in multivariate modeling to gain a better understanding of the relative significance of the parameters. However, the sparseness of the dataset made certain combinations of variables, like E_H and Cl^-, perfect predictors, precluding their use in a multivariate analysis.

For the purposes of the present study, though, this statistical analysis pointed towards parameters that are associated with problems in ZVI PRBs. Based on these results, the experiments described in the following chapters used influent solutions with high chloride and alkalinity as a control group, and oxidants – oxygen or nitrate – were added to some column influent solutions in order to determine their effect on solids production. Therefore, the experimental work allows a comparison of the performance of FeS-coated sands and ZVI in conditions expected to promote permeability loss.

Chapter 4: Methodology for Laboratory Experiments

4.1 Summary

This chapter describes the column experiments that were performed in the laboratory to assess the hydraulic behavior of ZVI and FeS under simulated subsurface conditions. All experiments and solids analyses were conducted at ambient laboratory temperature (21 – 25°C). Most experiments and analyses required maintaining an oxygen-free environment. Therefore, experiments involving the synthesis of FeS, coating FeS onto sands, or the preparation of column materials for solids analysis were conducted inside an anaerobic chamber (Coy Inc., Grass Lake, MI). The atmosphere in the chamber was approximately 95% nitrogen gas and 5% hydrogen gas; it was maintained oxygen-free with a palladium catalyst, and humidity was controlled with dessicant. Reagent-grade chemicals were used in all experiments, and all water used for column experiments was distilled and de-ionized (DDI). Milli-Q water (from a Millipore Milli-Q system, Billerica, MA) was used in the preparation of samples and standards for analytical equipment.

4.2 Materials

4.2.1 Zero-valent iron (ZVI)

ZVI was used as-received from Peerless Metals (Detroit, MI). Surface area, bulk composition, and other properties were discussed in Section 2.2.1. Figure 4.1shows SEM images of the as-received ZVI at various scales.

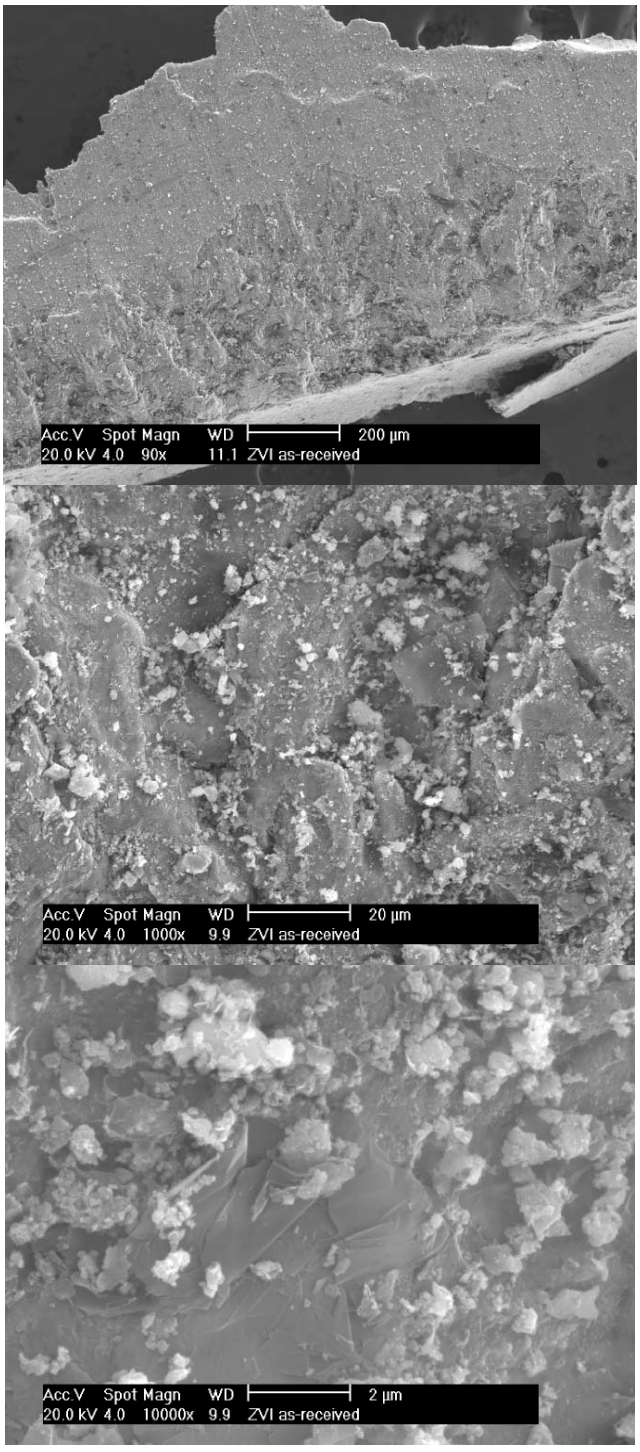

Figure 4.1: SEM micrographs of a grain of as-received ZVI. From top to bottom, scale bars are 200, 20, and 2 µm, respectively.

Given the nature of the ZVI production process, it is expected that the surface has fine-scale irregularities.

4.2.2 FeS synthesis and coating

The method for FeS synthesis was drawn from the work of Butler and Hayes (1998). Based on this method, 0.57M $FeCl_2$ and 1.1M Na_2S solutions were combined at a volume ratio of 1:0.6. The resulting slurry was stirred for 3 days. Solids were collected, and excess Na^+ and Cl^- was removed via centrifuging and decanting. The remaining FeS was centrifuged at 10,000 rpm, decanted, and rinsed with fresh DDI water. Originally, this procedure was repeated 8 times, but Han et al. (2009) found that five rinses were sufficient and reduced the risk of oxidation of the material or loss of FeS. After centrifuging, the solid was frozen and then freeze-dried under vacuum. Then, the synthesized FeS solid was stored in the anaerobic chamber at room temperature in glass vials sealed with Teflon-coated butyl rubber septa. The synthesized FeS was stored as a solid, rather than as a paste, for it has been shown that this material is very sensitive to oxygen exposure and that it is difficult to maintain unoxidized in solution for long periods of time (Morse and Arakaki 1993).

FeS, thus synthesized, has been found to have a high surface area. Using TEM (transmission electron microscopy), the specific surface area was estimated to be 103 m^2/g, which may be a low estimate due to particle aggregation (Jeong et al. 2008). Photon correlation spectroscopy by Jeong et al. (2008) puts the FeS surface area at 424 ± 130 m^2/g. Regardless of the bias of the estimate, it is clear that FeS has a specific surface area approximately 2 orders of magnitude higher than that of ZVI (Table 2.2).

FeS was coated onto sands according to the procedure of Han et al. (2009). The silica sand used as a substrate for FeS coating was Wedron 510 Silica Sand (Fairmount Mineral, Wedron, IL). As reported by Fairmount Mineral, this sand is rounded and consists of 99.65% SiO_2, 0.065% Al_2O_3 and 0.018% Fe_2O_3. Wedron sand was chosen based on its suitability for coating with iron sulfide based on work by Han (2009) that indicated that the naturally-occurring oxides on the sand surface improve the coating of FeS. Therefore, the sand was washed with DDI water before coating, but not acid-washed.

The washed Wedron natural sands were sieved using stainless steel sieves (ATM Test Sieves, Milwaukee, WI). The sands used were passed by the #70 sieve (210 µm) and retained on the #100 sieve (150 µm). Based on the particle size distribution of the original sand, this sieved sand was expected to have a d_{50} of 165 µm, and a specific surface area of 140 cm^2/g. Although the sieving process may alter the surface properties of the sand, it was found that the combination of sieving and the coating procedure described in the following paragraph produced a consistent coating of FeS onto the sand (Han 2009). Furthermore, sieving is a common practice in laboratory ZVI studies (e.g., Kohn and Roberts 2006; Dwyer 2000a; Blowes et al. 1999; Orth and Gillham 1996).

FeS was coated onto the Wedron sand inside an anaerobic chamber. First, a suspension of 2 g/L FeS was mixed and allowed to stir for 24 hours. The solution pH was adjusted to 5.5 with 0.5N HCl and allowed to equilibrate for 2 hours. DDI-rinsed sand and the 2 g/L FeS solution were mixed at a 1:1 volume ratio and rotated end-over-end for three days. At the end of this time, the clear supernatant was discarded, and the FeS-coated sand was dried in the atmosphere of the anaerobic chamber.

The mean coating achieved in this research was 1.47×10^{-5} mole FeS/g sand. This coating was measured using the digestion technique discussed in Section 4.3.6. In comparison, Han reported a range of 1.2 – 4 mg FeS/g sand ($1.37 – 4.5 \times 10^{-5}$ mole FeS/g sand) (2009). Figure 4.2 presents SEM images of the FeS-coated sands. The surface of the FeS-coated sand is smooth relative to the as-received ZVI.

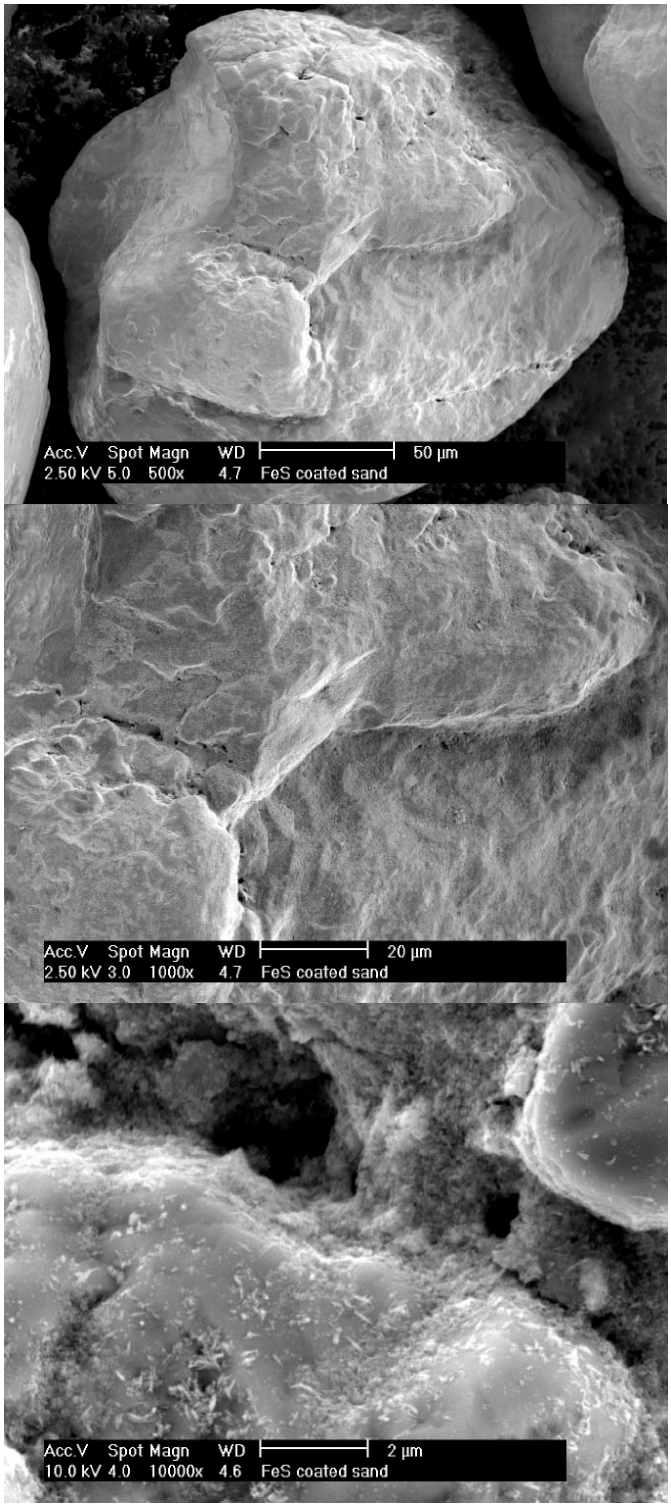

Figure 4.2: SEM micrographs of FeS-coated sand. From top to bottom, scale bars are 50, 20, and 2 µm, respectively.

4.3 Methods

4.3.1 Column setup

Column experiments were conducted in the ambient laboratory atmosphere, rather than in the glovebox. This allowed more control of the influent solutions introduced to the columns, as the gas phase in equilibrium with those solutions could be varied. All columns had an inner diameter of 5cm and a bed length of 25cm. These columns were made of Plexiglas, which has a permeability to oxygen of 0.1×10^{-13} cm^2 / s-Pa at 25°C (Altuglas International 2006). With the exception of the influent reservoirs, which were Nalgene (Rochester, NY) low-density polyethylene 20 L carboys, the fluid handling components used in this study were made of Swagelok (Solon, OH) 316 stainless steel tubing and connections. The pumps used in the study were either Varian Dynamax SD-200 (Varian, Palo Alto, CA) or SSI Series I (Scientific Systems Inc., State College, PA) pumps. Because running columns in an upflow mode has been shown to reduce entrapment of evolved gases, columns were run in this mode (Kamolpornwijit and Liang 2006; Vikesland et al. 2003). Figure 4.3 shows a schematic of the column system; components of the system are discussed in the following sections.

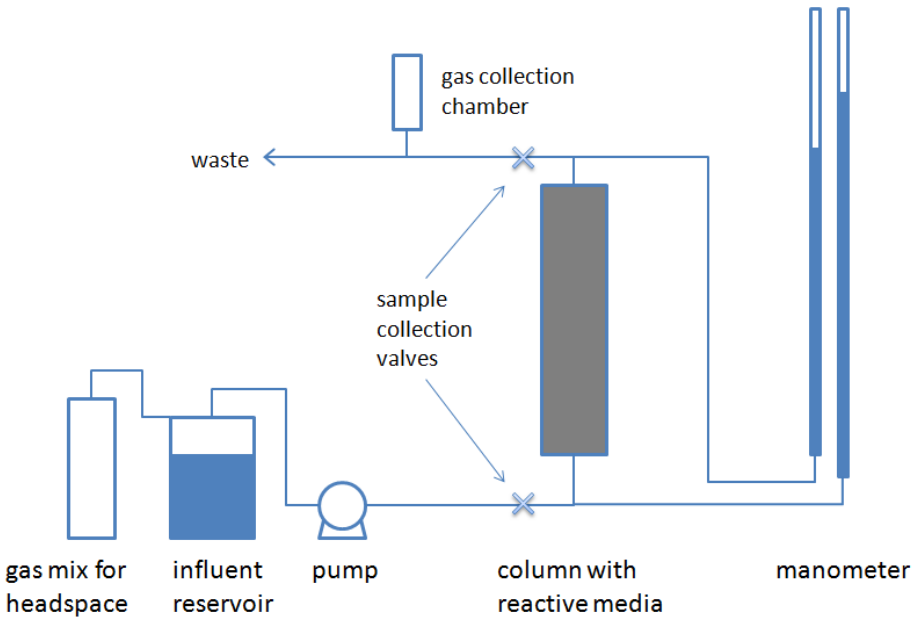

Figure 4.3: Schematic of column apparatus.

As discussed in Section 2.1.2, several common problems were identified with laboratory work. These included use of high flow rates and influent solutions that do not represent typical groundwater compositions, often because buffering agents were included. Given these considerations, this research project did not use an artificially high flow rate; instead, the flow rate chosen, 0.7 mL/min, is within the recommended range delineated by Roberts et al. (2002).

A method to reproducibly and homogeneously pack a column is of vital importance to column experiments, yet it often does not receive the attention it deserves. Following the recommendations of Schumacher (1990), mixtures of non-homogeneous grain sizes were mixed using a riffler (Soiltest, Evanston, Il). Schumacher (1990) presents data to show that five passes through the riffler homogenizes fine sand samples reproducibly, with a standard deviation of replicates of the particle size distribution of 0.05. This homogenization procedure, as well as the packing of the column, was conducted in the anaerobic chamber. To introduce the homogenized media into the column, methods from Oliveira at al. (1996) and Lebron and Robinson (2003) were adapted. Dry homogenized media were introduced into the column in small lofts (~ 0.5 cm) without pouring. Individual lofts were wetted and, finally, packed with an external vibration device (Homedics, Commerce Township, MI) and manual tapping. To determine the porosity of the column, the weight of the empty column, wet packed column, mass of reactive media, and mass of water used to pack the column were recorded.

4.3.2 Influent solutions

Anoxic influent solutions for the column experiments were prepared by first purging DDI water with 99.998% nitrogen gas (Cryogenic Gases, Detroit, MI). After purging, reagents were added, and the solution was stirred for 36 hours. After dissolution of all solid reagents, the influent solution was transferred to the influent reservoir.

Five compositions of influent solutions were used; these are summarized in Table 4.1. The first solution was pure DDI water that was equilibrated with the ambient laboratory atmosphere, i.e., this solution contained approximately 8 mg/L O_2. The remaining

solutions were variations on the composition of the groundwater at Monticello, UT. This groundwater was chosen as a model groundwater because the statistical analysis indicated that its high carbonate, chloride, and nitrate levels were likely to lead to high solids accumulation. Indeed, at the Monticello site itself, the hydraulic conductivity of the ZVI PRB was reduced by two orders of magnitude during the course of 5.5 years (Mushovic et al. 2006). The reported composition of this groundwater is presented in Table 4.2. While potassium concentrations were not reported for the Monticello PRB, potassium appears in the influent solution used in these experiments because potassium nitrate was used as the source for nitrate.

Table 4.1: Influent solutions used for column experiments. Concentrations are given in mg/L (with mM equivalent in parentheses).

Influent Solution Name	pH	DO	Ca^{2+}	CO_{3T}	Cl^-	NO_3^-	K^+	SO_4^{2-}	Mg^{2+}	Na^+
DDI water	7	8 (0.25)	nd	nd	nd	nd	nd	nd	nd	nd
calcium + carbonate	6	0 (0.0)	280 (7.0)	420 (7.0)	405 (11.4)	0 (0.0)	0 (0.0)	0 (0.0)	0 (0.0)	0 (0.0)
calcium + carbonate + $2O_2$	6	2 (0.06)	280 (7.0)	420 (7.0)	405 (11.4)	0 (0.0)	0 (0.0)	0 (0.0)	0 (0.0)	0 (0.0)
calcium + carbonate + nitrate	6	0 (0.0)	280 (7.0)	420 (7.0)	405 (11.4)	100 (1.6)	63 (1.6)	0 (0.0)	0 (0.0)	0 (0.0)
simulated Monticello	6.3	0 (0.0)	280 (7.0)	420 (7.0)	120 (3.4)	100 (1.6)	63 (1.6)	1170 (12.2)	61 (2.5)	292 (12.0)

Table 4.2: Monticello, UT groundwater composition (Mushovic et al. 2006)

Parameter	Value (mg/L unless otherwise indicated)
pH	6.51
E_H	159 mV
DO	0.44 mg/L
Alk	237 mg/L as $CaCO_3$
CO_{3T}	471
Ca^{2+}	275
SO_4^{2-}	1170
Cl^-	123
Mg^{2+}	69
NO_3-	118

Excluding the oxygenated, DDI influent solution, all solutions contained the same amount of calcium and carbonate, i.e., Ca^{2+} = 275 mg/L and CO_3^{2-} = 460 mg/L, with HCl added to adjust the pH to 6, a value selected to ensure undersaturation of $CaCO_3$(s). The solution "calcium + carbonate + $2O_2$" contained the same levels of calcium and carbonate, but 2 mg/L of oxygen were added. The solution "calcium + carbonate + nitrate" contained the same amount of calcium and carbonate, but with the addition of 100 mg/L of nitrate (added as KNO_3).

Finally, the solution "simulated Monticello" contained these same solutes, with the addition of ~1100 mg/L sulfate and ~70 mg/L magnesium. Reagents ($CaCO_3$, KNO_3, $MgSO_4.7H_2O$, $MgCl_2.6H_2O$, $NaHSO_4.H_2O$, NaOH) were chosen such that pH adjustment with HCl was not necessary, and the chloride concentration was therefore matched to the reported Monticello concentrations.

Influent reservoirs were Nalgene low-density polyethylene carboys (Nalgene, Rochester, NY), in which a controlled headspace gas mix (Cryogenic Gases, Detroit, MI) both prevented the introduction of oxygen and the off-gassing of carbon dioxide. For most solutions, this gas consisted of 15% carbon dioxide gas and 85% nitrogen gas. At the target pH of 6, this gas phase was in equilibrium with the aqueous phase, thus preventing

the loss of carbon dioxide as pumping increased the ratio of headspace to liquid volume. In one experiment, 5% oxygen was added to the gas mix, which is in equilibrium with 2 mg/L of oxygen in the aqueous phase. For those experiments in which fully oxygenated water was used, carbon dioxide was not present in the aqueous phase, so it was not necessary to control the headspace gas.

For those solutions with controlled dissolved oxygen levels, a constant gas flow of approximately 5 mL/min ensured a positive pressure in the reservoir headspace, thus preventing the intrusion of oxygen. The constant purging of non-oxygen-bearing gas through the reservoir headspace ensured a nearly oxygen-free environment in the reservoir. Measurements of DO (using the electrode described in Section 4.3.4) in the reservoirs were consistently <0.05 mg/L O_2.

4.3.3 Flow and hydraulic measurements

The flow rate in the column experiments was chosen to fall within natural groundwater conditions, but to also have a high mass flux of solutes. Based on the data presented in Table 2.7, a flow of 0.7 mL/min (~ 1 L/d) was chosen. In the ZVI columns, whose initial porosity was approximately 0.6, this corresponds to an average linear flow velocity of 0.85 m/d, slightly below the mean of 1.1 m/d reported in Table 2.6. In an FeS column, with an initial porosity of 0.32, this corresponds to an average flow velocity of 1.6 m/d, slightly above the mean.

Pressure transducers (model DP15-34, Validyne, Northridge, CA) were used to continuously monitor pressure at the influent and effluent of the columns; data from these transducers was collected using a UPC-607 computer interface card (Validyne). Partway through the experiments, the UPC-607 card malfunctioned, and subsequent pressure readings were collected using manometers connected to the influent and effluent ends of the columns. These manometers were filled with water and flushed prior to measurement. As noted in Section 2.3.2, measurements of hydraulic conductivity in ZVI systems tend to have high variability.

Table 4.3 summarizes the matrix of column experiments, and provides the values of parameters related to packing and flow. Pore volume (PV) is the total volume of void space in the column, so the flow rate may be expressed as PV per day. This parameter depends on the porosity of the column, whereas the volumetric flow rate, which was 0.7 mL/min for all experiments, does not.

Table 4.3: Summary of column experimental conditions, flow rates, and hydraulic conductivity

Column name	Influent solution	Initial porosity (-)	Flow rate (PV/d)	Flow velocity (cm/hr)	Initial K_H (m/d)
ZVI-0O_2	calcium + carbonate	0.61	3.4	3.5	8.0
ZVI-2O_2	calcium + carbonate + 2O_2	0.60	3.4	3.6	8.0
ZVI-O_2	DDI water	0.61	3.4	3.5	20.7
ZVI-NO_3	calcium + carbonate + nitrate	0.60	3.4	3.6	12.8
FeS-0O_2	calcium + carbonate	0.33	6.2	6.5	-
FeS-O_2	DDI water	0.32	6.4	6.7	12.8
FeS-NO_3	calcium + carbonate + nitrate	0.33	6.2	6.5	10.7
FeS-Mont	simulated Monticello	0.31	6.6	6.9	9.9

4.3.4 Aqueous analysis

Effluent samples were collected from a valve at the effluent end of the column (Figure 4.3). Influent samples were collected from a spigot on the influent reservoir or from a port before the solution entered the column. In both cases, at least 5 mL of sample was collected and discarded before sample collection began.

For measurement of total carbonate, a TOC analyzer (Shimadzu TOC-500, Kyoto, Japan) was used. Samples for carbonate measurement were collected in vials and immediately capped with aluminum foil to prevent gas exchange with the ambient laboratory atmosphere. Upon collection, sample vials were capped with aluminum foil and immediately transferred to the TOC analyzer for measurement.

Calcium, total iron, chloride, silica, magnesium, and arsenic were analyzed using an ELAN DRC-e Inductively Coupled Plasma - Mass Spectrometer (ICP-MS) (PerkinElmer, Shelton, CT). ICP samples were acidified with the addition of 20 µL of 70% nitric acid and stored in 15mL polypropylene centrifuge tubes (Thermo Fisher Scientific, Waltham, MA).

Nitrate, nitrite, and sulfate were measured using ion chromatography (IC). IC samples were filtered through 0.45 µm nylon syringe filters (GE Water & Process Technologies, Trevose, PA) and stored in glass target vials with aluminum crimp-tops and Teflon septa (National Scientific, Rockwood, TN). These samples were stored in a 4°C room and analyzed using an Dionex DX-100 Ion Chromatography (IC) system with a Dionex IonPac AS-14 chromatography column (Dionex Corp., Sunnyvale, CA).

Electrodes and meters (Thermo Scientific Orion, Beverly MA) were used to measure pH (model # 8102 BNUWP), Oxidation/Reduction Potential (ORP) (9678BNWP), dissolved oxygen (DO) (081010MD), ammonia (9512HPBNWP) and sulfide (Orion 96-16). Prior to all measurements, electrodes were calibrated as follows. The pH electrode was calibrated using pH 4, 7, and 10 buffers, and the slope of the pH electrode response was always 98 ± 2 mV / decade. The DO electrode was calibrated with a two point calibration curve: water-saturated air, and a cobalt chloride / sodium sulfite zero oxygen standard. The ORP electrode was calibrated using an E_H standard buffer, which allows for correction for the Standard Hydrogen Electrode (SHE). The offset from the measured potential to the corrected SHE E_H was 420 ± 4 mV. E_H values may be converted to pe values using Equation 2.1.

pH, E_H, and dissolved oxygen measurements were taken simultaneously using a set of flow-through cells designed to prevent exposure to the ambient laboratory atmosphere (Figure 4.4).

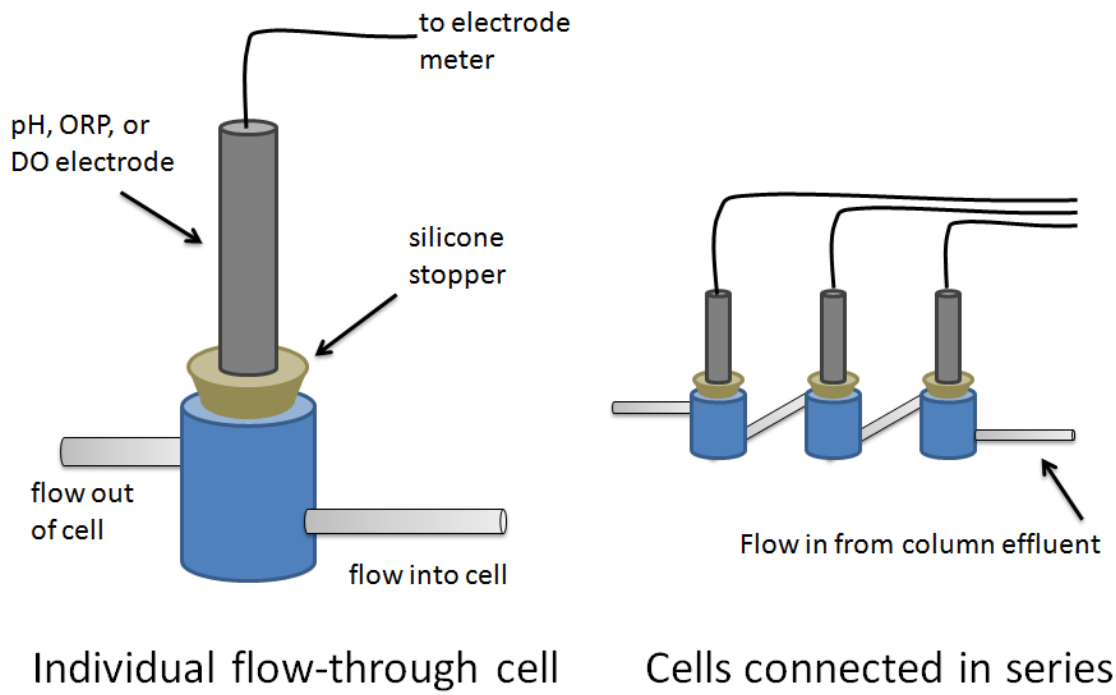

Figure 4.4: Diagram of flow-through cells for pH, E_H, or DO measurement, showing individual cell (left), and cells in series (right).

Each cell consisted of a cylindrical volume of PVC (polyvinyl chloride) plastic hollowed out to create a cavity. Influent and effluent ports to each cavity were drilled through the walls of the cylinder. Silicone stoppers fitted over the electrodes allowed the electrodes to be inserted into this cavity such that the stoppers sealed the cell. These three cells were connected in series and connected to the effluent line of the column (indicated by 'sample collection valves' in Figure 4.3). With a flow rate of 0.7 mL/min, the residence time of the cells was calculated to be approximately 1 hour. Data from these electrodes were logged for 2 hours past the time the readings stabilized. From this data series, a single point was calculated based on the average of the data during the time the reading was stable.

An example of data collected from a flow-through cell is presented in Figure 4.5, below. In this figure, there is initial scatter in the data, as the flow-through cell begins to be flushed with effluent from the column. After this initial equilibration period (~2 hours), the data collected showed little variability. At the end of the data collection, aerated DI was introduced to the cell in order to check the response of the electrode. Standard

deviations for the data collected during the stable period were used to estimate instrumental error.

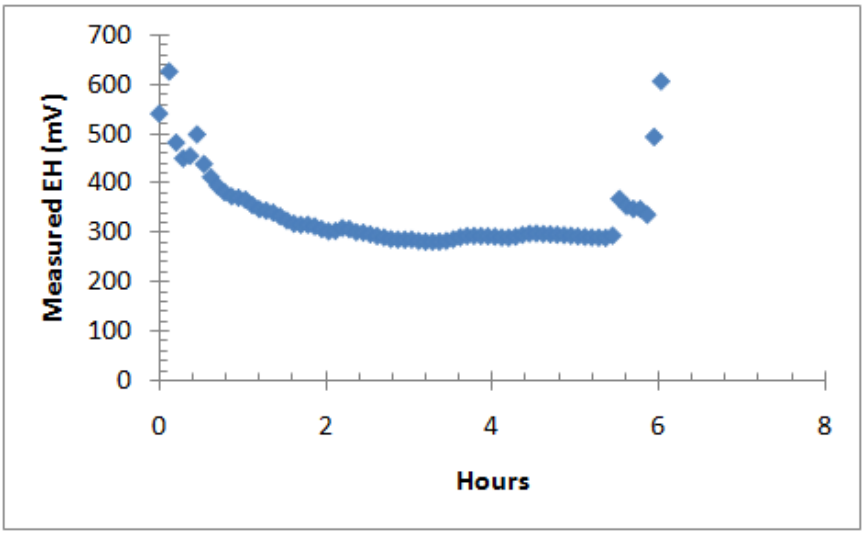

Figure 4.5: Example of time series of E_H measurements collected in flow-through cell.

The ammonia and sulfide electrode measurements required the addition of reagents to the effluent sample; therefore flow-through measurements were not possible. For both electrodes, calibration curves were generated to bracket sample values, and experiments were performed to confirm that matrix effects were not biasing measurements. Samples were collected using vials to minimize atmospheric exchange and were measured immediately after collection using the respective electrode. Sulfide electrode measurements were conducted in the anaerobic chamber (therefore, samples were transferred to the chamber immediately after collection); ammonia measurements were conducted in the ambient laboratory atmosphere. During measurement, the electrodes and sample vials were wrapped in parafilm in order to minimize gas exchange between the samples and the atmosphere.

4.3.5 Gas analysis

Gas was collected in the effluent lines of the columns using a three-way tube junction that allowed gas to migrate to the top of a 10 cm, dead-end length of glass tubing equipped with a septum stopper. The tubing allowed for collection of samples to

measure gas composition. The nitrogen and hydrogen content of the collected gas was measured. These samples were measured using a GOW-MAC series 580 gas chromatograph (GC) with a thermal conductivity detector (TCD) (GOW-MAC Instrument Co., Bethlehem, PA). Gas samples were collected using a gastight syringe (Precision Sampling Corp., Baton Rouge, LA) and were measured immediately after collection.

4.3.6 Solids analysis

In order to examine the reactive materials from the column experiments, the columns were destructively sampled at the conclusion of each experiment. This sampling took place in the anaerobic chamber. Reactive material was extruded from the column and sectioned into samples of approximately 5 cm in height. Samples were then stored without further treatment in closed containers in the anaerobic chamber prior to analysis. Samples were analyzed within 8 weeks of collection.

4.3.6.1 Digestion

Quantification of the amount of Fe on the coated sand provided information about solids accumulation and the coating of FeS onto natural sand. The extraction of iron sulfide from the sands requires a two-step extraction: Cooper and Morse (1998) found that some sulfides were incompletely removed with only hydrochloric acid. Han (2009) corroborated this observation and determined that nitric acid digestion was necessary as well. The same extraction procedure was used for ZVI and for FeS-coated sands.

The extraction method consisted of the following:

1. 5 mL of 12N HCl was added to 3 g of ZVI or FeS-coated sand in a 15 mL centrifuge tube.
2. The solution was completely mixed and left to stand for 15 min.
3. The supernatant was decanted into a 50 mL centrifuge tube.
4. 5 mL of 50% HNO_3 was added to the sand, mixed, and left to stand for 15 minutes.

5. The supernatant was decanted into the 50 mL centrifuge tube.
6. The sand was rinsed with 15 mL of DDI water, and the rinse supernatant was collected in the 50 mL tube for measurement.
7. The aggregated supernatant in the 50 mL tube was analyzed for iron and calcium.

4.3.6.2 Spectroscopic and surface analyses

Two techniques for surface analysis were used. The first, X-Ray Photoelectron Spectroscopy (XPS) provides information about the upper 10 nm of the surface of a sample. XPS can be used to determine the oxidation state of species in this surface layer. In addition, the relative stoichiometric abundance of species can be used to determine which minerals are present on the surface.

The XPS system was a Kratos Axis Ultra X-ray Photoelectron Spectrometer (Simadzu-Biotech, Columbia, MD). The incident source was a monochromated Al Kα x-ray (1486 eV), and the sample chamber was maintained at approximately 10^{-8} torr. Survey scans, used to provide information about average composition of the surface, were conducted using a pass energy of 160 eV. Higher-resolution narrow scans to provide information about the oxidation states of O(1s), Fe(2p), and S(2p) peaks were performed at 20 eV. For these narrow scans, 30-40 individual scans were taken and averaged to generate a single spectrum. The C1s peak (with binding energy = 284.5 eV) was used as a standard for instrument calibration; this normalization accounts for peak shifts due to surface charging (Renock et al. 2009) .

Spectral analysis was performed with the CasaXPS (http://www.casaxps.com/) processing software, for which a Kratos-specific element library is available. Survey scans were used to estimate surface composition; sensitivity factors for this semiquantitative estimate were taken from Wagner et al. (1981). Analysis of peak positions consisted of subtracting a Shirley baseline from the raw spectra, followed by peak deconvolution using Gaussian (80%) and Lorentzian (20%) peak shapes (Renock et al. 2009; Shirley 1972). Peak binding energies and full-width at half-maximum (FWHM) values were restricted to ranges reported in the literature, and are summarized in Table 4.4.

The narrows scans of the Fe($2p_{3/2}$) peak were modeled assuming contributions from species expected to be present in the samples and discussed in the literature: ferrous and ferric iron coordinated with oxygen and, in the case of FeS, sulfur. The Fe(II)-S bond was modeled with a single peak at 707.3 ± 0.1 eV (Mullet et al. 2002; Vaughan and Ridout 1971). Likewise, the Fe(II)-O bond was modeled with a single peak at 709-709.5 eV. The bonding of ferric iron, Fe(III), with oxygen and sulfur was modeled as a quartet of peaks, based on work by Gupta and Sen (1974). For these quartets of peaks, the peak ratio of higher binding energy peaks to lower binding energy peaks is used to constrain the fit. These fitting parameters are summarized in Table 4.4. In order to quantitatively estimate uncertainty in this peak deconvolution, a Monte Carlo analysis was used (Casa XPS 2009). In this method, artificial, random noise is added to the original spectrum and peak is re-processed. By iterating this process (n = 400), standard deviations of the peak deconvolution are calculated. As noted by Renock et al. (2009), interpretations of XPS spectra should be made with some caution: they represent a plausible description of the surface species, but not all possible species are included in the model, and thus the component peak model is not necessarily a definitive description of the surface.

Table 4.4: Parameters for fitting of the Fe(2p3/2) peak in XPS spectra

Peak	Bond	Peak center (ev)	Range (± ev)	Peak ratio[b]	FWHM[A]
$Fe2p_{(3/2)}$	Fe(II)-S	707.3	0.1	na	2
$Fe2p_{(3/2)}$	Fe(II)-O	709.25	0.25	na	2
$Fe2p_{(3/2)}$	Fe(III)-S	708.9	0.1	1	2
$Fe2p_{(3/2)}$	Fe(III)-S	709.9	0.1	0.66	2
$Fe2p_{(3/2)}$	Fe(III)-S	710.8	0.1	0.35	2
$Fe2p_{(3/2)}$	Fe(III)-S	711	0.1	0.1	2
$Fe2p_{(3/2)}$	Fe(III)-O	710.9	0.1	1	2
$Fe2p_{(3/2)}$	Fe(III)-O	712.1	0.1	0.66	2
$Fe2p_{(3/2)}$	Fe(III)-O	713.1	0.1	0.35	2
$Fe2p_{(3/2)}$	Fe(III)-O	714.1	0.1	0.1	2

Sources for Table 4.4 are A = Mullet et al. (Mullet et al. 2002) and B = Gupta and Sen (1974).

The second surface technique is Scanning Electron Microscopy with Energy Dispersive Spectroscopy (SEM-EDS); SEM allows for visualization of the surface of the reactive media particles, while EDS can be used to qualitatively assess the speciation and quantity of surface precipitates (e.g., Phillips et al. 2003). The SEM was a Philips XL30 Environmental SEM (FEI, Hillsboro, OR). Two types of samples were analyzed with the SEM. First, samples taken directly from the columns were analyzed without further preparation. For ZVI, images were collected using a 20kV electron beam, a spot size of 3, and a working distance of 5 mm. Images at magnifications of approximately 100 – 10,000x were collected. Secondly, samples were fixed in epoxy (Castolite Resin, Buehler Ltd., Lake Bluff, IL), sectioned, and ground to a flat surface, as was done by Roh et al. (2000) and Mackenzie et al. (1999). This epoxy technique allows for a unique view of the interstitial spaces in the reactive media.

4.3.7 Modeling

4.3.7.1 Calculated hydraulic conductivity losses

The aqueous calcium, carbonate, and total iron data may be used to estimate solids formation and porosity losses. A mass balance on calcium may be written by assuming that all calcium removed from the aqueous phase is retained as a calcium carbonate solid. Likewise, a molar balance on carbonate may be written by assuming that all carbonate removed from the aqueous phase is retained as either calcium carbonate or an iron carbonate phase, and the iron carbonate phase can account for the carbonate removal not accounted for by calcium carbonate removal.

The potential for iron solids formation may be estimated from two mechanisms that may oxidize ZVI: anaerobic corrosion (Equation 2.5) and oxidation by solutes such as nitrate or oxygen (Equation 2.6). Reardon (1995) estimated an anaerobic dissolution rate of ZVI by water of 0.7 mmol/kg-d. This corrosion rate was used to predict a total amount of iron corroded. Some of this iron leaves the column in the aqueous phase, and some remains in

the column as Fe(II) or Fe(III) solids. Aqueous concentrations of iron thus may be used to estimate the potential for iron solids formation.

For calculations of porosity loss, the selection of solid phases is important, for the solids' densities will impact the porosity. Based on identification of aragonite in the SEM analysis, aragonite was used as the calcium carbonate solid. In order to estimate lower and upper bounds for solids formation, two sets of iron carbonate and iron hydroxide phases were used in these calculations. The lower-bound set of solids was FeOOH and $FeCO_3$, which have relatively high densities, and hence occupy less volume per mole formed (Table 4.5). $Fe(OH)_3$ and carbonate green rust (CGR) were used to estimate high solid volumes, for they have lower densities. For each set of solids, porosity losses were estimated from the calcium and carbonate mass balances, in addition to the anaerobic iron corrosion rate. Then, reported densities and molecular weights (Table 4.5) were used to calculate a volume of precipitates. Using this calculated porosity loss, a permeability loss due *only* to solids was calculated based on the Kozeny-Carman relationship (Equation 2.19).

In addition to estimating permeability loss due only to solids, the Kozeny-Carman equation was used to calculate an effective, or saturated, porosity from measured hydraulic conductivity losses. This calculation is relevant for cases in which the porous media is no longer fully saturated. In such cases, the permeability loss due only to solids will not account for measured hydraulic conductivity losses. In unsaturated flow, the saturated porosity predicted from the Kozeny-Carman equation may be less than the actual porosity. In this case, the gas content of the void space was calculated from the following relationship:

$$n_{initial} = f_{solids} + \theta + a \qquad \textbf{(4.1)}$$

where $n_{initial}$ is the initial porosity, f_{solids} is the solids content (volume solids / total volume), θ is the water content (water volume / total volume), and a is the gas content (gas volume / total volume). Based on the estimated water content, the effective water

saturation and relative permeability may be calculated according to Equations 2.20 and 2.21.

A final consideration for the calculation of permeability loss is the spatial distribution of precipitates. As discussed in Section 2.3.2, it has been noted in the field that the zone of precipitate formation is often near the upgradient face of the PRB. Therefore, a range of permeability losses were calculated by restricting the region of the column (expressed as a column length fraction) over which the solids were assumed to form. Column length fractions of 1, 0.5, and 0.1 (corresponding to 25, 12.5, and 2.5 cm) were used.

4.3.7.2 Geochemical modeling

The geochemical modeling software package PHREEQC (Parkhurst and Appelo 1999) was used to model both the FeS and ZVI systems. PHREEQC allows for calculation of redox conditions based on other system parameters. Although PHREEQC has kinetic modeling capabilities, all simulations conducted here assumed equilibrium chemistry, since equilibrium predictions of, for example, precipitation will provide a conservative estimate of the quantity of precipitates.

In the model, the gas phase was treated in two different ways. First, a constant pressure of 1 atmosphere was maintained, and gas phases were allowed to form if their partial pressure exceeded one atmosphere. Secondly, the creation of gas phases was not allowed, although the partial pressures of gas phases were calculated. These partial pressures can thus provide information about the potential for total gas formation. These two approaches provide an upper and lower bond for gas formation expected in the system.

In the PHREEQC modeling, the reduction of inorganic to organic carbon was not considered, although the reduction of sulfate to sulfide was allowed, as well as the reduction of nitrate to nitrite, nitrogen gas, and ammonia. As noted in Section 2.2.3, the reduction of sulfate to sulfide is not expected to occur in the absence of biological mediation, nor is the reduction of nitrate by iron sulfide. By allowing these reductions to occur, conservative estimates of the *potential* – in a biologically-active field site - for pH increase, and hence solids production, were obtained.

The WATEQ4F database (Ball and Nordstrom 1991), which is based on the MINTEQ database (used by MINEQL+) but is expanded to include heavy metals (Appelo and Postma 2005), was used for all calculations. The thermodynamic data from the WATEQ4F database was expanded to include the solid phases identified in PRBs (Table 2.5). Carbonate green rust (CGR) and ferrous hydroxide, which are commonly identified in PRBs (Wilkin and Puls 2003; Roh et al. 2000), were two such phases. Morphology of solids in SEM indicated the possibility of CGR. While ferrous hydroxide was not directly identified, XPS analysis suggested the presence of ferrous iron. Although CGR and magnetite also have ferrous species, ferrous hydroxide was included to provide a non-carbonate, ferrous phase for the model. This set of solids is similar to that used by Li and Benson (2006), who found that $CaCO_3$, $FeCO_3$, and $Fe(OH)_2$ were the most important minerals to include in their geochemical model. Table 4.5 summarizes the solid phases included in the geochemical model for this research, and Appendix A presents the reaction data from the WATEQ4F database that were used in these simulations.

Table 4.5: Solid phases used in PHREEQC model, arranged in order of ascending molar volume normalized to moles Fe. These solid phases have been commonly found in PRBs (Jambor et al. 2005; Liang et al. 2003; Wilkin and Puls 2003).

Solid phase	Name	Fe oxid. State	Molec. Wt. (g/mol)	Density (g/cm^3)	Molar vol (cm^3/mol)	Molar vol. / mol. Fe
Fe0	ZVI	0	55.8	7.3[a]	7.6	7.6
Fe_2O_3	Maghemite	3	159.7	5.5[b]	29.1	14.5
Fe_3O_4	Magnetite	2.67	231.5	5.2[c]	45.0	15.0
Fe_2O_3	Hematite	3	159.7	5.3[c]	30.1	15.1
FeOOH	Goethite	3	88.8	4.4[c]	20.3	20.3
FeS	Mackinawite	2	87.9	4.1[b]	21.4	21.4
Fe_3S_4	Greigite	2.67	295.8	3.9[b]	75.5	25.2
$Fe(OH)_2$	Ferrous hydroxide	2	89.9	3.4[b]	26.4	26.4
$FeCO_3$	Siderite	2	115.8	4.0[c]	29.3	29.3
$Fe(II)_4Fe(III)_2(OH)_{12}CO_3{\cdot}2H_2O$	Carbonate green rust (CGR)	2.33	617.2	3.5[d]	176.3	29.4
$Fe(OH)_3$	Ferric hydroxide	3	106.9	3.1[c]	34.5	34.5
$CaCO_3$	Aragonite	na	100.1	2.7[c]	36.9	na

References for density values in Table 4.5 are as follows: a = Jeen et al. (2008), b = Patnaik (2003), c = Hurlbut and Klein (1977), d = Wilkin and Puls (2003).

Carbonate green rust and ferrous hydroxide are not included in the WATEQ4F database and thus had to be added. Because Gibbs free energy of formation ($\Delta G°_f$) data were not available for the WATEQ4F database, it was not possible to directly calculate equilibrium constants for these solids that would be self-consistent with the database. In order to add these species to the database, it was therefore necessary to back-calculate $\Delta G°_f$ values for their components. To accomplish this, species with agreed-upon $\Delta G°_f$ values in the literature were identified and used to determine $\Delta G°_f$ values for the components of CGR and $Fe(OH)_2$.

The reported $\Delta G°_f$ values for water ($\Delta G°_f$ =-237.1 kJ/mol), $Fe(OH)^+$ ($\Delta G°_f$ =-277.4 kJ/mol), and HCO_3^- ($\Delta G°_f$ =-586.8 kJ/mol) were consistent among authors (e.g., Drissi et al. 1995 and Génin et al. 1998). These values were therefore used to determine the $\Delta G°_f$ values in the WATEQ4F database for Fe^{2+}, Fe^{3+}, OH^-, and CO_3^{2-}. Gibbs free energy of formation values for CGR ($\Delta G°_f$ = -4042.79 kJ/mol) and $Fe(OH)_2$ ($\Delta G°_f$ = -486.6 kJ/mol)

were taken from Drissi et al. (1995). Using the $\Delta G°_f$ values, the following equilibrium constants were calculated for the following reactions:

$$\left[Fe_4^{II}Fe_2^{III}(OH)_{12}\right][CO_3 \cdot 2H_2O] + 12H^+ = 4Fe^{2+} + 2Fe^{3+} + 14H_2O + CO_3^{2-} \quad \textbf{(4.2)}$$

For carbonate green rust, log K = 39.07.

$$Fe(OH)_2 + 2H^+ = Fe^{2+} + 2H_2O \quad \textbf{(4.3)}$$

For ferrous hydroxide, log K = 14.39.

For each column, two different sets of simulations were conducted. In the first, all of the solids presented in Table 4.5 were included in the calculations as possible phases. This set was designated "all." The second set of simulations was meant to be a conservative estimate of solids formation, so for each oxidation state of iron, the solid with the highest molar volume per mole Fe was the only solids included as a possible precipitate. This restricted set of solids, designated "high vol.," consisted of $Fe(OH)_2$, $Fe(OH)_3$, ZVI, aragonite, siderite, and carbonate green rust (CGR).

Modeling of these systems requires an estimate of the effective concentration of reactive media that, when emplaced, may interact with the aqueous phase (Liang et al. 2003). Therefore, a range of concentrations was established based on different methods of estimation. First, the value for ZVI corrosion published by Reardon (1995) of 0.7 mmol/kg-d was used to set at lower bound. To convert this rate into a concentration, dimensions and flow rates of the current study were used: the 5 cm inner diameter, 25 cm long columns held about 1.3 kg of ZVI once packed. With a flow rate of 0.7 mL/min (1.08 L/day), this corrosion rate corresponds to an aqueous concentration of 0.85 mmol/L of ZVI introduced into the column. An upper bound for the effective concentration of ZVI was calculated based on the mass balance on carbonate and calcium. This mass balance was used to estimate formation of calcium carbonate and iron carbonate solids in the column (see Section 5.1.1). Based on this calculation, it was estimated that a total of 16.9 mmol/L of iron was necessary to account for the total carbonate loss in the system. This value is of the same order of magnitude as 20 mmol/L, which Liang et al. (2003)

found was the highest concentration of ZVI dissolution necessary to match measured geochemical data in the Y-12 Pathway 2 PRB.

In the FeS system, however, the total amount of FeS added to the column system is known. Based on the average coating of 1.47×10^{-5} mol FeS / g sand, the column dimensions noted above, and a packed porosity of 0.31, there are approximately 13.2 mmoles of FeS in a column. However, estimating the amount of FeS added for a batch calculation still requires some assumptions. Column experiments with FeS-coated sand and pH 5 buffered water indicated that FeS was dissolving at a rate that would not exhaust the FeS coating for over 2000 pore volumes (Han 2009). Based on this information, assuming that the FeS equilibrates with 1000 pore volumes, the effective FeS concentration is 0.076 mmol/L.

Based on the above considerations, a reasonable range for reactive media concentrations in the geochemical model is about 0.08 mM to 20 mM. Therefore, for batch equilibrium modeling of these systems, a range of 0.1 to 100 mM was chosen to span the estimated effective concentrations of reactive media and provide information about behavior at concentrations about half an order of magnitude higher.

Chapter 5: Zero-Valent Iron (ZVI) Column Experiments

The statistical analysis showed that high alkalinity, chloride, and nitrate concentrations were linked to PRBs being classified as "at-risk." Furthermore, results in bench scale tests in the laboratory and field-scale reactive cells (e.g., Mackenzie et al. 1999) suggested that oxygen may also be a key player in plugging. Therefore, five column experiments using ZVI and containing high carbonate and calcium, high nitrate, and moderate oxygen concentrations were conducted. At the conclusion of the experiments, the columns were sectioned, analyzed, and modeled using the approaches described in Chapter 4. Table 5.1 summarizes the experimental conditions for the column experiments conducted with ZVI.

Table 5.1: Summary of ZVI column experimental conditions

Column name	Influent solution	Influent pH	Initial K_H (m/d)	Initial porosity (-)	Flow rate (mL/min)	Flow rate (PV/d)	Flow velocity (cm/hr)
ZVI-0O_2	calcium + carbonate	6	8.0	0.61	0.7	3.4	3.5
ZVI-2O_2	calcium + carbonate + 2 mg/L O_2	6	8.0	0.60	0.7	3.4	3.6
ZVI-O_2	DDI water	7	20.7	0.61	0.7	3.4	3.5
ZVI-NO_3	calcium + carbonate + nitrate	6	12.8	0.60	0.7	3.4	3.6

See Table 4.1 for a more detailed description of the composition of the influent solutions.

5.1 ZVI-0O_2 column

The column designated ZVI-0O_2 received an influent solution high in calcium, carbonate, and chloride, but free of dissolved oxygen. Because these constituents were correlated in

adverse permeability changes in PRBs, it was anticipated that this column could lose hydraulic conductivity due to accumulation of carbonate solids.

5.1.1 Column results

Figure 5.1 show the effluent E_H over time for the column designated ZVI-0O_2 column. E_H readings during the first 100 pore volumes were consistently lower than later readings. Even with this increase, the column was still strongly reducing. This result is consistent with the fact that ZVI is a strong reducing agent and consistent with E_H values measured in the field, which average < -300 mV (Table 2.4). As discussed in Section 4.3.4, error bars for the E_H and pH measurements were calculated based on the standard deviation of time series data collected in the flow-through cells.

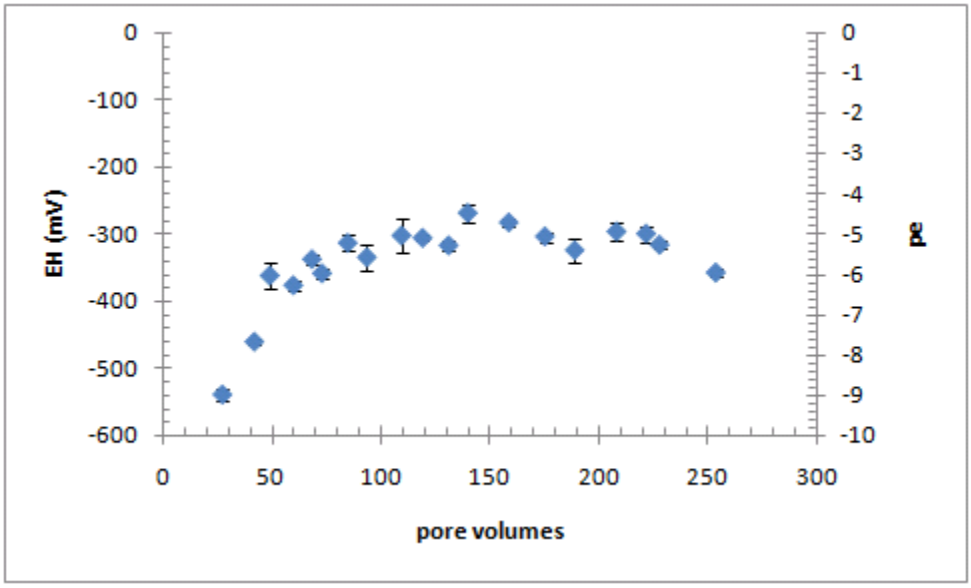

Figure 5.1: Effluent E_H in the column designated ZVI-0O_2 column as a function of pore volumes injected into the column.

Figure 5.2 shows the effluent pH for the same column. The effluent pH was, on average, about two pH units higher than the influent, which was adjusted to pH 6. Again, this is finding is in keeping with pH values measured in field PRBs, which showed an average increase of about 2.5 pH units (Table 2.4).

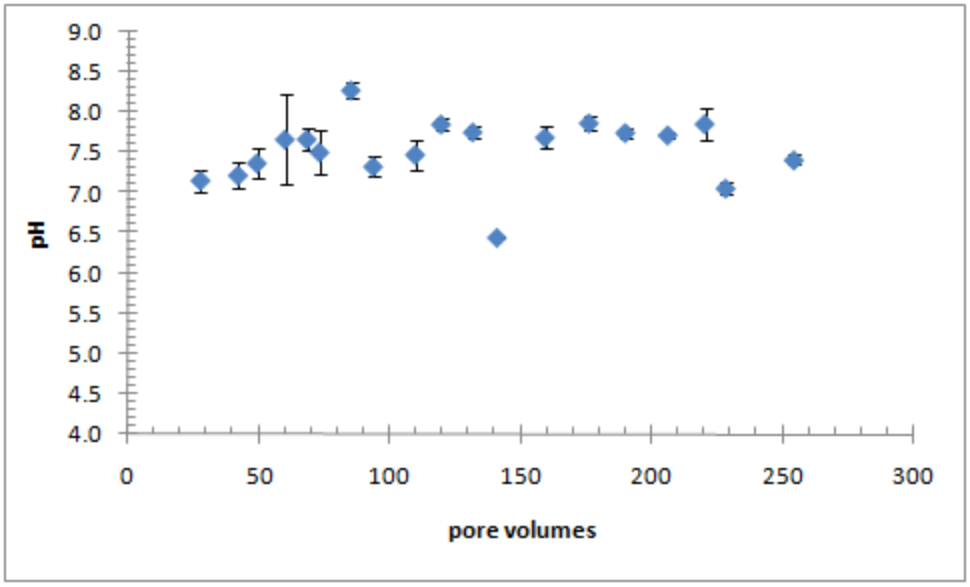

Figure 5.2: Effluent pH in the column designated ZVI-0O_2 as a function of pore volumes injected into the column.

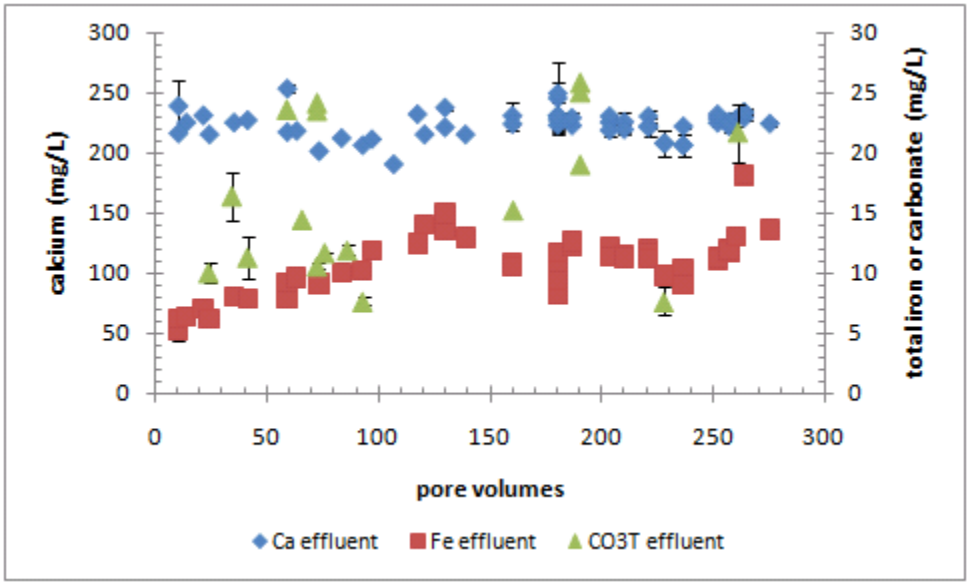

Figure 5.3: Aqueous calcium, total iron, and total carbonate concentrations in the ZVI-0O_2 column effluent as a function of pore volumes injected into the column.

Figure 5.3 shows the effluent calcium concentrations from the column designated ZVI-0O_2 column. Calcium, which had an influent value of 280 mg/L, had an effluent value that ranged between 200 and 250 mg/L. The removal of calcium is most likely linked to the increase in pH, as the observed increase created geochemical conditions in which calcium and carbonate were over-saturated with respect to calcite and aragonite ($CaCO_3$(s)), resulting in the precipitation of calcium-containing solids.

Carbonate, too, was removed in this column (Figure 5.3); the fraction removed was much higher than that for calcium. The effluent concentration for carbonate ranged from 8 to 25 mg/L, as compared with an influent concentration of 420 mg/L; this indicates a removal of about 400 mg/L. Carbonate removal was stoichiometrically greater than the calcium removal, suggesting the formation of an iron carbonate solid in addition to the formation of calcite or aragonite. Aqueous total iron is also shown in Figure 5.3. These data show a clear increase during the first 100 pore volumes; subsequently, the effluent total iron concentrations appear to level off.

The raw pressure drop data along this column, measured by the manometer in centimeters of water, are shown in Figure 5.4, with corresponding hydraulic conductivities shown in Figure 5.5.

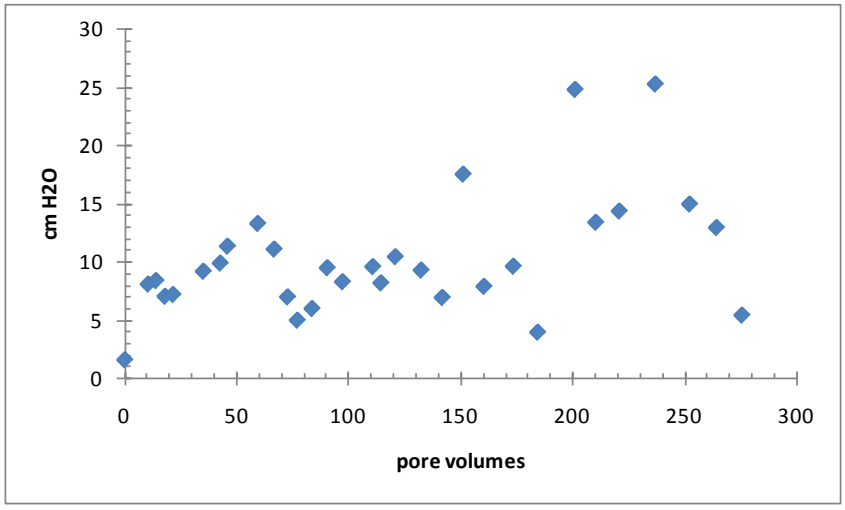

Figure 5.4: Pressure drop along the ZVI-0O_2 column as a function of pore volumes injected into the column.

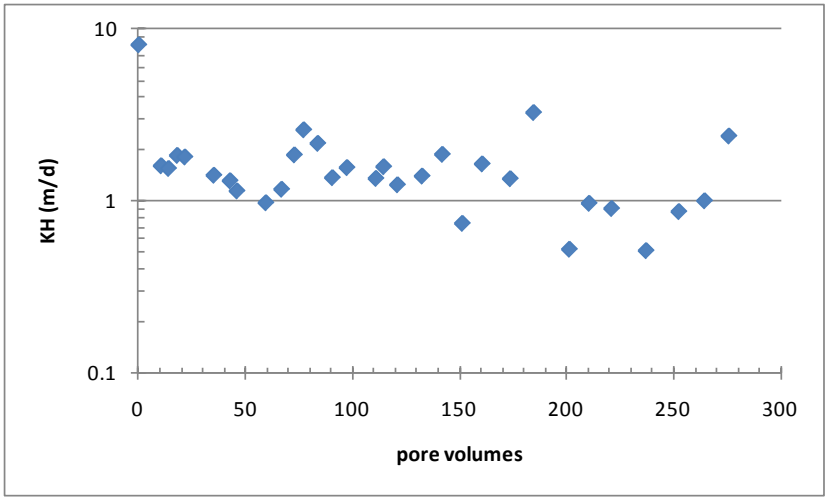

Figure 5.5: Hydraulic conductivity in the column designated ZVI-0O_2 calculated from pressure drop as a function of pore volumes injected into the column.

The scatter observed in the hydraulic conductivity and pressure data is likely caused by the passage of bubbles through the manometer. In these experiments, the ZVI columns, which were initially saturated, were observed to become partially unsaturated as bubbles of gas accumulated in the pore spaces. The presence of hydrogen is expected, for the corrosion of iron by water, as described by Equation 2.5, will produce hydrogen gas. Such gas production has been reported to create high variability in hydraulic conductivity data (Jeen et al. 2006). For this column, one measurement of the eluted gas was made using a GC-RGA (reduction gas analyzer), which is designed to measure low concentrations of gas. With this method, the eluted gas was found to have a hydrogen concentration of approximately 80%, but with an error of, roughly, 50%. Although this measurement is far from precise, this measurement confirmed the production of hydrogen gas.

The loss of calcium and carbonate and the decrease in hydraulic conductivity in the column suggests the formation of solids. To investigate the accumulation of solids in the column, the column was sectioned and examined by SEM.

5.1.2 Solids analysis

Figure 5.6 shows a wide field view of a grain of ZVI taken from the influent end of this column at the conclusion of the experiment (approximately 275 pore volumes). The

elongated crystals shown in detail in (Figure 5.7) appear pure white because they are nonconductive and accumulate charge from the incident electron beam in the SEM. EDS analysis of these crystals indicates the presence of calcium and absence of iron, and their morphology matches that of aragonite presented by Phillips (2003) (Figure 2.5). It is clear, however, that the aragonite crystals do not cover the surface.

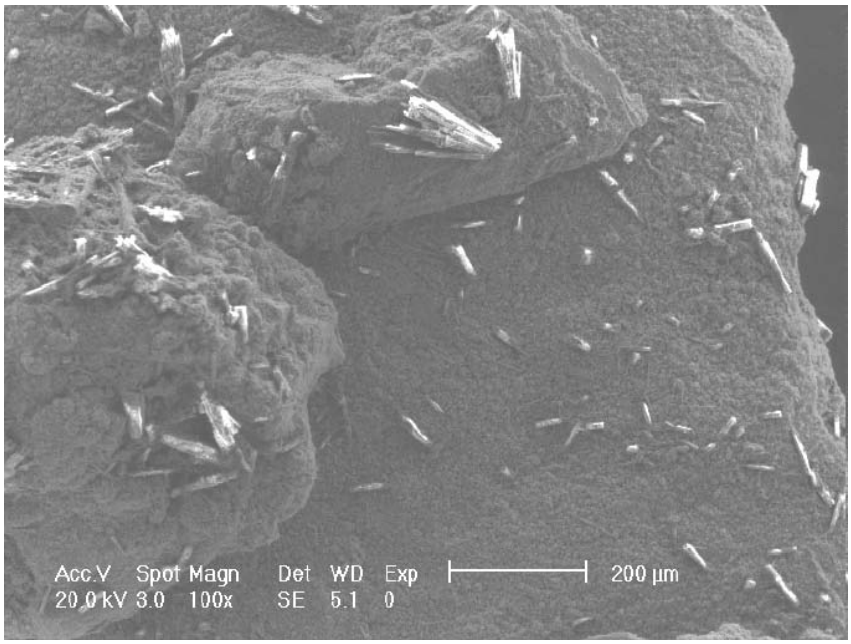

Figure 5.6: SEM of influent sample from ZVI-0O_2 column showing patchy covering by $CaCO_3$ crystals.

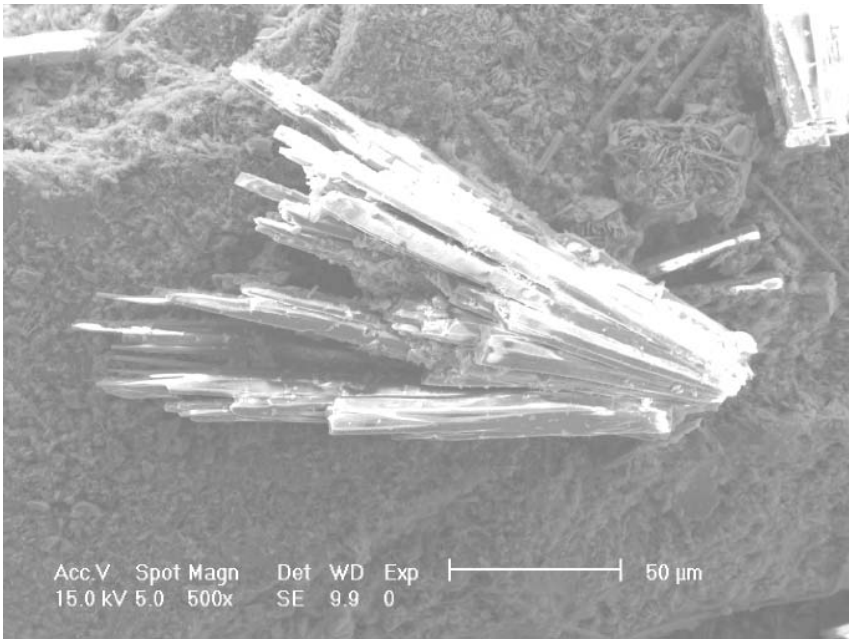

Figure 5.7: SEM of influent sample from ZVI-0O_2 column showing a $CaCO_3$ crystal.

A closer inspection, however, shows a very clear surface covering (Figure 5.8).

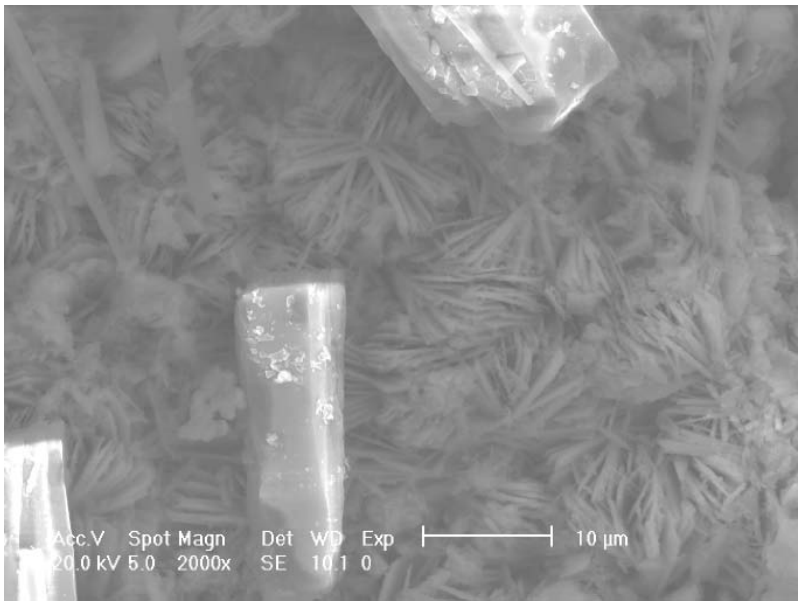

Figure 5.8: SEM of influent sample from ZVI-0O_2 column showing $CaCO_3$ crystals and iron grain surface covering.

The needle-like growths in Figure 5.8 are structurally similar to goethite (Figure 2.5). The presence of nodules on the needle-like precipitates is observed in Figure 5.9. These nodules could be the incipient formation of siderite or green rust crystals, examples of which are shown in Figures 2.5 and 2.6.

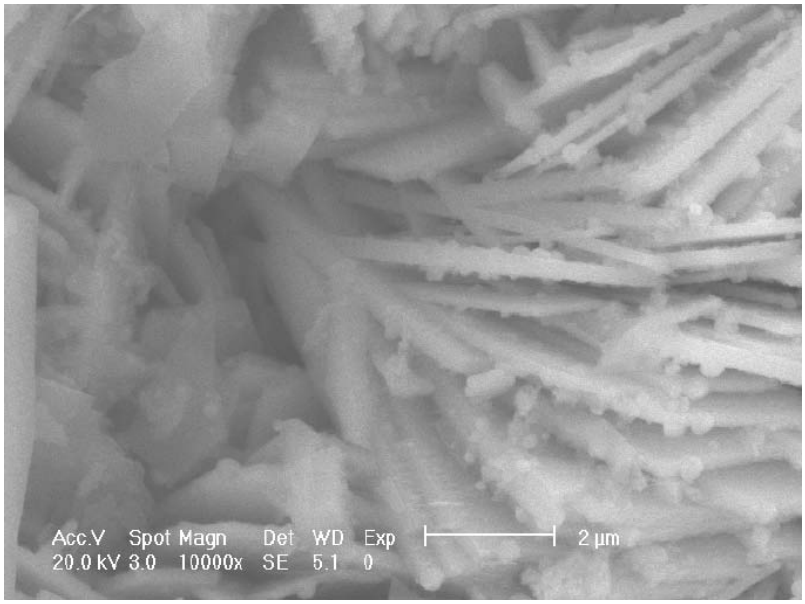

Figure 5.9: SEM of influent sample from ZVI-0O_2 column showing the fine structure of the surface covering.

Based on these SEM images (Figures 5.6 - 5.9), it is clear that the ZVI surface has been covered by a coating that was formed during the column experiment. (The as-received ZVI surface is shown in Figure 4.1.) This coating can be visualized more clearly in cross-section. Figure 5.10 shows the hexagonal aragonite crystals and the surface coating that were observed in the previous images (with detail shown in Figure 5.11). The lower right half of Figure 5.10, below the diagonal running from bottom left to upper right, is the interior of a grain of ZVI. Along the edge of the ZVI, running from lower left to upper right, is a layer of the platy, needle-like precipitates. Extending away from this layer is a less dense layer of a mixture of aragonite (hexagonally shaped, as seen in Figure 5.11) and smaller clusters of needles or platy particles similar to those observed on the surface of the ZVI.

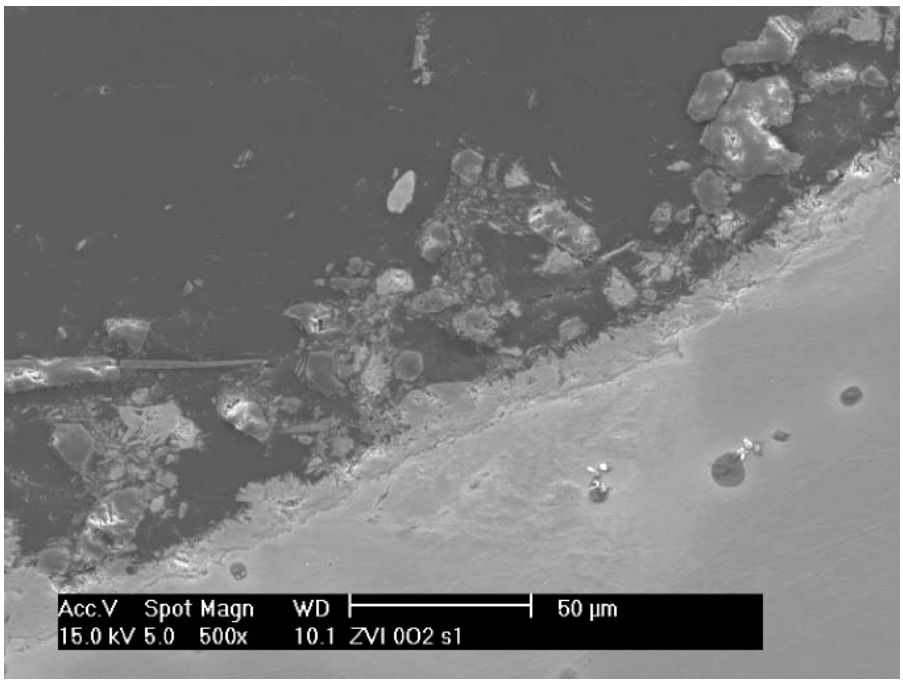

Figure 5.10: Cross-section of surface precipitates with aragonite crystals on grains of ZVI from the influent end of ZVI-0O_2 column.

Based on the SEM micrographs of the non-epoxied samples, such as Figure 5.6, it appears that $CaCO_3$ precipitates sat close to the surface of the ZVI grain; in images of the cross-section, such as Figure 5.10, it appears that the $CaCO_3$ and other precipitates are not flush with the surface. It is possible that the crystals are sitting on the surface and are supported at points, such that a cross-section makes them appear to float. Alternatively,

the process of adding the epoxy may have slightly dislodged particles that were not tightly bound to the surface.

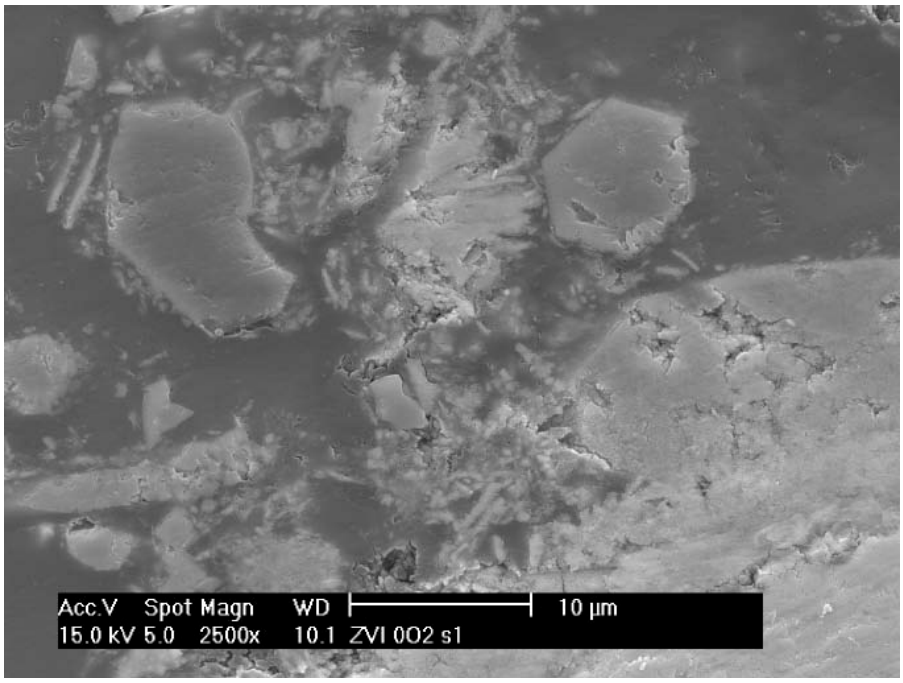

Figure 5.11: Cross-section of surface covering on grains of ZVI from influent end of ZVI-0O_2 column.

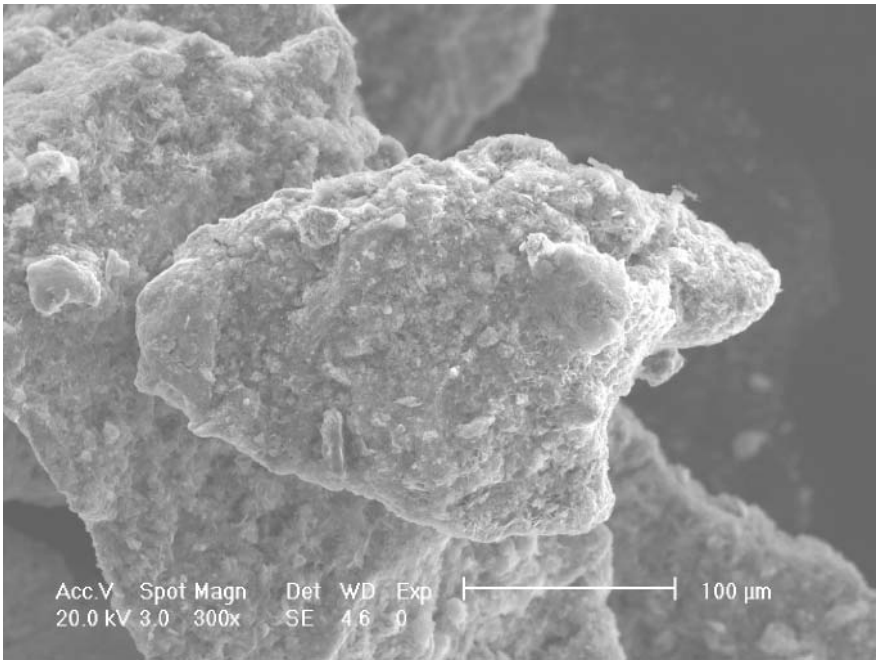

Figure 5.12: SEM of effluent sample from ZVI-0O_2 column showing a less regular surface covering.

Samples from the effluent end of the column reveal a very different surface morphology. Figure 5.12 shows a wide angle view of a ZVI grain from this location. No calcium carbonate crystals are evident, and the morphology of the surface covering (Figure 5.13) is more varied than it was in the influent sample. The relative lack of calcium carbonate crystals indicates that a spatial gradient existed, and that $CaCO_3$ tended to precipitate near the influent end of the column.

An examination of the fine structure of these particles (Figure 5.13) shows a surface composed of a variety of smaller and finer crystals than were evident in the influent section (shown in Figure 5.6).

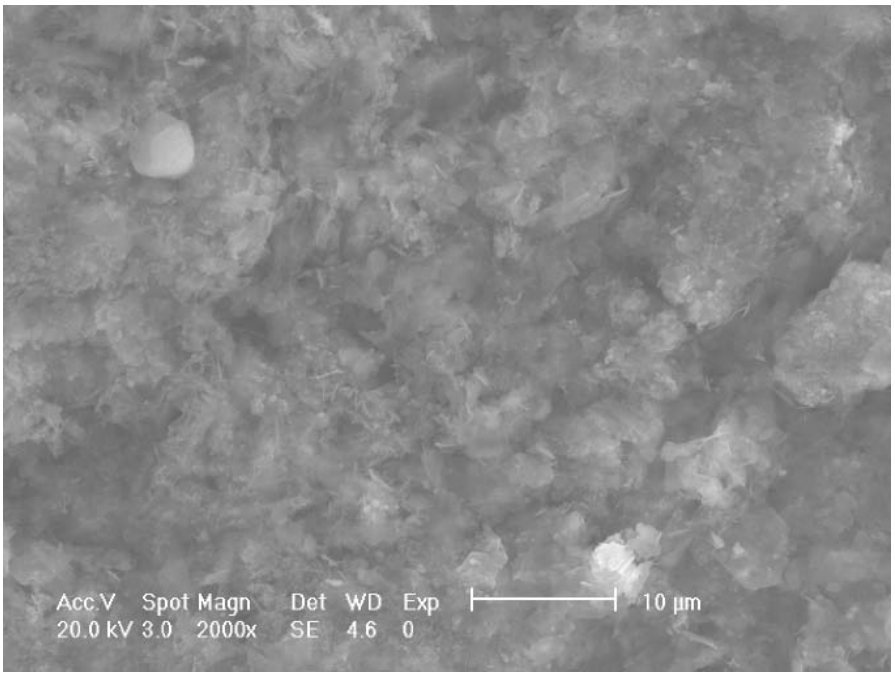

Figure 5.13: SEM of surface covering of sample from the effluent section of the ZVI-0O_2 column.

A closer view of the surface observed in the ZVI-0O_2 column (Figure 5.14) confirms the absence of needle-like components; rather, there are hexagonal plates covered by nodules, a morphology consistent with carbonate green rust (Figure 2.6). An examination of the epoxied and polish cross sections (Figures 5.15 and 5.16) from the effluent end of the ZVI-0O_2 column also reveal differences from the influent section. Whereas the latter showed a consistent layer of precipitates, the samples from the effluent end show a less regular (although sometimes substantial) layer. This layer does not appear as densely

packed as the precipitates from the influent end, and there are no aragonite crystals, which is in keeping with the observation of the non-epoxied samples.

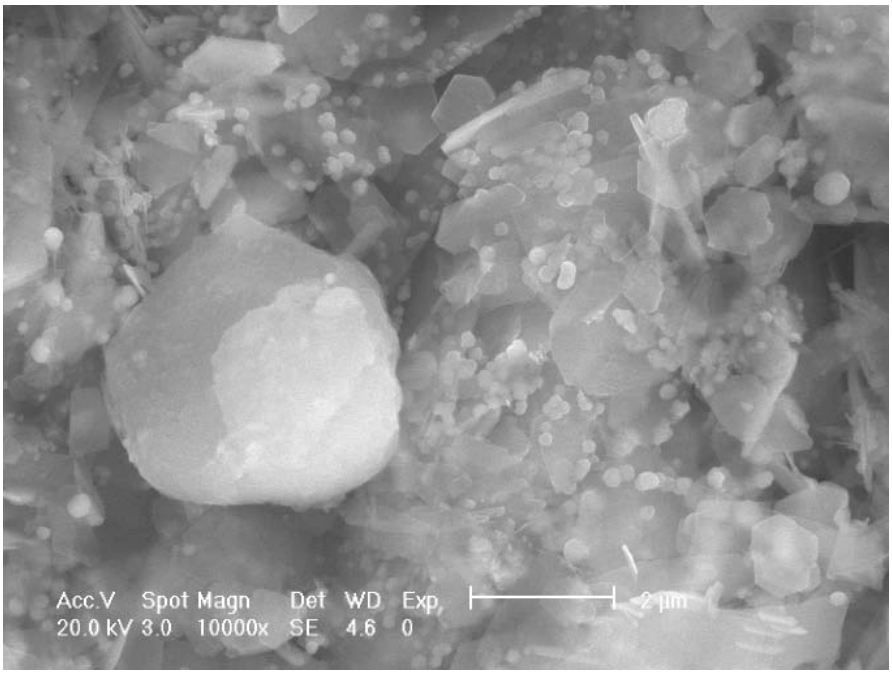

Figure 5.14: SEM of fine structure of ZVI-0O_2 effluent sample.

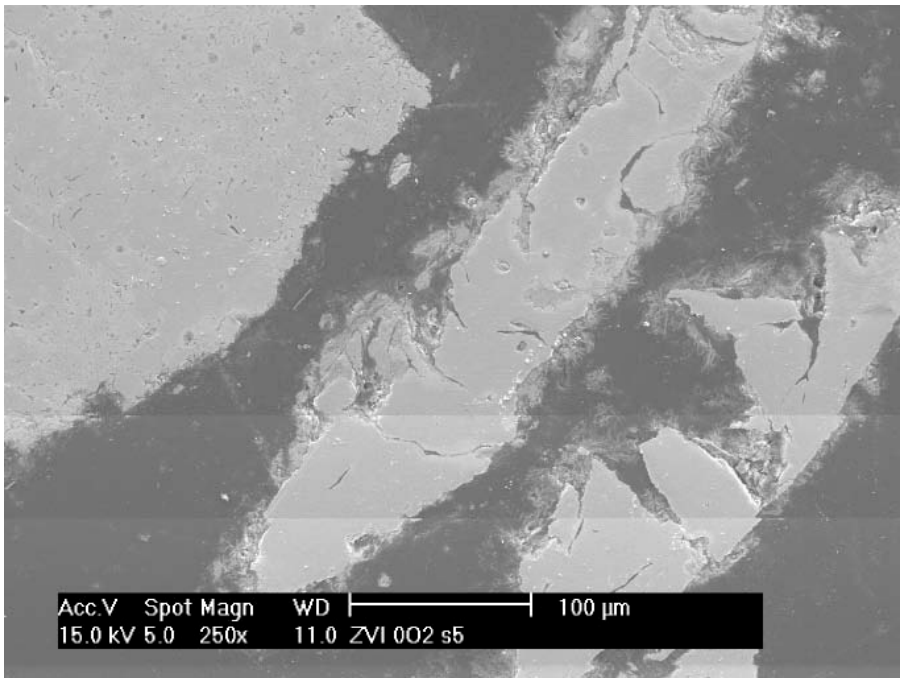

Figure 5.15: Cross-section of grains of ZVI from effluent end of ZVI-0O_2 column.

The non-uniformity of the surface coating is clear in Figure 5.16, as is the elongated nature of the individual precipitates, which could have the form of either needles or plates.

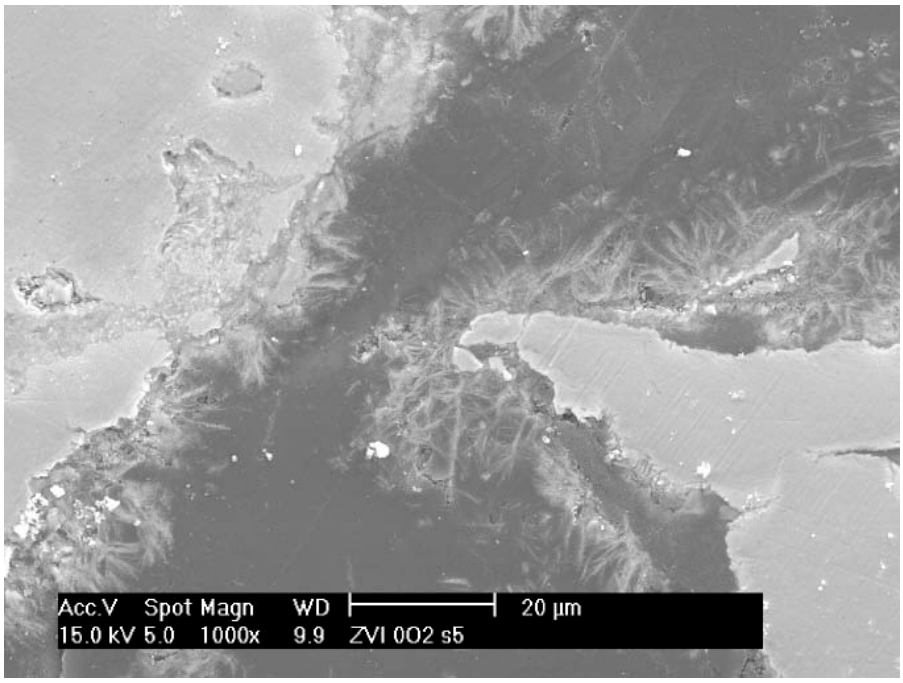

Figure 5.16: Cross-section of grains of ZVI from effluent end of ZVI-0O_2 column.

Overall, SEM images of samples from the influent and effluent ends of this column provide qualitative evidence for the removal of calcium and carbonate as bulk precipitates of aragonite on the solid surface, as well as for a geochemical gradient influencing the composition of surface precipitates.

5.1.3 Modeling

5.1.3.1 Calculations of hydraulic conductivity loss

The analysis of the effluent from the ZVI-0O_2 column and the SEM analysis of samples from that column may be combined in calculations of the potential for solids accumulation, porosity loss, and permeability reduction in the column. The SEM images presented above provide evidence for the presence of aragonite. Evidence for an iron

carbonate solid is less clear. However, calculations of permeability loss can be made using conservative assumptions and thus may still be a useful tool in this analysis.

For this column, the measured $k_{final}/k_{initial}$ was 0.063, from which an effective water content, θ, of 0.27 was calculated, based on the Kozeny-Carman equation. This measured reduction in permeability corresponds to a K_H fraction loss of 0.63 per 100 PV. As described in Section 4.3.7, lower and upper bounds for total porosity losses and gas production over time may be calculated. Table 5.2 presents the results for calculations of water and gas content based on the measured K_H loss, the Kozeny-Carman equation (Equation 2.19), and the power law relationship of Wyllie (1962) (Equation 2.20). Table 5.3 shows results for the hydraulic conductivity loss attributable to the formation of solid and gas phases. In each cell below, the dash indicates the range of values: the first value is calculated assuming low-density solids (FeOOH and $FeCO_3$) precipitates, and the second is based on high-density solids ($Fe(OH)_3$ and CGR).

Table 5.2: Summary of calculations for unsaturated permeability and solids, water, and gas content for ZVI-0O_2 column.

Column fraction for precipitation	Final porosity (initial = 0.61)	f_{solids} (V_{solids} / V_{tot})	a (V_{gas} / V_{tot})	S_w (θ / final porosity)	$k_{final}/k_{initial}$ (from Se^3)
1	0.58 - 0.49	0.026 - 0.12	0.30 - 0.21	0.47 - 0.56	0.080 - 0.15
0.5	0.55 - 0.37	0.053 - 0.23	0.28 - 0.10	0.49 - 0.74	0.094 - 0.37
0.1	0.34 - 0.00	0.26 - 1.0	0.07 - 0.00	0.80 - 0.00	0.49 - 0.00

Table 5.3: Summary of calculations for K_H loss (per 100 PV) attributable to solids and gas formation in the ZVI-0O_2 column.

Column fraction for precipitation	Solids K_H loss (per 100 PV)	Gas K_H loss (per 100 PV)
1	0.064 - 0.26	0.57 - 0.37
0.5	0.12 - 0.48	0.51 - 0.16
0.1	0.53 - 1.00	0.11 - 0.00

These tables indicate that the high-volume solids, CGR and $Fe(OH)_3$, could – in theory – completely account for the hydraulic conductivity loss, but only if the zone of their precipitation is restricted to the first 10% of the column. However, the low-volume

solids, FeOOH and $FeCO_3$, cannot account for the observed loss in hydraulic conductivity, even when restricted to the smallest precipitation zone. This suggests that the gas phase is an important contributor to permeability loss. In Table 5.2, predictions of relative permeability to the water phase are higher than the observed value of 0.063 but are closest for the calculation of high-density solids precipitating along the entire length of the column.

5.1.3.2 Geochemical modeling

The column designated ZVI-$0O_2$ was modeled in batch, equilibrium systems (as discussed in Section 4.3.7) with a water composition matching that of the influent to this column. As discussed in Section 4.3.7.2, a matrix of four sets of simulations were conducted. One variable was whether a gas phase was allowed to form, and the second was the choice of solids. The simulations designated "all" includes the solids commonly identified in PRBs (Table 4.5): ZVI, $Fe(OH)_2$, $Fe(OH)_3$, goethite, hematite, maghemite, magnetite, aragonite, siderite, and carbonate green rust. In the second simulation, the solid phases that were included in the calculation were selected from the first set and included, for each oxidation state of iron, the solid with the highest volume per mole of iron. These solids, referred to as "high vol." in the following figures, included $Fe(OH)_2$, $Fe(OH)_3$, ZVI, aragonite, siderite, and carbonate green rust (CGR).

Figure 5.17 shows a comparison of the pH and pe values predicted in the model without headspace, and Figure 5.18 compares these parameters in the model in which a gas phase was allowed to form. The increase in pH and decrease in pe are consistent with the dissolution of ZVI, which produces hydroxide anions and liberates electrons to the solution, according to Equation 2.5. Indeed, ZVI, because it is thermodynamically unstable in water, is never predicted to exist at equilibrium by model. Hence, the addition of ZVI is equivalent to the addition of iron and electrons to the system.

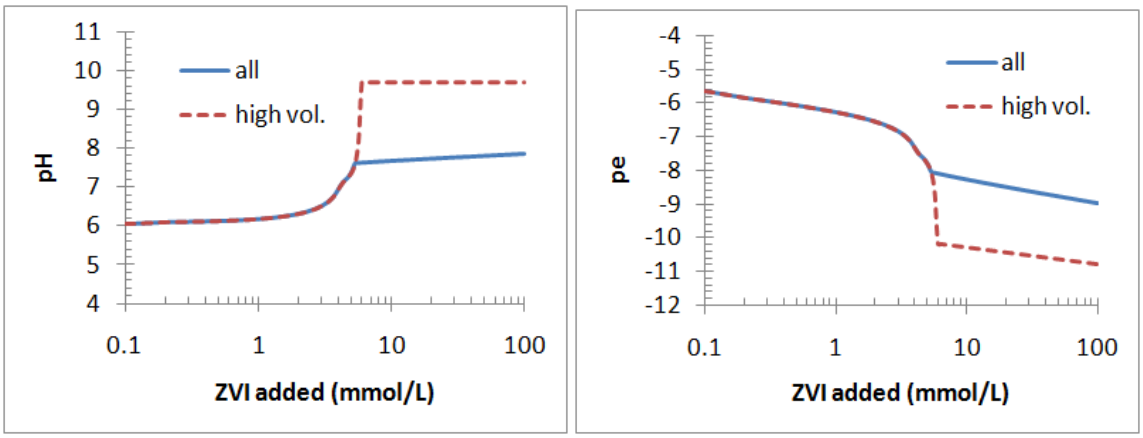

Figure 5.17: Equilibrium, model of ZVI-0O_2 system without gas phase: predictions of pH (left) and pe (right), allowing all solids or only high-volume solids to precipitate.

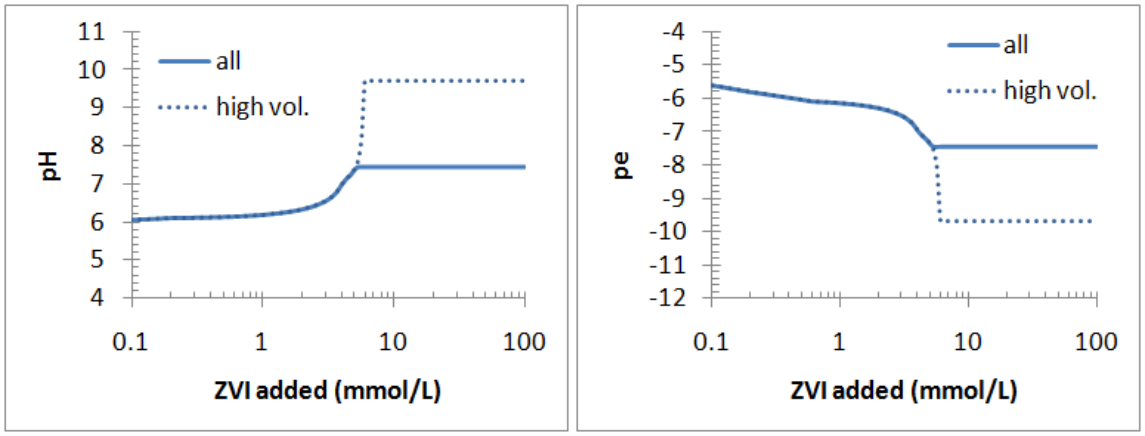

Figure 5.18: Equilibrium, model of ZVI-0O_2 system with gas phase: predictions of pH (left) and pe (right), allowing all solids or only high-volume solids to precipitate.

Comparison of simulations with (Figure 5.18) and without (Figure 5.17) a gas phase show that the presence or absence of a gas phase does not strongly influence the model behavior. The shape of the pH and pe curves, as well as the differences between the behavior of the high volume and unrestricted solid phase models may be explained by considering the prediction of solid phases.

Figure 5.19 compares predictions for precipitate formation of the model with gas production utilizing the unrestricted and high-volume solid sets. As with the pH and pe predictions, the differences between simulations with and without gas were negligible. The model predicted identical amounts of siderite and aragonite and similar amounts of iron (hydr)oxide. The difference is that $Fe(OH)_2$ is predicted with the high-volme set of solids, whereas magnetite is predicted with the unrestricted set.

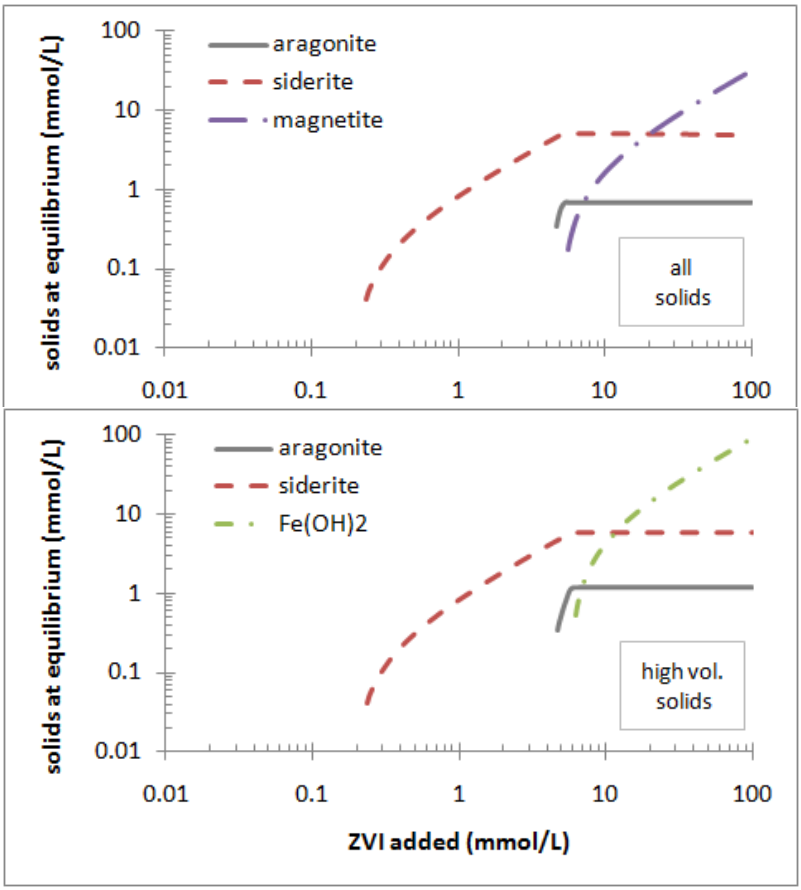

Figure 5.19: Equilibrium solids predicted in the model of the ZVI-0O_2 system with gas formation allowed, with unrestricted solids (top) and high-volume solids (bottom).

Figure 5.19 shows that in both simulations, siderite is predicted to be the only phase precipitating up until 7 mM ZVI is added. Below this level of ZVI addition, the pH increase is buffered by the presence of carbonate, which has an initial aqueous concentration of 7 mM. Once there is more ZVI in the system than carbonate, excess iron begins to precipitate as either $Fe(OH)_2$, in the case of the high volume set of solids, or magnetite, in the case of the unrestricted set. The solids, in turn, affect the pH and pe of the systems. Magnetite, as shown in Table 2.5, is a mixed Fe(II/III) solid, the precipitation of which generates eight protons. Therefore, the precipitation of magnetite counteracts the pH increase caused by the ZVI and fixes the pe at a level between Fe(II) and Fe(III). In contrast, the precipitation of $Fe(OH)_2$, an Fe(II) solid, fixes the pe at a lower level, and only consumes two protons when it is formed, so does not counteract the pH increase to the same degree.

Figure 5.20 shows the model predictions for the hydraulic conductivity loss in the ZVI-$0O_2$ system for both the unrestricted and high-volume solid simulations. These calculations of hydraulic conductivity loss were made according to the procedure described in Section 4.3.7.1. Figure 5.21 shows an expanded view of the model behavior for the right panel (K_H loss due to solids and gas formation) of Figure 5.20.

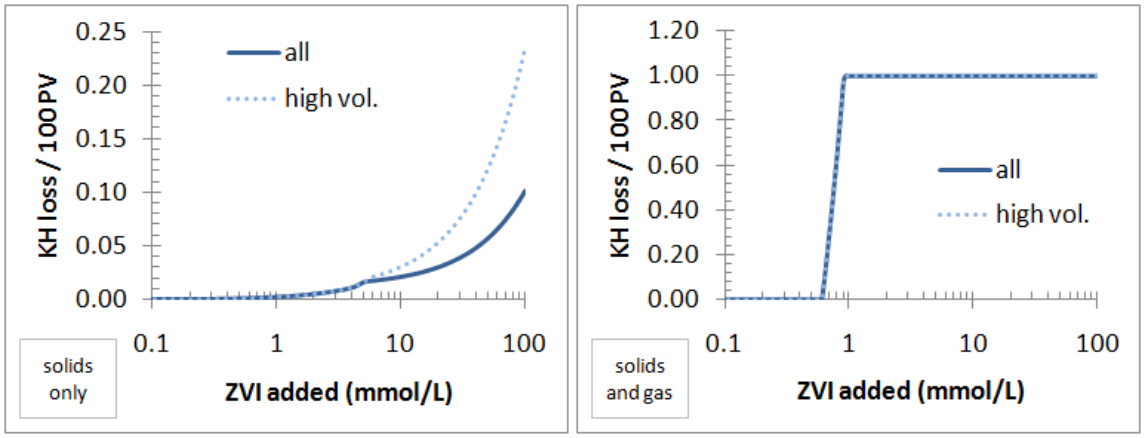

Figure 5.20: Comparison of hydraulic conductivity loss predicted in the model of the ZVI-$0O_2$ system due to solids (left) and solids and gas formation (right), with unrestricted (all) and high volume (high vol.) solids precipitation allowed.

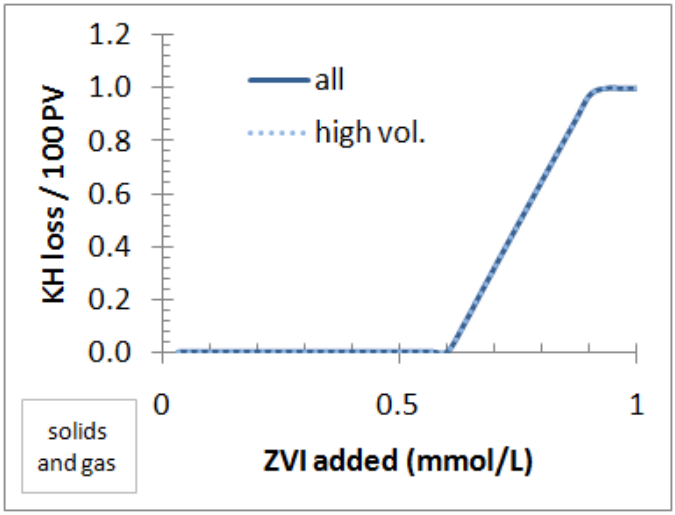

Figure 5.21: Expanded view of hydraulic conductivity loss predicted in the ZVI-$0O_2$ system due to the formation of solids and gas, for the unrestricted set of solids and the high-volume (high vol.) set.

It is evident, by comparing the right and left panels of Figure 5.20, that the presence of gas has a substantial effect on hydraulic conductivity loss. The generation of gas as a function of ZVI added in this model is shown in Figure 5.22. In this simulation, gas produced is retained in the batch system, thus occupying pore space, while the pressure

remains constant at 1 atm. Because gas cannot escape, this model is taken as an extreme, worst-case scenario of the possibility for hydraulic conductivity loss.

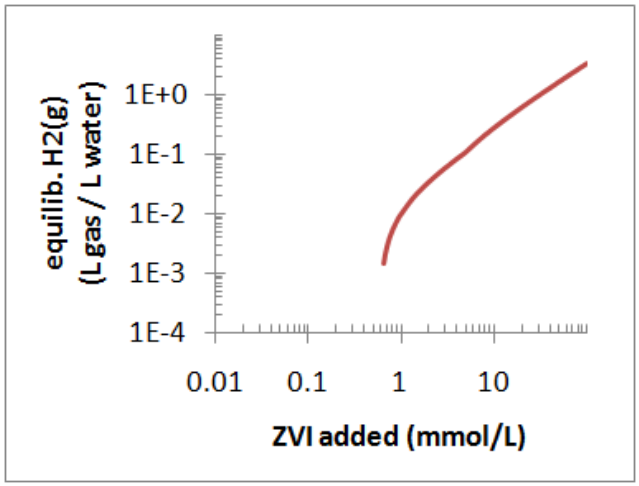

Figure 5.22: Model predictions of hydrogen gas generation in the model of the ZVI-0O_2 system for total pressure = 1 atm.

The actual equilibrium hydraulic conductivity loss is expected to lie between the simulations presented in Figure 5.20. Considering the hydraulic conductivity loss predicted due to solids, it is the difference between $Fe(OH)_2$ and magnetite that drives the difference between the curves in the left panel of Figure 5.20, since both systems have the same amount of carbonate solids. $Fe(OH)_2$ has a density of 3.4 g/cm^3, while magnetite has a density of 5.2 g/cm^3. However, the difference between solids is even greater if the amount of iron in each solid is considered. Magnetite occupies 15 cm^3/mole Fe, while $Fe(OH)_2$ occupies 26.4 cm^3/mole Fe, nearly double the amount for magnetite (Table 4.5). As ZVI dissolves, $Fe(OH)_2$ can precipitate at a 1:1 molar ratio; in contrast, it takes three moles of ZVI to form one mole of magnetite. Therefore, the curves in Figure 5.20 represent a range for solids accumulation and hydraulic conductivity loss in the model of the ZVI-0O_2 system. The measured values for the column system do, indeed, lie between these two extremes, for solids alone cannot account for the observed hydraulic conductivity loss, yet the column did not completely lose hydraulic conductivity.

5.2 ZVI-2O_2 column

The analysis of field sites using ZVI for PRBs indicated that many of the sites had non-zero dissolved oxygen concentrations (Table 2.4). Of the 16 PRBs, the average influent dissolved oxygen level was 1.7 mg/L. Therefore, 2 mg/L was chosen to reflect typical field conditions. Because the interaction of ZVI with oxygen (as shown in Equation 2.6) is expected to increase the pH, it is anticipated that the conditions for the precipitation of solids will be more favorable than in the ZVI-0O_2 column. This column used an influent solution identical to that of the ZVI-0O_2 column, but with the addition of 2 mg/L of dissolved oxygen. Other experimental conditions, such as flow rate, were also identical.

5.2.1 Column results

Figure 5.23 shows that the redox conditions in the column designated ZVI-2O_2 are as reducing as they were in the ZVI-0O_2 column. During the course of the experiment, the lowest effluent E_H values were recorded during the first 100 PV of operation, as in the ZVI-0O_2 column. It therefore appears that the addition of 2 mg/L O_2 did not alter the effluent redox conditions during the time frame of this experiment.

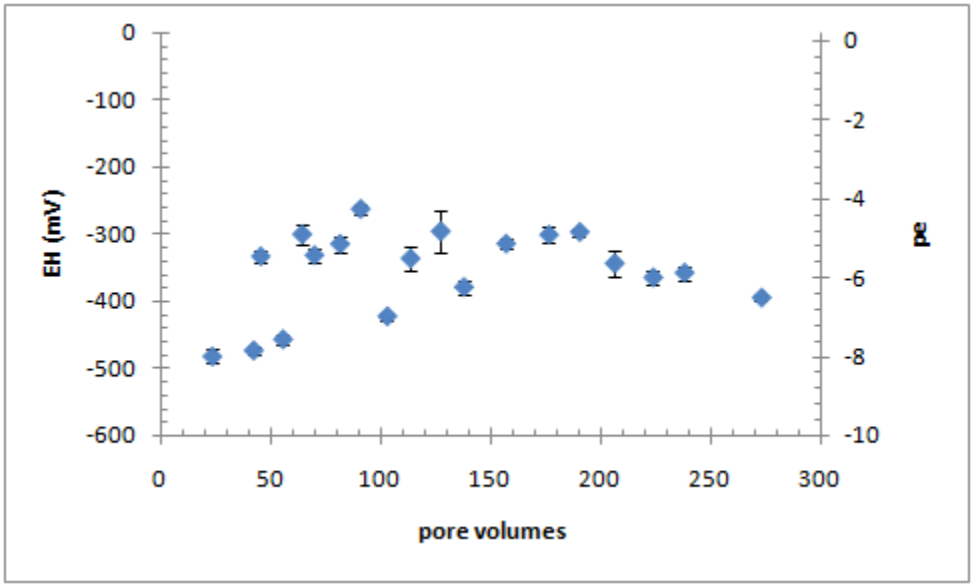

Figure 5.23: Effluent E_H in the column designated ZVI-2O_2 as a function of pore volumes injected into the column.

In this column, the influent pH was 6, and the effluent pH was approximately two units higher; consequently, there was not a significant difference between the effluent pH of this column, shown in Figure 5.24, and the effluent pH of the column receiving 0 mg/L of oxygen, shown in Figure 5.2.

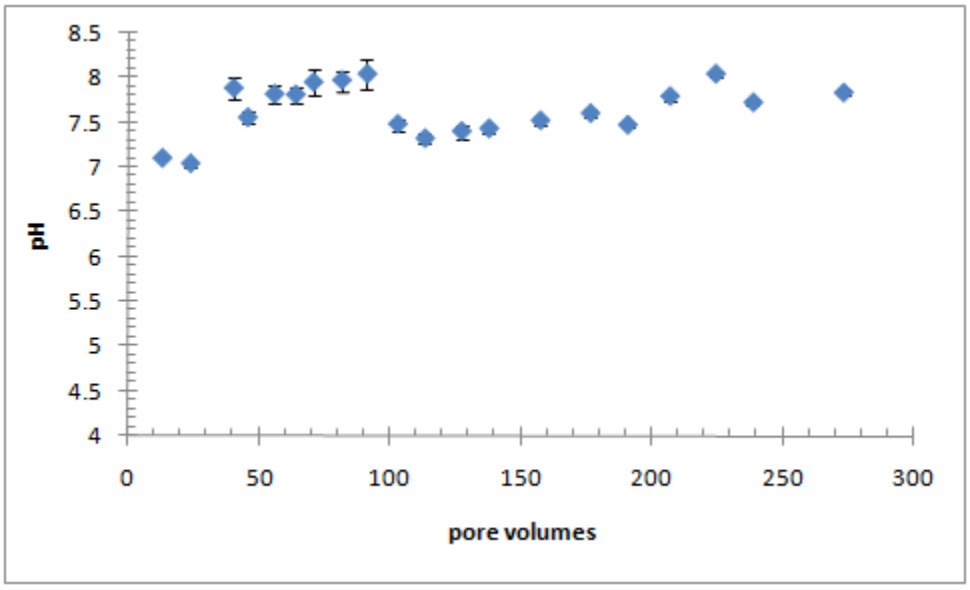

Figure 5.24: Effluent pH in the column designated ZVI-2O_2 as a function of pore volumes injected into the column.

Figure 5.25 shows that the pressure difference along the ZVI column containing 2 mg/L of O_2 increased over the 300 pore volumes of the experiment, increasing from a pressure difference of essentially 0 cm H_2O to 70 cm H_2O. This pressure difference is nearly three times the maximum pressure difference in the ZVI-0O_2 column, which reached 25 cm of H_2O.

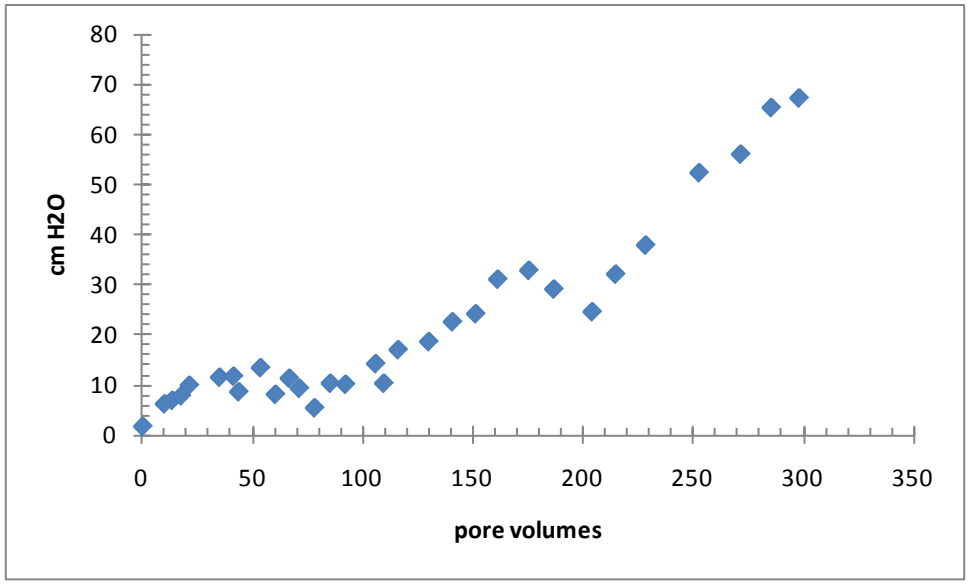

Figure 5.25: Pressure drop along the column designated ZVI-2O$_2$ as a function of pore volumes injected into the column.

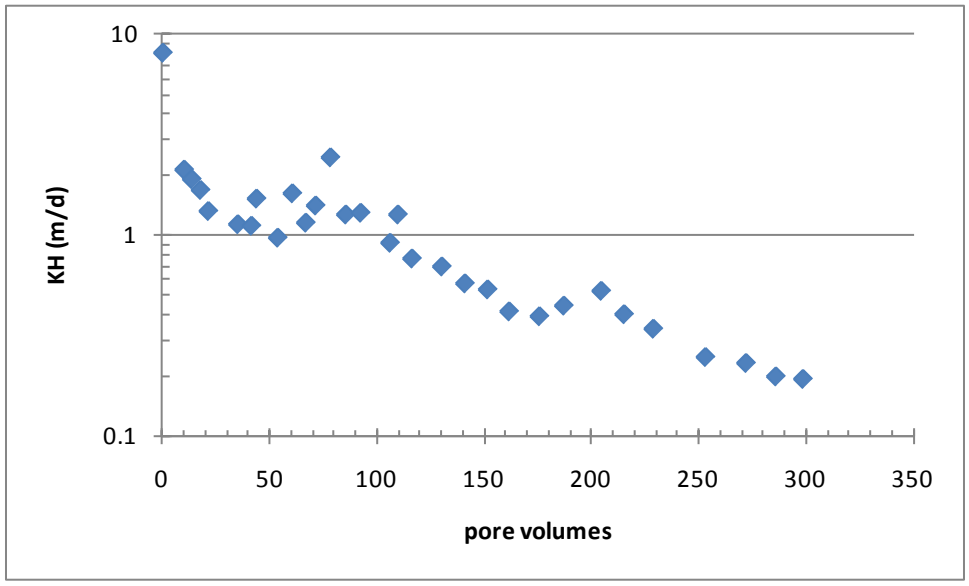

Figure 5.26: Hydraulic conductivity in the column designated ZVI-2O$_2$ calculated from pressure drop as a function of pore volumes injected into the column.

The corresponding decrease in hydraulic conductivity, shown in Figure 5.26, indicates a steady decrease in K_H. The total decrease in K_H depends on the selection of a starting value. If the first data point is a true indication of the clean bed hydraulic conductivity of this column, then the total K_H loss is close to two orders of magnitude (from ~9 to ~0.2 m/d). If the initial K_H is closer to 2 m/d, the value at 10 pore volumes, then the total K_H loss is approximately one order of magnitude.

A loss of hydraulic conductivity is expected to be caused by the accumulation of solids and the generation of gases. Figure 5.27 shows the effluent calcium and total iron concentrations for the ZVI-2O_2 column. Effluent calcium values averaged about 225 mg/L, which represents an average calcium removal of about 55 mg/L. This removal is marginally higher than that observed in the ZVI-0O_2 column (Figure 5.3). The effluent iron concentration, however, shows a magnitude and trend similar to that observed in the ZVI-0O_2 column. Effluent carbonate values ranged from 10 to 27 mg/L, down from the influent concentration of 420 mg/L. Gas collected from the effluent line of this column was analyzed for hydrogen content, and it was found to be about 85%. This suggests that anaerobic corrosion of ZVI (Equation 2.5) was occurring.

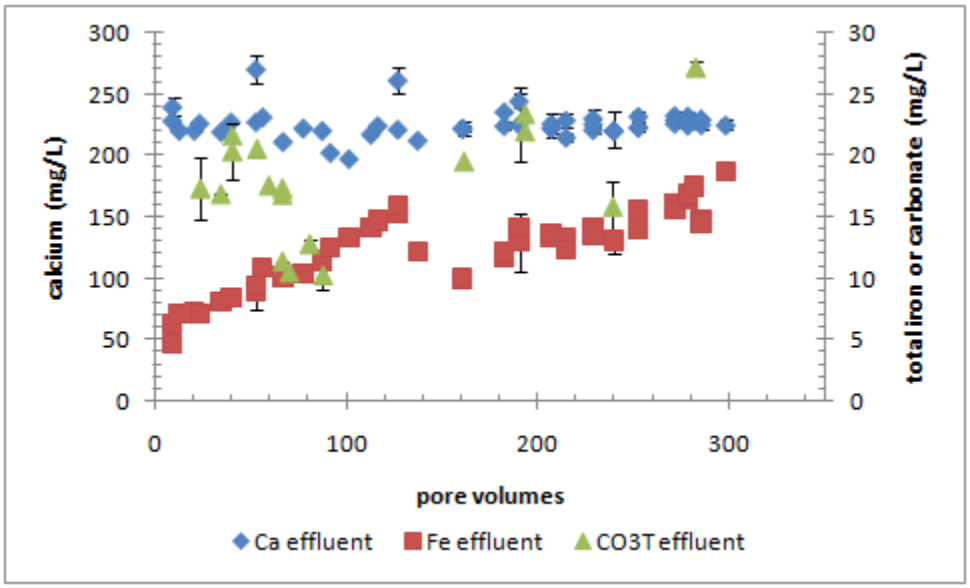

Figure 5.27: Aqueous calcium, total iron, and total carbonate concentrations in the effluent of the column designated ZVI-2O_2 as a function of pore volumes injected into the column.

5.2.2 Solids analysis

Figure 5.28 shows the surface of a grain of ZVI from the influent end of the column receiving 2mg/L of dissolved oxygen. This sample was taken at the conclusion of the column experiment, during which 300 pore volumes of solution passed through the column. The occasional calcium carbonate crystal is noticed, but such crystals are not as common as they were in the ZVI-0O_2 column. As before, the surface covering of iron (hydr)oxides is striking. A closer view of this covering is shown in Figure 5.29, and

Figure 5.30 shows the fine structure of the surface covering. Additionally, in Figure 5.28, the aragonite crystals that are observed appear to be individual, rather than formed in clusters, in contrast to the morphology in the samples from the influent end of the ZVI-$0O_2$ column. Like that column, however, the aragonite crystals appear to have formed on top of the basal surface covering.

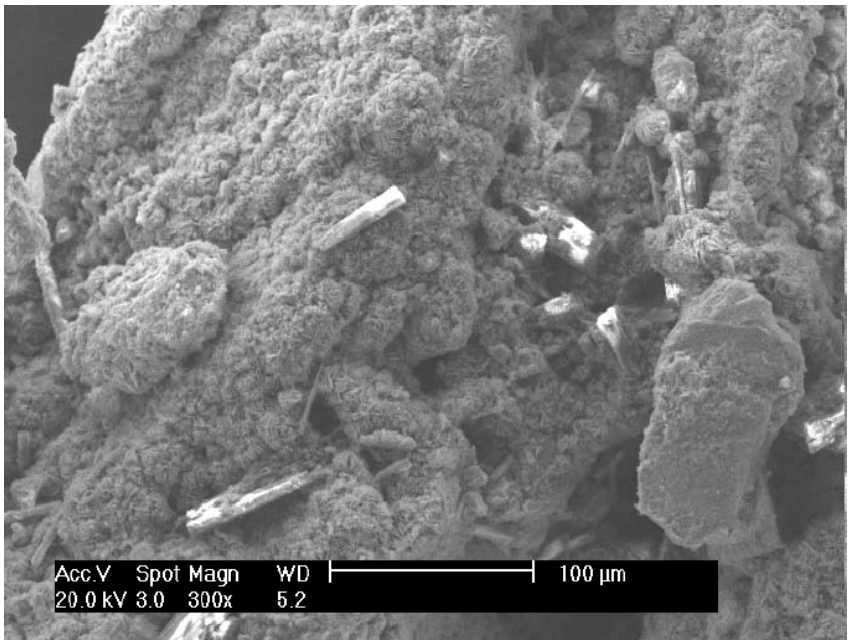

Figure 5.28: Grain of ZVI from the influent end of ZVI-$2O_2$ column, with calcium carbonate and iron (hydr)oxide surface covering.

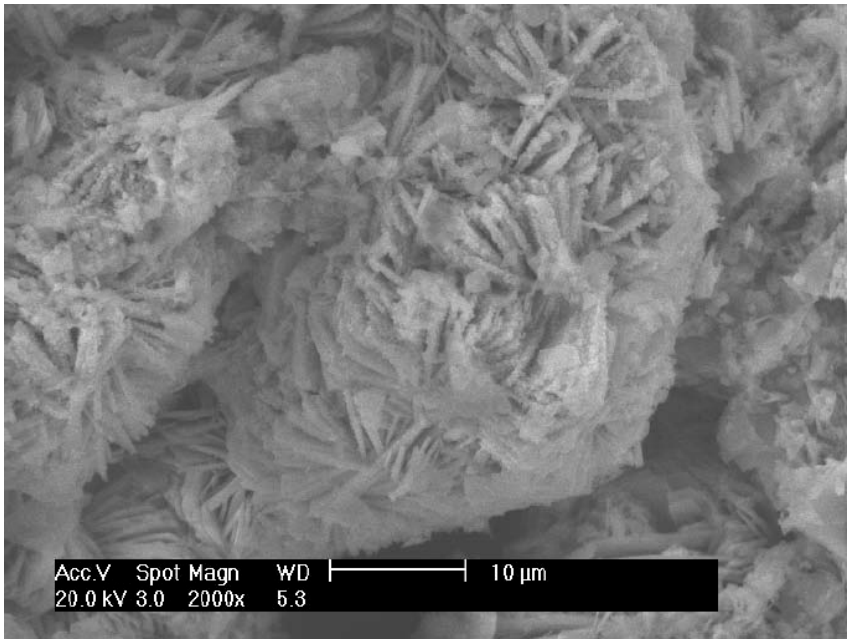

Figure 5.29: Surface covering on influent sample from ZVI-$2O_2$ column.

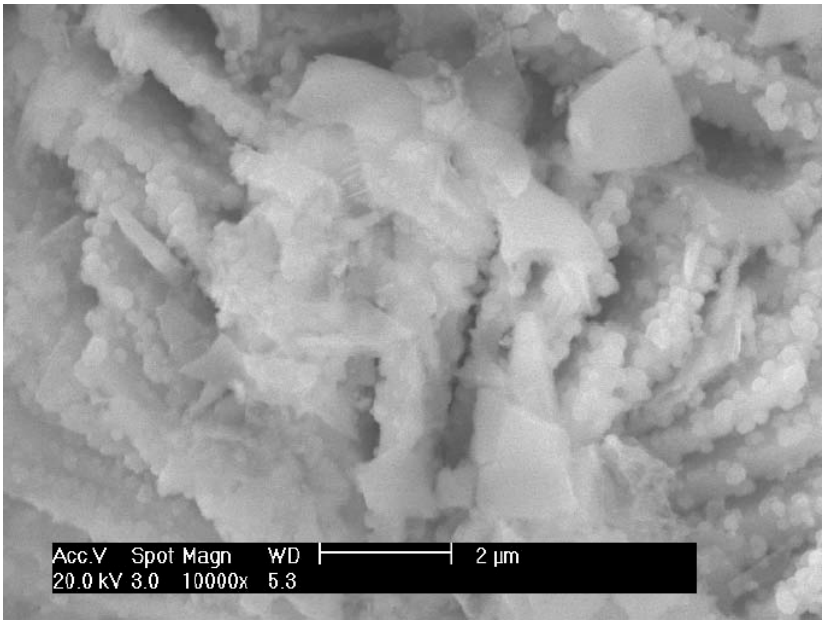

Figure 5.30: Fine structure of surface covering an influent sample from ZVI-2O_2 column.

The fine structure observed in Figure 5.30 is similar to that seen in the ZVI-0O_2 column influent section (Figure 5.9): needle-like structures covered by nodules.

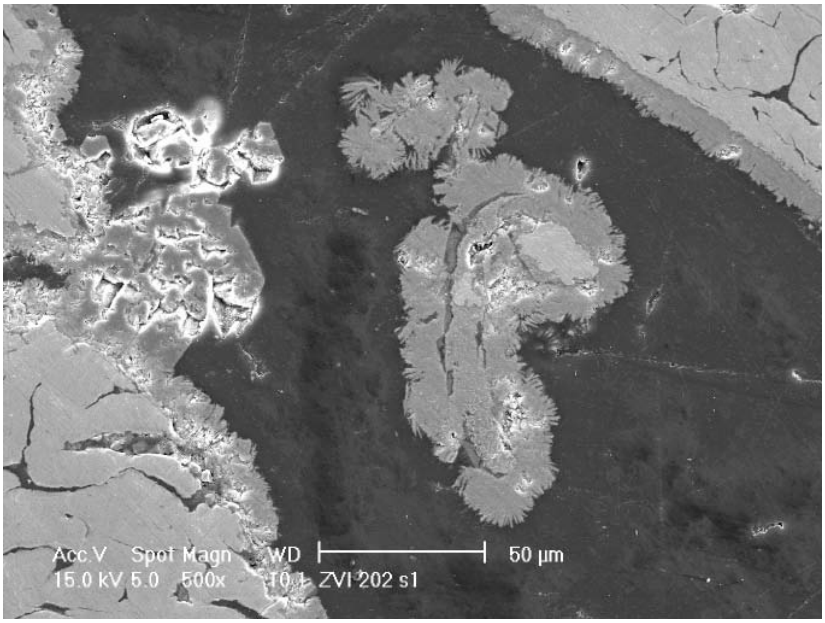

Figure 5.31: Cross-section of grains of ZVI from influent end of the ZVI-2O_2 column.

An examination of the cross-sections of samples from the influent end of the ZVI-2O_2 column, shown in Figure 5.31, reveals a consistent and dense layer of needle or plate-like precipitates on the surface of the iron. A similar pattern was seen in the influent end of

the ZVI-$0O_2$ column (Figure 5.10). The thickness of these precipitates is approximately 10-25 µm, similar to the value in the ZVI-$0O_2$ column. In addition to the carpet-like covering of precipitates, a large mass of $CaCO_3$ precipitates (the large mass with whitish edges in the upper left quadrant of the image) can be seen in Figure 5.31. Although the non-epoxied sample (e.g., Figure 5.28) suggested sparse $CaCO_3$ precipitation, this SEM image indicates that clusters of $CaCO_3$ precipitates also formed.

The effluent sample does not appear to be covered to the same degree as the influent sample was, as Figure 5.32 shows. Figure 5.33, a closer view of this surface, shows that the morphology of the surface covering in this sample is less needle-like and more platy. The fine-structure of the surface is feathery, with indications of hexagonal crystals.

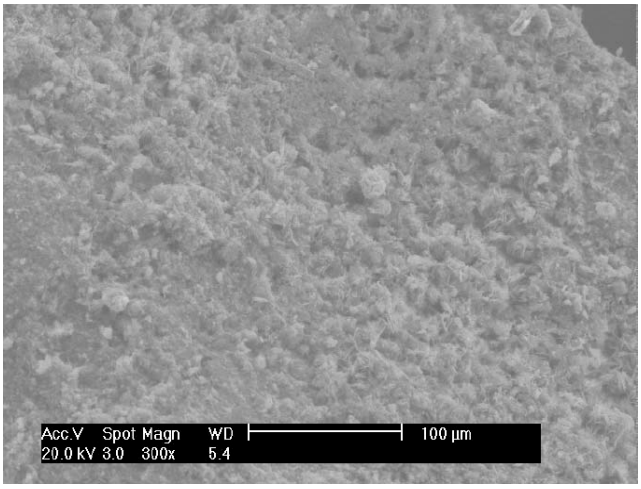

Figure 5.32: Surface of grain of ZVI from the effluent section of the ZVI-$2O_2$ column.

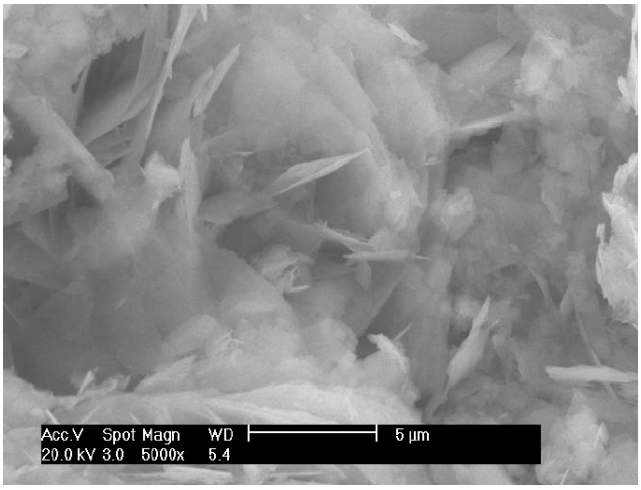

Figure 5.33: Fine structure of surface covering from the effluent section of the ZVI-$2O_2$ column.

Similar to the results in the ZVI-0O_2 column, the precipitates that have formed in the effluent section of the column are less dense than those found in the influent section. Figure 5.34 shows a grain of ZVI covered by such a precipitate layer, and Figure 5.35 shows a closer view of a typical grain of ZVI. Although less dense than the layer observed in the influent section (Figure 5.31), it is consistent and ranges from 10-25 µm, similar to the thicknesses observed in the effluent samples from the ZVI-0O_2 column (Figure 5.13).

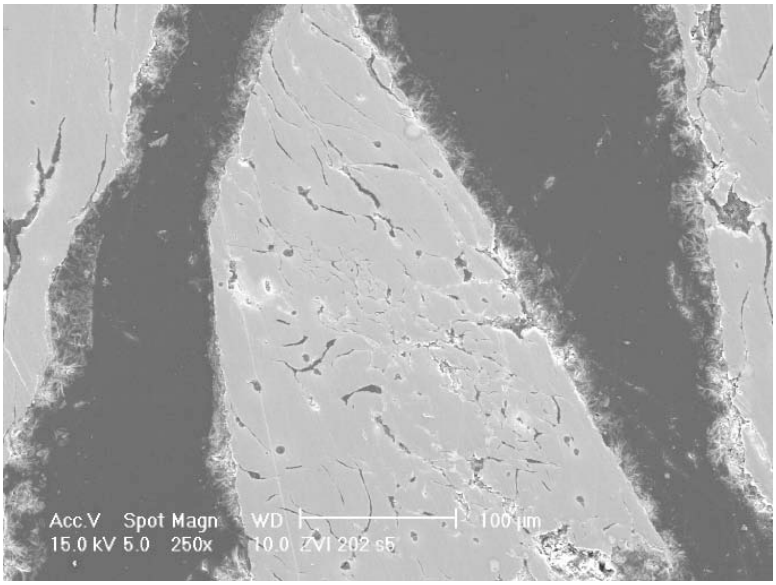

Figure 5.34: Cross-section of grains of ZVI from effluent end of the ZVI-2O_2 column; scale is 100 µm.

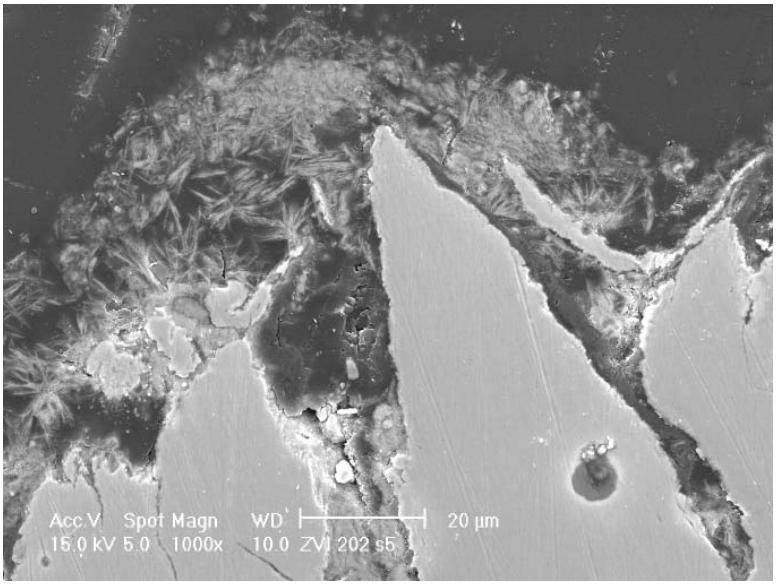

Figure 5.35: Cross-section of grains of ZVI from effluent end of the ZVI-2O_2 column; scale is 20 µm.

Investigation of the solid phase by SEM has provided evidence for the identification of aragonite, as well as for spatial variability of precipitates. This information is used to inform the modeling of this system, described below.

5.2.3 Modeling

5.2.3.1 Calculations of hydraulic conductivity loss

Assuming again that calcium carbonate precipitation accounts for all the calcium removal and a stoichiometrically equivalent carbonate removal, the total amount of solids precipitation expected based on calcium and carbonate solids may be calculated.

For this column, the measured $k_{final}/k_{initial}$ was 0.024, from which an effective water content, θ, of 0.20 was calculated. This measured reduction in permeability corresponds to a K_H fraction loss of 0.71 per 100 PV. Table 5.4 presents the results for calculations (as described in Section 4.3.7) of water and gas content based on the measured K_H loss, the Kozeny-Carman equation (Equation 2.19), and the power law relationship between effective saturation, S_e, and relative permeability to the water phase of (Equation 2.20). Table 5.5 shows results for the hydraulic conductivity loss attributable to the formation of solid and gas phases. In each cell below, the dash indicates the range of values: the first value is calculated assuming low-density solids (FeOOH and $FeCO_3$) precipitates, and the second is based on high-density solids ($Fe(OH)_3$ and CGR).

Table 5.4: Summary of calculations for unsaturated permeability and solids, water, and gas content for ZVI-2O_2 column.

Column fraction for precipitation	Final porosity (initial = 0.60)	f_{solids} (V_{solids} / V_{tot})	a (V_{gas} / V_{tot})	S_w (θ / final porosity)	$k_{final}/k_{initial}$ (from Se^3)
1	0.57 - 0.48	0.028 - 0.13	0.38 - 0.28	0.35 - 0.42	0.025 - 0.051
0.5	0.55 - 0.35	0.055 - 0.25	0.35 - 0.15	0.36 - 0.57	0.031 - 0.15
0.1	0.33 - 0.00	0.28 - 1.0	0.13 - 0.0	0.61 - 0.0	0.19 - 0.00

Table 5.5: Summary of calculations for K_H loss (per 100 PV) attributable to solids and gas formation in the ZVI-2O_2 column.

Column fraction for precipitation	Solids K_H loss (per 100 PV)	Gas K_H loss (per 100 PV)
1	0.064 - 0.26	0.57 - 0.37
0.5	0.12 - 0.48	0.51 - 0.16
0.1	0.53 - 1.00	0.11 - 0.00

These calculations show that gas production is an important consideration for hydraulic conductivity loss. For the high-density solids, the gas content is expected to be between 13 and 38% (Table 5.4), depending on the fraction of the column over which solids are assumed to form. For the low-density, high-volume solids, this gas content is smaller – and is zero if the precipitation region is only 10% of the column length – but it is still likely to be non-negligible. Table 5.5 shows a similar finding: the fractional hydraulic conductivity reduction per 100 PV due to gas formation is expected to be greater than 0.1, except for the aggressive assumption of high-volume solids and a small precipitation zone.

5.2.3.2 Geochemical modeling

The ZVI-2O_2 column was modeled as a batch, equilibrium system, both with and without gas formation. Because the SEM analysis of samples from this column provided evidence for certain phases, two sets of simulations were again conducted. The set designated "all" allows all the solids listed in Table 4.5 to precipitate, while the simulations designated "high vol." were restricted to a following solids: $Fe(OH)_2$, $Fe(OH)_3$, ZVI, aragonite, siderite, and carbonate green rust (CGR). Figure 5.36 shows the results for model calculations of pe and pH for the ZVI-2O_2 system with these two sets of solid phases. As was the case with the ZVI-0O_2 system, inclusion or exclusion of gas did not significantly affect pH, pe, or solids formation.

Because 2 mg/L O_2 is equivalent to 0.125 mM O_2, the oxidizing effects of oxygen would be prominent for levels of ZVI addition below 0.125 mM. Since the range for ZVI concentration begins at 0.1 mM, oxygen has an effect only at the lowest ZVI additions. With the exception of the fact that the pe is high at 0.1 mM ZVI, the pe and pH values

shown in Figure 5.36 are nearly identical to the model predictions for the ZVI-0O_2 system (Figure 5.17). Points where the derivatives of these curves are not smooth can likewise be explained by the precipitation of solids.

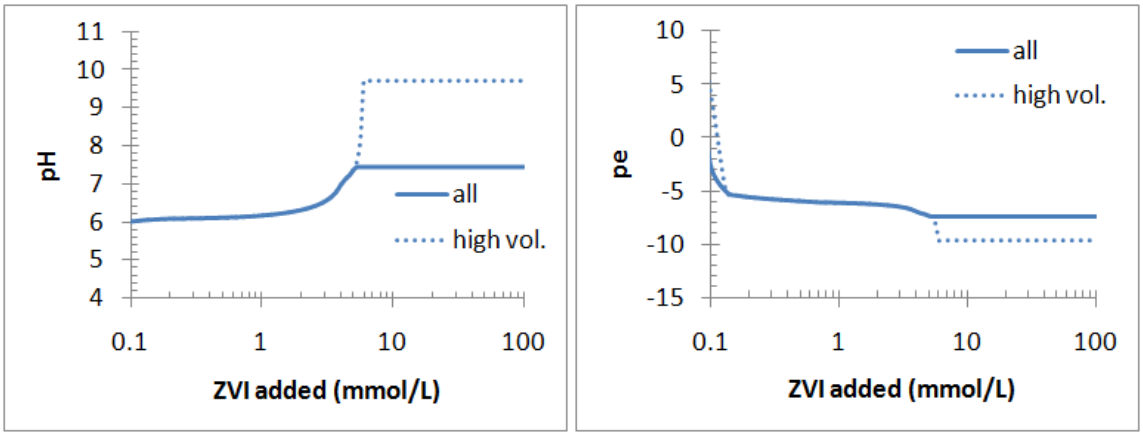

Figure 5.36: Equilibrium model of ZVI-2O_2 system predictions of pH (left) and pe (right), allowing all or high-volume solids to precipitate.

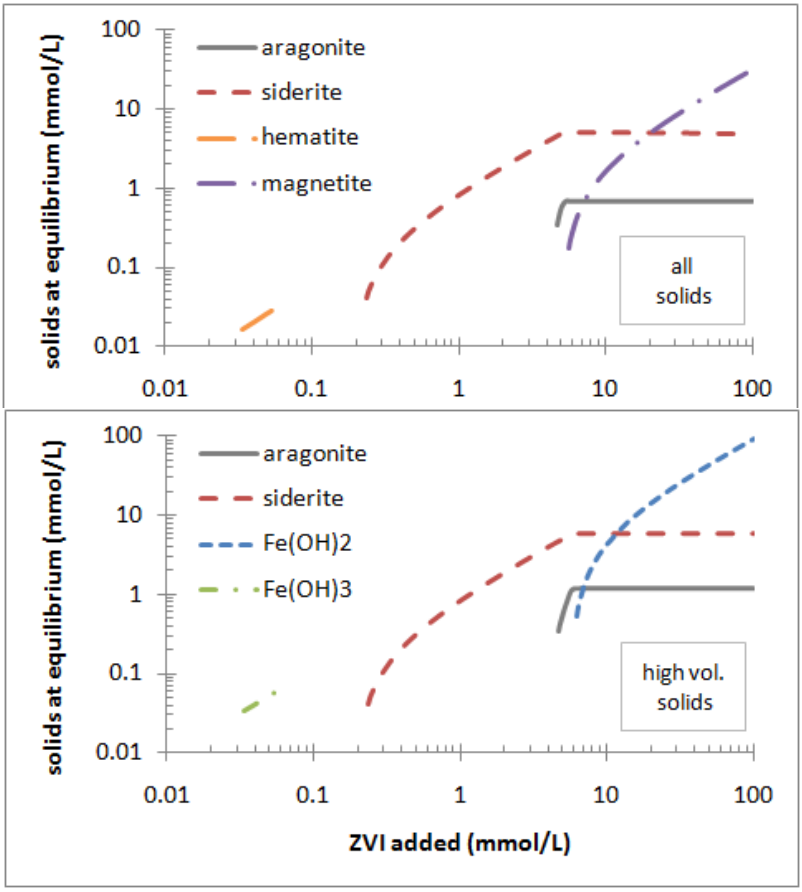

Figure 5.37: Equilibrium solids predicted in the model of the ZVI-2O_2 system, with unrestricted solids (top) and high-volume solids (bottom).

Figure 5.37 presents the model predictions for solids precipitation in both the high-volume and unrestricted systems. The model predicts that magnetite precipitates in the unrestricted set of solids, while $Fe(OH)_2$ precipitates in the high-volume set, similar to the results in the ZVI-$0O_2$ system. Again, it is these solids that drive the differences between the pH and pe curves seen in Figure 5.36. Figure 5.38 shows the calculated hydraulic conductivity loss using the Kozeny-Carman equation, based on the model predictions of solid precipitation (left) and solids and gas formation (right). The differences between magnetite and $Fe(OH)_2$ drive the difference between the "all" and "high-vol." curves in Figure 5.38.

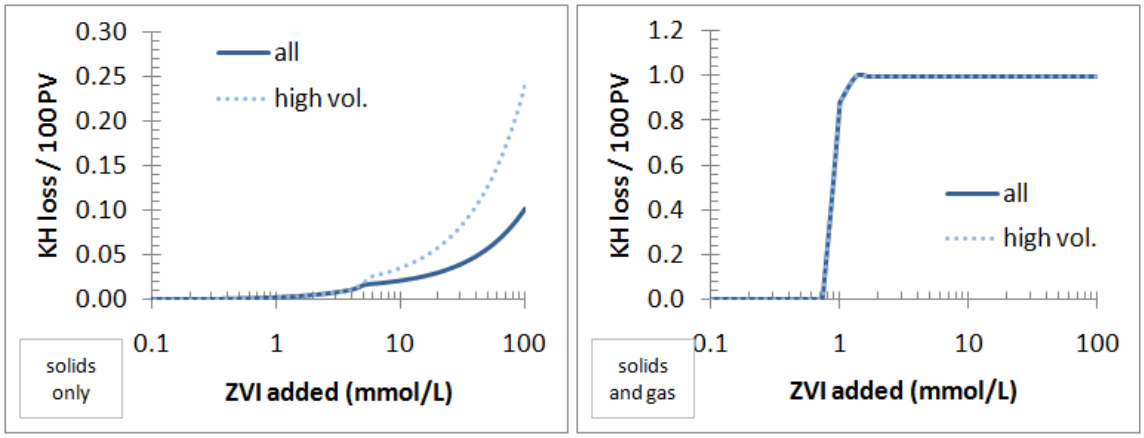

Figure 5.38: Comparison of hydraulic conductivity loss predicted in the model of the ZVI-$2O_2$ system with unrestricted (all) and high-volume (high vol.) solids precipitation allowed, with gas formation not considered (left) and allowed (right).

For simulations without gas formation (in the left panel of Figure 5.38), the maximum calculated hydraulic conductivity loss was 25% in 100 PV. In contrast, the measured hydraulic conductivity loss in the ZVI-$2O_2$ column was greater than 97% over nearly 300 pore volumes. Assuming even the largest amount of ZVI added in the model (100 mM) was representative of the conditions in the column, and assuming that $Fe(OH)_2$ was the dominant iron hydroxide solid, Figure 5.38 indicates that solids production alone could not account for the observed hydraulic conductivity loss. The calculations presented at the beginning of this section, based on mass balances on calcium and carbonate, are also unable to account for the observed loss.

For the simulations with gas formation (right panel of Figure 5.38), it is observed that additions of ZVI greater than about 1 mmol/L are sufficient to reduce hydraulic

conductivity to zero. As noted for the ZVI-0O_2 column (Section 5.1.3.2), the model simulation of gas production does not apply directly to a field or column setting. In the model, gas cannot escape and is not constrained by increasing pressure. This simulation, therefore, represents a worst-case scenario.

5.3 ZVI-O_2 column

In addition to ZVI columns containing 0 mg/L O_2 and 2 mg/L O_2, a ZVI column experiment with oxygenated DDI water was conducted. Calcium and carbonate were not used in the influent solution in order to establish a baseline level of permeability loss due only to the presence of oxygen. The oxygen level was set through equilibration with the ambient atmosphere, and this value was measured to be approximately 8 mg/L oxygen.

5.3.1 Column results

Figure 5.39 shows that the effluent pH of the column designated ZVI-O_2 was higher – reaching a pH of 9 – than the effluent pH of the columns receiving 0 and 2 mg/L of oxygen. In contrast to the columns with lesser concentrations of O_2, the effluent pH of the ZVI-O_2 showed a decrease with time, falling from about pH 9 to pH 8.

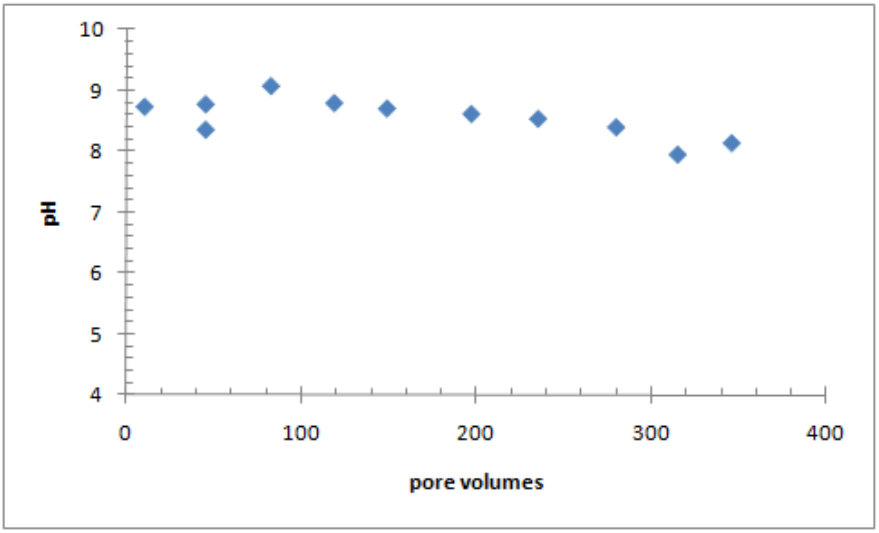

Figure 5.39: Effluent pH in the column designated ZVI-O_2 as a function of pore volumes injected into the column.

Figure 5.40 shows the pressure drop along the ZVI-O_2 column. With a high incoming level of oxygen, the high effluent pH of this column may be taken as evidence that iron was being oxidized, as shown by the production of hydroxide ions in Equation 2.6. This oxidation, in turn, produces ferric iron, which is insoluble at high pH and will combine with oxygen and hydroxide to form solids. The accumulation of these solids, as well as the potential buildup of hydrogen gas created by the anaerobic corrosion of iron, reduce the hydraulic conductivity and increase the increase in pressure drop along the column. The values of pressure drop along the column – reaching values greater than 300 cm H_2O – are much larger than those seen in the ZVI-0O_2 and ZVI-2O_2 column, which reached pressure drops of 25 to 70 cm H_2O, respectively.

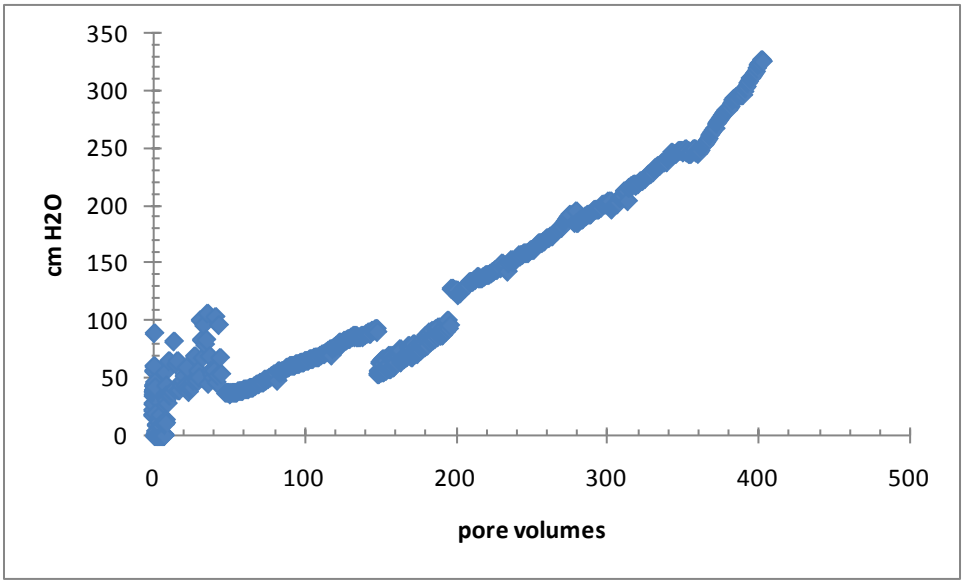

Figure 5.40: Pressure drop along the column designated ZVI-O_2 as a function of pore volumes injected into the column.

Figure 5.41 shows the values of hydraulic conductivity in the ZVI-O_2 column. Because this column had a higher flow rate (8 mL/min) than the ZVI-2O_2 and ZVI-0O_2 columns (0.7 mL/min), a given hydraulic conductivity of ZVI will correspond to a larger pressure drop in the ZVI-O_2 column (Equation 2.13). Thus, relatively high values of pressure drop along the column do not correspond to equally large changes in hydraulic conductivity.

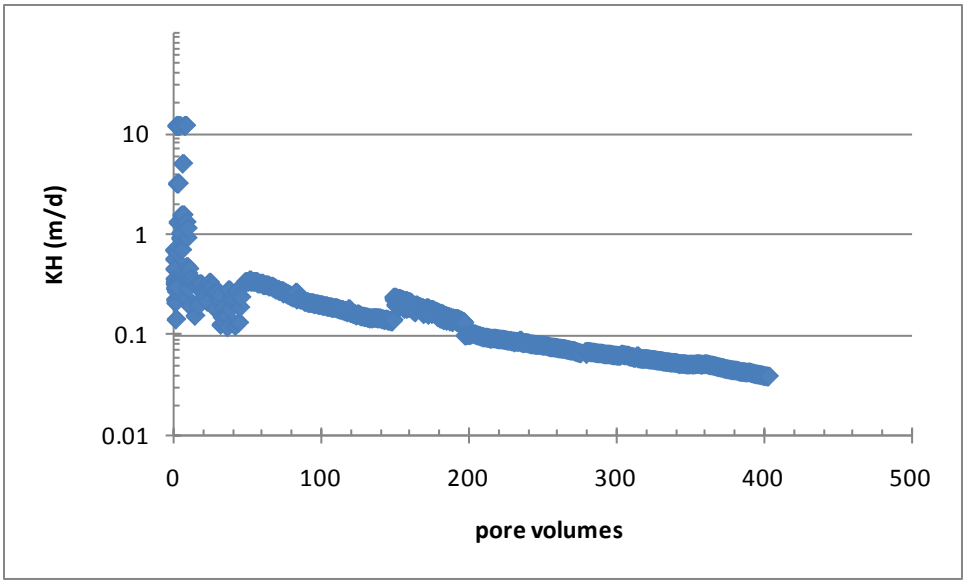

Figure 5.41: Hydraulic conductivity in the column designated ZVI-O_2 calculated from the pressure drop along the column as a function of pore volumes injected into the column.

Because the period of initial column operation showed a large degree of scatter in the measurement of pressure drop, it is difficult to pinpoint an initial hydraulic conductivity, and hence, a total hydraulic conductivity drop. Extrapolating backwards from the smooth portions of the curve (beginning around 50 pore volumes), it appears that the total hydraulic conductivity loss was between one and two orders of magnitude.

To investigate the production of precipitates, solid samples were taken from the column at the conclusion of the experiment and investigated using SEM.

5.3.2 Solids Analysis

Because no calcium or carbonate was present in the influent solution of this column, only iron (hydr)oxides were expected to form. SEM images of ZVI grains from the effluent end of this column show what appears to be a patchy coverage by precipitates (Figure 5.42). One can, however, observe precipitates in the interstitial pore space (running from the upper left to lower right of the figure).

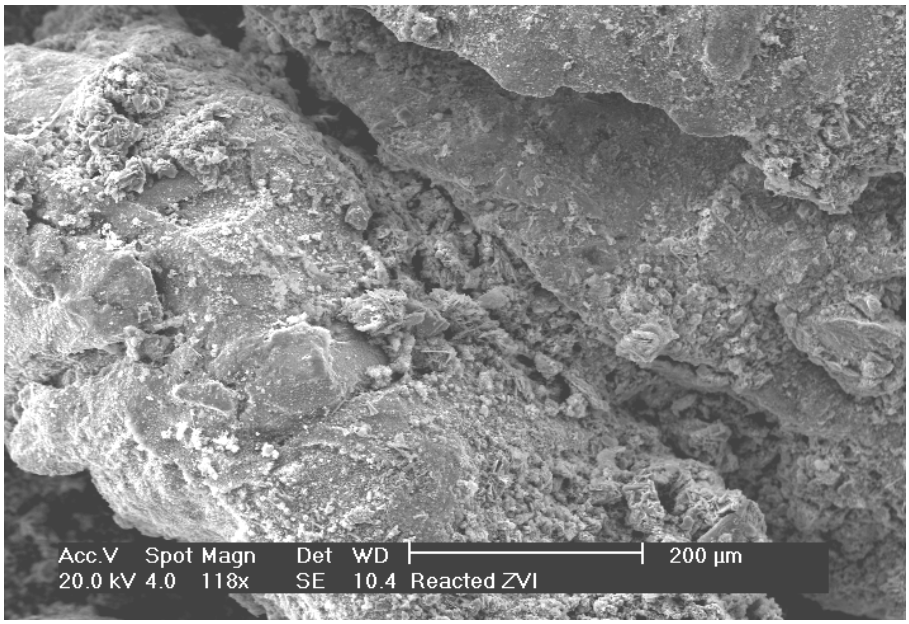

Figure 5.42: Grains of ZVI from the effluent end of the ZVI-O_2 column.

Figure 5.43 shows a closer view of this interstitial space. While there is substantial precipitation in the center of this figure, the lower left region, for example, appears to have fewer precipitates, somewhat like as-received ZVI (Figure 4.1)

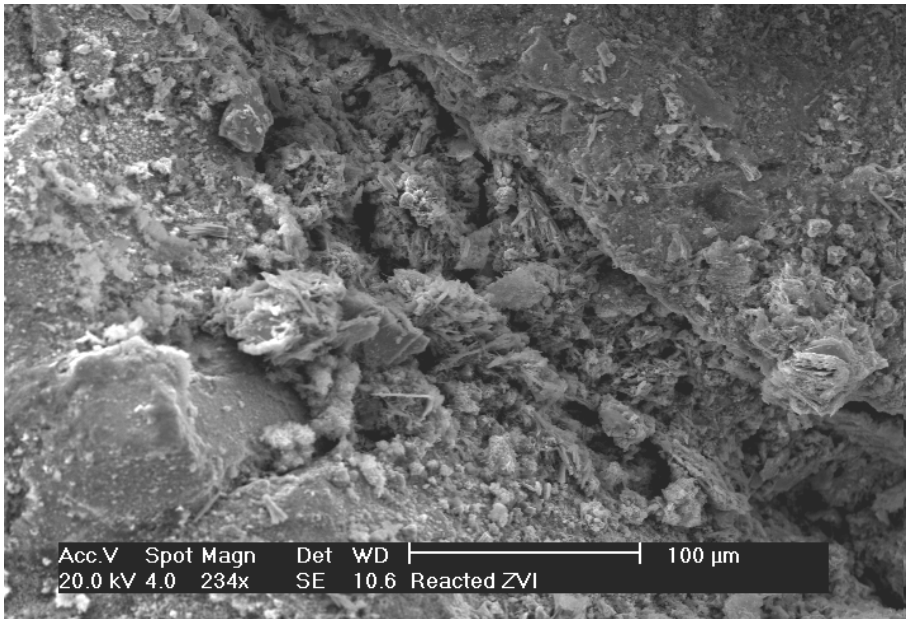

Figure 5.43: Surface coating on grains from the effluent end of the ZVI-O_2 column.

A view of the morphology of some of these precipitates is shown in Figure 5.44. In large part, they are composed of needle-like crystals.

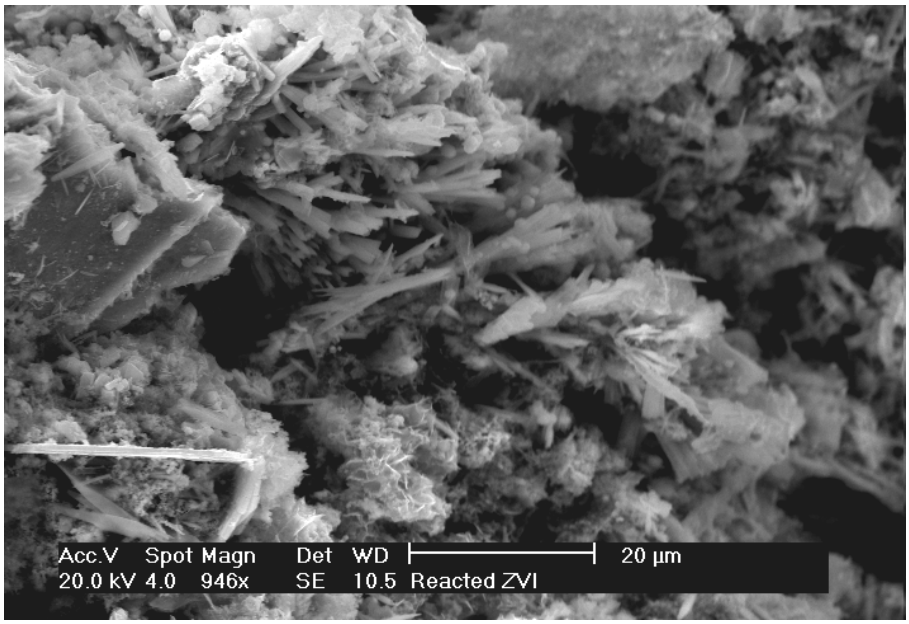

Figure 5.44: Morphology of the surface coating on a grain from the effluent end of the ZVI-O_2 column.

Figure 5.45 is a cross-sectional view of the solids from the effluent end of the ZVI-O_2 column; it shows regions of extensive and minimal precipitation. The dark region on the left side of Figure 5.45 is a large interstitial pore space, which is now filled with epoxy. In this area, precipitates on ZVI (the lighter gray regions) are minimal. However, in the spaces between the ZVI grains, there is complete filling by precipitates.

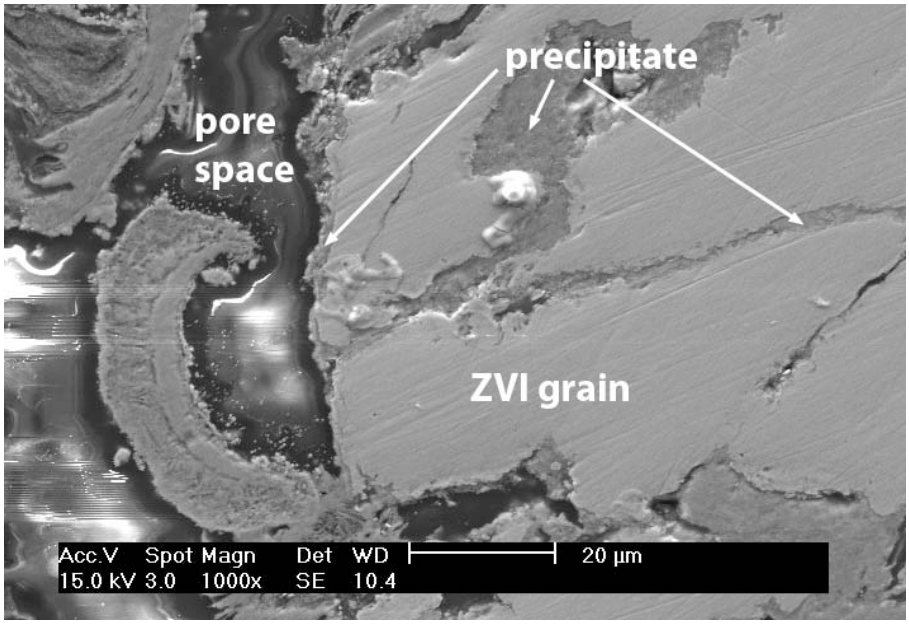

Figure 5.45: Cross-section of grains from the effluent section of the ZVI-O_2 column.

Because of the sectioning process, it is not possible to determine the morphology of the precipitates that fill the smaller interstitial spaces in Figure 5.45. In sum, the SEM images of samples from the ZVI-O_2 column provide evidence for the formation of iron solids, the effects of which are calculated below.

5.3.3 Modeling

5.3.3.1 Calculations of hydraulic conductivity

The ZVI-O_2 column did not receive calcium or carbonate in the influent solution. However, the potential for solids formation may still be estimated from two mechanisms that may oxidize ZVI: anaerobic corrosion (Equation 2.5) and oxidation by oxygen (Equation 2.6). Reardon (1995) estimated an anaerobic dissolution rate of ZVI by water of 0.7 mmol/kg-d.

For this column, the measured $k_{final}/k_{initial}$ was 0.003, from which an effective water content, θ, of 0.10 was calculated. This measured reduction in permeability corresponds to a K_H fraction loss per 100 PV of 0.76. As described in Section 4.3.7, lower and upper bounds for total porosity losses and gas production may be calculated. Table 5.6 presents the results for calculations of water and gas content based on the measured K_H loss, the Kozeny-Carman equation (Equation 2.19), and the power law relationship of Wyllie (1962) (Equation 2.20). Table 5.7 shows results for the hydraulic conductivity loss attributable to the formation of solid and gas phases. In each cell below, the dash indicates the range of values: the first value is calculated assuming a low-density solid (FeOOH) precipitates, and the second is based on the formation of a high-density solid ($Fe(OH)_3$).

Table 5.6: Summary of calculations for unsaturated permeability and solids, water, and gas content for ZVI-O_2 column.

Column fraction for precipitation	Final porosity (initial = 0.61)	f_{solids} (V_{solids} / V_{tot})	a (V_{gas} / V_{tot})	S_w (θ / final porosity)	$k_{final}/k_{initial}$ (from Se^3)
1	0.598 - 0.598	0.0005 - 0.0008	0.50 - 0.50	0.17 - 0.17	0.0012 - 0.0012
0.5	0.598 - 0.597	0.0010 - 0.0016	0.50 - 0.49	0.17 - 0.17	0.0012 - 0.0012
0.1	0.594 - 0.591	0.0050 - 0.0078	0.49 - 0.49	0.17 - 0.17	0.0012 - 0.0013

Table 5.7: Summary of calculations for K_H loss (per 100 PV) attributable to solids and gas formation in the ZVI-O_2 column.

Column fraction for precipitation	Solids K_H loss (per 100 PV)	Gas K_H loss (per 100 PV)
1	0.0009 - 0.0013	0.758 - 0.757
0.5	0.0017 - 0.0026	0.757 - 0.756
0.1	0.0086 - 0.0131	0.750 - 0.745

Based on the anaerobic corrosion rate of ZVI of 0.7 mmol/kg-d (Reardon 1995), the total amount of iron dissolved during the course of this experiment is expected to be 24 mmol of iron. Oxidation due to the 8 mg/L of dissolved oxygen introduced to the column is expected to be 42 mmol of iron. If it is assumed – conservatively – that no iron left the column in the aqueous phase, then there are 66 mmol of iron available to form solids. If this iron all forms high-volume $Fe(OH)_3$, then there is the potential to form 1.1 cm^3 of solids, with a corresponding loss of hydraulic conductivity of 1.4%. Clearly, solids formation alone cannot account for the observed hydraulic conductivity loss.

The calculations for gas content, a, in Table 5.6 range from 0.49 to 0.50. Since the total final porosity is 0.59-0.60, this represents a large portion of the pore space occupied by gases. This is also evident in the Table 5.7, since the K_H losses attributable to gases are much larger, regardless of the length of the zone of precipitation and solids type, than the losses attributable to solids.

5.3.3.2 Geochemical modeling

For geochemical modeling of the ZVI-O_2 system, the same sets of solids that were used for the ZVI-$0O_2$ and ZVI-$2O_2$ columns were used in this system, with the exception of carbonate solids, because neither carbonate nor calcium was present in the influent solution.

Figure 5.46 shows model predictions for pH and pe using these two different sets of solids. Gas is allowed to form in this model, but, as before, the effect of the formation of the gas phase on the pH, pe, and solid formation is negligible. In these simulations, with the lack of buffering from the carbonate species, pH rises more quickly than it did in the ZVI systems with carbonate. The dissolved oxygen level in these systems is 8 mg/L, which corresponds to 0.5 mM O_2. The predicted pe indicates that at additions of ZVI less than 0.5 mM, oxygen is present and thus keeps the pe high.

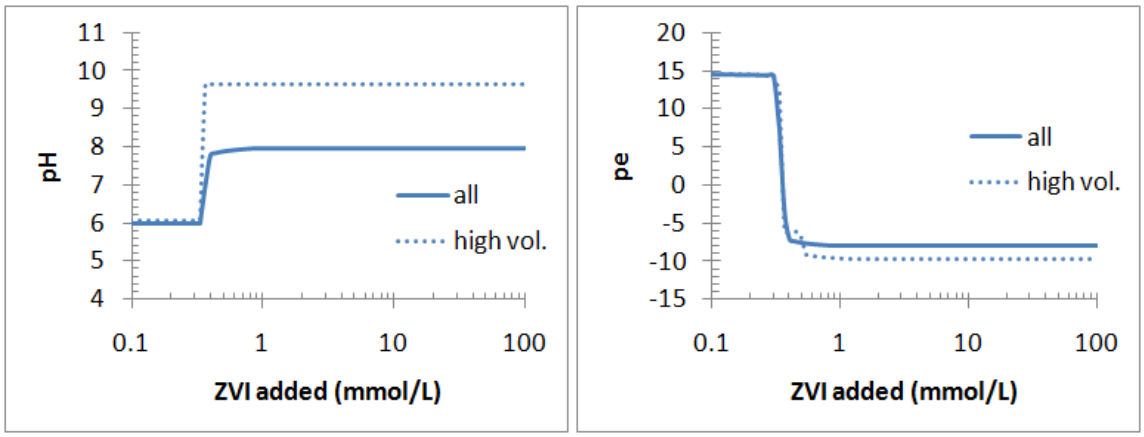

Figure 5.46: Equilibrium model of ZVI-O_2 system predictions, with gas phase allowed, of pH (left) and pe (right), allowing all solids or high volume (high-vol.) to precipitate.

Figure 5.47 shows the model predictions for solids precipitation in the ZVI-O_2 system. With no carbonate present, the only solids that are formed are iron (hydr)oxides; thus the mass of solids formed tracks monotonically with the addition of ZVI. In the top panel of Figure 5.47, hematite, an iron (III) solid, is expected to form while oxygen is present and pe is high. Once all the oxygen is reduced, the system switches to a negative pe and magnetite is predicted to be the only solid formed. The bottom panel of Figure 5.47 shows the model predictions when solids are restricted to the high-volume set. In this

case, the iron (III) solid that forms is $Fe(OH)_3$; when the oxygen is consumed by ZVI, the lower valency solid is $Fe(OH)_2$. In both cases though, the ZVI dissolves and transforms directly into either an Fe(II) or Fe(III) solid.

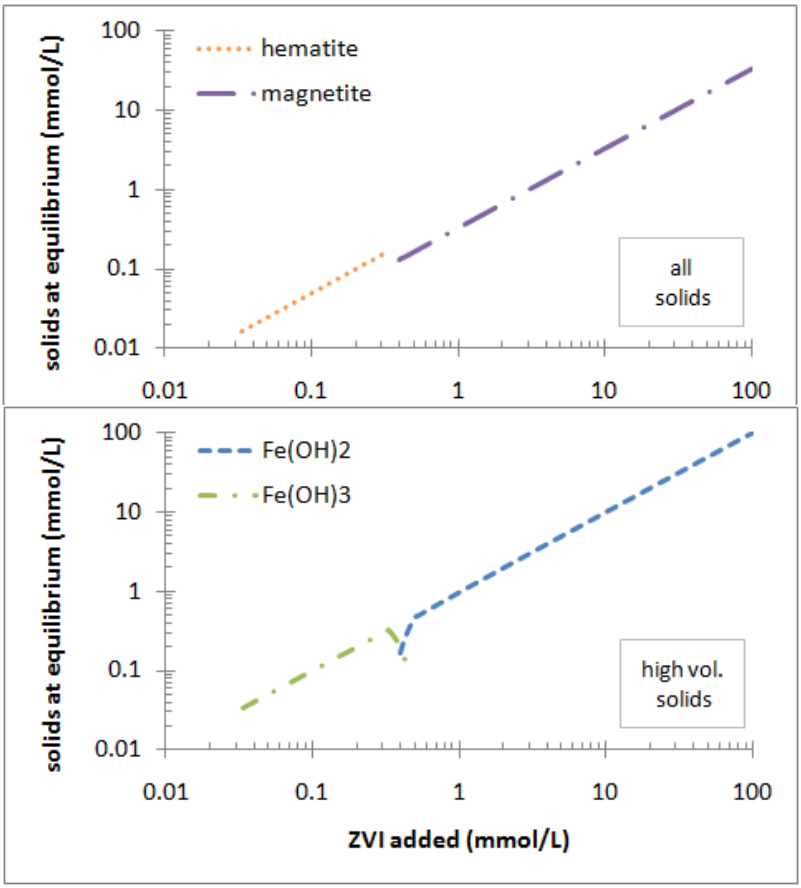

Figure 5.47: Equilibrium solids predicted in the model of the ZVI-O_2 system, with unrestricted (top) and high-volume solids (bottom).

The effect of these Fe(II) and Fe(III) solids on the hydraulic conductivity of the porous matrix depends on the stoichiometric amount of iron in the solid and the density of the solid. The volume occupied by hematite or magnetite, which each contain multiple iron atoms per formula unit and are dense, is less than that occupied by $Fe(OH)_2$ or $Fe(OH)_3$, which each contain one iron atom per formula and are relatively less dense. Earlier in this section, the permeability loss in this column, based on the oxidation of ZVI by 8 mg/L of O_2 and the anaerobic corrosion of ZVI by water was calculated to be 1.4% over the course of over 400 pore volumes. There is a large discrepancy in this calculated value and the model predictions – which climb to over 20% / 100 PV with $Fe(OH)_2$

precipitating at high levels of ZVI added. This difference is due to the fact that the model assumes equilibrium; therefore, all of the ZVI dissolves and reforms as another solid. As only a fraction of the total ZVI in the column did dissolve, the laboratory column did not reach equilibrium. Even if the amount of ZVI available in the column is overestimated, it is worth noting that the largest model estimates cannot account for the hydraulic conductivity loss of 99% that was observed in the column.

However, the effect of solid phase precipitates is small relative to the effect of the production of gases. Figure 5.48 shows the calculated hydraulic conductivity loss in the ZVI-O_2 model for simulations with (right) and without (left) gases.

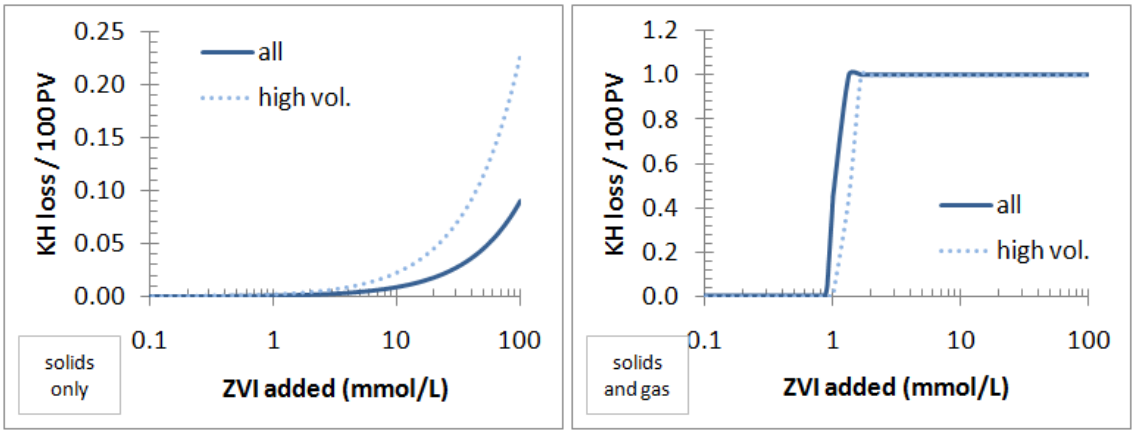

Figure 5.48: Comparison of hydraulic conductivity loss predicted in the model of the ZVI-O_2 system with unrestricted (all) and high-volume (high vol.) solids precipitation for systems with no gas formation (left) and gas formation (right) allowed.

As before, the model predicts significant production of hydrogen gas. This gas, in turn, is retained in the batch system and has deleterious effects on the calculated permeability. The right panel of Figure 5.48 shows the effects of the gas production on permeability. This gas-driven permeability loss is an upper-bound estimate; the actual value of permeability loss lies in between the systems with and without the formation of a gas phase.

5.4 ZVI-NO_3 column

The column designated ZVI-NO_3 received an influent composition similar to that of the ZVI-$0O_2$ column, but with the addition of 100 mg/L of nitrate. This level of nitrate was found, in combination with pH, to be a perfect predictor for "at-risk" PRBs, as discussed in Chapter 3. Furthermore, it is close to the value of nitrate reported for the Monticello, UT PRB (Morrison et al. 2002). Because of its high concentration of nitrate, the influent solution used in this experiment has the largest potential for oxidation, with respect to total equivalents per volume of solution, of any of the influent solutions used with the ZVI columns.

5.4.1 Column results

Figure 5.49 shows the effluent E_H as a function of pore volumes injected. Even in the presence of 100 mg/L nitrate, the redox conditions in this column were still reducing.

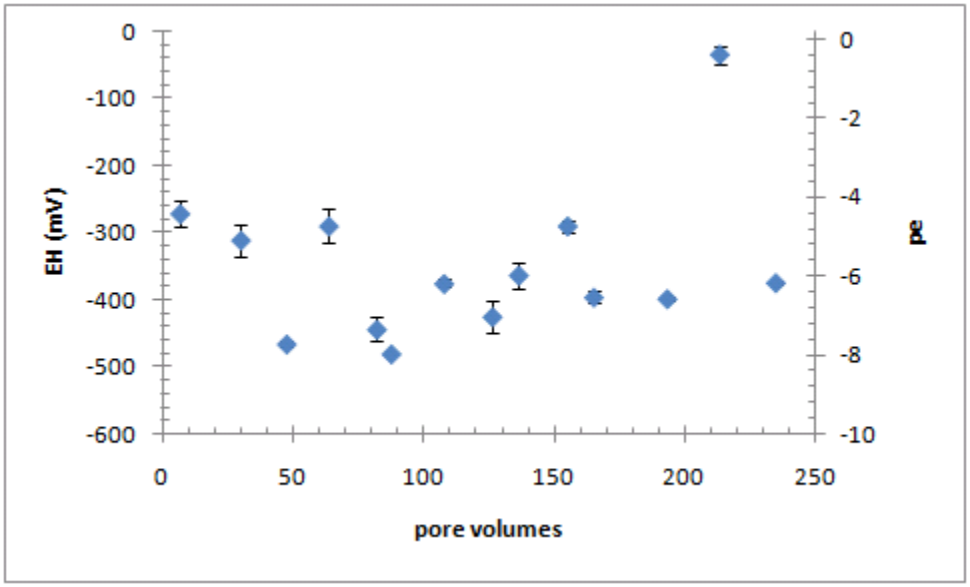

Figure 5.49: Effluent E_H in the column designated ZVI-NO_3 as a function of pore volumes injected into the column.

Figure 5.50 shows that the initial effluent pH of this column was approximately 9. With an influent pH value of 6, this column produced the largest pH change of the four ZVI columns, with the change decreasing somewhat over time.

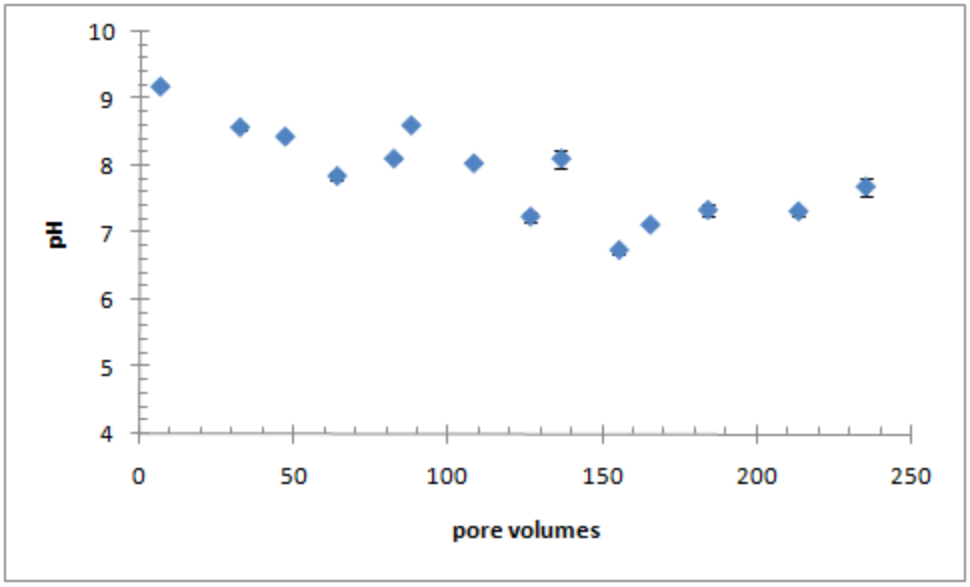

Figure 5.50: Effluent pH in the column designated ZVI-NO_3 as a function of pore volumes injected into the column.

At these high pH values, the precipitation of solids is expected. Indeed, the removal of calcium in this column was more significant than in the other ZVI columns. Figure 5.51 shows that the effluent calcium concentrations were consistently between 160 and 180 mg/L, indicating that approximately 40% of the influent calcium was being retained in the column. Total effluent iron concentrations, on the other hand, showed the same increase with time that was observed in the other ZVI columns. Carbonate removal in the ZVI-NO_3 column (Figure 5.51) was about 95% and was consistent with the results from the previous ZVI columns.

Gas production was also observed in this column. The analysis of gas collected from the column effluent revealed the presence of both nitrogen and hydrogen gases. Measurements taken at 60 pore volumes showed 61% N_2 (± 28%) and 23% H_2 (± 3%). At 130 pore volumes, the gas composition was 49% N_2 (± 9%) and 48% H_2 (± 11%). Finally, at 140 pore volumes, 57% N_2 (error not available) and 53% H_2 (± 27%) were measured.

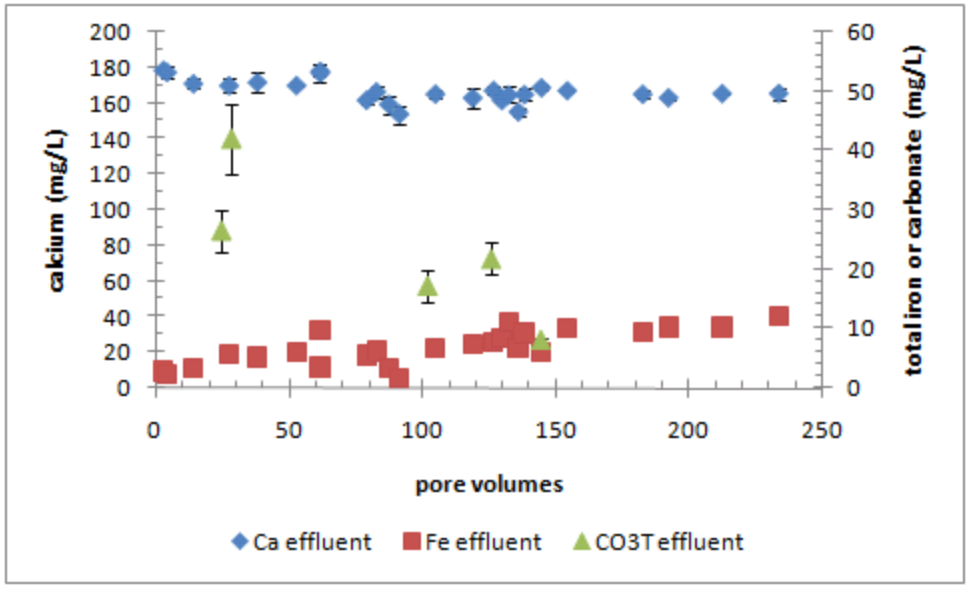

Figure 5.51: Aqueous calcium, total iron, and total carbonate concentrations in the effluent of the column designated ZVI-NO_3 as a function of pore volumes injected into the column.

Measurements of NO_3^- concentration in the effluent of the column were consistently below the detection limit of 1 mg/L. Measurements of aqueous NH_3 concentrations taken at 38, 77, and 123 pore volumes showed effluent NH_3 concentrations of 34 mg/L NH_3 (± 1.8), 28 mg/L (± 6.0), and 57 mg/L (± 6.5) respectively. While NO_2^- was not detected in the column effluent, the presence of N_2(g), and these aqueous measurements indicate that NO_3^- was being reduced by the ZVI, according to the half-reactions presented in Table 2.3.

The combined effects of solids precipitation and gas accumulation in the pore space are indicated in Figure 5.52, which shows two regions of increasing pressure drop along the column over time. Up to 200 pore volumes, the pressure drop increases slowly. After 200 pore volumes, the pressure drop along the column rises rapidly. Unfortunately, the column experiment could not be continued to determine whether the pressure measurements would continue to increase, for the effluent flange of this column cracked, possibly due to the increase in pressure.

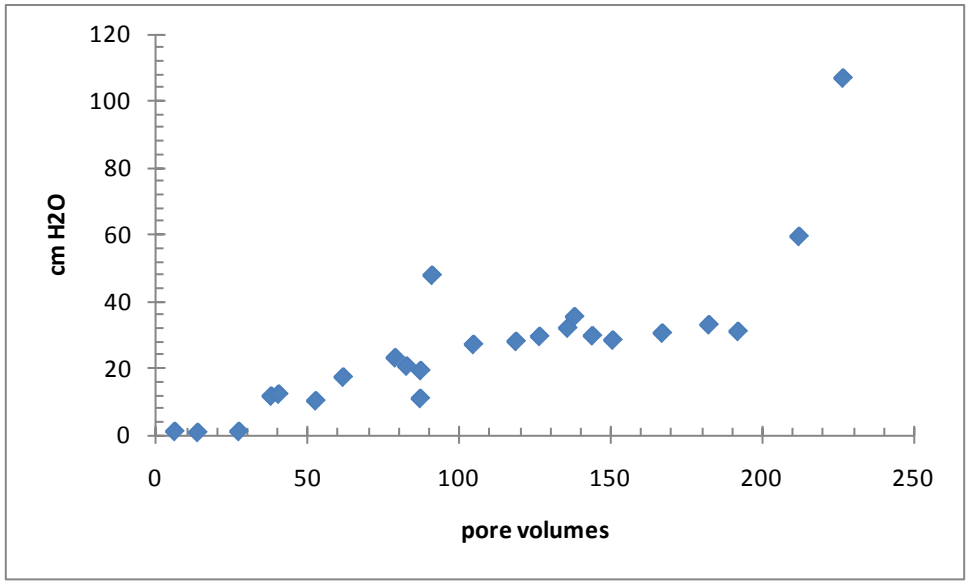

Figure 5.52: Pressure drop along the column designated ZVI-NO_3 as a function of pore volumes injected into the column.

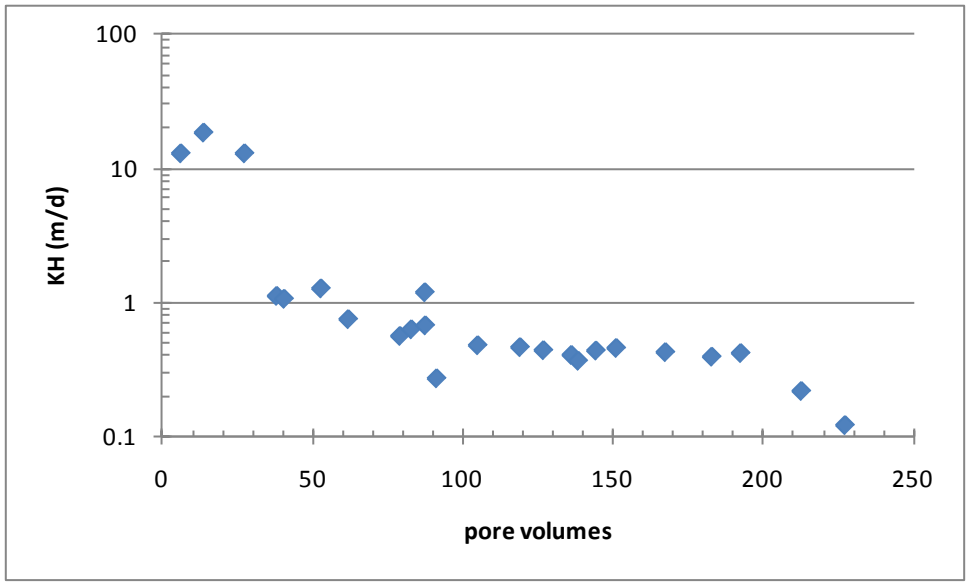

Figure 5.53: Hydraulic conductivity in the column designated ZVI-NO_3 calculated from pressure drop as a function of pore volumes injected into the column.

The hydraulic conductivity loss in the ZVI-NO_3 column (Figure 5.53) is much larger than the 46% decrease predicted by the accumulation of solids. Therefore, it is assumed that gas production accounts for a large portion of the hydraulic conductivity loss. Nonetheless, based on the degree of calcium removal in the column, it was expected that calcium carbonate and other solids would be present on the surfaces of the ZVI grains. Therefore, samples of the columns, dissected at the end of the experiment, were investigated with SEM.

5.4.2 Solids Analysis

Figure 5.54 shows a grain of ZVI from the influent section of the ZVI-NO_3 column. Patches of elongated aragonite crystals are observed on the surface, similar to those in the ZVI-$0O_2$ column (Figure 5.6). As before, the surface upon which the calcium carbonate crystals are found is a layer of platy precipitates, which is similar to the goethite shown in Figure 2.5. These precipitates have entirely covered the ZVI surface, as Figures 5.55 and 5.56 show.

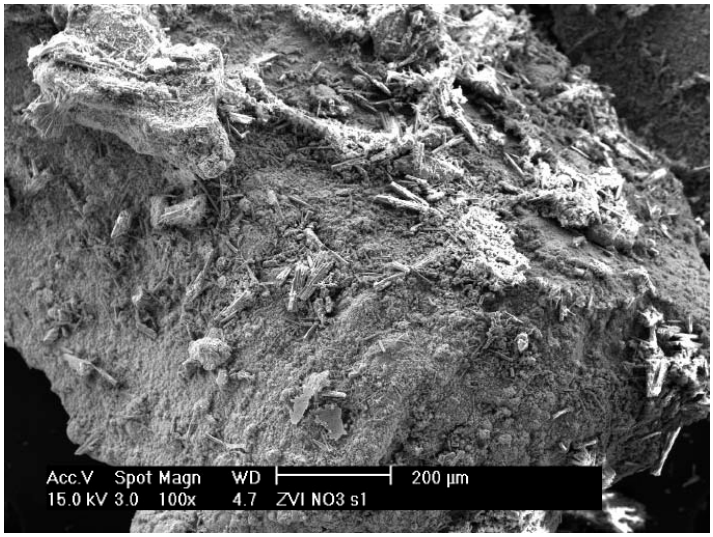

Figure 5.54: Surface of a grain of ZVI from the ZVI-NO_3 column influent section showing patchy covering of calcium carbonate precipitates.

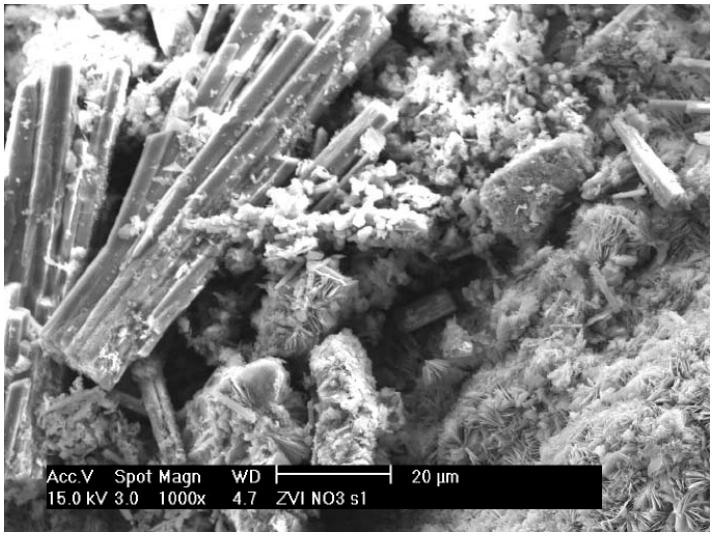

Figure 5.55: Surface of a grain of ZVI from the ZVI-NO_3 column influent section showing aragonite crystals (upper left) and iron hydroxide covering.

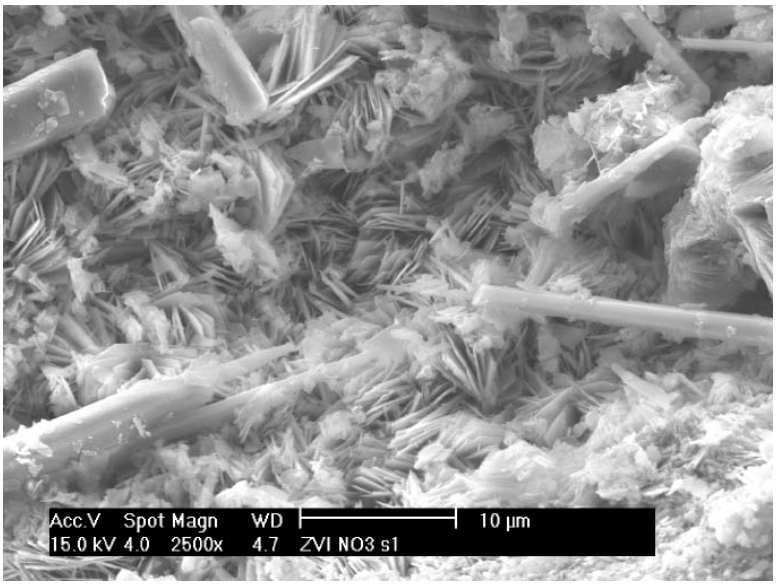

Figure 5.56: Platy precipitates from the ZVI-NO_3 column influent section.

Cross-section SEM images of samples from the influent end of the ZVI-NO_3 column show a very thick and consistent covering of ZVI grains (Figure 5.57).

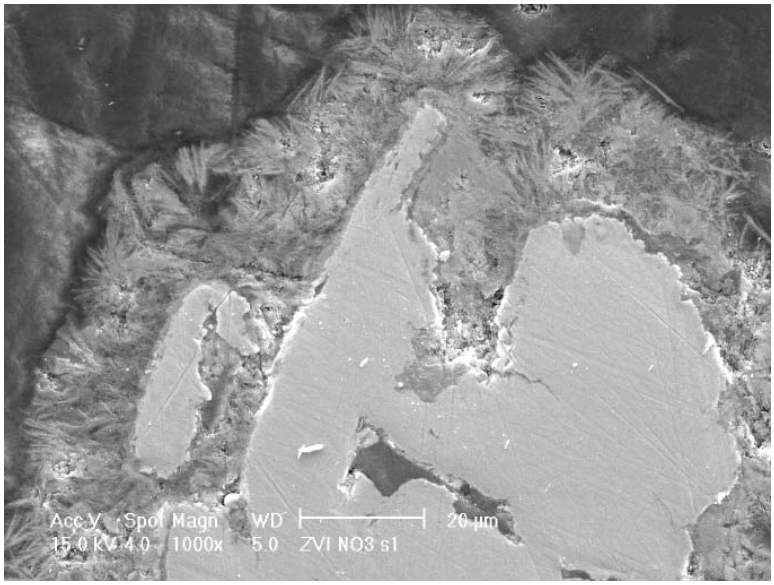

Figure 5.57: Cross-section of grains of ZVI from influent end of the ZVI-NO_3 column.

Again, the precipitates observed on the ZVI surface, since they are viewed in two dimensions, could be either needle or plate-like, which is consistent with the morphology of precipitates observed in the samples that were not cross-sectioned.

In the effluent end of the column, SEM analysis indicates less calcium carbonate, and a different covering of the surface. A grain of ZVI from the effluent end of the column is shown in Figure 5.58; only one cluster of aragonite crystals is visible.

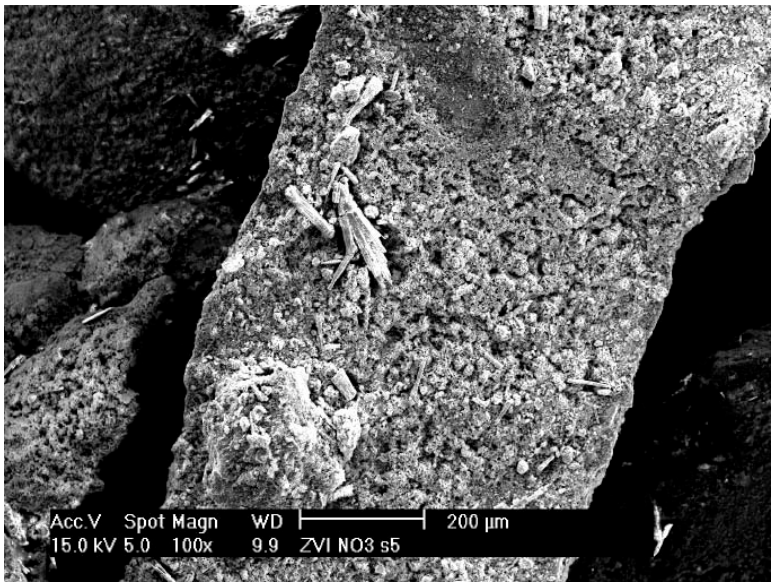

Figure 5.58: Surface precipitates with single cluster of aragonite on grain of ZVI from effluent section of the ZVI-NO_3 column.

A closer look at the precipitates that cover the grain shows a different morphology than was present on grains at the influent end of the column. These precipitates are now clearly platy, and more disordered, as Figure 5.59 shows.

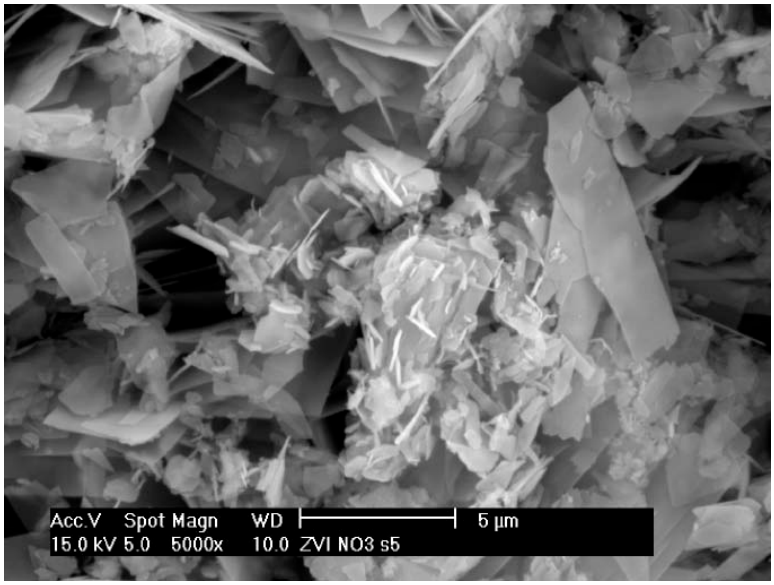

Figure 5.59: Close-up of platy precipitates from the effluent section of the ZVI-NO_3 column.

A cross-sectional analysis of these ZVI grains shows regions of uniform (the top portion of Figure 5.60) and patchy coverage (the bottom portion). A detail of the patchy coverage is shown in Figure 5.61. As before, the precipitates that are directly covering the ZVI surface may have needle or plate-like morphology.

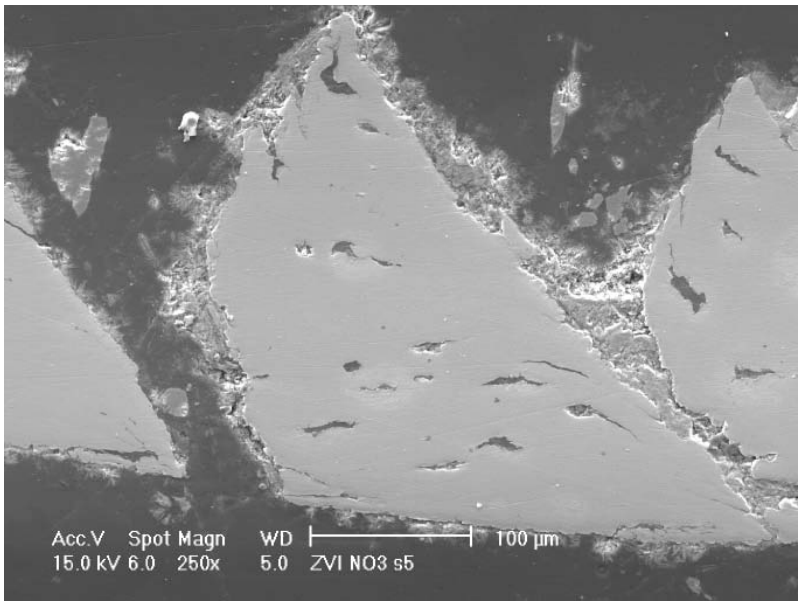

Figure 5.60: Cross-section of grains of ZVI from the effluent end of the ZVI-NO_3 column.

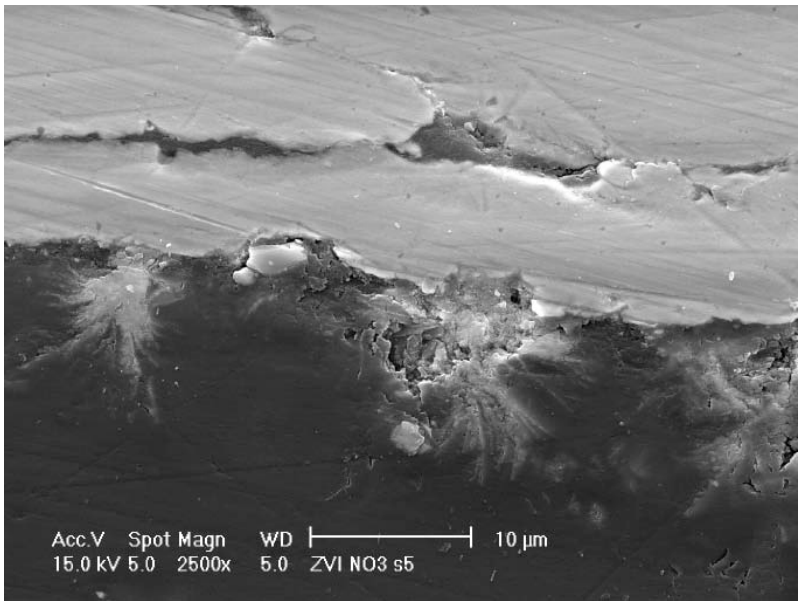

Figure 5.61: Cross-section of grains of ZVI from the effluent end of the ZVI-NO_3 column showing patchy precipitate coverage.

SEM micrographs from the influent and effluents ends of the ZVI-NO_3 column therefore show a spatial gradient: more calcium carbonate is observed in the influent section than the effluent section (Figure 5.54 vs. 5.58), and the thickness of the precipitate layer appears greater in the influent than in the effluent sections (Figure 5.57 vs. 5.60). However, it is clear that precipitates are forming throughout the column. The following section calculates the potential for permeability loss due to these solids.

5.4.3 Modeling

5.4.3.1 Calculations of hydraulic conductivity loss

For this column, the measured $k_{final}/k_{initial}$ was 0.007, from which an effective water content, θ, of 0.14 was calculated. This measured reduction in permeability corresponds to a K_H fraction loss of 0.89 per 100 PV. As described in Section 4.3.7, lower and upper bounds for total porosity losses and gas production may be calculated. Table 5.8 presents the results for calculations of water and gas content based on the measured K_H loss, the Kozeny-Carman equation (Equation 2.19), and the power law relationship of Wyllie (1962) (Equation 2.20). Table 5.9 shows results for the hydraulic conductivity loss attributable to the formation of solid and gas phases. In each cell below, the dash indicates the range of values: the first value is calculated assuming low-density solids (FeOOH and $FeCO_3$) precipitates, and the second is based on high-density solids ($Fe(OH)_3$ and CGR).

Table 5.8: Summary of calculations for unsaturated permeability and solids, water, and gas content for the ZVI-NO_3 column.

Column fraction for precipitation	Final porosity (initial = 0.60)	f_{solids} (V_{solids} / V_{tot})	a (V_{gas} / V_{tot})	S_w (θ / final porosity)	$k_{final}/k_{initial}$ (from Se^3)
1	0.58 - 0.49	0.026 - 0.117	0.30 - 0.21	0.47 - 0.56	0.080 - 0.145
0.5	0.55 - 0.37	0.053 - 0.234	0.28 - 0.10	0.49 - 0.74	0.094 - 0.369
0.1	0.34 - 0.00	0.263 - 1.000	0.07 - 0.00	0.80 - 0.00	0.486 - 0.000

Table 5.9: Summary of calculations for K_H loss (per 100 PV) attributable to solids and gas formation in the ZVI-0O_2 column.

Column fraction for precipitation	Solids K_H loss (per 100 PV)	Gas K_H loss (per 100 PV)
1	0.075 - 0.23	0.82 - 0.66
0.5	0.15 - 0.42	0.75 - 0.47
0.1	0.58 - 1.00	0.31 - 0.00

These tables indicate that permeability reduction due to gases must be invoked in order to match the observed hydraulic conductivity loss, with the exception of the situation of high-volume solids precipitating in the first 10% of the column. Thus, the gas content, a, is expected to be appreciable, with a maximum value of 0.30 in the case of low-volume solids precipitating throughout the column. The corresponding K_H loss attributable to gas is large as well (Table 5.9), with an upper bound of a fractional K_H loss of 0.82 / 100 PV.

5.4.3.2 Geochemical modeling

Based on the findings from the SEM analysis of samples from the column, the model of the ZVI-NO_3 system again consisted of two simulations, one in which all solids were allowed to precipitate, and one in which the permissible solid phases were restricted to a high-volume set (Section 4.3.7.2). Figure 5.62 shows the equilibrium model predictions for the pH and pe in the ZVI-NO_3 system for simulations with high-volume and unrestricted solids. The simulations for the system with gas formation allowed, and the simulations in which gases were not considered had similar predictions of pH, pe, and solids formation.

Two factors are at play in Figure 5.62. First, because carbonate is present at 7mM, pH increases for ZVI additions below this level are muted by the buffer capacity. Secondly, nitrate is present at 1.6 mM. Therefore, the pe of the system remains high while nitrate is present and is part of a controlling redox couple.

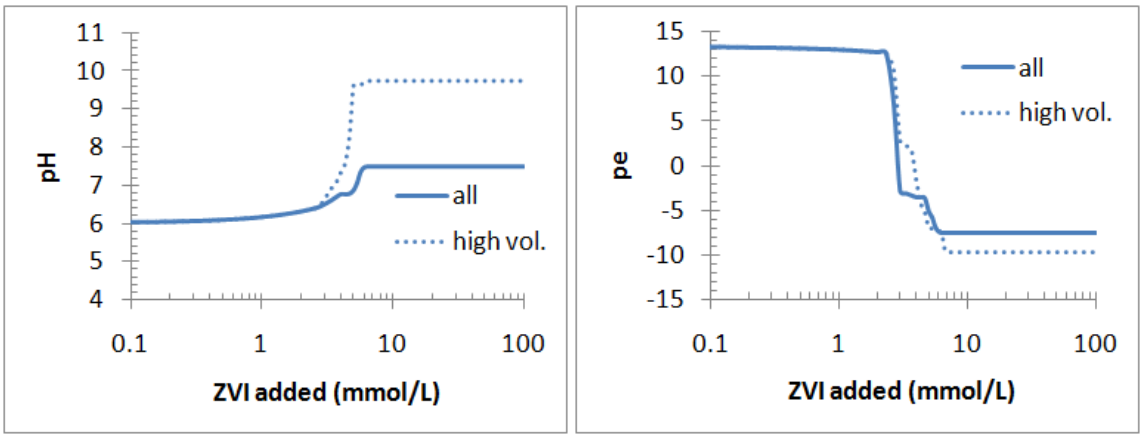

Figure 5.62: Equilibrium model of ZVI-NO_3 system predictions of pH (left) and pe (right), allowing all or high-volume (high-vol) solids to precipitate, in simulations with gas phase formation allowed.

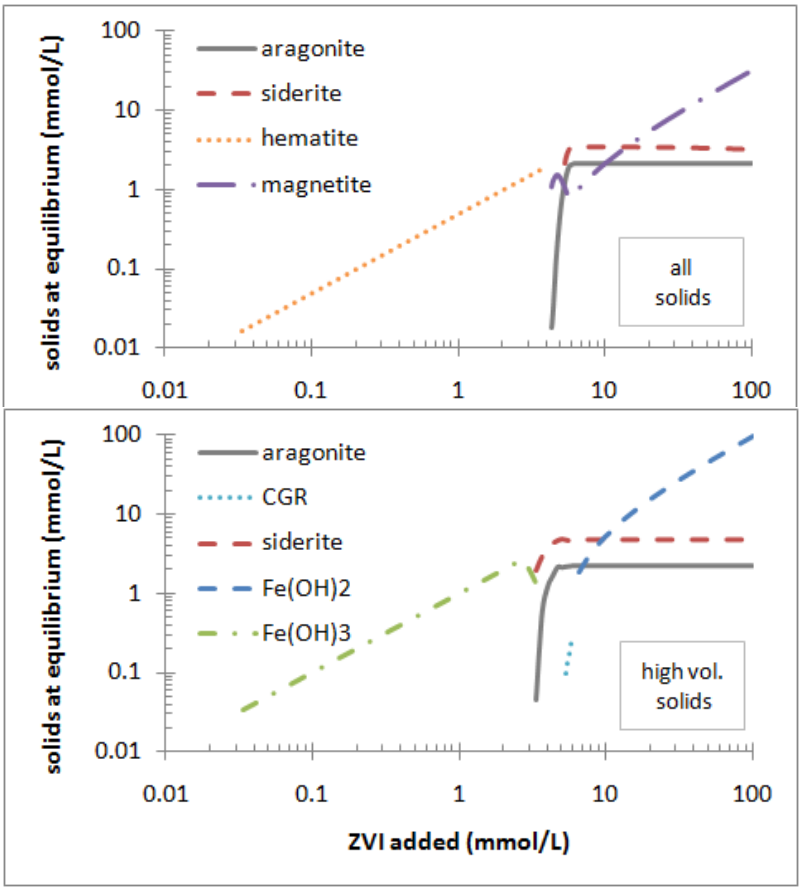

Figure 5.63: Equilibrium solids predicted in the model of the ZVI-NO_3 system, with unrestricted solids (top) and high-volume solids (bottom).

Figure 5.63 shows the model predictions for solids precipitation in the ZVI-NO_3 system. For additions of ZVI that are less than that necessary to reduce all of the 1.6 mM NO_3^-, Fe(III) solids are formed in both simulations, in keeping with the high pe observed in

Figure 5.62. As the buffer capacity of the carbonate species is used up, the system switches to the state of oversaturation with respect to carbonate solids, and they begin to precipitate in both simulations.

The left panel of Figure 5.64 shows the changes in hydraulic conductivity calculated based solely on the solids precipitated in the simulations of the ZVI-NO_3 system. Again, the difference in controlling solids in the two simulations creates a range of hydraulic conductivity losses. Above 10mM added ZVI, both simulations reach a point where additional ZVI dissolves and re-precipitates as either magnetite (in the case of unrestricted) or $Fe(OH)_2$ (in the case of high-volume solids). As noted earlier, the difference in stoichiometric amounts of iron and the densities of these two solids is responsible for the difference in the curves observed in the left panel of Figure 5.64.

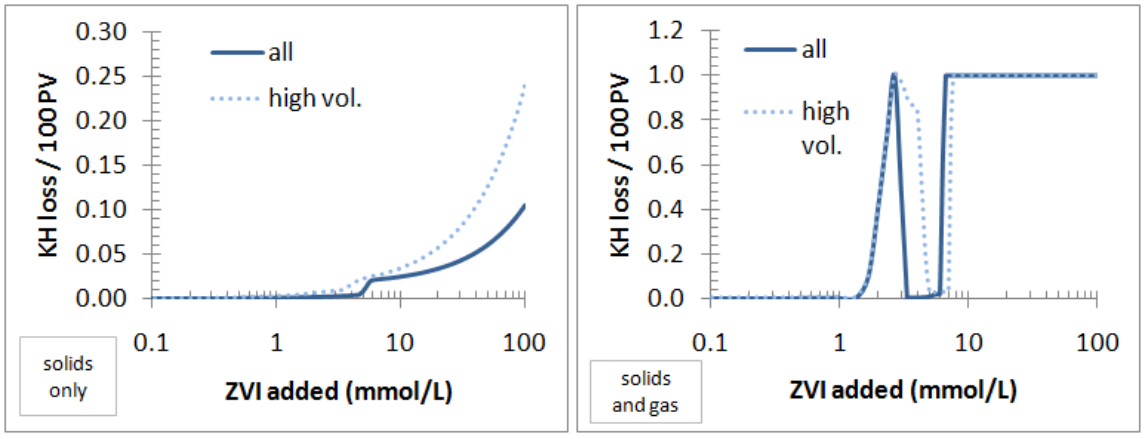

Figure 5.64: Comparison of hydraulic conductivity loss predicted in the model of the ZVI-NO_3 system with unrestricted (all) and high-volume (high-vol.) solids precipitation allowed. Calculations for the model with no gas formation are in the left panel, while the right panel shows the system with gas formation allowed.

The right panel of Figure 5.64, in contrast, shows the calculated hydraulic conductivity loss for the simulations in which a gas phase is allowed to form. Of note is an intermediate peak, occurring around 2 mmol/L of ZVI added, which is attributable to the formation of N_2 gas. At ZVI additions of approximately 5 mmol/L, though, the system becomes more reducing, and N_2 is reduced to NH_3, resulting in a model prediction of a minimal K_H loss. At even higher ZVI addition, the system is highly reducing, H_2 gas is formed, and the permeability is once again adversely affected.

5.5 Summary

Column experiments with a range of oxidant levels have highlighted many similarities with respect to geochemical behavior, and strong differences with respect to hydraulic behavior. Figure 5.65 summarizes the effluent E_H data for the ZVI columns (E_H was not measured in the ZVI-O_2 column). Reducing conditions were created in the ZVI columns, regardless of the level of incoming oxygen or nitrate. These reducing conditions were maintained for over 200 pore volumes.

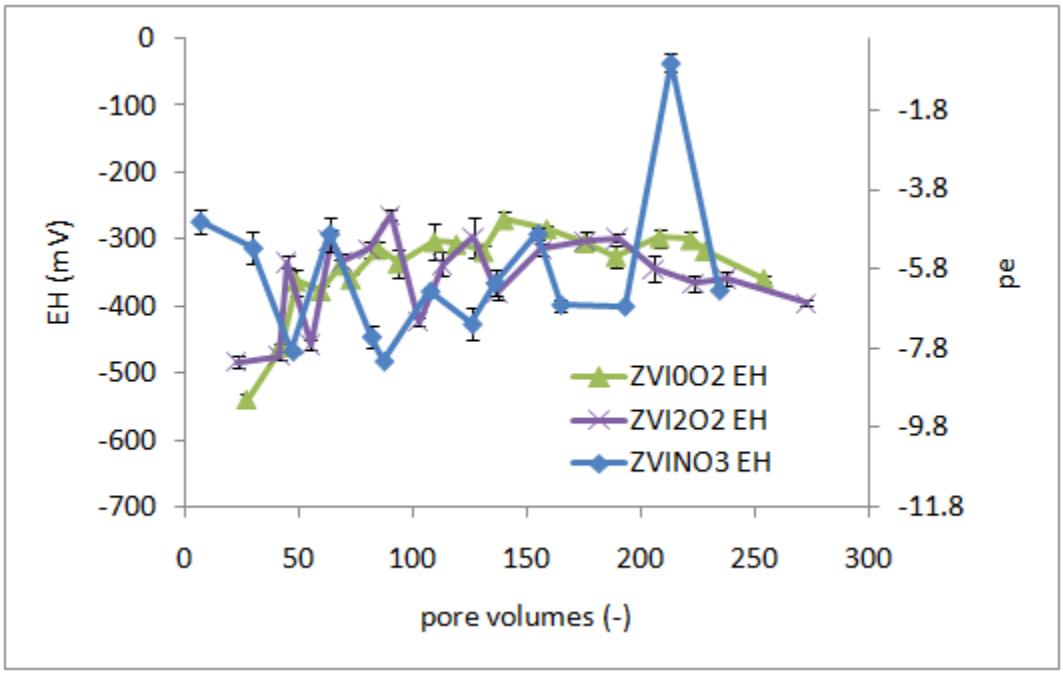

Figure 5.65: Measured values of E_H in ZVI columns (summarizes data presented Figures 5.1, 5.23, and 5.49).

The reducing conditions are consistent with the oxidation of ZVI; also consistent with this oxidation – whether it is by water or by an oxidant – is a pH increase (Figure 5.66). The pH increase (from an influent value of 6 to an effluent value of > 9, initially) was largest for the ZVI-NO_3 column, which received the largest amount of oxidant in terms of eq/L. The ZVI-NO_3 and ZVI-O_2 columns, which received 100 mg/L of NO_3^- and 8 mg/L of O_2, respectively, were the only columns to show a clear decrease in effluent pH with time.

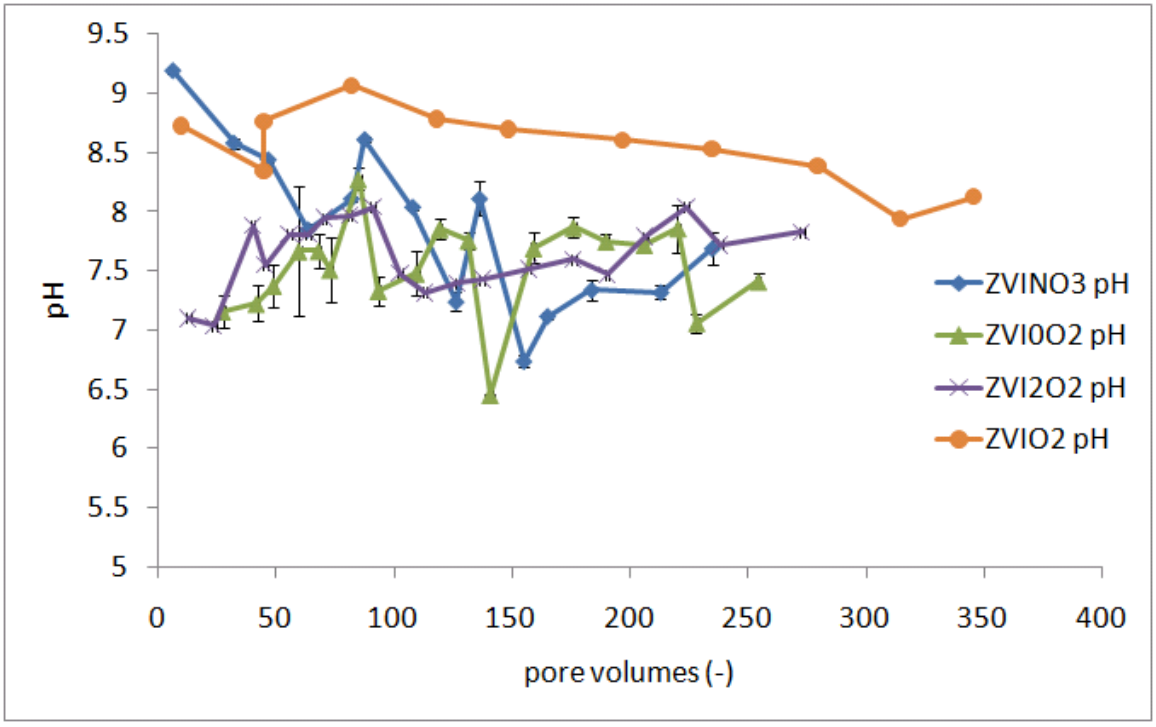

Figure 5.66: Measured effluent pH in all ZVI columns (pH influent = 6 with the exception of pH influent = 7 for ZVI-O_2) (summarizes data presented in Figures 5.2, 5.24, 5.39, and 5.50).

In all cases, however, the effluent pH put the system in a condition of oversaturation with respect to calcium carbonate. Consistent with this was the observed removal of calcium and carbonate in the columns. Removal of both species did not show a temporal trend, and the amount of calcium removed was correlated with the amount of influent oxidant: calcium removal was largest for the ZVI-NO_3 column, with a difference between influent and effluent concentrations of more than 100 mg/L. The ZVI-O_2 column did not receive calcium carbonate, and the ZVI-$2O_2$ column and ZVI-$0O_2$ column each removed between 30 and 80 mg/L of calcium.

Mass balances on calcium, carbonate, and iron (using anaerobic corrosion and oxidant levels) were used to calculate calcium carbonate, iron carbonate, and iron (hydr)oxide solids formation. Even with conservative assumptions, the predicted solids could not account for the observed hydraulic conductivity reductions observed in the ZVI columns, shown in Figure 5.67.

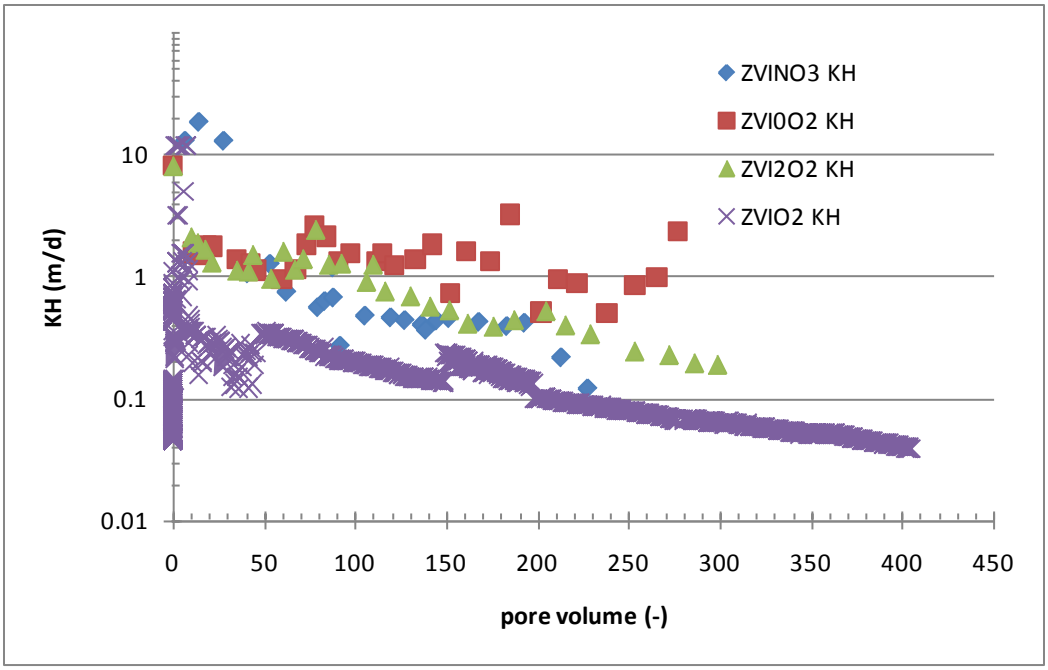

Figure 5.67: Hydraulic conductivity measured in ZVI columns (summarizes data presented in Figures 5.5, 5.26, 5.41, and 5.53).

The magnitude of hydraulic conductivity reduction appears to be correlated with the amount of oxidant in the influent solution. However, the amount of oxidant was not correlated with the amount of solids calculated to have formed. This information is presented in Table 5.10, which shows molar and volumetric amounts of calculated solids formation, normalized to 100 pore volumes. In this table, the left columns correspond to mmol and cm^3 of calcium carbonate solids, while the right columns show different amounts of iron carbonate formation, depending on which iron carbonate solid is assumed to form. The ZVI-O_2 column is set apart at the bottom, for it did not receive calcium carbonate, and calculations of the iron (hydr)oxide solids were based on the anaerobic corrosion of iron and the presence of 8 mg/L O_2, as discussed in Section 4.3.7.

Table 5.10: Solids formation in ZVI columns for calcium carbonate, iron carbonate, and iron (hydr)oxide solids (normalized to 100 PV), calculated on the basis of a mass balance

	Calcium carbonate		Iron carbonates			
				$FeCO_3$	ICH[A]	CGR[A]
column	mmol Ca/ 100 PV	cm^3 / 100 PV	mmol Fe / 100 PV	cm^3 / 100 PV	cm^3 / 100 PV	cm^3 / 100 PV
ZVI-$0O_2$	40	1.5	158	4.3	8.3	25.9
ZVI-$2O_2$	36	1.3	173	4.3	8.3	26.0
ZVI-NO_3	81	3.0	105	3.5	6.8	21.2
				Iron (hydr)oxides		
				FeOOH	Ferrihydrite	$Fe(OH)_3$
ZVI-O_2	-	-	10.7	0.22	0.24	0.26

A: ICH = iron carbonate hydroxide; CGR = carbonate green rust

In Table 5.10, the ZVI-NO_3 column, because it had the greatest calcium removal, is calculated to have the greatest formation of calcium carbonate. Because the carbonate removal was similar in all columns, however, this implies that the formation of iron carbonate solids was less in the ZVI-NO_3 column than in the ZVI-$0O_2$ and ZVI-$2O_2$ columns. The ZVI-O_2 column is calculated to have between one and two orders of magnitude less solids formation than those columns receiving calcium and carbonate. In Table 5.11, the corresponding calculated hydraulic conductivity reduction based on solids production is shown.

Table 5.11: Calculated fractional reduction in K_H for ZVI columns (normalized to 100 PV)

K_H fraction reduction / 100 PV

column	$CaCO_3$ + $FeCO_3$	$CaCO_3$ + ICH[A]	$CaCO_3$ + CGR[A]
ZVI-$0O_2$	0.060	0.092	0.204
ZVI-$2O_2$	0.058	0.090	0.198
ZVI-NO_3	0.071	0.097	0.195
	FeOOH	Ferrihydrite	Fe(OH)3
ZVI-O_2	0.0012	0.0015	0.0018

A: ICH = iron carbonate hydroxide; CGR = carbonate green rust

As before, the larger calcium carbonate formation in the ZVI-NO_3 column impacts the trends observed in Table 5.11. In the first column, the calcium carbonate formation

dominates the solids production because $FeCO_3$ does not represent a large net volume addition – the Fe in this solid came from ZVI, representing a volume loss. However, green rust – because it incorporates OH^- and H_2O – represents a relatively larger volume addition. Therefore, when green rust is allowed to form, the ZVI-$0O_2$ and ZVI-$2O_2$ columns, which had relatively larger carbonate removal – show a K_H loss similar to the ZVI-NO_3 column.

Even with the most conservative assumptions about solids formation, solid precipitation cannot account for the observed hydraulic conductivity decreases shown in Figure 5.67. Therefore, it is likely that evolved gas may be responsible for the remainder of the hydraulic conductivity loss. Among the columns receiving calcium and carbonate, there is a trend: the measured K_H fraction loss per 100 PV increases with increasing oxidant level. Because the solids production is calculated to be similar (Table 5.11), the fraction attributable to gas increases with increasing oxidant level.

Chapter 6: Iron Sulfide (FeS) Column Experiments

To complement the set of experiments with ZVI, a similar set of experiments was conducted with systems utilizing FeS-coated sand as the reactive media. Han (2009) used FeS-coated sands in column experiments with buffered influent solutions containing arsenic, but without additional background constituents typically found in groundwater. These experiments were meant to compare the behavior of the FeS system to that of the ZVI system. These experiments are summarized in Table 6.1, below. A flow rate of 0.7 mL/min was used for all columns.

Table 6.1: Summary of FeS column experiments

Column name	Influent solution	pH	Initial K_H (m/d)	Initial porosity (-)	Flow rate (PV/d)	Flow velocity (cm/hr)
FeS-$0O_2$	calcium + carbonate	6	12.8	0.33	6.2	6.5
FeS-O_2	DDI water	7	10.7	0.33	6.4	6.7
FeS-NO_3	calcium + carbonate + nitrate	6	9.9	0.31	6.2	6.5
FeS-Mont	simulated Monticello	6.3	14.3	0.32	6.6	6.9

Table 4.1 has a detailed description of the composition of the influent solutions.

6.1 FeS-$0O_2$ column

The column designated FeS-$0O_2$ received a deoxygenated influent solution with 7mM calcium and carbonate (280 mg/L calcium and 420 mg/L carbonate). It was anticipated that geochemical changes in the column would increase the pH, causing calcium carbonate and other iron (hydr)oxides to precipitate.

6.1.1 Column results

Over the course of nearly 180 pore volumes of influent solution injected into the FeS-$0O_2$ column, no significant geochemical changes were detected, as indicated by pH and calcium measurements. pH was measured at 110 and 175 pore volumes; the influent solution had a pH of 6, and effluent values were 6.0 and 6.1, respectively. ICP analysis of the concentration of calcium in the effluent showed no change from the influent concentration. The average of five effluent calcium measurements from 67-170 pore volumes was 290 mg/L, while the average influent value was 291 mg/L. The fact that the influent and effluent concentrations were essentially the same indicates that no precipitation of a calcium solid was taking place.

The pressure drop along the column was measured at regular intervals. Figure 6.1 presents these raw data. Despite the scatter in the data – especially during column start up –there is not a clear trend indicative of a change in hydraulic conductivity. Figure 6.2 shows the hydraulic conductivities based on these data. The hydraulic conductivity is essentially flat, and the one or two order of magnitude changes that were observed the ZVI columns are not apparent in the FeS-$0O_2$ system.

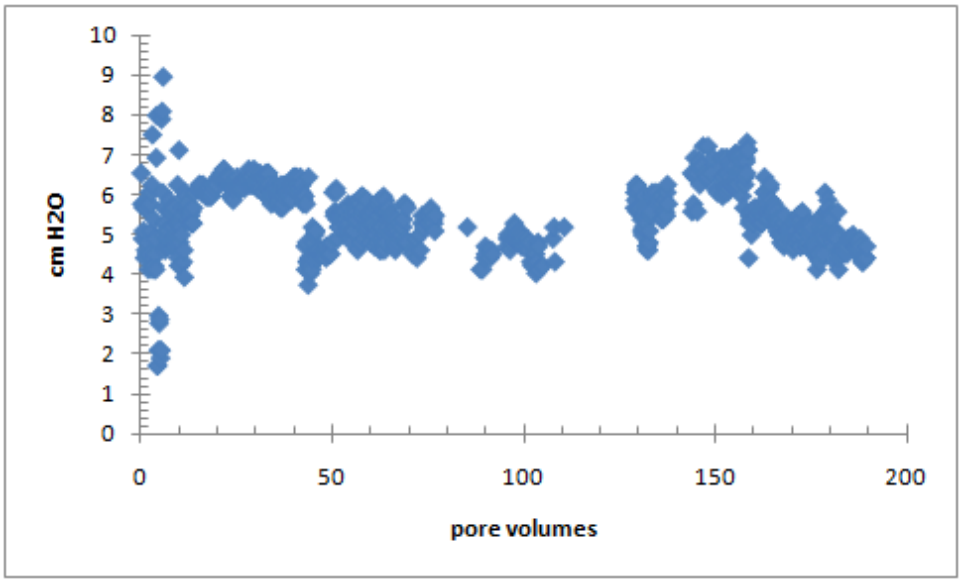

Figure 6.1: Pressure drop along the column designated FeS-$0O_2$.

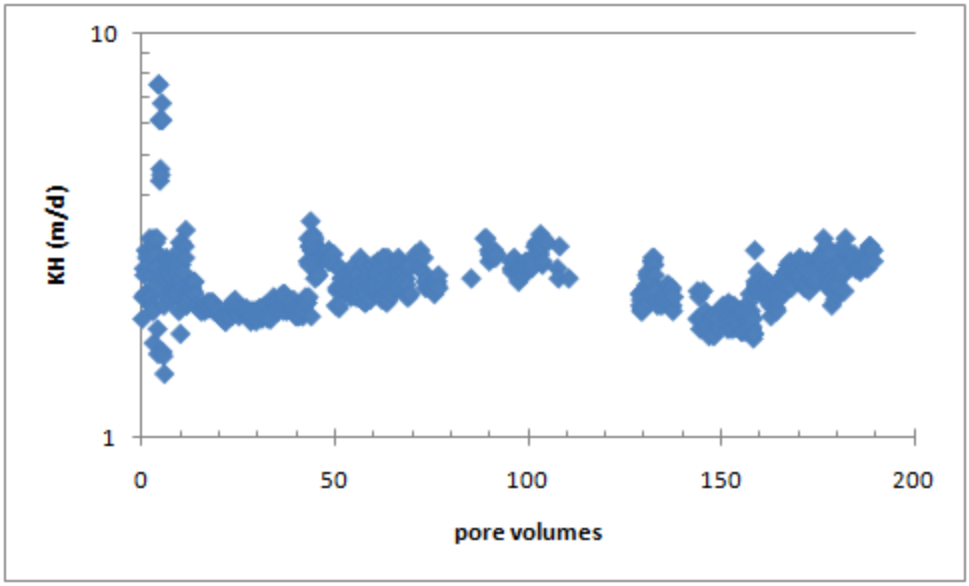

Figure 6.2: Calculated hydraulic conductivity in the FeS-0O_2 column as a function of pore volumes injected.

The combination of these pieces of evidence (i.e., no pH change, no calcium removal, and no hydraulic conductivity change) suggests that conditions in the column did not create supersaturation of any calcium solids. Furthermore, the constant pH conditions and the fact that column retained its black color over time indicate that FeS dissolution (Equation 2.7) did not proceed to the extent that FeS was removed from the sand.

Although the aqueous phase did not provide evidence for solids accumulation, and samples were not able to be analyzed spectroscopically, geochemical modeling was conducted to confirm that solids accumulation would be unlikely.

6.1.2 Modeling

As discussed in Section 4.3.7, batch, equilibrium models of this system consisted of FeS additions spanning 0.1 to 100 mM. In these models, the set of solids that were allowed to precipitate was not restricted in any simulations. In all model predictions for the FeS-0O_2 system, the equilibrium pH was 6.01-6.02, and the pe was -2.41 to -2.49 (E_H ~ -140 mV) (Figure 6.3). There was some minor solids formation along with some phase changes: greigite (Fe_3S_4) and hematite (Fe_2O_3) form, though both were at amounts that were two orders of magnitude less (on a molar basis) than FeS. The maximum partial pressures of

hydrogen and hydrogen sulfide gas were $P_{H2(g)} = 8x10^{-8}$ atm and $P_{H2S(g)} = 6.5x10^{-5}$ atm. Thus, no gases were formed, so simulations with and without the formation of a gas phase were identical.

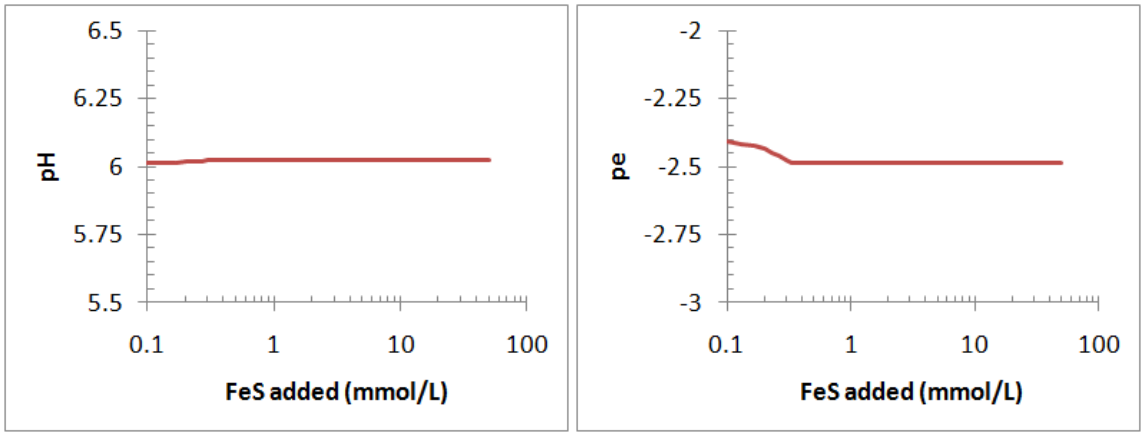

Figure 6.3: Equilibrium model of FeS-0O_2 system (100 mg/L NO_3^-) showing pH (left) and pe (right).

Overall, this model indicates that FeS in equilibrium with aqueous phases containing calcium and carbonate will not reach the pH values necessary for precipitation of carbonate solids. Even if the FeS is oxidized to other phases, the resulting composition of solid phases is expected to be as permeable as the original FeS-coated sand, because the equilibrium solids do not appreciably change the solids mass in the system. Therefore, modeling of this column, yielded results in keeping with those observed in the laboratory.

6.2 FeS-O_2 column

Like the ZVI column that received fully oxygenated water, this column, designated FeS-O_2, received distilled, de-ionized water that was in equilibrium with the ambient laboratory atmosphere and did not have any additional solutes such as calcium or carbonate.

6.2.1 Column results

For this column, the influent pH was close to 7, with a variability of ± 0.5 pH units. Figure 6.4 shows the effluent pH of this system, which indicates that the pH was generally stable after the initial measurements.

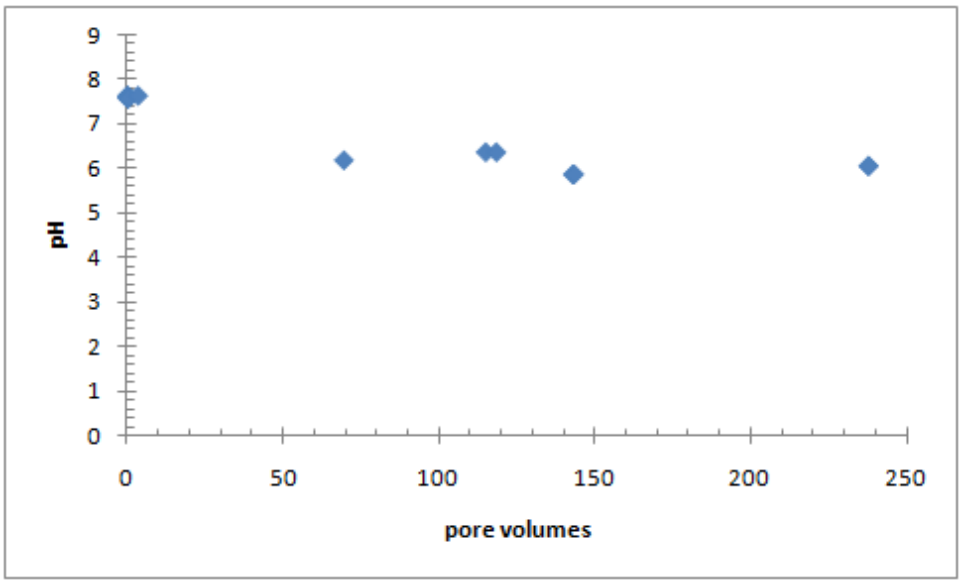

Figure 6.4: Effluent pH in the column designated FeS-O_2 as a function of pore volumes injected into the column.

The effluent iron concentrations were also stable: total iron in the effluent was consistently below the detection limit of 80 µg/L. For an oxidized system, it is expected that aqueous iron concentrations would be low, since ferric iron is relatively insoluble.

The only change observed in this column was that, over time, the FeS-coated sand in the column lost its black color, and took on an orange-brown hue (Figure 6.5). This change in color is indicative of a transition from ferrous to ferric solids, consistent with the oxidation brought about by the oxygen in the influent solution.

Figure 6.5: FeS-O_2 column changes in color: initially (left), and at 230 PV (right).

6.2.2 Modeling

For batch, equilibrium modeling of this system, the oxygen level was assumed to be 8 mg/L = 0.25 mmol/L. Again, a range of 0.1 to 100 mM FeS was used. The calculated equilibrium gas partial pressures were $P_{H2(g)} = 8x10^{-8}$ atm, and $P_{H2S(g)} = 6.5x10^{-5}$ atm. Across the range of added FeS concentrations, the pH was consistently between 5.9 and 6.0, and the pe was likewise stable between -2.3 and -2.4, with the following exception: at concentrations of FeS less than 0.11mM, the pe was above 14, because the water/oxygen couple controlled the pe.

The threshold of 0.11 mM FeS comes from a consideration of equivalents. For oxidants in this system, there is a concentration of 0.25 mM O_2 (8 mg/L O_2), which introduces 4 mM eq / mM O_2; thus, the oxidant concentration is 1 mM equivalents. FeS is the reductant in this system, and the oxidation of FeS can produce a total of 9 eq/M, as the Fe(II) to Fe(III) transition produces 1 electron, and the S(-II) to S(VI) transition produces 8 electrons. Thus, 0.11 mM FeS produces 1 mM equivalents (0.11 mM FeS * 9 eq/mM FeS). However, the lower limit of the modeling range was 0.1 mM, meaning that the oxygen had a significant impact only at the minimum FeS addition.

In this equilibrium model, some solids transformation took place, which is consistent with the observations above. Figure 6.6 shows the equilibrium solids concentration as a function of the addition of FeS. Note that for FeS concentrations less than approximately 1.1 mM, the FeS that is added is entirely transformed to greigite and hematite.

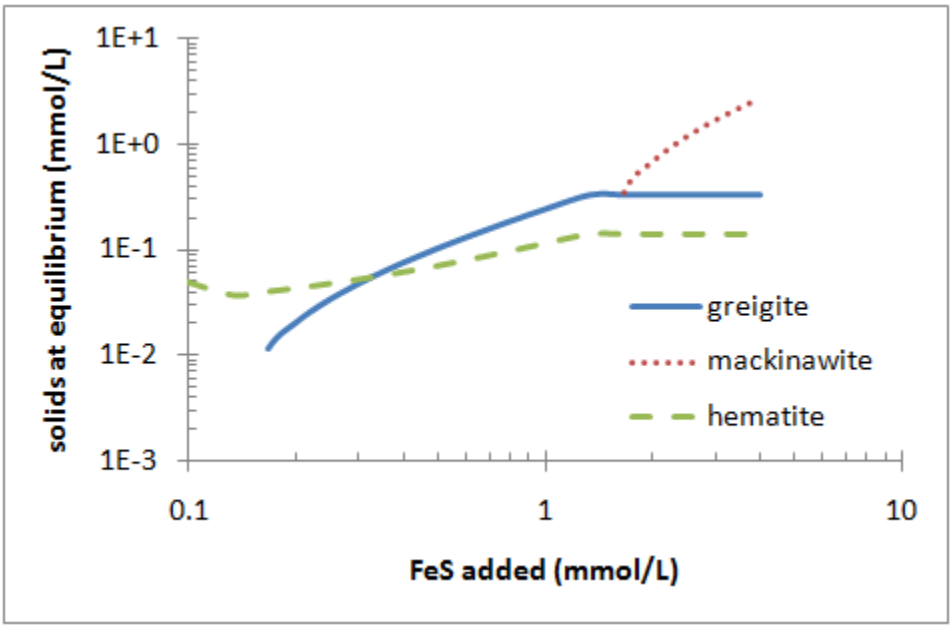

Figure 6.6: Solids predicted in the equilibrium model of the system designated FeS-O_2.

Because the changes in the solid phase shown in Figure 6.6 represent the addition of minimal mass to the solid phase (as only hematite incorporates additional species), there is very little accumulation of new solids and a concomitantly low decrease in permeability. At the highest concentration of added FeS (100 mM), the solids production corresponds to a K_H loss of only 0.003 % per 100 PV, based on the Kozeny-Carman equation (Equation 2.19).

6.3 FeS-NO_3 column

The influent solution of this column, designated FeS-NO_3, was similar to that of the column designated FeS-0O_2; however, 100 mg/L of nitrate was added (Table 4.1). 100 mg/L of nitrate was found to be strongly correlated with at-risk classification for ZVI PRBs, as discussed in Chapter 3. In the field, where bacterial mediation of the reduction of nitrate is possible, the influent solution to this column represents a higher level of

potential oxidation, as measured by the number of oxidizing equivalents per liter, than the previous FeS columns. However, in these laboratory experiments, oxidation of FeS by nitrate is not expected.

6.3.1 Column results

Figure 6.7 shows the measured redox potential in the column effluent versus pore volumes injected into the column. The data show a large degree of scatter after about 200 pore volumes. From a theoretical perspective, it is difficult to explain the presence of 500 mV swings in E_H in this system. The E_H electrode was calibrated before each measurement, and raw mV readings were always within the range prescribed by the manufacturer. If there were a large intrusion of oxygen in the column, for example, that drove the entire system to a positive E_H value, it is unlikely that the system would revert back to reducing conditions.

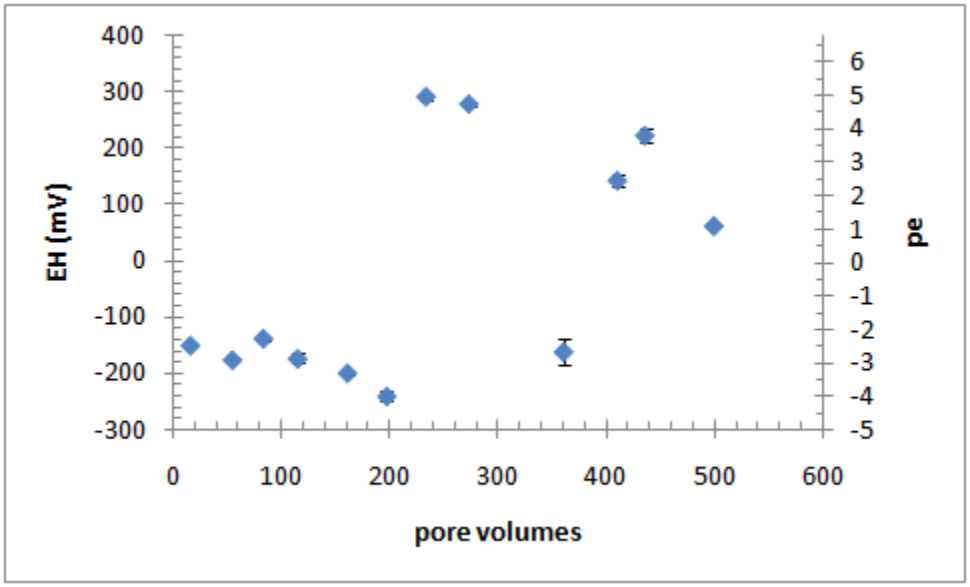

Figure 6.7: Effluent E_H in the FeS-NO_3 column as a function of pore volumes injected into the column.

Another explanation for the variability in these data is the experimental apparatus. After the first high E_H reading was confirmed by a second, some of the tubing in the effluent line of this column was found to have small leaks, as indicated by the presence of iron

staining around the fittings. This tubing was replaced, and the staining did not occur again. However, it is possible that other leaks had developed in the effluent lines of the system, such that the effluent values measured in the flow-through cells were not indicative of the values in the column itself.

Effluent pH data for this column show a large degree of consistency, again with the exception of a point around 300 pore volumes (Figure 6.8). If there were leaks in the effluent of the system, this errant pH data point could be a product of that problem. Despite the fluctuations in the E_H and pH data, there is a large degree of consistency in the readings up to 200 pore volumes. Regardless of the source of the variability, conclusions drawn from this data are not affected by that variability.

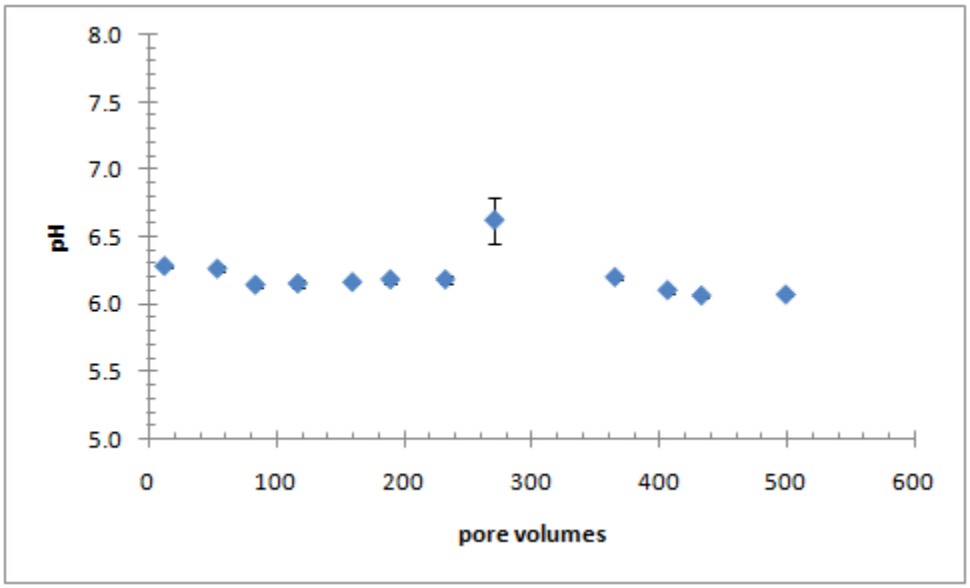

Figure 6.8: Effluent pH in the FeS-NO_3 column as a function of pore volumes injected into the column.

Figure 6.9 shows constant effluent calcium concentrations and, after an initial equilibration period, constant total iron concentrations. The calcium values indicate that no calcium was being retained in the column; therefore, it appears that calcium carbonate solids were not precipitating. The iron concentrations show initially high values (> 25 mg/L total iron), followed by a decrease to an average of 2.04 mg/L between 200 and 500 pore volumes. This behavior matches that reported by Han (2009); in an FeS-coated sand

receiving an influent solution buffered to pH 5, the effluent concentration of iron was initially high but then stabilized at 3.5 x 10^{-2} mM (1.95 mg/L).

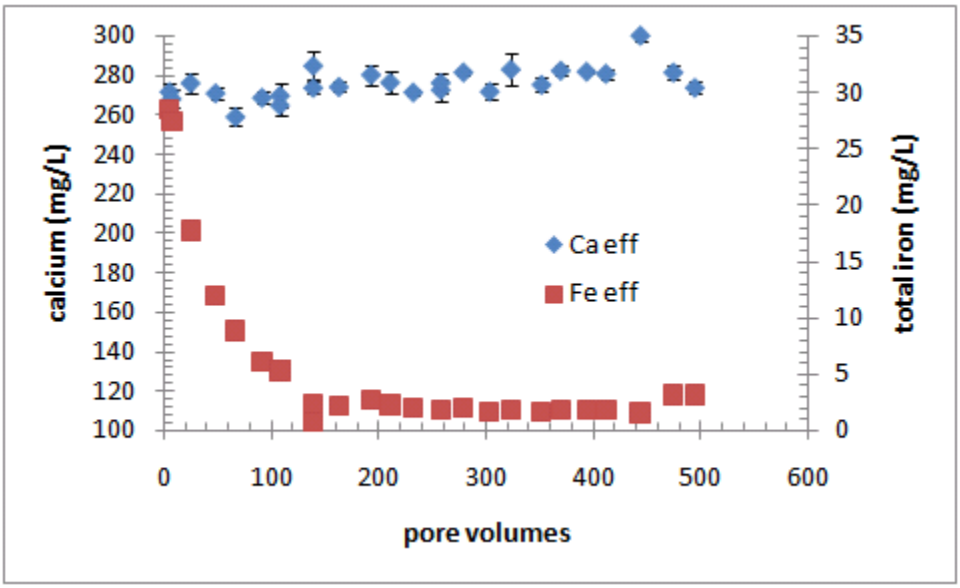

Figure 6.9: Aqueous calcium and total iron concentrations in the effluent of the FeS-NO_3 column as a function of pore volumes injected into the column.

There was no difference between measurements of influent and effluent carbonate concentrations, indicating that carbonate-containing solids were also not precipitating. Measurements of pressure drop along the column, shown in Figure 6.10, generally fall between 0.5 and 2.0 cm H_2O. This finding is consistent with the hypothesis that solids were not forming in this column. There is scatter in the data, particularly after 250 pore volumes. This variability may be related to the experimental problems that caused variable E_H measurements (Figure 6.7), as leaks in the effluent tubing would affect the measured pressure drop. Note, also, that the scale of the ordinate axis is smaller than that used in the ZVI chapter, since the range of pressure drops measured in the ZVI systems exceeded 100 cm H_2O in some cases. Thus, the variability seen in Figure 6.10 is quite small, and the overall trend is clearly indicative of the lack of formation of solids in the column, regardless of the scatter in the data.

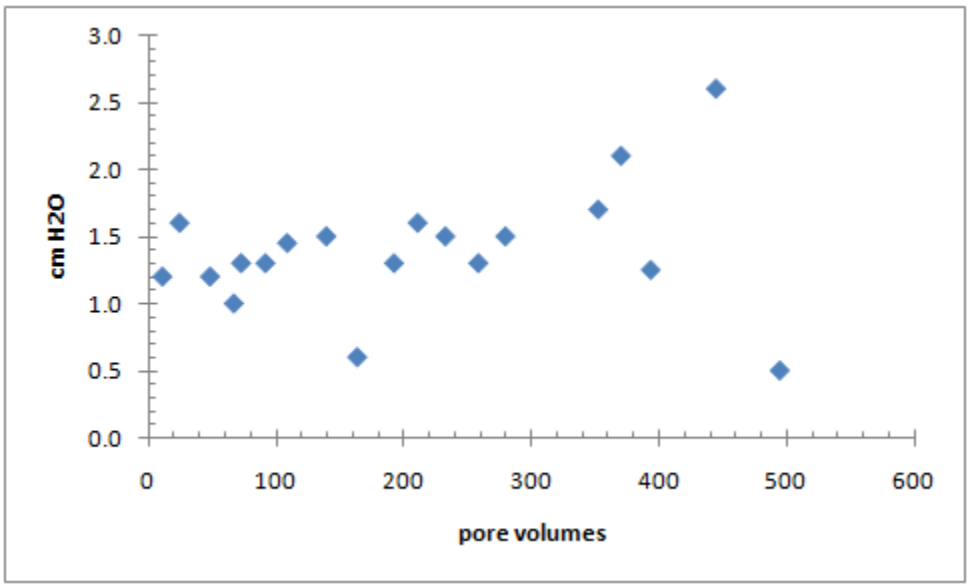

Figure 6.10: Pressure drop along the FeS-NO_3 column as a function of pore volumes injected into the column.

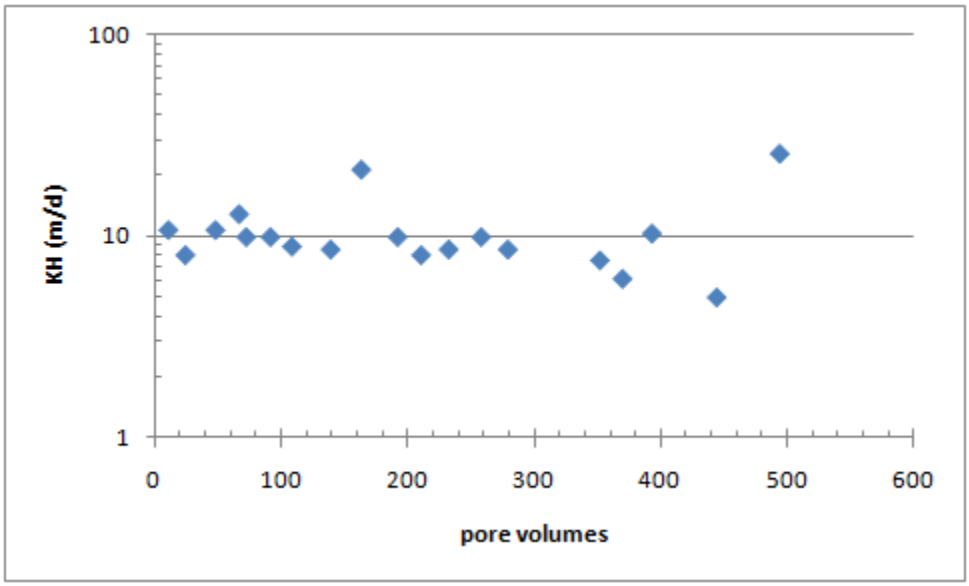

Figure 6.11: Hydraulic conductivity in the FeS-NO_3 column calculated from pressure drop as a function of pore volumes injected into the column.

Figure 6.11 presents the hydraulic conductivity of the column versus pore volumes, which does not show a trend with time. Taken together, the analysis of samples of the effluent from the FeS-NO_3 column and the measurements of pressure indicate that this column was not removing solutes from the influent solution, and therefore, did not experience a loss of hydraulic conductivity with time.

6.3.2 Solids Analysis

In order to conduct SEM and XPS analyses of samples from this column; the column was destructively sampled at the conclusion of the experiment.

6.3.2.1 SEM

Figure 6.12 shows a grain of FeS-coated sand taken from the influent of the FeS-NO_3 column. At the scale of this micrograph, 50 µm, the surface appears generally smooth, although there are some steps and other minor surface features.

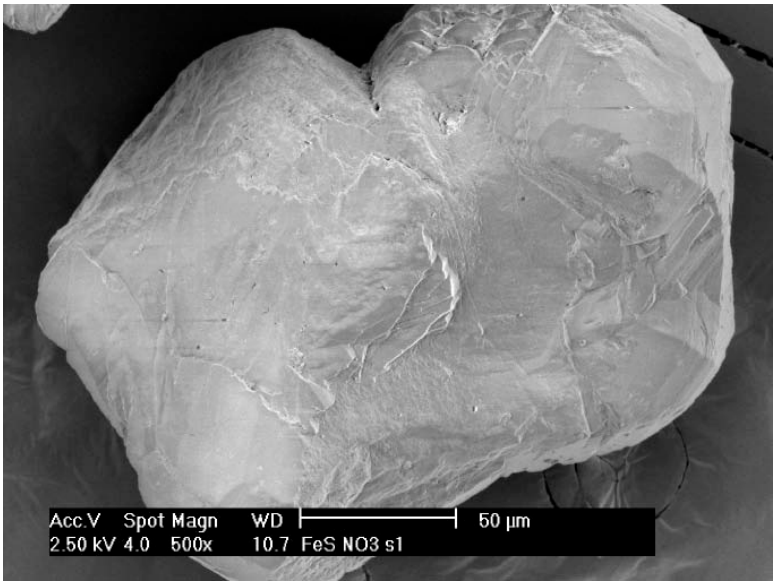

Figure 6.12: Grain of FeS-coated sand from the influent section of the FeS-NO_3 column.

Figure 6.13 shows two closer views of the surface of this grain. There are regions that still appear smooth, even at a 2 µm scale, and there are regions with some surface irregularities, but the scale of those irregularities appears to be <1 µm. These areas may be indicative of a patchy coating of FeS (Han 2009). These images are quite similar to the SEM micrographs of unused FeS-coated sand (Figure 4.2), suggesting that there was not an appreciable amount of solids production.

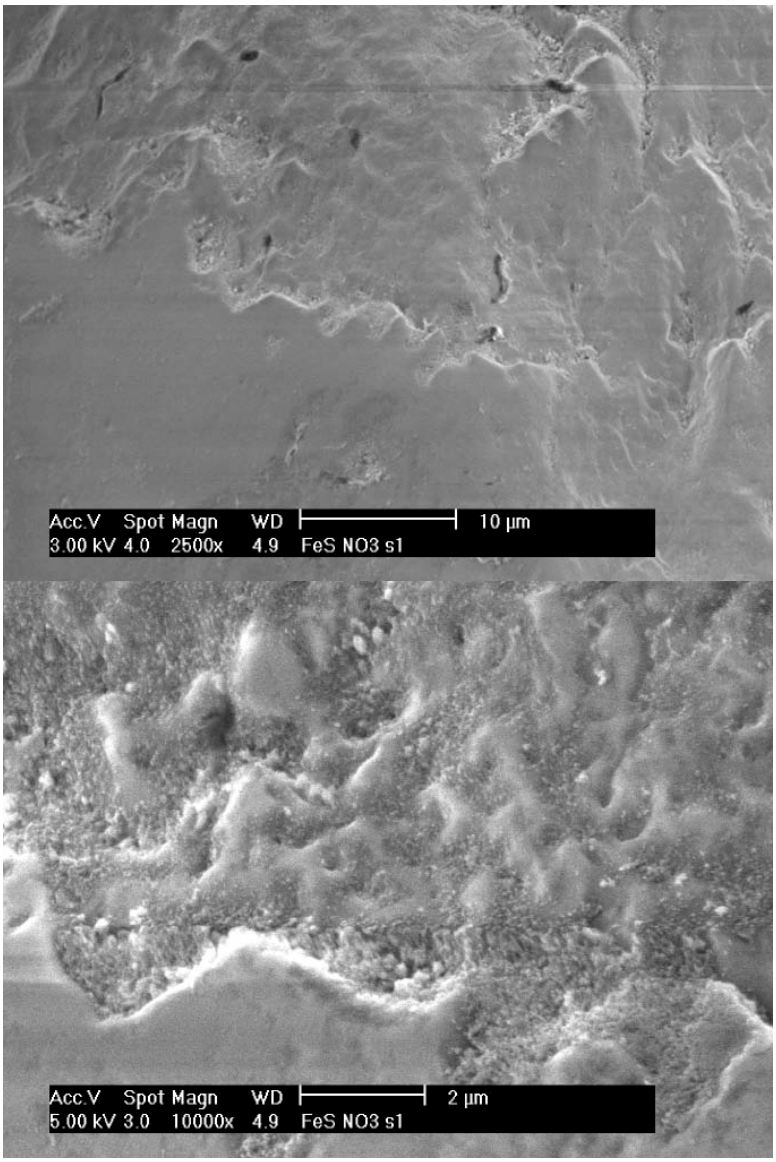

Figure 6.13: Closer views (10 µm scale, top; 2 µm scale, bottom) of a sample from the influent section of the FeS-NO_3 column.

These SEM images of samples from the FeS-NO_3 column indicate a lack of precipitates. When contrasted with the micrographs of ZVI grains presented in Chapter 5, it is clear that any irregularities on the surface – even if they are due to precipitates formed during operation of the column – would not have a substantial impact on the pore space of this column.

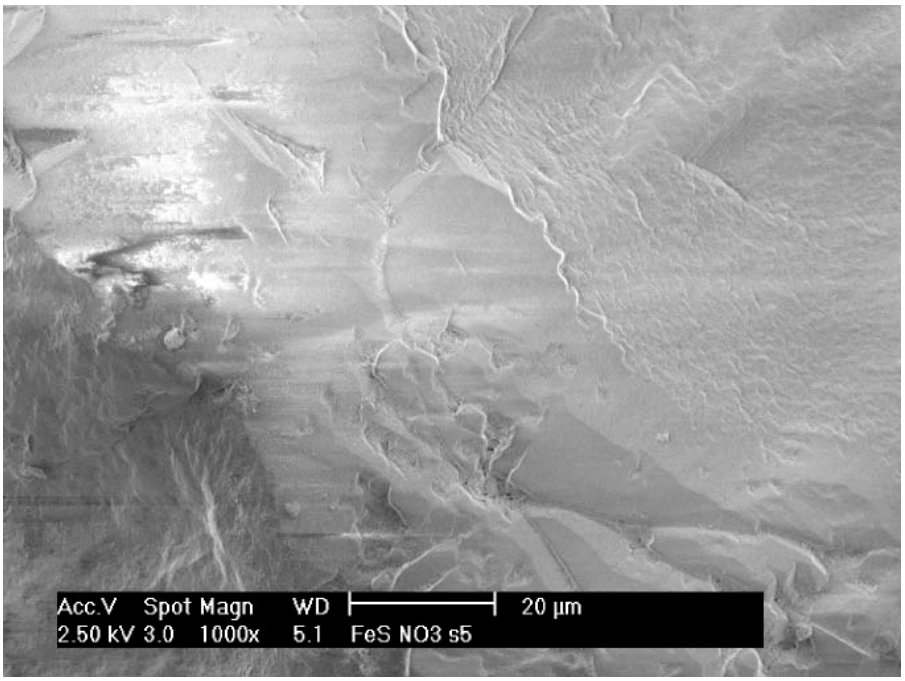

Figure 6.14: Surface of grain of FeS-coated sand from the effluent section of the FeS-NO_3 column.

Figure 6.14 shows the surface of a grain of FeS-coated sand from the effluent section of the FeS-NO_3 column. The surface is similar to the surface of the samples from the influent section of the column. Indeed, both the influent and effluent samples from the FeS-NO_3 column have similar surface morphology: they are generally smooth, with irregularities and patchiness occurring only at the sub-micron scale. Because the grains of FeS-coated sand do not appear to have accumulated solids, it is difficult to distinguish between influent and effluent samples in these images, as was possible with micrographs of ZVI samples.

6.3.2.2 XPS

Given that the SEM analysis of samples from the FeS column indicated no appreciable solids formation, XPS was used to examine the solid surface. As noted in Section 4.3.6.2, XPS provides information about the surface species present, and peak deconvolution may be used to create a plausible description of the surface species.

XPS analysis of the $Fe2p_{(3/2)}$ peak for the FeS-NO_3 column indicates that the iron sulfide in this column may have changed phase to some degree, and undergone some oxidation,

but that a significant portion of iron surface species have a similar oxidation state to that of fresh FeS. The $Fe2p_{(3/2)}$ peak is shown in Figure 6.15, below.

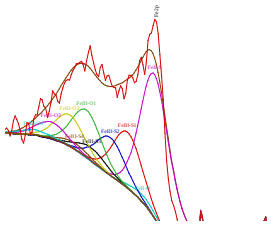

Figure 6.15: Decomposition of Fe2p $_{(3/2)}$ peak for sample from influent section of FeS-NO_3 column.

In Figure 6.15, the raw XPS data are shown as a jagged red line; individual peak components are labeled as sub peaks, and the sum of these peaks is shown above them. The raw data for this measurement and the others presented in this work is the average of 30 to 40 scans of the surface. In this peak decomposition, the Fe(II)-S bond accounted for 40% (± 2.8%) of the total area, the Fe(III)-S bonds accounted for 31% (± 3.2%), and the Fe(III)-O bonds accounted for 27% (± 3.2%) of the area; the balance was accounted for by the Fe(II)-O bond. Although the Fe(II)-S is the single largest peak, ferric species account for the majority in total. This split indicates the possibility of the presence of a ferric sulfide species, such as greigite (which has mixed iron valency), as well as mixed valency oxide species, such as magnetite, or a fully ferric species, such as hematite.

Since XPS only provides information about the uppermost surface layers, this technique cannot provide information about the speciation of phases below this surface layer.

For comparison, Figure 6.16 shows the $Fe2p_{(3/2)}$ peak decomposition for unused FeS-coated sand. In this peak, the Fe(II)-S bond is 31% (± 3.2%) of the area, the Fe(III)-S bond is 34% (± 3.6%), the F(III)-O bond contributes 31% (±3.25) of the area, and the Fe(II)-O bond contributes the balance.

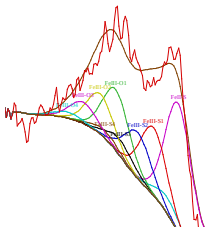

Figure 6.16: Decomposition of Fe2p $_{(3/2)}$ peak for unused FeS-coated sand.

Comparing the FeS-coated sand $Fe2p_{(3/2)}$ peak to that for the influent section of the FeS-NO_3 column (Figure 6.15), it appears that the FeS-NO_3 sample is marginally more reduced. Given the uncertainty associated with XPS interpretation, this result is taken to mean that the surface state of iron in the two samples is similar. This result suggests that

the influent solution to the FeS-NO_3 column did not oxidize the FeS surface, as would be expected given results in the literature (Section 2.2.3.2).

Figure 6.17, below, shows the $Fe2p_{(3/2)}$ peak for a sample from the effluent end of the FeS-NO_3 column. In contrast to the sample from the influent end, the Fe(III)-O bond comprised a larger percent of the peak area. In the effluent sample, the Fe(II)-S bond is 27% (± 2.5%) of the area, while the Fe(III)-O bond is 38% (2.6%).

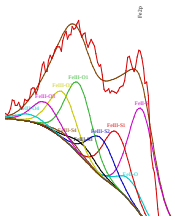

Figure 6.17: Decomposition of Fe2p (3/2) peak for sample from effluent section of FeS-NO_3 column.

Although the effluent section of the FeS-NO_3 column thus appears to be more oxidized than the influent section (Figures 6.15 and 6.17), these two scans provide more evidence for the hypothesis that experimental issues associated with the effluent section of the column and its tubing may have impacted the measurements of pH and E_H. The influent section is the one that receives the full flux of an oxidant; therefore, if the oxidant were responsible for the perceived oxidation in the effluent (Figure 6.17), the influent section would likewise be oxidized. Indeed, if the oxidant were responsible for the oxidation

observed in the effluent section, one of two things would have happened: either both the influent and effluent sections would have been oxidized, or, if the influent section had enough capacity to reduce the oxidant, the influent section could have been oxidized while the effluent section remained in its original state. Since the XPS data do not support either of these scenarios, it is reasonable to conclude that the oxidant is not responsible for the observed oxidation of the effluent sample. As noted in Section 4.3.6.2, XPS provides information about the surface species present, and peak deconvolution may be used to create a plausible description of the surface species. However, these models are not meant to be a definitive description of the surface.

6.3.3 Modeling

The FeS-NO_3 column was modeled by adding 1.6 mM nitrate (100 mg/L), along with calcium and carbonate at 7mM, to systems containing 0.1 to 100 mM FeS. Note that, as discussed in Section 2.2.3.2, nitrate is *not*, by itself, expected to oxidize FeS. However, it is possible that bacteria may mediate this reduction. To create a conservative estimate for the potential for solids formation, this model allows this reduction to occur. This assumption of bacterial mediation means that the results of this model are not directly applicable to the experimental column work. *Without* the reduction of nitrate by Fes, the model for this system is essentially the same as that presented for the FeS-$0O_2$ column (Section 6.3.3).

In the equilibrium model of the FeS-NO_3 column, the equilibrium partial pressures of hydrogen and hydrogen sulfide gases were consistently small: $P_{H2(g)} = 8x10^{-8}$ atm, and $P_{H2S(g)} = 6.5x10^{-5}$ atm, similar to the modeling results for the columns designated FeS-$0O_2$ and FeS-O_2. Figure 6.18 shows that, with significant amounts of oxidant (i.e., nitrate acting via bacterial mediation) available, the pH reached approximately 6.5, which is 0.5 pH units higher than the FeS systems without nitrate. Also shown is the pe of the system, which indicates oxidizing conditions when nitrate was present, and moderately reducing conditions (between pe values of -2 and -3) once sufficient FeS is present to reduce all of the added nitrate to other species.

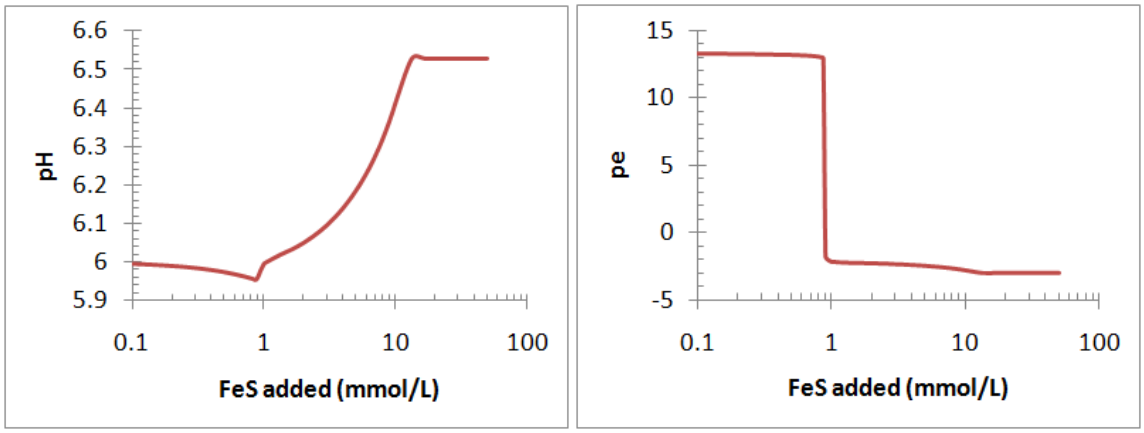

Figure 6.18: Equilibrium model of FeS-NO_3 system (100 mg/L NO_3^-) showing pH (left) and pe (right).

There are two points in the relationship between the concentration of FeS added and pH and pe curves where sharp changes are observed (Figure 6.18). These points define regimes that affect solids production and speciation. At low values of FeS addition, most of the nitrate added remains as either nitrate or nitrogen gas (the production of nitrite is never predicted in the model), and the nitrate/nitrogen couple controls the pe. At 0.9 mM FeS addition, the reducing potential due to this solid is 0.9mM FeS * 9 eq/mM FeS (Section 6.2.2), or 8.1 mM of reducing equivalents. The reduction of nitrate to nitrogen gas requires 5 mM eq/ mM NO_3^-; with 1.61 mM of NO_3^- added, this is 8.05 mM eq of oxidant. Therefore, once the FeS concentration exceeds 0.9 mM FeS, the pe becomes negative as the controlling couple switches from N(V)/N(0) to N(0)/N(-III). Between 1 and 10 mM FeS, the conditions in the system progressively become more reducing, and the ratio of N(0) to N(-III) continues to fall. At approximately 10 mM FeS, the reducing potential of FeS can no longer drive further reduction to ammonia, and the pe reaches a plateau. As a result, the pH ceases to increase. It should be noted that the pH does not increase sufficiently to cause oversaturation, and hence precipitation, of carbonate solids.

Figure 6.19 shows that, although carbonate solids are not formed, some solids transformation does take place. Corresponding to the pe of the system (Figure 6.18), there are three regions of solids formation. When conditions are oxidizing, all of the FeS that is added is transformed to hematite, a ferric oxide. At FeS additions greater than 0.9 mM (as calculated above), the pe remains reducing, and greigite, a mixed-valency iron solid, begins forming. After 10 mM FeS, when the concentrations of the N(0)/N(-III)

couple are in equilibrium with FeS itself, FeS added remains present and becomes the dominant solid.

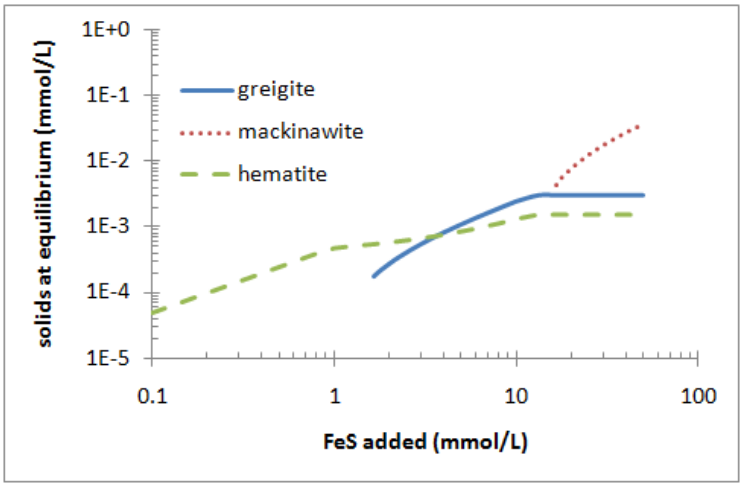

Figure 6.19: Equilibrium solids predicted in the model of the FeS-NO_3 system.

Hematite is the only solid formed in this model system (which assumes biologically-mediated oxidation of FeS) that incorporates new mass, as it is composed of iron and oxygen. However, as Figure 6.19 shows, hematite is the controlling solid only at low FeS concentrations. Furthermore, its density is higher than that of FeS (Table 4.5), so its formation can lead to a decrease in solid volume. At higher additions of FeS, the solids present are either FeS itself or greigite, the formation of which does not require an addition of mass. Therefore, the K_H loss predicted, based on the porosity change and the Kozeny-Carman equation, in this model is small: 0.067 % per 100 PV at highest FeS addition (100 mM).

6.4 FeS-Mont column

The composition of the influent solution to the FeS-Mont column was designed to mimic the groundwater conditions at Monticello, UT (Table 4.1). This experiment was conducted with the goal of determining how an FeS-coated sand would perform with respect to solids formation in what have proven to be challenging field conditions for a ZVI PRB.

6.4.1 Column results

Figure 6.20 shows the redox conditions in the FeS-Mont column were initially quite reducing, in keeping with initial results from the FeS-NO_3 column (Figure 6.7).

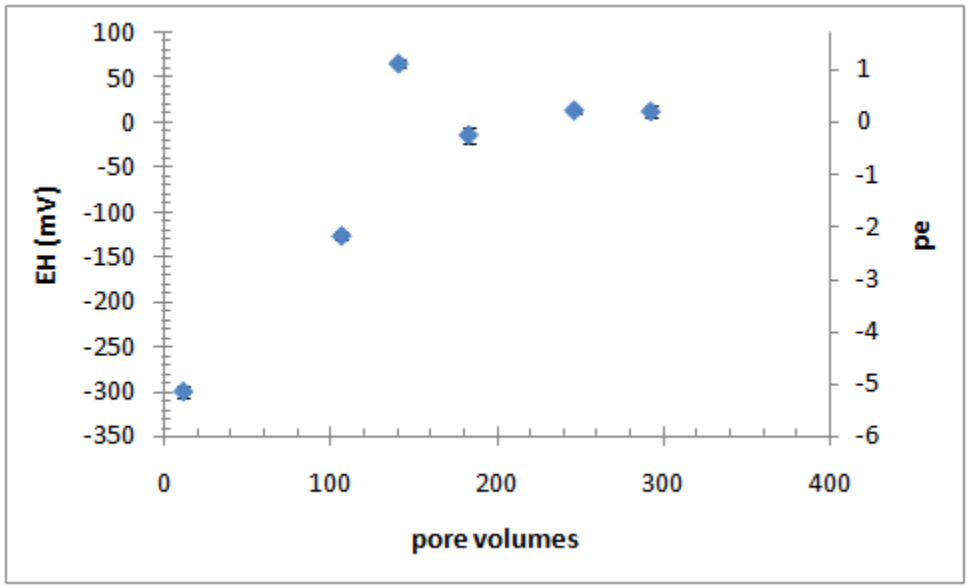

Figure 6.20: Effluent E_H in the FeS-Mont column as a function of pore volumes injected into the column.

However, Figure 6.20 also indicates a rapid increase in E_H values. This can be explained by a pump failure at 125 pore volumes that resulted in the introduction of ambient laboratory air into this column. The pump was immediately repaired, and flow continued, but this clearly affected at least a portion of this column. Figure 6.21 shows the area of the intrusion in the FeS-Mont column, with a comparison to the FeS-NO_3 column.

In the case of ZVI, the accumulation of precipitates and the production of a gas phase in the reactive media due to the presence of oxidants negatively impacted the hydraulic conductivity of the column. Therefore, although it was unplanned, the introduction of a gas phase and an oxidant (oxygen) represent a test of adverse conditions for this FeS column.

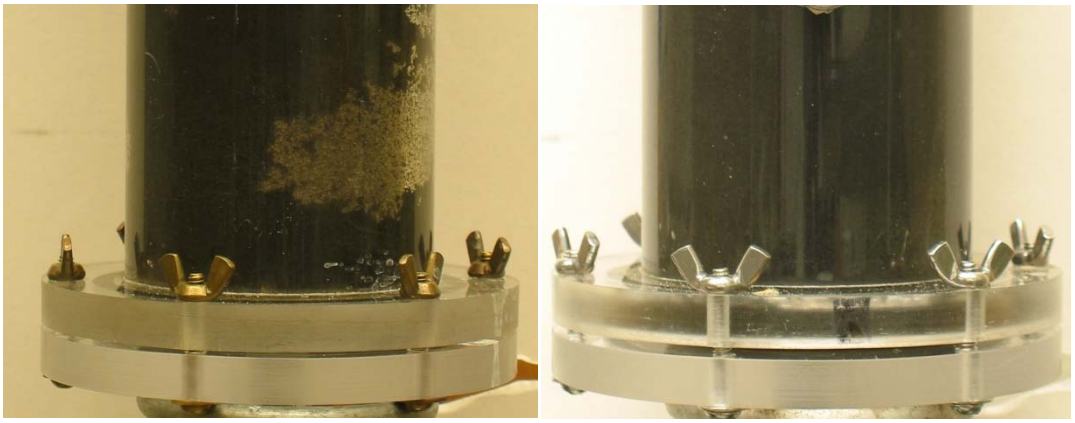

Figure 6.21: Oxygen intrusion into the influent section of the FeS-Mont column at approximately 125 pore volumes (left) as compared to the influent of the FeS-NO_3 column (right).

The area in which the oxygen appears to have had the greatest impact is visible on the right hand side of the FeS-Mont column. The color change is caused both by a change from the blackish FeS to an rust-colored (presumably) ferric phase, and by the desaturation of this portion of the column, which changes the way that solids on the interior of the column appear when viewed from the outside. This desaturation meant that a gas phase was temporarily present in the columns.

In contrast to the changes in redox potential, Figure 6.22 shows that the pump failure and oxygen intrusion do not appear to have had a significant impact on the pH. Over nearly 300 pore volumes of column operation, the pH was consistently between 6.3 and 6.5.

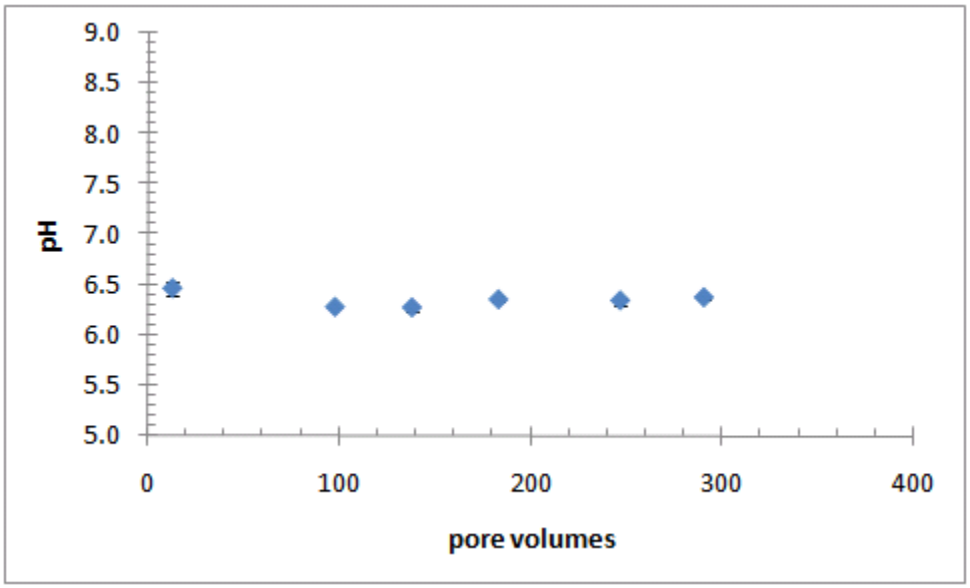

Figure 6.22: Effluent pH in the FeS-Mont column as a function of pore volumes injected into the column.

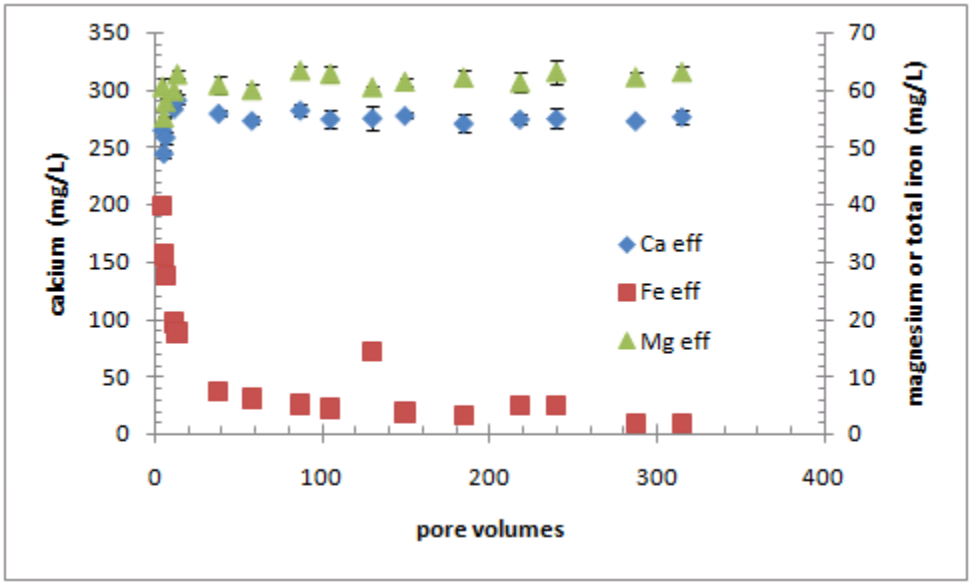

Figure 6.23: Aqueous calcium and total iron concentrations in the effluent of the FeS-Mont column as a function of pore volumes injected into the column.

Figure 6.23 shows the effluent calcium, magnesium, and total iron concentrations from the FeS-Mont column. Calcium concentrations were stable at approximately 280 mg/L, the same value as the influent concentration, which indicates that no calcium was retained in the column. Likewise, effluent magnesium was approximately 60 mg/L; with an influent concentration of 61 mg/L, these data indicate that no magnesium was being retained in the column. Effluent total iron values showed, during the first 100 pore volumes, a rapid decay to a stable value for the remainder of the experiment, again with the exception of the high iron value measured at the time of the oxygen intrusion. The average iron concentration between 150 pore volumes and the end of the experiment was 3.4, although the final two measurements were 1.8 mg/L, which is close to the steady state iron effluent concentration at pH 5 reported by Han (2009). The behavior of calcium and iron concentrations in the effluent of the FeS-Mont column appears to be quite similar to that of the FeS-NO_3 column, with the exception of a spike in the iron concentration associated with the oxygen intrusion.

Effluent carbonate concentrations, like those in the FeS-NO_3 column, were essentially the same as the influent carbonate values, indicating that no carbonate solids were being formed in the column. Measurements of nitrate, sulfate, and magnesium likewise showed no change from the influent to the effluent.

The pressure measured along the column is largely consistent with the deduction, based on the aqueous phase analysis, that no solids were being formed. As Figure 6.24 shows, the pressure drop along the column was largely unchanged, again with the exception of the oxygen intrusion, which desaturated portions of the column, at around 125 pore volumes.

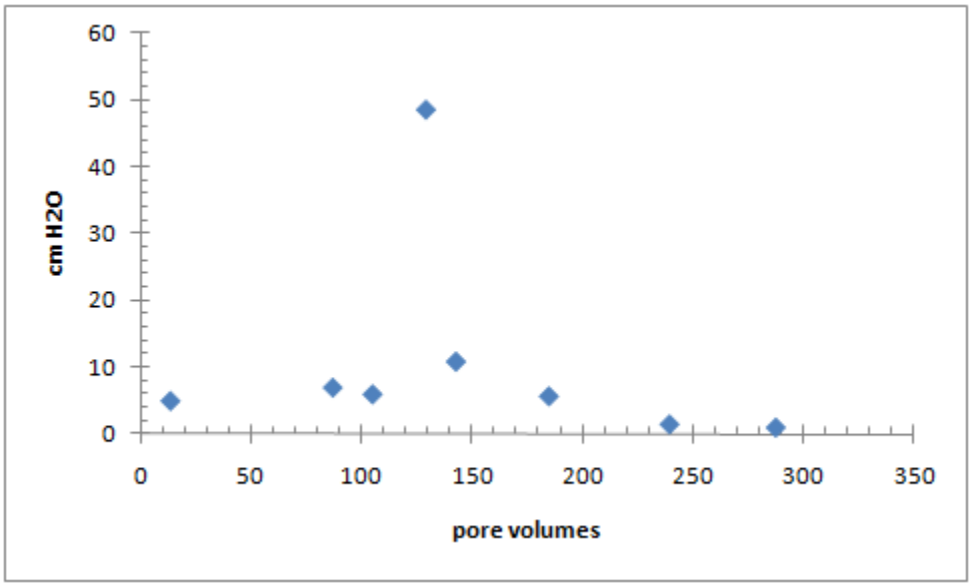

Figure 6.24: Pressure drop along the FeS-Mont column as a function of pore volumes injected into the column.

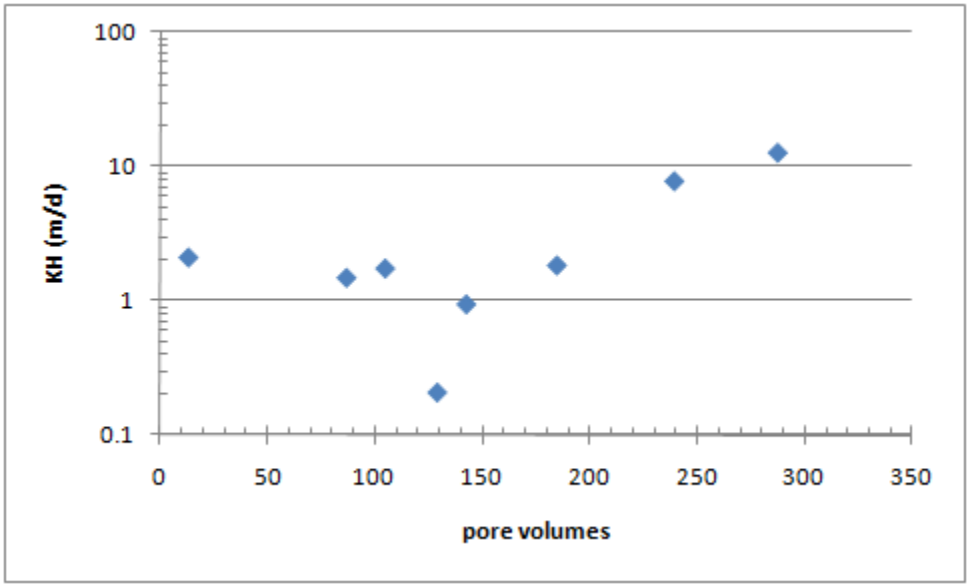

Figure 6.25: Hydraulic conductivity in the FeS-Mont column calculated from pressure drop as a function of pore volumes injected into the column.

Figure 6.25 shows the hydraulic conductivity calculated from the pressure drop along the column. These values are stable for the first 100 pore volumes, followed by a sharp decrease in hydraulic conductivity due to the pump failure and gas introduction at 125 pore volumes, followed by an apparent increase in hydraulic conductivity over time. This increase is believed to be an experimental artifact: this column was run simultaneously with the column designated ZVI-NO_3 (Section 5.4), which experienced a large increase in pressure drop along the column toward the end of its operation. This development required rearrangement of the manometers in order to connect a manometer with a large enough scale to the column designated ZVI-NO_3. While the pressure drop along the column should not change based on the measurement device, it is possible that the switching of manometers inadvertently altered the columns. If, for example some gas had been trapped in the effluent lines of the column during packing, and that gas was dislodged while switching the manometers, an apparent increase in hydraulic conductivity would be observed.

The timing of the change in hydraulic conductivity at the later stages of the FeS-Mont column suggests that the inadvertent disruption to the system caused by switching manometers is a likely explanation for the apparent increase. This experimental issue aside, it is reasonable to assume that the FeS-Mont column was not experiencing changes in hydraulic conductivity due to the accumulation of solids or gas.

6.4.2 Solids Analysis

In order to conduct SEM and XPS analyses of samples from this column, the column was destructively sampled at the conclusion of the experiment.

6.4.2.1 SEM

Microscopy of influent and effluent grains from the FeS-Mont column suggest that solids accumulation in this column was not appreciable, corroborating findings from the aqueous phase analysis. However, the influent section of this column did show evidence of some non-crystalline covering. A grain from the influent end of this column is shown

in Figure 6.26, and a grain from the effluent end of this column is shown in Figure 6.27, with a detailed view shown in Figure 6.28. Comparing these figures, it is clear that there is no significant accumulation of solids on the surfaces.

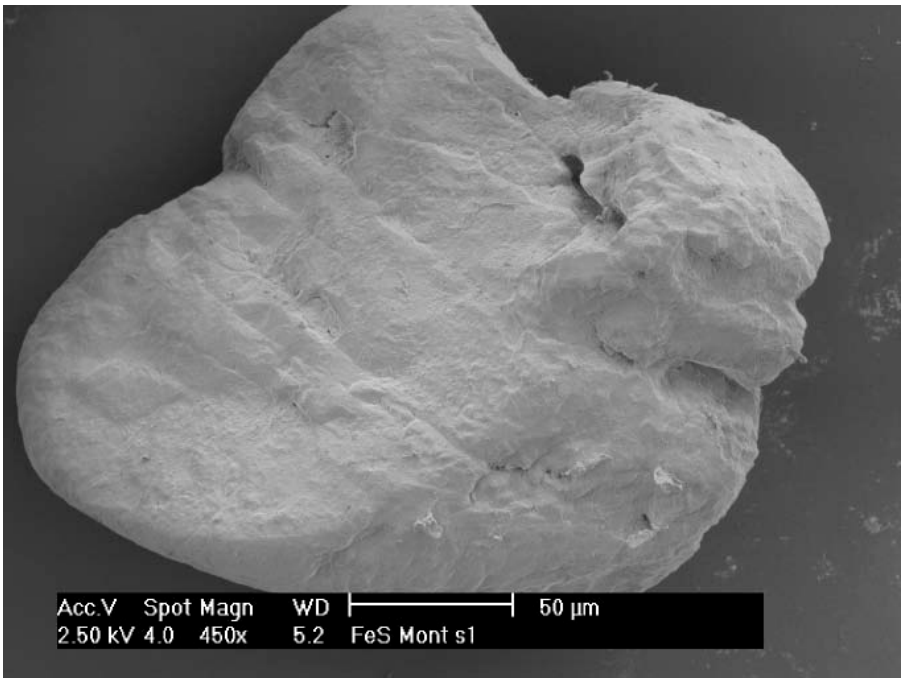

Figure 6.26: Grain of FeS-coated sand from the influent section of the FeS-Mont column.

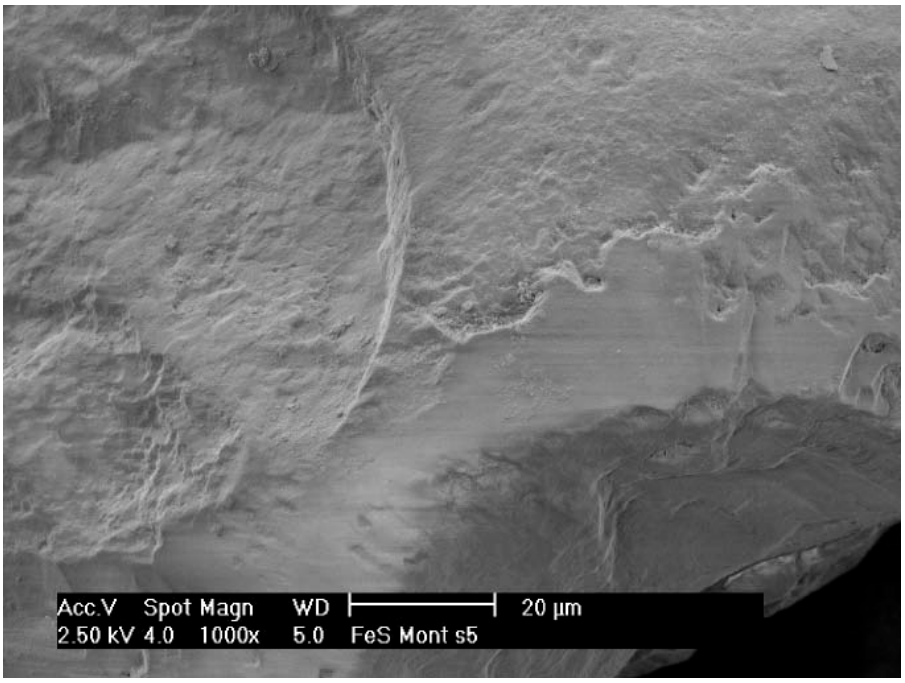

Figure 6.27: SEM micrograph of sample from the effluent section of the FeS-Mont column.

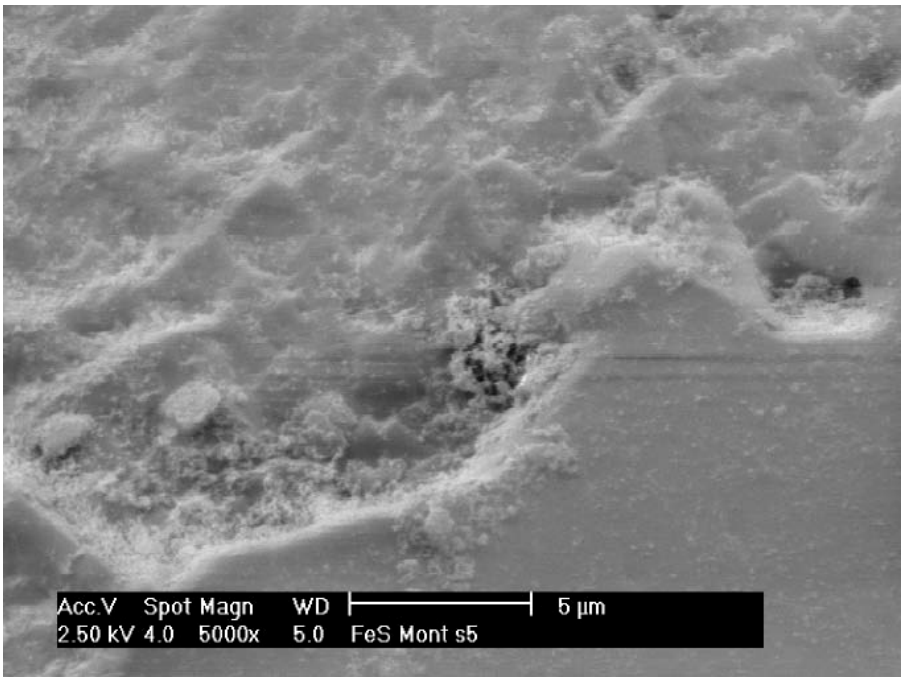

Figure 6.28: Closer view of smooth and rough areas in surface of sample from the effluent of the FeS-Mont column.

The SEM micrographs of effluent samples from the FeS-Mont column (Figures 6.27 and 6.28) are quite similar to those obtained for the FeS-NO_3 column (Figure 6.14), as well as for freshly prepared FeS-coated sand (Figure 4.2). The surface is generally smooth, with some sections being smoother than others; in those areas with irregularities, the scale of the topography appears to be less than 2 µm.

Overall, the surfaces of grains of FeS-coated sand from the FeS-Mont column indicate that no significant solids accumulated on the reactive media.

6.4.2.2 XPS

Figure 6.29 shows the $Fe2p_{(3/2)}$ peak of a sample from the influent section of the FeS-Mont column. This peak shows a composition of a predominantly Fe(III)-bonded surface. In contrast, the FeS-NO_3 column influent and effluent samples (Figures 6.15 and 6.17) and the FeS-coated sand (Figure 6.16) showed a mix of Fe(II) and Fe(III) bonds. When this peak is decomposed into individual contributions, the Fe(III)-O bond accounts for 84% (± 2.0%) of the peak area, with the Fe(III)-S bond accounting for the remainder.

This indication of oxidation in the influent section of the column is consistent with the observation of the intrusion of ambient air into this section of the column.

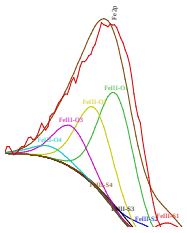

Figure 6.29: Decomposition of Fe2p $_{(3/2)}$ peak of a sample of FeS-coated sand from influent section of FeS-Mont column.

The peak deconvolution for an effluent sample is shown below in Figure 6.30. In this peak, the Fe(II)-S peak accounts for 34% (± 2.6%) of the total peak area, the Fe(II)-O peak contributes 12% (± 2.3), and the Fe(III)-S and Fe(III)-O peaks add 29% (± 2.9%) and 25% (± 2.6%), respectively. This is a distribution of component peaks similar to that measured for FeS-coated sand (Figure 6.16) and the FeS-NO_3 column (Figures 6.15 and 6.17). This distribution stands in contrast to the influent $Fe2p_{(3/2)}$ peak presented in Figure 6.29, which is dominated by Fe(III)-O bonds. In Figure 6.30, the lack of a clear shift in valency relative to the original FeS-coated sand suggests that the interaction between the solid phase and the aqueous phase in the system did not significantly alter the oxidation state of the iron.

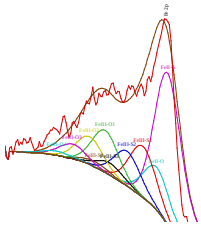

Figure 6.30: Decomposition of Fe2p $_{(3/2)}$ peak of a sample from the effluent section of the FeS-Mont column.

XPS analysis of solid samples from the FeS-Mont column corroborates observations made about the intrusion of oxygen to the column, as well as about the minimal reaction between the aqueous phase and solid phase. The former is indicated by shift in peak composition of the influent samples, and the latter is indicated by the similarity of peak composition between this column and unreacted FeS-coated sand (Figure 6.16).

6.4.3 Modeling

The FeS-Mont system, like the FeS-NO_3 system (Section 6.3.3), received an influent solution with oxidants that would require biological mediation to oxidize FeS. The model of this system allows this oxidation in an effort to assess a worst-case scenario in the field. Figure 6.31 shows the pH and pe of the modeled FeS-Mont system. The pH is relatively stable until enough FeS (0.9 mM, as shown in Section 6.3.3) is added to

completely reduce nitrate, switching the controlling redox couple, similar to the behavior in the FeS-NO_3 system.

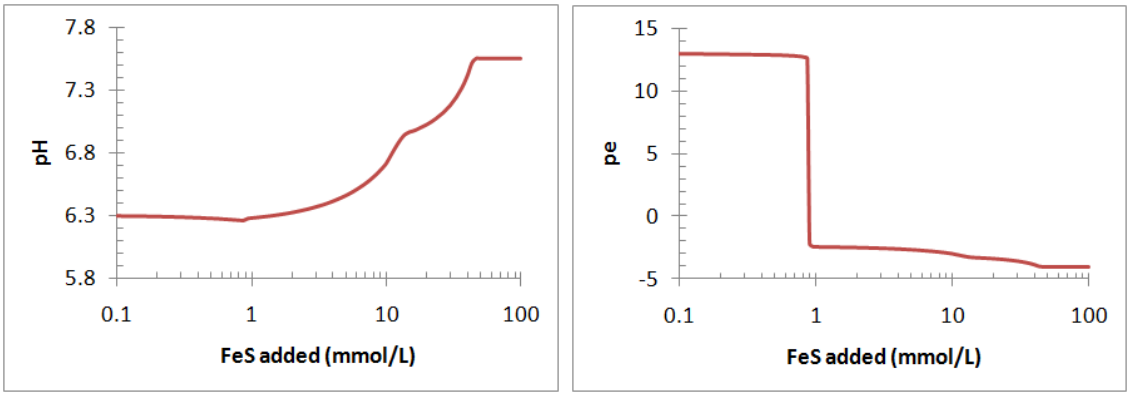

Figure 6.31: Equilibrium pH (left) and pe (right) for the model of FeS-Mont system.

The calculated pH in this system plateaus at 7.5, corresponding to an addition of 80 mM FeS or greater. This represents an increase of 1 pH unit over the maximum pH in the FeS-NO_3 system (Figure 6.18). This change can be attributed to the reduction of sulfate to sulfide (Table 2.3), which is possible because the sulfate in this system (1170 mg/L, or 12.2 mM) constitutes an additional supply of oxidant. This system therefore has the highest equilibrium pH values obtained in the modeling of the FeS systems. Figure 6.32 shows that this pH increase leads to the oversaturation of some carbonate solids, which begin to precipitate. Note that the analysis of the aqueous phase of this column did not indicate that magnesium was being removed (Figure 6.23), as would be required for the precipitation of dolomite.

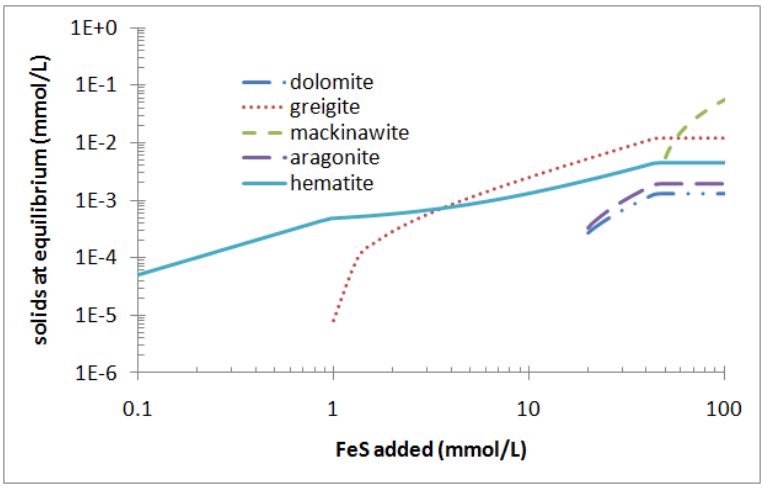

Figure 6.32: Calculated equilibrium solids formation in the FeS-Mont system.

In Figure 6.32, there is a connection between the dominant solids and the pe-pH regime observed in Figure 6.31. At low values of FeS addition, the FeS is unstable and is converted to the ferric solid hematite; once the pe shifts (at approximately 0.9 mM FeS), the mixed valency greigite becomes the end phase. Once the pH is high enough to produce an oversaturation of carbonate solids, dolomite and aragonite begin to precipitate. Finally, once an equilibrium is reached between the reducing power of the FeS and the sulfate/sulfide and nitrogen/ammonia couples, at approximately 50 mM FeS addition, then FeS remains in solution and becomes the dominant solid.

It is the formation of carbonate solids, which represent the addition of significant mass, rather than simply the transformation from FeS to greigite (Fe_3S_4), that contributes to appreciable new solids mass in the equilibrium model of the FeS-Mont system. Figure 6.33 shows the calculated reduction in hydraulic conductivity as a function of the amount of FeS added. This modeling result suggests that this mass and the accompanying porosity loss correspond to a small hydraulic conductivity loss.

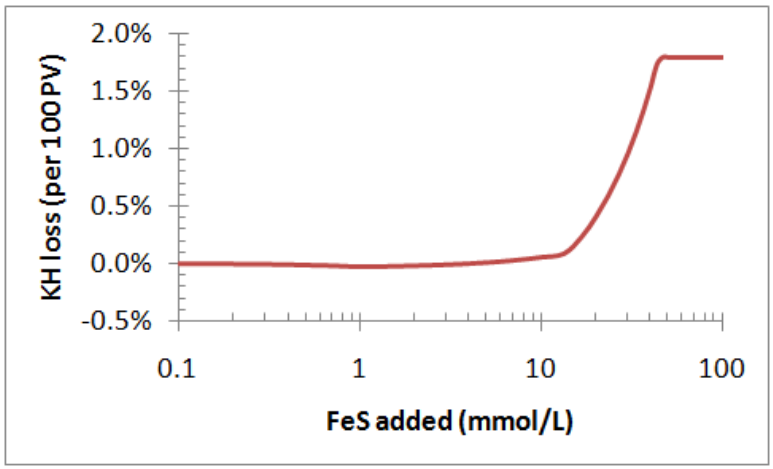

Figure 6.33: K_H loss predicted for equilibrium model of the FeS-Mont system.

The hydraulic conductivity loss shown in Figure 6.33 has two important features: first, there is no hydraulic conductivity loss for FeS additions less than approximately 10 mM. Up until this point, no carbonate solids precipitate. Once they begin to precipitate, the hydraulic conductivity loss plateaus once all available calcium (7 mM), carbonate (7 mM), and magnesium (2.8 mM) have been removed from solution. Secondly, the

maximum hydraulic conductivity loss is about 2%, which is small relative to the hydraulic conductivity loss predicted and observed in the ZVI systems.

This equilibrium modeling suggests the major player for hydraulic conductivity loss in FeS systems is the precipitation of solids that do not contain iron. Because the density of FeS is in the same range as the density of other iron sulfide and iron oxide phases (see Table 4.5), a transition of FeS to these phases will not result in a large increase in solids volume.

6.5 Summary

Figure 6.34 shows that, regardless of the influent solution, the effluent pH of the FeS-coated sand columns is generally less than 6.5. This effluent pH represents a pH increase of less than 0.5 pH units. The effluent E_H measurements taken from the FeS columns indicate that reducing conditions were created, at least initially. The FeS-NO_3 (Section 6.3.1) and FeS-Mont (Section 6.4.1) columns had higher E_H values towards the end of their operation, but problems with the experimental setup appear to have been part of the cause for these increased values. However, the experimental issues encountered with the FeS column systems do not detract from the preponderance of evidence: that the FeS system shows less pH increase, solids production, and gas production than does the ZVI system.

Given the pH values measured in the effluent of the columns, carbonate-bearing compounds remained undersatured and thus did not precipitate. Figure 6.35 shows the hydraulic conductivity measured in the FeS columns as a function of pore volumes of flow. While there is some variation in each column's data, there are no apparent trends. This indicates that solids accumulation was not occurring to an extent sufficient to impact the hydraulic conductivity of the columns. Furthermore, the lack of gas bubbles observed in the columns and lack of gas collected in the column effluent lines indicates that no gases reached a sufficiently high partial pressure to form bubbles within the porous matrix, consistent with the results of the geochemical modeling.

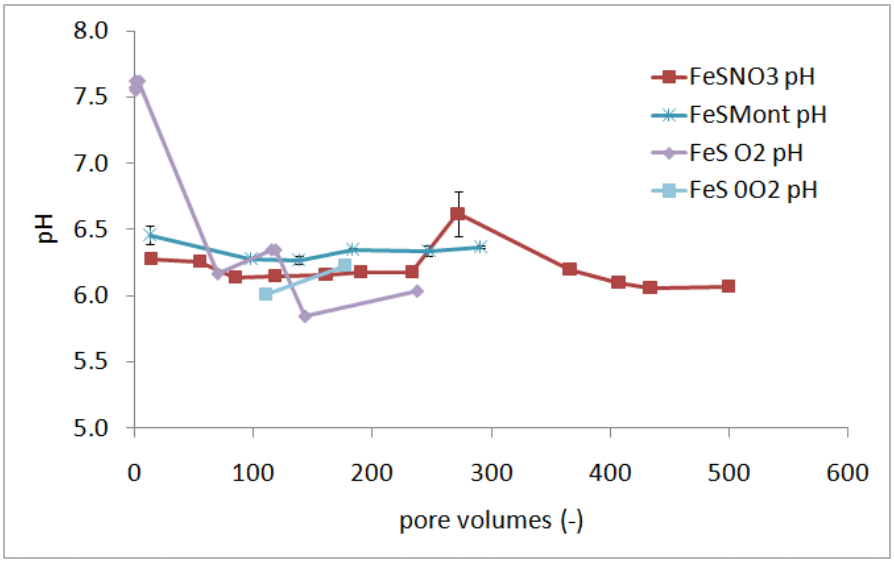

Figure 6.34: Comparison of effluent pH measurements in FeS columns as a function of pore volume (summarizes data presented in Figures 6.4, 6.8, and 6.22).

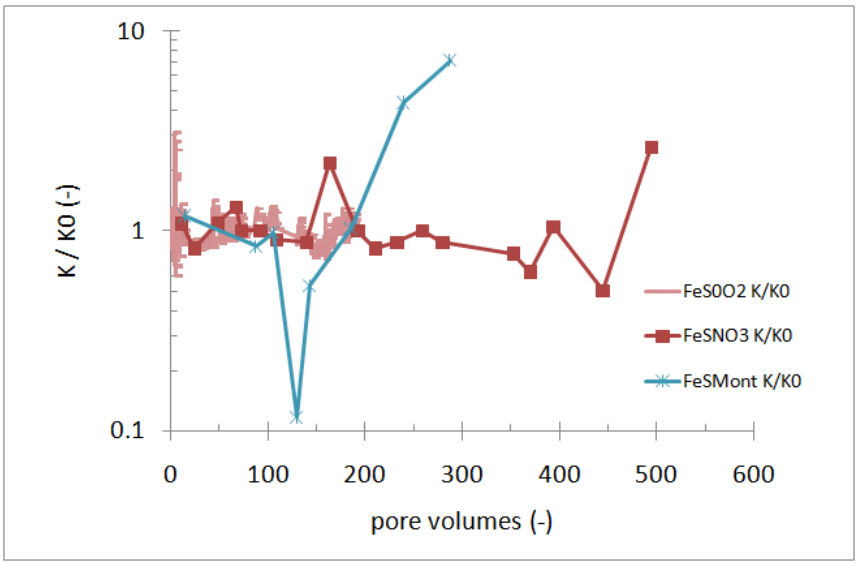

Figure 6.35: Comparison of hydraulic conductivity measurements in FeS columns (summarizes data presented in Figures 6.2, 6.11, and 6.25).

Spectroscopic analysis of samples from the influent and effluent sections of selected columns indicates that the redox state of the iron present in the surfaces of the sample did not change appreciably from its initial condition. One exception to this observation is the FeS-Mont influent sample, which was largely oxidized, due to oxygen intrusion during the operation of the column. The binding energies of the $Fe2p_{(3/2)}$ peaks from these samples are summarized in Table 6.2.

Table 6.2: $Fe2p_{(3/2)}$ peak center values for FeS column samples

Sample	$Fe2p_{(3/2)}$ peak center (eV)
Unused FeS-coated sand	707.4
FeS-NO_3 influent	707.0
FeS-NO_3 effluent	707.0
FeS-Mont influent	711.0
FeS-Mont effluent	706.8

Indeed, with the exception of the FeS-Mont influent, all of the peak centers for the $Fe2p_{(3/2)}$ peaks are lower than that of the FeS-coated sand, indicating that exposure to the influent solutions in these columns did not oxidize the surface iron appreciably. Given that microbial communities that could mediate the oxidation of FeS by the nitrate and sulfate in the influent solutions were not expected to be present in these columns, this result is expected.

Batch, equilibrium geochemical modeling of the FeS column systems also provided evidence that pH increase, solids accumulation, and a concomitant reduction in hydraulic conductivity are not expected to be significant in an FeS system with high calcium and carbonate concentrations. This finding was true even for systems in which it was assumed that high nitrate or sulfate concentrations were reduced. Figure 6.36 summarizes pH and pe behavior for the FeS systems. Designated $0O_2$, O_2, NO_3, and Mont, these systems correspond to increasing amounts of potential oxidants.

The oxidants in this system provide the potential for pH increase, but this occurs only when the FeS concentration is sufficient to reduce these species. For nitrate, this reduction would occur in a real system only if there were biological mediation of this reduction. These models have allowed this reduction in order to make a conservative estimate for the potential for solids formation. Before that point, the pe of the system is high, as the controlling redox couple contains an oxidized species such as O_2 or NO_3^-. In these models, once a stoichiometric amount of FeS was added to the system, the reducing power of FeS was sufficient to completely reduce 8 mg/L of O_2 and 100 mg/L of NO_3^- to

N_2(g). At the levels of FeS considered here, there was not sufficient reducing power to completely convert all N to NH_3.

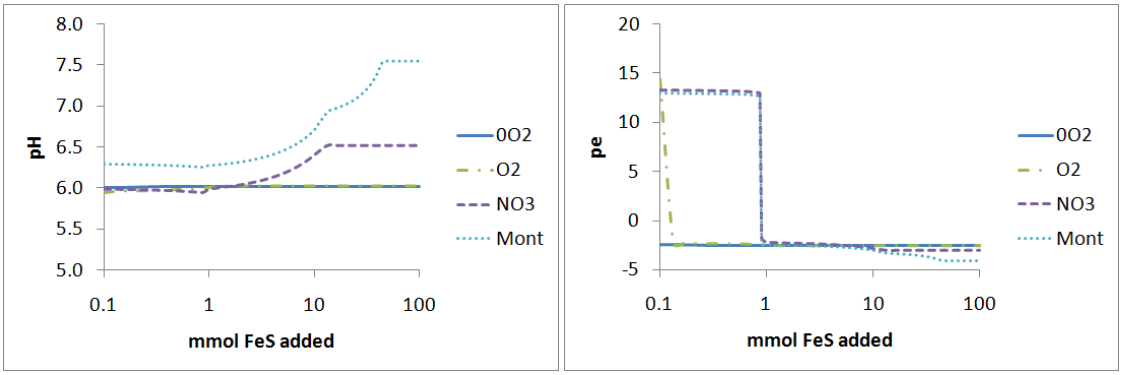

Figure 6.36: Comparison of pH (left) and pe (right) predicted in equilibrium models of FeS systems (summarizes data presented in Figures 6.3, 6.18, and 6.31).

Because of the moderate pH increases observed in most systems, the model predicted minimal precipitation of carbonate-bearing solids. There was, however, conversion of FeS to hematite (in oxidizing conditions) and to greigite in moderately reducing conditions. The presence of these ferric and ferric/ferrous solids is supported by XPS analysis of the $Fe2p_{(3/2)}$ peaks from the FeS-NO_3 and FeS-Mont columns, which showed evidence of both Fe(II) and Fe(III) bonds. These solids do not lead to an appreciable increase in solids volume: even though hematite requires the incorporation of new mass, its density is higher than that of FeS, and greigite does not represent the addition of new mass.

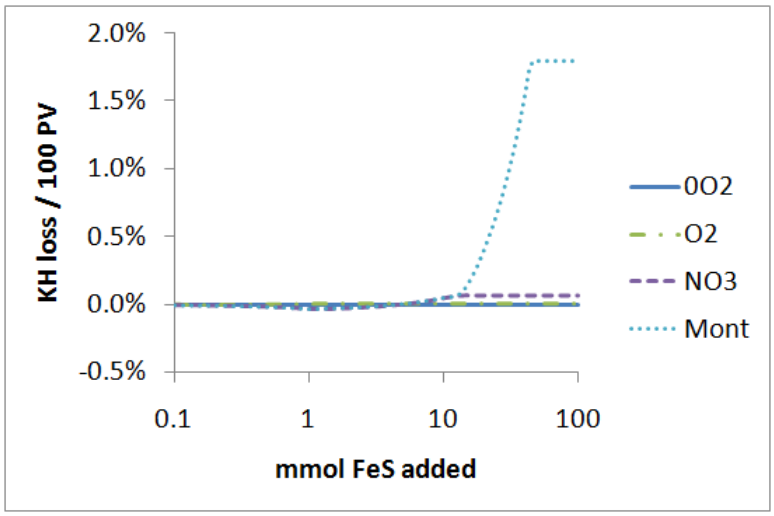

Figure 6.37: Comparison of model predictions for K_H loss is FeS systems (data for FeS-Mont are repeated from Figure 6.33).

Figure 6.37 shows the effect of solids formation on the hydraulic conductivity of FeS systems. Clearly, the precipitation of new solids is only of concern in the FeS-Mont column, and then only if the reduction of sulfate is biologically-mediated. At FeS concentrations above 10 mM, the pH increase in the FeS-Mont system is sufficient to oversaturate carbonate-bearing compounds. However, the precipitation of such compounds is expected to cause, at most, a 1.8% loss in hydraulic conductivity over 100 pore volumes of operation. As shown in column experiments and geochemical modeling, the prospect for precipitation or gas production in FeS-based systems is minimal. This lack of permeability loss is, from a hydraulic point of view, a strong recommendation for FeS as a reactive material in subsurface applications.

Chapter 7: Comparison of Potential for Solids Formation in ZVI and FeS Systems

The ZVI and FeS systems studied in this work share some basic properties: they are reduced iron media with the capability to remove contaminants from groundwater and the potential to interact with background solutes. If such solutes form solid phases, they may reduce the hydraulic conductivity of the media or inhibit the media from interacting with the aqueous phase, either of which may adversely affect the long-term performance of the PRB.

However, these reactive media are fundamentally different. Considering their physical properties, ZVI is a dense, angular, granular material, while FeS is less dense and, in the research presented here, has been coated onto a natural silica sand whose grains are generally spherical. As a result of this difference, the porosity of the columns packed with ZVI is about twice that the columns packed with FeS-coated sand. This porosity difference has implications for the total amount of solids that could be formed before complete plugging occurs; however, other system differences may be more critical in determining the extent to which plugging occurs.

As a result of the fact that FeS was coated onto sands before being packed into columns, another critical system difference is the total mass of ZVI or FeS present in a column. Considering the amount of reactant mass, a ZVI column has three orders of magnitude more mass than does an FeS-coated sand column. Per cubic centimeter of packed media in the column, the ZVI in these columns is present at approximately 2,600 mg ZVI / cm^3, as compared to 2.3 mg FeS / cm^3. On a molar basis, this is 47 mmol ZVI / cm^3 and 0.026 mmol FeS / cm^3.

However, comparing the ZVI and FeS columns based on the total mass of reactive material in a column is only one metric by which to compare these systems. A more

thorough consideration of the system suggests it is important to consider the fraction of reactive material accessible to the aqueous phase. In the case of FeS-coated sands, the thickness of the FeS layer is expected to be approximately 1 nm, based on the average amount of FeS coated onto the sands and assuming a uniform coating thickness. Therefore, it can be assumed that all of the FeS present is accessible to the aqueous phase. For ZVI, however, it is not likely the case that all emplaced ZVI is accessible to the aqueous phase. SEM micrographs of sectioned ZVI column samples were presented in Chapter 5; the focus of these micrographs was the region of the aqueous-solid interface. Figure 7.1 shows such a sample taken from the influent of the ZVI-2O_2 column.

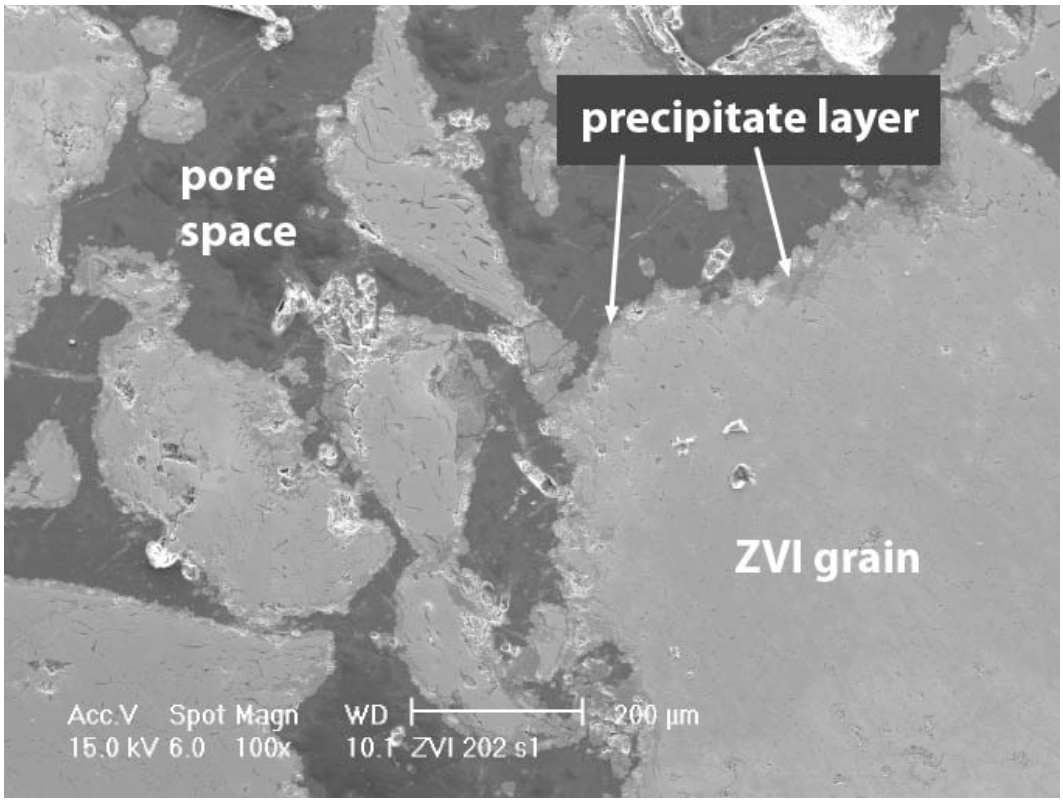

Figure 7.1 View of multiple ZVI grains from the influent section of the column designated ZVI-2O_2.

In Figure 7.1, each ZVI grain is ringed with a layer of precipitates, ranging in thickness from approximately 10 to 50 µm, which are a slightly darker gray. Viewed at this scale, it is clear that the centers of the ZVI grains have not interacted with the aqueous phase. Thus, the total mass of ZVI is not an accurate measure of the accessible mass of ZVI. In

the absence of quantitative information about the accessible ZVI mass, the calculations that follow have estimated accessible fractions of 1, 0.5, and 0.1. Because the calculated FeS thickness is on the order of 1 nm, it is assumed that all of the FeS is accessible to the aqueous phase.

However, a mass or molar basis is not the only metric by which reactive media may be compared. Surface area may be a crucial property, especially with respect to removal of contaminants. Table 2.2 summarizes the range of specific surface areas reported for ZVI from different vendors and used in both laboratory and field studies. In Table 2.2, the specific surface areas for ZVI generally range between 1 and 2 m^2/g; one measurement of Peerless ZVI (the ZVI used in this study) had an upper bound close to 3 m^2/g. In comparison, FeS has a much higher specific surface area. Jeong et al. (2008) reported a specific surface area of 424 ± 130 m^2/g for FeS synthesized according to the procedure described in this research. Therefore, the specific surface area of FeS appears to be at least two orders of magnitude greater than that of ZVI.

A more sophisticated comparison of ZVI and FeS-coated sand systems is possible based on a combination of factors: the fraction of ZVI that is accessible for interactions with aqueous phase and on reported specific surface area values. Table 7.1 presents calculations based on the columns using these considerations that compare total ZVI and FeS surface areas based on a range of accessible fractions of ZVI (1 to 0.1).

Table 7.1: Comparison of total surface areas for ZVI and FeS columns, based on ranges of accessible mass for ZVI and specific surface areas for FeS (Jeong et al. 2008).

Parameter	ZVI			FeS
mass in column (g)	1300			1.12
accessible fraction	1	0.5	0.1	1
accessible mass (g)	1300	650	130	1.12
specific surface area (m^2/g)	2	2	2	425
accessible area (m^2)	2600	1300	260	476

As noted above, determining what fraction of ZVI is available is not quantitatively possible based on the techniques used in this study. However, a qualitative estimation based on Figure 7.1 suggests that 50 or 10% are not unreasonable. FeS is expected to

have a total surface area of 476 m^2. In comparison, assuming 10% of ZVI is accessible for interaction with the aqueous phase, the total surface area of the ZVI system is approximately half of the FeS value.

Since reactions controlled by surface area were not the focus of this study, it should be emphasized that the "accessible mass" row of Table 7.1 is the most straightforward point of comparison. Based on the assumption of 10% of ZVI being available for interaction with the aqueous phase and 100% of the FeS being available, there would be two orders of magnitude more ZVI mass than FeS mass in the column systems in this study. However, if surface area were a controlling factor for contaminant removal, then a ZVI and an FeS system designed to have the same treatment capacity could have differences in mass similar to those in this study. This difference does not make comparison of these column results impossible; rather, it indicates that direct comparisons between the ZVI and FeS columns should be made cautiously. However, the column results, in concert with theory and modeling, can provide insight into expected differences between the two systems

Thermodynamic considerations provide a key insight in this respect: even if equal amounts of the reactive media were present and accessible to the aqueous phase, it would be expected that the change in the ZVI columns would be greater than that in the FeS columns. This observation is based on the fact that, at equilibrium, ZVI is not stable in water; FeS, on the other hand can be. Figure 7.2 shows a pe-pH diagram for the iron-carbonate system, in which $Fe_T = 1x10^{-5}$ M and $CO_{3T} = 1x10^{-3}$M. Overlaid on this diagram is the stability region of FeS (in grey) from an iron-sulfur diagram in which $S_T = 1x10^{-3}$ M and $CO_{3T} = 1x10^{-3}$ M.

Because the region of FeS stability was prepared assuming different solution conditions, the diagram should not be taken to indicate that both FeS and $FeCO_3$ are predicted to coexist at present at a certain pe-pH combination. However, this diagram does indicate that there are regions in which FeS is stable in water. In contrast, ZVI is consistently below the $H_2O - H_2(g)$ stability line. Therefore, the driving force for dissolution of ZVI in water is greater than the driving force for dissolution of FeS in water. Furthermore,

Equation 2.5 shows that for every mole of ZVI oxidized to Fe^{2+} by water, 2 moles of OH^- are generated. In contrast, for every mole of FeS that dissolved according to Equation 2.7, only one mole of H^+ is consumed.

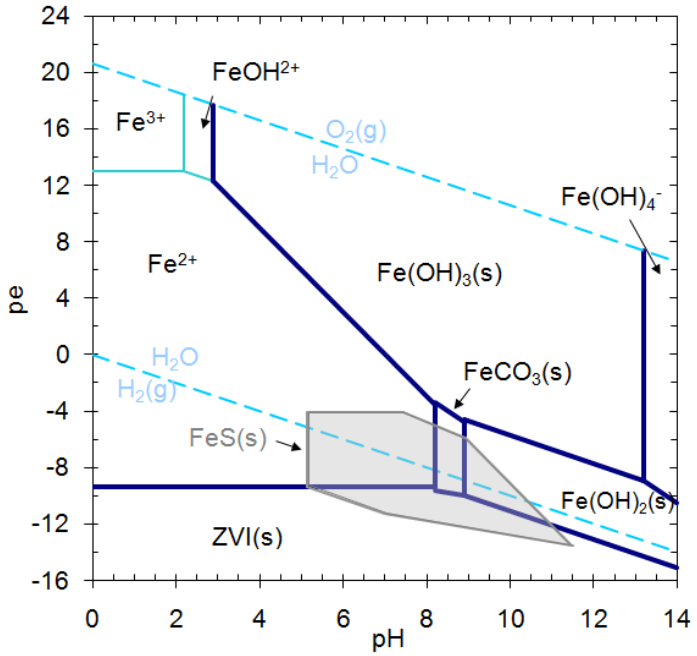

Figure 7.2: Stability diagram for Fe and CO_3 system with overlay of FeS stability: $Fe_T = 1x10^{-5}$, CO_{3T} = 1x10-3, ST = 1x10-3. Log K values for equilibrium reactions are from Stumm and Morgan (1996).

Thus, assuming reducing conditions (i.e., not allowing for the oxidation of S^{2-}), this stoichiometric difference indicates that, even if equal amounts of ZVI and FeS were present *and* equal amounts were dissolved to produce equal numbers of Fe^{2+} cations, the pH change would be expected to be greater in the ZVI system.

7.1 Comparison of aqueous results

As argued above, for equal amounts of reactive material, a greater pH increase is expected with ZVI than with FeS. In the columns in this study, the total molar amount of FeS was two to three orders of magnitude smaller than amount of ZVI. Therefore, pH increases are expected in the ZVI columns, while any pH change in the FeS columns is expected to be minimal. Figure 7.3 shows a comparison of the effluent pH values measured in the ZVI and FeS columns.

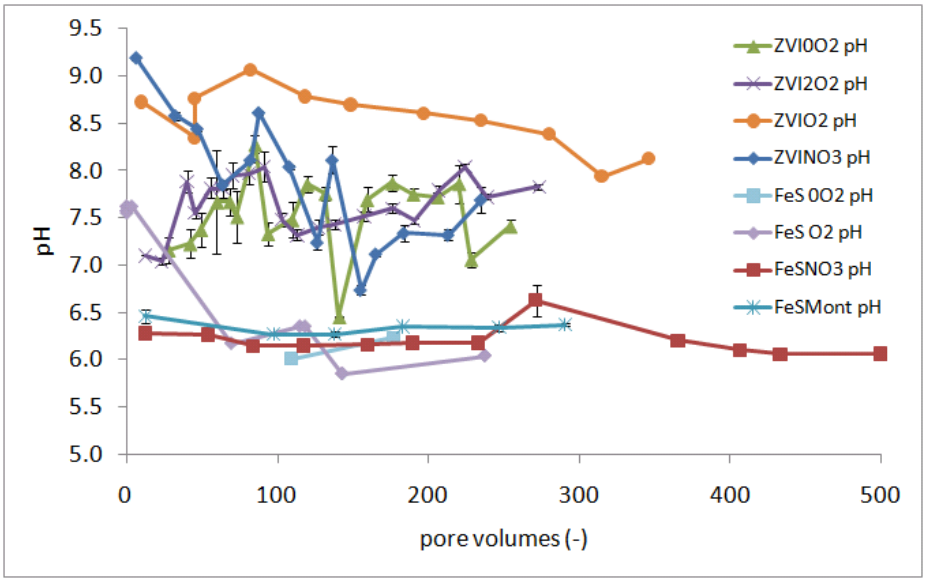

Figure 7.3: Comparison of measured effluent pH values for ZVI and FeS columns (summarizes data presented in Figures 5.2, 5.24, 5.39, 5.50, 6.4, 6.8, and 6.22).

In Figure 7.3, effluents values of pH from FeS columns are consistently between 6 and 6.5. In contrast, the ZVI effluent pH values are all higher than the FeS effluent pH values. The amount of oxidant in the system affects the effluent pH for ZVI and does not appear to do so for FeS. This finding is consistent with the model predictions.

With the exception of the columns designated ZVI or FeS-O_2, which received oxygenated water with no additional solutes, the influent solutions to these columns carried 7 mM each of calcium and carbonate. Therefore, the pH increase in the ZVI column will shift the speciation of bicarbonate to carbonate, thus moving $CaCO_3$(s), and other solids to a condition of super-saturation, enabling them to precipitate. All ZVI columns that received calcium and carbonate in the influent showed removal of those species. This removal indicated that $CaCO_3$(s), as well as other iron carbonate solids, may have been precipitating. In contrast, the FeS columns did not show any removal of calcium or carbonate, and thus there was no aqueous phase evidence for the precipitation of carbonate solids.

7.2 Comparison of solids analyses

SEM micrographs of grains of reactive media taken from the columns at the completion of the experiments support the hypothesis that calcium and carbonate were precipitating in the ZVI columns, but not in the FeS columns. The ZVI columns had a surface coating of two distinct types of precipitates: discrete columnar crystals of aragonite and a surface coating of iron (hydr)oxides (e.g., Figure 5.8). In contrast, there were no solids observed in the FeS system (e.g., Figure 6.13) that were comparable in quantity or morphology to those in the ZVI system.

XPS analysis of iron sulfide system samples indicated that the some of the oxidants introduced to the FeS systems, nitrate and sulfate, did not appreciably affect the mix of ferrous and ferric species in the iron sulfide. In the absence of biological mediation, this result is not surprising. Although XPS analysis of the FeS column that received oxygenated water was not possible, samples from the influent section of the FeS-Mont column provided evidence about the effects of oxygen on the FeS coating. Oxygen was inadvertently introduced to the column due to a pump failure, and this oxygen visibly changed the color of the grains and shifted the $Fe2p_{(3/2)}$ peak composition strongly towards Fe(III)-O bonds, suggesting oxidation of the FeS surface.

7.3 Comparison of hydraulic changes

Very clear differences were observed in hydraulic behavior of the ZVI and FeS systems. Figure 7.4 shows the ratio of measured to initial hydraulic conductivity of ZVI and FeS columns. The scatter in the data for the ZVI systems is likely due to the passage of gas bubbles through the lines that connected to the manometer.

Figure 7.4 indicates that none of the FeS columns show, on the whole, an appreciable change in hydraulic conductivity. The ZVI columns, on the other hand, are split into three groups. The ZVI-$0O_2$ column shows a large degree of scatter, but generally appears to have lost less than one order magnitude of hydraulic conductivity over the first 200 pore volumes.

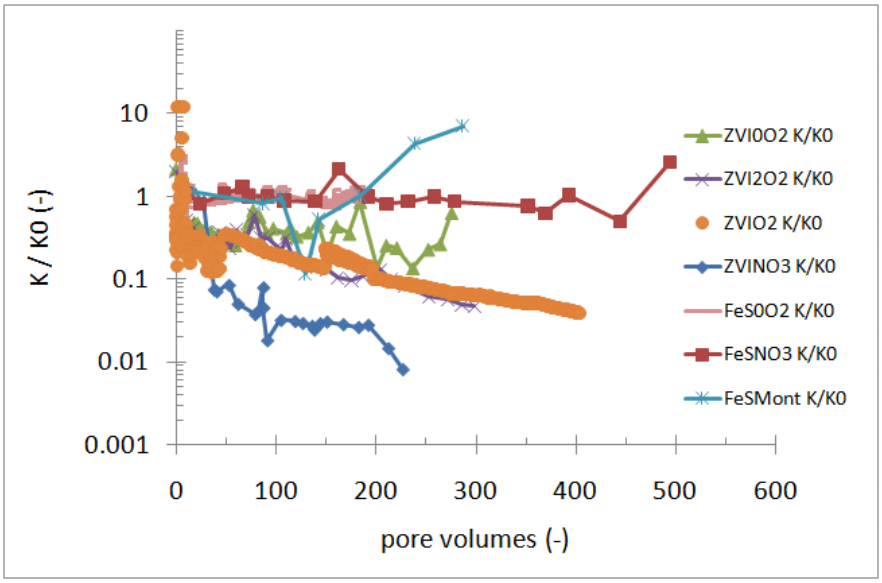

Figure 7.4: Comparison of hydraulic conductivity in ZVI and FeS column systems (summarizes data presented in Figures 5.5, 5.26, 5.41, 5.53, 6.2, 6.11, and 6.25).

The columns receiving 2 and 8 mg/L of O_2, designated ZVI-2O_2 and ZVI-O_2, track together and lost approximately one order of magnitude of hydraulic conductivity by 200 pore volumes. Finally, the column receiving 100 mg/L NO_3^-, designated ZVI-NO_3, lost approximately two orders of magnitude of hydraulic conductivity by 200 pore volumes. As noted in Chapter 5, calculations of the hydraulic conductivity loss that is expected based on changes in calcium and carbonate concentrations do not fully account for the observed losses in hydraulic conductivity. Therefore, it is hypothesized that gas generation in the columns is responsible for a large fraction of the measured permeability loss in the ZVI columns. While permeability reduction of *in situ* PRBs due to gas accumulation has not been reported in the literature, it is possible that gas has accumulated at some of the PRBs that have failed.

7.4 Comparison of geochemical modeling

Modeling of the ZVI and FeS systems provides a tool to compare experimental results for systems with different mass amounts of reactive media. Simulations assuming equilibrium is reached in batch systems, the approach used in this research, do not capture the complexity of a flowing system with possible kinetic limitations. However,

they do provide insight into the potential for solids formation, gas production, and the concomitant permeability loss in these systems. In order to make a conservative estimate, it is assumed – in the case of the FeS-NO_3 and FeS-Mont systems – that oxidation of FeS by nitrate and sulfate, which requires biological mediation, may occur.

Modeling results indicate that for equal amounts of reactive material, the pH increase and the production of solids is expected to be greater in the ZVI system than in the FeS system. Figure 7.5 shows the model predictions of pH for selected ZVI and FeS systems: those receiving a deoxygenated, 7 mM calcium and carbonate solution, with no additional oxidants (designated $0O_2$) or with 1.6 mM nitrate (designated NO_3). Figure 7.6 shows model predictions for hydraulic conductivity loss for these systems. In both figures, the changes predicted in the ZVI systems are greater than those in the FeS system. In addition, ZVI models show that the production of $H_2(g)$, if that gas is not allowed to escape the system, has severe ramifications for the calculated hydraulic conductivity. In contrast, gases are not predicted to form in the FeS system.

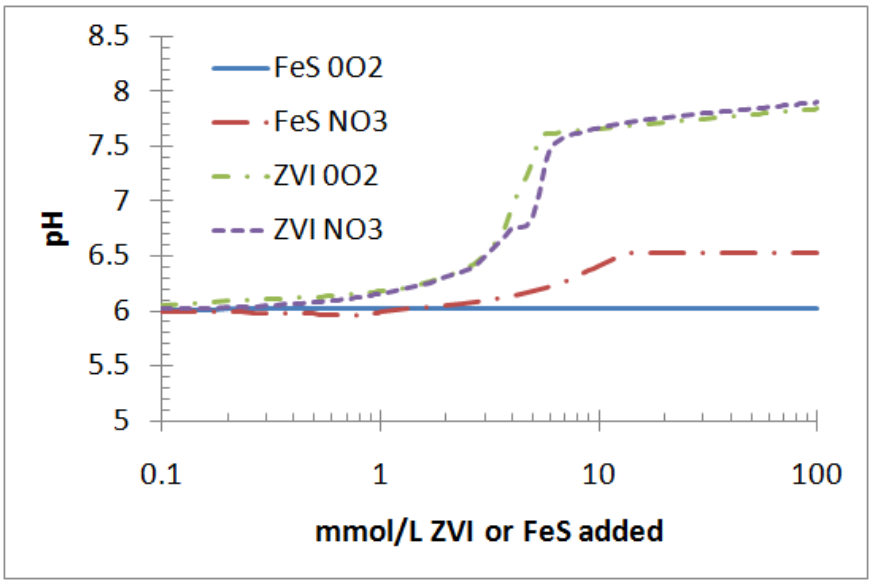

Figure 7.5: Comparison of equilibrium pH model for varying amounts of ZVI or FeS in a solution containing 7mM calcium and carbonate (summarizes data presented in Figures 5.17, 5.62, and 6.36).

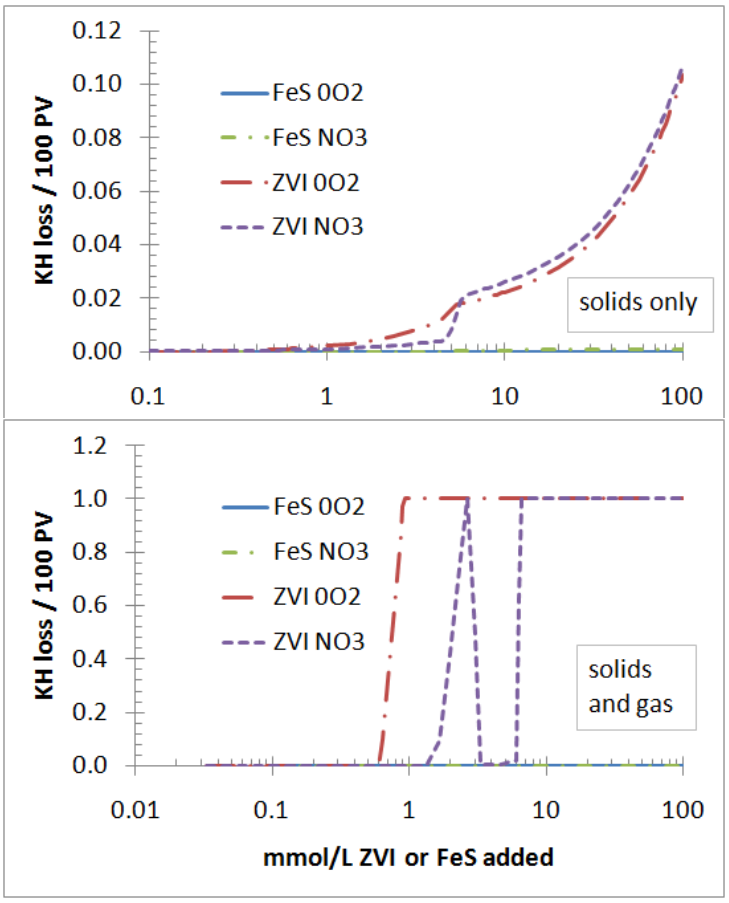

Figure 7.6: Comparison of model predictions of hydraulic conductivity loss with no gas formation (top) and with gas formation (bottom) for varying amounts of ZVI or FeS in a solution containing 7mM calcium and carbonate (summarizes data presented in Figures 5.20, 5.64, and 6.37).

In addition to considering the systems above on the basis of equal amounts of reactant, they can also be viewed on the basis of equal amounts of geochemical changes. For example, the data in Figure 7.5 indicate that it would take about 10 mM of FeS to produce a pH increase of 0.5 pH units in a system with nitrate, while approximately 3 mM of ZVI would produce the same increase in the same system. However, such a pH increase is not predicted for the FeS-$0O_2$ system, at least for the ranges of mass of FeS addition considered here. Likewise, Figure 7.6 indicates there are no amounts of FeS, in either the $0O_2$ or NO_3 systems, that can produce the hydraulic conductivity loss predicted for the $0O_2$ or NO_3 ZVI systems.

As discussed earlier, ZVI is a dense solid that is not inherently stable in aqueous systems. Therefore, an equilibrium model will predict that ZVI will dissolve, increasing the pH,

producing hydrogen gas, and re-forming as solids of lower density that incorporate species from the solution, such as hydroxide and carbonate anions.

FeS, on the other hand, can exist in the aqueous phase, and if it does dissolve and re-precipitate, the new solids formed will have a density comparable to that of FeS. Because the driving force for a pH increase is less in FeS systems than in ZVI, the potential for forming carbonate solids is reduced in the FeS system. These properties lead to a smaller net change in solids mass and volume.

Modeling work presented herein largely focused on fixing the solution composition and varying the amount of reactive material. However, for the purposes of comparison between ZVI and FeS, it is also instructive to fix the reactive media and vary solutes and the solution. Figure 7.7 presents the results for modeling of a system with 5 mM of either ZVI or FeS. The total amount of calcium and carbonate in the system is varied from 10^{-3} mM to 10 mM, a range that spans concentrations found in natural systems.

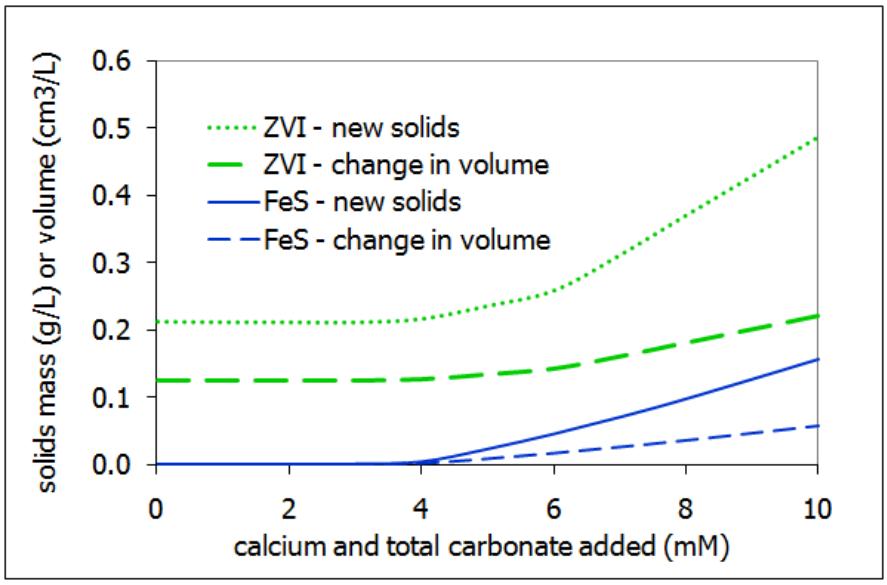

Figure 7.7: Change in solids mass and volume with 5mM addition of ZVI or FeS and varying calcium and carbonate.

The data presented in Figure 7.7 indicate that from the point of view of solids production, there are consistent differences between ZVI and FeS. First, the total amount of new solids and the net change in volume is consistently positive for ZVI, even at low levels of calcium and carbonate, due to the formation of non-carbonate, iron (hydr)oxide solids. In

contrast, FeS does not experience appreciable solids changes in this low-solute region. Once the total calcium carbonate available to the system is above 5mM, the amount of reactive material used in this model, both systems experience a net increase in the total amount of solids formed. As shown in Table 2.4, the mean value for influent calcium and total carbonate for the PRBs analyzed in Chapter 3 is approximately 6 mM. Figure 7.7 therefore suggests that high calcium and carbonate could be a problem for both systems, but the degree of the problem is expected to be more severe for ZVI than for FeS.

Chapter 8: Conclusion

8.1 Summary

A range of column experiments with granular ZVI and FeS-coated sand has indicated the potential for oxidants to lead to hydraulic conductivity loss in ZVI systems and suggested that the potential for such permeability loss in FeS systems is less. Column experiments had similar surface areas of ZVI or FeS, but the mass of ZVI was greater by two to three orders of magnitude. Nonetheless, the reservoir of FeS was not exhausted, as columns packed with FeS-coated sand remained black throughout the experiments.

ZVI is a solid phase that is thermodynamically unstable in natural redox conditions in water, while FeS is stable. Oxidants entering a ZVI system can affect the ZVI by driving the dissolution of ZVI further. This dissolution, in turn, can result in layer of precipitates forming on the ZVI. In these experiments, from a purely hydraulic conductivity standpoint, the buildup of precipitates has not proved to be as problematic as originally suspected, based on experiences reported in the literature. The solids production inferred from the aqueous phase analyses, as well as the modeling conducted on the ZVI systems, implies that the hydraulic conductivity loss observed in these columns cannot be accounted for by solids production alone. Therefore, it appears that the gas phase produced in the ZVI columns is a key player in hydraulic conductivity loss. Gas may be generated from the reduction of water to hydrogen or from the reduction of nitrate to nitrogen gas. It is these gases that may be responsible for the majority of the observed hydraulic conductivity loss in these columns systems. While gas production has not been implicated in permeability reduction of *in situ* PRBs, it is possible that gas has accumulated, due to capping or absence of microbial communities, at some of the PRBs that have failed.

FeS, while it is a metastable phase that may transform to other iron sulfide phase, is not thermodynamically unstable in aqueous systems. This means that its dissolution is driven by solubility, and that the phase can exist in an aqueous system. Therefore, the pH increase observed and predicted to occur in FeS systems is consistently less than that in ZVI systems, which indicates that solids accumulation is expected to be larger in a ZVI system than in an FeS system. Furthermore, gas generation is not expected to be an issue in FeS systems. As a result, the FeS system is expected to be free of some of the same problems observed in the ZVI system.

8.2 Future work

The research presented in this dissertation has addressed some of the hydraulic issues associated with longevity of ZVI PRBs and has provided evidence for the suitability, from a hydraulic perspective, of FeS-based materials for PRB applications. This research has investigated effects at the column scale, and it has shown that the interplay between aqueous, gas, and solid-phase chemistry is responsible for these effects. In ZVI PRBs, one of the key players in hydraulic conductivity loss appears to be the generation of gas. Therefore, one of the most productive areas for future work would involve improving the understanding the formation and impact of the gas phase. At the pore-scale, a micromodel would be a useful tool for this objective. A micromodel could provide evidence about the buildup of gases in pore spaces, and the movement of gas through a porous matrix. These experiments could be small-scale and short-term, and could involve variations in pore size distribution, oxidant level, and flow rate.

Building on knowledge about gas generation and movement at the pore scale, future column experiments should be better able to provide information about the gas phase. Various pieces of evidence could be collected and integrated, including quantitative determination of pore space at the column walls that is occupied by gases, measurements of the weight of the column with time, and collection of all gas passing out of the effluent. Information gathered from these would allow for a more thorough understanding of gas evolution and movement through the column.

Bearing in mind the field application of ZVI media, future work should also seek to identify differences in gas phase generation and transport between column and field systems. One of the key limitations of the current experimental approach is that gases are confined in the columns, whereas a field PRB is closer to an unconfined system. An experimental setup that allowed for gas transport out of the system, such as a two-dimensional model of a phreatic aquifer, could provide information about how gases may leave an actual PRB system. In such a model, two parallel plates oriented vertically could be filled with zones of sand and a zone of ZVI, to mimic a PRB. The system would not be fully saturated, but water would flow in the bottom section of the plates, allowing for interaction of ZVI with the aqueous phase, but also allowing for escape of gases out of the top of the model.

For the FeS system, one of the key questions about its geochemical behavior with important implications for field applications is the stability of the FeS with respect to oxidants. It has been shown in this research that oxygen transforms the FeS to a ferric phase, and that nitrate does not appear to oxidize FeS. However, other oxidants in the field, such as nitrite, could present challenges to FeS; a series of batch screening tests would provide useful information. Assessing the changes in the solid phase has been limited to XPS, since techniques such as X-Ray Diffraction is currently not feasible because of the relatively small amount of FeS present relative to silica sand. Coating or emplacing larger quantities of FeS would allow for the use of XRD to understand changes to the solid phase.

Another important question raised in this research concerns the mass of reactive material. Current techniques for coating FeS have resulted in masses of FeS that are two to three orders of magnitude less than ZVI, on a volume basis. Improving the coating method, emplacing particulate FeS during column packing, creating granular FeS, or using some combination of these approaches to put more FeS into a porous matrix is a crucial step towards field application of an FeS-based system. Such an experiment would allow a direct comparison of FeS to ZVI behavior.

The numerical modeling approach of this research could be refined, as well. In this work, the geochemical models were equilibrium, batch systems. It is anticipated that the inclusion of kinetic limitations and transport mechanisms would have a large effect on the behavior of both ZVI and FeS systems. Incorporating kinetic data into a model with transport could, provided that sufficient rate information is available, better describe this system by incorporating spatial and temporal changes. This is of concern because this research program used flow rates that were at the upper end of those expected in natural systems. However, simply incorporating kinetic and transport into the model would likely be insufficient: the important role of the gas phase in these experiments suggest that any numerical model will be incomplete unless it accounts for the generation of gas and allows for multi-phase flow.

Appendix

This appendix presents thermodynamic data from the WATEQ4F database (Ball and Nordstrom 1991) used in this research. Data are grouped into aqueous species, solid phases, gas phases, and redox reactions. Two solid phases, Carbonate Green Rust and $Fe(OH)_2(s)$, which are marked with asterisks, were added to the database, as described in Section 4.3.7.

Species	Reaction	Log K
Aqueous species		
$CaCO_3$	$Ca^{+2} + CO_3^{-2} = CaCO_3$	3.224
$CaHCO_3^+$	$Ca^{+2} + HCO_3^- = CaHCO_3^+$	1.106
$CaHSO_4^+$	$Ca^{+2} + HSO_4^- = CaHSO_4^+$	1.08
$CaOH^+$	$Ca^{+2} + H_2O = CaOH^+ + H^+$	-12.78
$CaSO_4$	$Ca^{+2} + SO_4^{-2} = CaSO_4$	2.3
CO_2	$CO_3^{-2} + 2\,H^+ = CO_2 + H_2O$	16.681
$Fe(HS)_2$	$Fe^{+2} + 2HS^- = Fe(HS)_2$	8.95
$Fe(HS)_3^-$	$Fe^{+2} + 3HS^- = Fe(HS)_3^-$	10.987
$Fe(OH)_2$	$Fe^{+2} + 2H_2O = Fe(OH)_2 + 2H^+$	-20.57
$Fe(OH)_2^+$	$Fe^{+3} + 2H_2O = Fe(OH)_2^+ + 2H^+$	-5.67
$Fe(OH)_3$	$Fe^{+3} + 3H_2O = Fe(OH)_3 + 3H^+$	-12.56
$Fe(OH)_3^-$	$Fe^{+2} + 3H_2O = Fe(OH)_3^- + 3H^+$	-31
$Fe(OH)_4^-$	$Fe^{+3} + 4H_2O = Fe(OH)_4^- + 4H^+$	-21.6
$Fe(SO_4)_2^-$	$Fe^{+3} + 2SO_4^{-2} = Fe(SO_4)_2^-$	5.38
$Fe_2(OH)_2^{+4}$	$2Fe^{+3} + 2H_2O = Fe_2(OH)_2^{+4} + 2H^+$	-2.95
$Fe_3(OH)_4^{+5}$	$3Fe^{+3} + 4H_2O = Fe_3(OH)_4^{+5} + 4H^+$	-6.3
$FeCl^+$	$Fe^{+2} + Cl^- = FeCl^+$	0.14
$FeCl^{+2}$	$Fe^{+3} + Cl^- = FeCl^{+2}$	1.48
$FeCl_2^+$	$Fe^{+3} + 2Cl^- = FeCl_2^+$	2.13
$FeCl_3$	$Fe^{+3} + 3Cl^- = FeCl_3$	1.13
$FeCO_3$	$Fe^{+2} + CO_3^{-2} = FeCO_3$	4.38

Species	Reaction	Log K
$FeHCO_3^+$	$Fe^{+2} + HCO_3^- = FeHCO_3^+$	2
$FeHSO_4^+$	$Fe^{+2} + HSO_4^- = FeHSO_4^+$	1.08
$FeHSO_4^{+2}$	$Fe^{+3} + HSO_4^- = FeHSO_4^{+2}$	2.48
$FeOH^+$	$Fe^{+2} + H_2O = FeOH^+ + H^+$	-9.5
$FeOH^{+2}$	$Fe^{+3} + H_2O = FeOH^{+2} + H^+$	-2.19
$FeSO_4$	$Fe^{+2} + SO_4^{-2} = FeSO_4$	2.25
$FeSO_4^+$	$Fe^{+3} + SO_4^{-2} = FeSO_4^+$	4.04
H_2CO_3	$HCO_3^- + H^+ = H_2CO_3$	6.351
HCO_3^-	$H^+ + CO_3^{-2} = HCO_3^-$	10.329
HS^-	$H_2S = HS^- + H^+$	-6.994
HSO_4^-	$H^+ + SO_4^{-2} = HSO_4^-$	1.988
KSO_4^-	$K^+ + SO_4^{-2} = KSO_4^-$	0.85
$MgCO_3$	$Mg^{+2} + CO_3^{-2} = MgCO_3$	2.98
$MgHCO_3^+$	$Mg^{+2} + HCO_3^- = MgHCO_3^+$	1.07
$MgOH^+$	$Mg^{+2} + H_2O = MgOH^+ + H^+$	-11.44
$MgSO_4$	$Mg^{+2} + SO_4^{-2} = MgSO_4$	2.37
N_2	$2\ NO_3^- + 12\ H^+ + 10\ e^- = N_2 + 6\ H_2O$	207.08
$NaCO_3^-$	$Na^+ + CO_3^{-2} = NaCO_3^-$	1.27
$NaHCO_3$	$Na^+ + HCO_3^- = NaHCO_3$	-0.25
$NaSO_4^-$	$Na^+ + SO_4^{-2} = NaSO_4^-$	0.7
NH_3	$NH_4^+ = NH_3 + H^+$	-9.252
$NH_4SO_4^-$	$NH_4^+ + SO_4^{-2} = NH_4SO_4^-$	1.11
OH^-	$H_2O = OH^- + H^+$	-14
S^{-2}	$HS^- = S^{-2} + H^+$	-12.918
S_2^{-2}	$HS^- = S_2^{-2} + H^+$	-14.528
S_3^{-2}	$HS^- = S_3^{-2} + H^+$	-13.282
S_4^{-2}	$HS^- = S_4^{-2} + H^+$	-9.829
S_5^{-2}	$HS^- = S_5^{-2} + H^+$	-9.595
S_6^{-2}	$HS^- = S_6^{-2} + H^+$	-9.881
Solid phases		
Anhydrite	$CaSO_4 = Ca^{+2} + SO_4^{-2}$	-4.36
Aragonite	$CaCO_3 = Ca^{+2} + CO_3^{-2}$	-8.336
Brucite	$Mg(OH)_2 + 2H^+ = Mg^{+2} + 2H_2O$	16.84
Calcite	$CaCO_3 = Ca^{+2} + CO_3^{-2}$	-8.48

Species	Reaction	Log K
Carbonate Green Rust (CGR)*	$[Fe^{II}_4Fe^{III}_2(OH)_{12}][CO_3 \cdot 2H_2O]+12H^+=4Fe^{2+}+2Fe^{3+}+14H_2O+CO_3^{2-}$	39.07
Dolomite	$CaMg(CO_3)_2 = Ca^{+2} + Mg^{+2} + 2CO_3^{-2}$	-17.09
$Fe(OH)_2$(s)*	$Fe(OH)_2 + 2H^+ = Fe^{2+} + 2H_2O$	14.39
$Fe(OH)_3$(a)	$Fe(OH)_3 + 3H^+ = Fe^{+3} + 3H_2O$	4.891
Goethite	$FeOOH + 3H^+ = Fe^{+3} + 2H_2O$	-1
Greigite	$Fe_3S_4 + 4H^+ = 2Fe^{+3} + Fe^{+2} + 4HS^-$	-45.035
Gypsum	$CaSO_4{:}_2H_2O = Ca^{+2} + SO_4^{-2} + 2H_2O$	-4.58
Hematite	$Fe_2O_3 + 6H^+ = 2Fe^{+3} + 3H_2O$	-4.008
Mackinawite	$FeS + H^+ = Fe^{+2} + HS^-$	-4.648
Maghemite	$Fe_2O_3 + 6H^+ = 2Fe^{+3} + 3H_2O$	6.386
Magnesite	$MgCO_3 = Mg^{+2} + CO_3^{-2}$	-8.029
Magnetite	$Fe_3O_4 + 8H^+ = 2Fe^{+3} + Fe^{+2} + 4H_2O$	3.737
Siderite	$FeCO_3 = Fe^{+2} + CO_3^{-2}$	-10.89
Sulfur	$S + 2e^- = S^{-2}$	-15.0262
Gas phases		
CO_2(g)	CO_2 (g) = CO_2 (aq)	-1.468
H_2(g)	H_2 (g) = H_2 (aq)	-3.15
H_2S(g)	H_2S (g)= H_2S (aq)	-0.997
N_2(g)	N_2 (g) = N_2 (aq)	-3.26
NH_3(g)	NH_3 (g) = NH_3 (aq)	1.77
O_2(g)	O_2 (g) = O_2 (aq)	-2.898
Redox reactions		
Fe^{+3} / Fe^{+2}	$Fe^{+2} = Fe^{+3} + e^-$	-13.02
H^+ / H_2	$2\ H^+ + 2\ e^- = H_2$	-3.15
H_2O / O_2	$2H_2O = O_2 + 4H^+ + 4e^-$	-86.08
NO_3^- / NH_4^+	$NO_3^- + 10H^+ + 8e^- = NH_4^+ + 3H_2O$	119.077
NO_3^- / NO_2^-	$NO_3^- + 2H^+ + 2e^- = NO_2^- + H_2O$	28.57
S (s) / S^{-2}	$S + 2e^- = S^{-2}$	-15.026
SO_4^{-2} / H_2S	$SO_4^{-2} + 10H^+ + 8e^- = H_2S + 4H_2O$	40.644

References

Abdelmoula, M., P. Refait, S. H. Drissi, J. P. Mihe, and J. R. Génin. 1996. Conversion electron Mössbauer spectroscopy and X-ray diffraction studies of the formation of carbonate-containing green rust one by corrosion metallic iron in $NaHCO_3$ and ($NaHCO_3$+NaCl) solutions. *Corrosion Science* 38 (4): 623-633.

Agrawal, A., and P. G. Tratnyek. 1996. Reduction of nitro aromatic compounds by zero-valent iron metal. *Environmental Science & Technology* 30 (1): 153-160.

Ahlfeld, D., and W. R. Dripps. 2003. Groundwater Issues. In *Water: Science, Policy, and Management*, eds. Richard Lawford, Denise Fort, Holly Hartman and Susanna Eden, 79-98. Washington, D.C.: American Geophysical Union.

Al-Agha, M. R., S. D. Burley, C. D. Curtis, and J. Esson. 1995. Complex cementation textures and authigenic mineral assemblages in recent concretions from the Lincolnshire Wash (east coast, UK) driven by Fe(0) to Fe(II) oxidation. *Journal of the Geological Society of London* 152: 157-171.

Altuglas International. 2006. Plexiglas Physical Properties. http://www.plexiglas.com/expert (accessed September 1, 2007).

Appelo, C. A. J., and D. Postma. 2005. *Geochemistry, Groundwater and Pollution*. 2nd ed. New York: Balkema.

Arakaki, T., and J. W. Morse. 1993. Coprecipitation and adsorption of Mn(II) with mackinawite (FeS) under conditions similar to those found in anoxic sediments. *Geochimica et Cosmochimica Acta* 57 (1): 9-14.

Ball, J. W., and D. K. Nordstrom. 1991. *User's Manual for WATEQ4F, with Revised Thermodynamic Data Base and Test Cases for Calculating Speciation of Major, Trace, and Redox Elements in Natural Waters.* Denver, CO: USGS, Report # 91-183.

Beak, D. G., and R. T. Wilkin. 2009. Performance of a zerovalent iron reactive barrier for the treatment of arsenic in groundwater: Part 2. Geochemical modeling and solid phase studies. *Journal of Contaminant Hydrology* 106 (1-2): 15-28.

Benner, S. G., D. W. Blowes, W. D. Gould, R. B. Herbert Jr., and C. J. Ptacek. 1999. Geochemistry of a permeable reactive barrier for metals and acid mine drainage. *Environmental Science & Technology* 33 (16): 2793-2799.

Berner, R. A. 1967. Thermodynamic stability of sedimentary iron sulfides. *American Journal of Science* 265 (9): 773-785.

Berner, R. A. 1964. Iron sulfides formed from aqueous solution at low temperatures and atmospheric pressure. *Journal of Geology* 72 (3): 293-306.

Billon, G., B. Ouddane, J. Laureyns, and A. Boughriet. 2001. Chemistry of metal sulfides in anoxic sediments. *Physical Chemistry Chemical Physics* 3 (17): 3586-3592.

Blowes, D. W., R. W. Gillham, C. J. Ptacek, R. W. Puls, T. A. Bennett, S. F. O'Hannesin, C. Hanton-Fong, and J. Bain. 1999. *In Situ Permeable Reactive Barrier for the Treatment of Hexavalent Chromium and Trichloroethylene in Ground Water: Volume 1. Design and Installation.* Washington, D.C.: United States Environmental Protection Agency, Report # EPA/600/R99/095A.

Blowes, D. W., C. J. Ptacek, S. G. Benner, C. W. T. McRae, T. A. Bennett, and R. W. Puls. 2000. Treatment of inorganic contaminants using permeable reactive barriers. *Journal of Contaminant Hydrology* 45 (1-2): 123-137.

Blowes, D. W., R. W. Puls, R. W. Gillham, C. J. Ptacek, T. A. Bennett, J. Bain, C. Hanton-Fong, and C. J. Paul. 1999. *In Situ Permeable Reactive Barrier for the Treatment of Hexavalent Chromium and Trichloroethylene in Ground Water. Volume 2. Performance Monitoring.* Washington, D.C.: United States Environmental Protection Agency, Report # EPA/600/R99/095B.

Boursiquot, S., M. Mullet, and J. Ehrhardt. 2002. XPS study of the reaction of chromium (VI) with mackinawite (FeS). Paper presented at ECASIA '01 Proceedings of the 9th European Conference on Applications of Surface and Interface Analysis, Sep 30-Oct 5, 2001, Avignon, France.

Brown, J. R., G. M. Bancroft, W. S. Fyfe, and R. A. N. McLean. 1979. Mercury removal from water by iron sulfide minerals. An electron spectroscopy for chemical analysis (ESCA) study. *Environmental Science & Technology* 13 (9): 1142-1144.

Butler, E. C., and K. F. Hayes. 2001. Factors influencing rates and products in the transformation of trichloroethylene by iron sulfide and iron metal. *Environmental Science & Technology* 35 (19): 3884-3891.

Butler, E. C., and K. F. Hayes. 2000. Kinetics of the transformation of halogenated aliphatic compounds by iron sulfide. *Environmental Science & Technology* 34 (3): 422-429.

Butler, E. C., and K. F. Hayes. 1999. Kinetics of the transformation of trichloroethylene and tetrachloroethylene by iron sulfide. *Environmental Science and Technology* 33 (12): 2021-2027.

Butler, E. C., and K. F. Hayes. 1998. Effects of solution composition and pH on the reductive dechlorination of hexachloroethane by iron sulfide. *Environmental Science & Technology* 32 (9): 1276-1284.

Carman, P. C. 1939. Permeability of saturated sands, soils, and clays. *Journal of Agricultural Science* 29: 262-273.

Casa XPS. 2009. Uncertainties in Peak Parameters. http://www.casaxps.com/help_manual/error_analysis.htm (accessed January 4, 2009).

Chapuis, R. P., and M. Aubertin. 2003. On the use of the Kozeny-Carman equation to predict the hydraulic conductivity of soils. *Canadian Geotechnical Journal* 40 (3): 616-628.

Charbeneau, R. J. 2000. *Groundwater Hydraulics and Pollutant Transport*. Upper Saddle River, NJ: Prentice Hall.

Civan, F. 2001. Scale effect on porosity and permeability: Kinetics, model, and correlation. *AICHE Journal* 47 (2): 271-287.

Coles, C. A., S. Ramachandra Rao, and R. N. Yong. 2000. Lead and cadmium interactions with mackinawite: Retention mechanisms and the role of pH. *Environmental Science & Technology* 34 (6): 996-1000.

Cooper, D. C., and J. W. Morse. 1998. Extractability of metal sulfide minerals in acidic solutions: Application to environmental studies to trace metal contamination within anoxic sediments. *Environmental Science & Technology* 32 (8): 1076-1078.

D'Andrea, P., K. C. K. Lai, P. Kjeldsen, and I. M. C. Lo. 2005. Effect of groundwater inorganics on the reductive dechlorination of TCE by zero-valent iron. *Water, Air and Soil Pollution* 162 (1-4): 401-420.

Davison, W. 1991. The solubility of iron sulphides in synthetic and natural waters at ambient temperature. *Aquatic Sciences* 53 (4): 309-329.

Davison, W., N. Phillips, and B. J. Tabner. 1999. Soluble iron sulfide species in natural waters: Reappraisal of their stoichiometry and stability constants. *Aquatic Sciences* 61 (1): 23-43.

Demond, A. H., K. Rathfelder, and L. M. Abriola. 1996. Simulation of organic liquid flow in porous media using estimated and measured transport properties. *Journal of Contaminant Hydrology* 22 (3-4): 223-239.

Devlin, J. F., and K. O. Allin. 2005. Major anion effects on the kinetics and reactivity of granular iron in glass-encased magnet batch reactor experiments. *Environmental Science & Technology* 39 (6): 1868-1874.

Devlin, J. F., J. Klausen, and R. P. Schwarzenbach. 1998. Kinetics of nitroaromatic reduction on granular iron in recirculating batch experiments. *Environmental Science & Technology* 32 (13): 1941-1947.

Drissi, S. H., P. Refait, M. Abdelmoula, and J. R. Génin. 1995. The preparation and thermodynamic properties of Fe(II)-Fe(III) hydroxide-carbonate (green rust 1) - Pourbaix diagram of iron in carbonate-containing aqueous media. *Corrosion Science* 37 (12): 2025-2041.

Duran, J. M., J. L. Vogan, and J. R. Stening. 2000. Reactive Barrier Performance in a Complex Contaminant and Geochemical Environment. In *Chemical Oxidation and Reactive Barriers: Remediation of Chlorinated and Recalcitrant Compounds*,

eds. Godage B. Wickramanayake, Arun R. Gavaskar and Abraham S. C. Chen, 401-408. Columbus, Ohio: Battelle Press.

Dwyer, B. P. 2000a. *Design, Construction and Monitoring of a Permeable Reactive Barrier Technology for use at Rocky Flats Environmental Technology Site (RFETS).* Albuquerque, NM: Sandia National Laboratories, Report # SAND-2000-2702.

Dwyer, B. P. 2000b. *Evaluation of a Permeable Reactive Barrier Technology for use at Rocky Flats Environmental Technology Site (RFETS).* Albuquerque, NM: Sandia National Laboratories, Report # SAND-2000-0075.

EPA. 2002. *Field Applications of in Situ Remediation Technologies: Permeable Reactive Barriers.* Washington, D.C.: United States Environmental Protection Agency, Office of Solid Waste and Emergency Response.

EPA. 1999. *Field Applications of in Situ Remediation Technologies: Permeable Reactive Barriers.* Washington, D.C.: United States Environmental Protection Agency, Office of Solid Waste and Emergency Response, Report # 542-R-99-002.

ESTCP. 2003. *Evaluating the Longevity and Hydraulic Performance of Permeable Reactive Barriers at Department of Defense Sites.* Washington, DC: U.S. Department of Defense, Environmental Security Technology Certification Program, Report # CU-9907.

Faraway, J. J. 2006. *Extending the Linear Model with R: Generalized Linear, Mixed Effects and Nonparametric Regression Models*. Boca Raton: Chapman & Hall/CRC.

Farquhar, M. L., J. M. Charnock, F. R. Livens, and D. J. Vaughan. 2002. Mechanisms of arsenic uptake from aqueous solution by interaction with goethite, lepidocrocite, mackinawite, and pyrite: An X-ray absorption spectroscopy study. *Environmental Science & Technology* 36 (8): 1757-1762.

Farrell, J., M. Kason, N. Melitas, and T. Li. 2000. Investigation of the long-term performance of zero-valent iron for reductive dechlorination of trichloroethylene. *Environmental Science & Technology* 34 (3): 514-521.

FRTR. 2002. *Evaluation of Permeable Reactive Barrier Performance: Revised Report.* Cincinnati, OH: Federal Remediation Technologies Roundtable; Tri-Agency Permeable Reactive Barrier Initiative.

Fruchter, J. S. 2002. In situ treatment of chromium-contaminated groundwater. *Environmental Science & Technology* 36 (23): 464A-472A.

Furukawa, Y., J. W. Kim, J. Watkins, and R. T. Wilkin. 2002. Formation of ferrihydrite and associated iron corrosion products in permeable reactive barriers of zero-valent iron. *Environmental Science & Technology* 36 (24): 5469-5475.

Gallegos, T. J., S. P. Hyun, and K. F. Hayes. 2007. Spectroscopic investigation of the uptake of arsenite from solution by synthetic mackinawite. *Environmental Science & Technology* 41 (22): 7781-7786.

Gavaskar, A. R. 1999. Design and construction techniques for permeable reactive barriers. *Journal of Hazardous Materials* 68 (1-2): 41-71.

Gavaskar, A. R., N. Gupta, B. Sass, W. Yoon, R. Janosy, E. Drescher, and J. Hicks. 2000. *Design, Construction and Monitoring of the Permeable Reactive Barrier in Area 5 at Dover Air Force Base.* Columbus, OH: Battelle, Report # AFRL-ML-TY-2000-4546.

Gavaskar, A. R., N. Gupta, B. M. Sass, T. C. Fox, R. Janosy, K. J. Cantrell, and R. Olfenbuttel. 1997. *Design Guidance for Application of Permeable Barriers to Remediate Dissolved Chlorinated Solvents.* Tyndall AFB, FL: United States Air Force, Report # DG 1110-345-117.

Gavaskar, A. R., N. Gupta, B. M. Sass, R. J. Janosy, and D. O'Sullivan. 1998. *Permeable Barriers for Groundwater Remediation: Design, Construction, and Monitoring*. Columbus: Battelle Press.

Gavaskar, A. R., W. S. Yoon, J. Sminchack, B. Sass, N. Gupta, J. Hicks, and V. Lal. 2005. *Long Term Performance Assessment of a Permeable Reactive Barrier at Former Naval Air Station Moffett Field.* Port Hueneme, CA: Naval Facilities Engineering Command, Report # CR 05-006-ENV.

Génin, J. R., G. Bourrié, F. Trolard, M. Abdelmoula, A. Jaffrezic, P. Refait, V. Maitre, B. Humbert, and A. Herbillon. 1998. Thermodynamic equilibria in aqueous suspensions of synthetic and natural Fe(II)-Fe(III) green rusts; occurrences of the mineral in hydromorphic soils. *Environmental Science & Technology* 32 (8): 1058-1068.

Gillham, R. W. 1999. In situ remediation of VOC-contaminated groundwater using zero-valent iron: Long-term performance. Paper presented at Challenges Posed by Urban & Industrial Contaminants, Freemantle, Western Australia, March 1999.

Gillham, R. W., and S. F. O'Hannesin. 1994. Enhanced degradation of halogenated aliphatics by zero-valent iron. *Ground Water* 32 (6): 958-967.

Gillham, R. W., and S. F. O'Hannesin. 1992. Metal-catalyzed abiotic degradation of halogenated organic compounds. Paper presented at IAH Conference: Modern Trends in Hydrogeology, Hamilton, Ontario, May 10-13.

Gillham, R. W., S. F. O'Hannesin, and W. S. Orth. 1993. Metal enhanced abiotic degradation of halogenated aliphatics: Laboratory tests and field trials. Paper presented at 6th Annual Environmental Management and Technology Conference, Rosemont, IL, March 9-11.

Goldhaber, M. B., and I. R. Kaplan. 1975. Controls and consequences of sulfate reduction rates in recent marine sediments. *Soil Science*: 1.

Goldhaber, M. B., and I. R. Kaplan. 1974. The Sulfur Cycle. In *The Sea, Vol. 5: Marine Chemistry*, ed. Edward D. Goldberg, 569-655. New York: John Wiley.

Gu, B. 2005a. Iron Reactive Barrier at the Oak Ridge Y-12 Site: Mineralogical Characteristics. http://www.esd.ornl.gov/~b26/minerals.htm (accessed 4/1, 2005).

Gu, B. 2005b. Iron Reactive Barrier at the Oak Ridge Y-12 Site: Project Summary. http://www.esd.ornl.gov/~b26/barrier.htm (accessed 4/1, 2005).

Gu, B., T. J. Phelps, L. Y. Liang, M. J. Dickey, Y. Roh, B. L. Kinsall, A. V. Palumbo, and G. K. Jacobs. 1999. Biogeochemical dynamics in zero-valent iron columns: Implications for permeable reactive barriers. *Environmental Science & Technology* 33 (13): 2170-2177.

Gu, B., D. B. Watson, D. H. Phillips, and L. Y. Liang. 2002. Biogeochemical, Mineralogical, Hydrological Characteristics of an Iron Reactive Barrier used for Treatment of Uranium and Nitrate. In *Handbook of Groundwater Remediation using Permeable Reactive Barriers: Applications to Radionuclides, Trace Metals, and Nutrients*, eds. David L. Naftz, Stan J. Morrison, James A. Davis and Christopher C. Fuller, 305-342. San Diego, CA: Academic Press.

Gupta, R. P., and S. K. Sen. 1974. Calculation of multiplet structure of core p-vacancy levels. *Physical Review B (Solid State)* 10 (1): 71-7.

Han, Y. S. 2009. Iron sulfide-coated sand for remediation of arsenic(III)-contaminated anoxic groundwater. Ph.D. Dissertation, University of Michigan.

Han, Y. S., T. J. Gallegos, A. H. Demond, and K. F. Hayes. 2009. FeS coated-sand for removal of arsenic(III) under anaerobic conditions: Coating method and characterization. *Water Research* (in review).

Hardy, L. I., and R. W. Gillham. 1996. Formation of hydrocarbons from the reduction of aqueous CO_2 by zero-valent iron. *Environmental Science & Technology* 30 (1): 57.

Henderson, A. D., and A. H. Demond. 2007. Long-term performance of zero-valent iron permeable reactive barriers: A critical review. *Environmental Engineering Science* 24 (4): 401-423.

Herbert, R. B., Jr., S. G. Benner, and D. W. Blowes. 2000. Solid phase iron-sulfur geochemistry of a reactive barrier for treatment of mine drainage. *Applied Geochemistry* 15 (9): 1331-1343.

Herbert, R. B., Jr., S. G. Benner, A. R. Pratt, and D. W. Blowes. 1998. Surface chemistry and morphology of poorly crystalline iron sulfides precipitated in media containing sulfate-reducing bacteria. *Chemical Geology* 144 (1-2): 87-97.

Hingston, F. J. 1981. A Review of Anion Adsorption. In *Adsorption of Inorganics at Solid-Liquid Interfaces*, eds. Marc A. Anderson, Alan J. Rubin, 51-90. Ann Arbor, MI: Ann Arbor Science.

Hosmer, D. W., and S. Lemeshow. 1989. *Applied Logistic Regression*. New York: John Wiley.

Huerta-Diaz, M. A., A. Tessier, and R. Carignan. 1998. Geochemistry of trace metals associated with reduced sulfur in freshwater sediments. *Applied Geochemistry* 13 (2): 213-233.

Hurlbut, C. S.,Jr, and C. Klein. 1977. *Manual of Mineralogy*. New York: John Wiley.

Hutson, S. S., N. L. Barber, J. F. Kenny, K. S. Linsey, D. S. Lumia, and M. A. Maupin. 2004. *Estimated use of Water in the United States in 2000.* Reston, VA: U. S. Geological Survey, Report # C 1268.

Hyland, M. M., G. E. Jean, and G. M. Bancroft. 1990. XPS and AES studies of Hg(II) sorption and desorption reactions on sulphide minerals. *Geochimica et Cosmochimica Acta* 54 (7): 1957-1967.

ITRC. 2005. *Permeable Reactive Barriers: Lessons Learned / New Directions.* Washington, D.C.: Interstate Technology & Regulatory Council, Permeable Reactive Barriers Team, Report # PRB-4.

Jain, A., K. P. Raven, and R. H. Loeppert. 1999. Arsenite and arsenate adsorption on ferrihydrite: Surface charge reduction and net OH^- release stoichiometry. *Environmental Science & Technology* 33 (8): 1179-1184.

Jambor, J. L., M. Raudsepp, and K. Mountjoy. 2005. Mineralogy of permeable reactive barriers for the attenuation of subsurface contaminants. *Canadian Mineralogist* 43 (6): 2117-2140.

Jean, G. E., and G. M. Bancroft. 1986. Heavy metal adsorption by sulphide mineral surfaces. *Geochimica et Cosmochimica Acta* 50 (7): 1455-1463.

Jeen, S. W., R. W. Gillham, and D. W. Blowes. 2006. Effects of carbonate precipitates on long-term performance of granular iron for reductive dechlorination of TCE. *Environmental Science & Technology* 40 (20): 6432-6437.

Jeen, S. W., K. U. Mayer, R. W. Gillham, and D. W. Blowes. 2007. Reactive transport modeling of trichloroethene treatment with declining reactivity of iron. *Environmental Science & Technology* 41 (4): 1432-1438.

Jeen, S., D. W. Blowes, and R. W. Gillham. 2008. Performance evaluation of granular iron for removing hexavalent chromium under different geochemical conditions. *Journal of Contaminant Hydrology* 95 (1-2): 76-91.

Jeong, H. Y., J. H. Lee, and K. F. Hayes. 2008. Characterization of synthetic nanocrystalline mackinawite: Crystal structure, particle size, and specific surface area. *Geochimica et Cosmochimica Acta* 72 (2): 493-505.

Jeong, H. Y., and K. F. Hayes. 2003. Impact of transition metals on reductive dechlorination rate of hexachloroethane by mackinawite. *Environmental Science & Technology* 37 (20): 4650-4655.

Jeong, H. Y., B. Klaue, J. D. Blum, and K. F. Hayes. 2007. Sorption of mercuric ion by synthetic nanocrystalline mackinawite (FeS). *Environmental Science and Technology* 41 (22): 7699-7705.

Johnson, T. L., W. Fish, Y. A. Gorby, and P. G. Tratnyek. 1998. Degradation of carbon tetrachloride by iron metal: Complexation effects on the oxide surface. *Journal of Contaminant Hydrology* 29 (4): 379-398.

Jury, W. A., and R. Horton. 2004. *Soil Physics*. 6th ed. Hoboken, N.J.: John Wiley.

Kamolpornwijit, W., L. Y. Liang, O. R. West, G. R. Moline, and A. B. Sullivan. 2003. Preferential flow path development and its influence on long-term PRB performance: Column study. *Journal of Contaminant Hydrology* 66 (3-4): 161-178.

Kamolpornwijit, W., and L. Liang. 2006. Investigation of gas production and entrapment in granular iron medium. *Journal of Contaminant Hydrology* 82 (3-4): 338-356.

Kielemoes, J., P. De Boever, and W. Verstraete. 2000. Influence of denitrification on the corrosion of iron and stainless steel powder. *Environmental Science & Technology* 34 (4): 663-671.

Kiilerich, O., J. W. Larsen, C. Nielsen, and L. D. Deigaard. 2000. Field results from the use of a permeable reactive wall. Paper presented at Chemical Oxidation and Reactive Barriers: Remediation of Chlorinated and Recalcitrant Compounds: The Second International Conference on Remediation of Chlorinated and Recalcitrant Compounds, Monterey, CA, May 22-25.

Kinniburgh, D. G., and M. L. Jackson. 1981. Cation Adsorption by Hydrous Metal Oxides and Clays. In *Adsorption of Inorganics at Solid-Liquid Interfaces*, eds. Marc A. Anderson, Alan J. Rubin, 91-160. Ann Arbor, MI: Ann Arbor Science.

Kjeldsen, P., and I. A. Fulgsang. 2000. Demonstration program on reactive barrier technologies using zero-valent iron. Paper presented at ConSoil 2000, Leipzig, Germany, 18-22 Sept 2000.

Kjeldsen, P., and T. Locht. 2000. Removal of TCE and chromate in reactive barriers using zero-valent iron: Laboratory experiments. Paper presented at ConSoil 2000, Leipzig, Germany, 18-22 Sept 2000.

Klausen, J., J. Ranke, and R. P. Schwarzenbach. 2001. Influence of solution composition and column aging on the reduction of nitroaromatic compounds by zero-valent iron. *Chemosphere* 44 (4): 511-517.

Klausen, J., P. J. Vikesland, T. Kohn, D. R. Burris, W. P. Ball, and A. L. Roberts. 2003. Longevity of granular iron in groundwater treatment processes: Solution composition effects on reduction of organohalides and nitroaromatic compounds. *Environmental Science & Technology* 37 (6): 1208-1218.

Klein, R., and H. Schad. 2000. Results from a full-scale funnel-and-gate system at the BEKA site in tubingen (germany) using zero-valent iron. Paper presented at ConSoil 2000, Leipzig, Germany, Sept. 18-22.

Köber, R., F. Giarolli, M. Ebert, and A. Dahmke. 2005. Long-term performance of Fe^0-PRBs to treat arsenic and 1,2-DCE(*cis*) under different geochemical conditions. Paper presented at First International Symposium on Permeable Reactive Barriers, Belfast, Northern Ireland, March 2004.

Köber, R., O. Schlicker, M. Ebert, and A. Dahmke. 2002. Degradation of chlorinated ethylenes by Fe^0: Inhibition processes and mineral precipitation. *Environmental Geology* 41 (6): 644-652.

Kohn, T., and A. L. Roberts. 2006. The effect of silica on the degradation of organohalides in granular iron columns. *Journal of Contaminant Hydrology* 83 (1-2): 70-88.

Korte, N. E. 2001. *Zero-Valent Iron Permeable Reactive Barriers: A Review of Performance.* Oak Ridge, TN: Oak Ridge National Laboratory, Report # ORNL/TM-2000/345.

Korte, N. E., L. Y. Liang, B. Gu, M. T. Muck, J. L. Zutman, R. M. Schlosser, R. L. Siegrist, T. C. Houk, and Q. Fernando. 1997a. *In Situ Treatment of Mixed Contaminants in Groundwater: Application of Zero-Valence Iron and Palladized Iron for Treatment of Groundwater Contaminated with Trichloroethene and Technetium-99.* Oak Ridge, TN: Oak Ridge National Laboratory, Report # ORNL/TM-13530.

Korte, N. E., O. R. West, L. Y. Liang, M. J. Pelfrey, and T. C. Houk. 1997b. A field-scale test facility for permeable reactive barriers at the Portsmouth Gaseous Diffusion Plant. *Federal Facilities Environmental Journal* 8 (3): 105-114.

Kozeny, J., and P. Forchheimer. 1928. Capillary flow of water in soils: Ueber Kapillare Leitung des Wassers im Boden. *Gas Und Wasserfach* 71 (19): 437-438.

Lackovic, J. A., N. P. Nikolaidis, and G. M. Dobbs. 2000. Inorganic arsenic removal by zero-valent iron. *Environmental Engineering Science* 17 (1): 29-39.

Lai, K. C. K., P. Kjeldsen, and I. M. C. Lo. 2005. Evaluation of the hydraulic performance of a full-scale permeable reactive barrier by a tracer study. Paper presented at First International Symposium on Permeable Reactive Barriers, Belfast, March 2004.

Lai, K. C. K., I. M. C. Lo, V. Birkelund, and P. Kjeldsen. 2006. Field monitoring of a permeable reactive barrier for removal of chlorinated organics. *Journal of Environmental Engineering* 132 (2): 199-210.

Lebron, I., and D. A. Robinson. 2003. Particle size segregation during hand packing of coarse granular materials and impacts on local pore-scale structure. *Vadose Zone Journal* 2 (3): 330-337.

Lee, J. H. 2009. Chemical optimization of in situ emplacement of nano-particulate iron sulfide in porous media. Ph.D. Dissertation, University of Michigan.

Lennie, A. R., S. A. T. Redfern, P. F. Schofield, and D. J. Vaughn. 1995. Synthesis and Rietveld crystal structures refinement of mackinawaite, tetragonal FeS. *Mineralogical Magazine* 59 (4): 677-683.

Lennie, A. R., S. A. T. Redfern, P. E. Champness, C. P. Stoddart, P. F. Schofield, and D. J. Vaughan. 1997. Transformation of mackinawite to greigite: An in situ X-ray powder diffraction and transmission electron microscope study. *American Mineralogist* 82 (3-4): 302-309.

Li, L., C. H. Benson, and E. M. Lawson. 2006. Modeling porosity reductions caused by mineral fouling in continuous-wall permeable reactive barriers. *Journal of Contaminant Hydrology* 83 (1-2): 89-121.

Liang, L. Y., N. E. Korte, B. Gu, R. Puls, and C. Reeter. 2000. Geochemical and microbial reactions affecting the long-term performance of in situ 'iron barriers'. *Advances in Environmental Research* 4 (4): 273-286.

Liang, L. Y., N. E. Korte, G. R. Moline, and O. R. West. 2001. *Long-Term Monitoring of Permeable Reactive Barriers: Progress Report.* Oak Ridge National Laboratory, Report # ORNL/TM-2001/1.

Liang, L. Y., A. B. Sullivan, O. R. West, G. R. Moline, and W. Kamolpornwijit. 2003. Predicting the precipitation of mineral phases in permeable reactive barriers. *Environmental Engineering Science* 20 (6): 635-653.

Liang, L. Y., O. R. West, N. E. Korte, J. D. Goodlaxson, D. A. Pickering, J. L. Zutman, F. J. Anderson, C. A. Welch, M. J. Pelfrey, and M. J. Dickey. 1997. *The X-625 Groundwater Treatment Facility: A Field-Scale Test of Trichloroethylene Dechlorination using Iron Filings for the X-120/X-749 Groundwater Plume.* Oak Ridge, TN: Oak Ridge National Laboratory, Report # ORNL/TM--13410.

Lien, H., and R. T. Wilkin. 2005. High-level arsenite removal from groundwater by zero-valent iron. *Chemosphere* 59 (3): 377-386.

Lin, S., F. Krause, and G. Voordouw. 2009. Transformation of iron sulfide to greigite by nitrite produced by oil field bacteria. *Applied Microbiology and Biotechnology* 83 (2): 369-376.

Lindberg, R. D., and D. D. Runnells. 1984. Ground water redox reactions: An analysis of equilibrium state applied to E_H measurements and geochemical modeling. *Science* 225 (4665): 925-927.

Mackenzie, P. D., D. P. Horney, and T. M. Sivavec. 1999. Mineral precipitation and porosity losses in granular iron columns. *Journal of Hazardous Materials* 68 (1): 1-17.

Manning, B. A., M. L. Hunt, C. Amrhein, and J. A. Yarmoff. 2002. Arsenic(III) and arsenic(V) reactions with zerovalent iron corrosion products. *Environmental Science & Technology* 36 (24): 5455-5461.

Matheson, L. J., W. C. Goldberg, W. D. Bostick, and L. Harris. 2002. Analysis of Uranium-Contaminated Zero Valent Iron Media Sampled from Permeable Reactive Barriers Installed at U.S. Department of Energy Sites in Oak Ridge, Tennessee, and Durango, Colorado. In *Handbook of Groundwater Remediation using Permeable Reactive Barriers: Applications to Radionuclides, Trace Metals, and Nutrients*, eds. David L. Naftz, Stan J. Morrison, James A. Davis and Christopher C. Fuller, 343-367. San Diego, CA: Academic Press.

Matsuo, M., M. Kawakami, and K. Sugimori. 2000. Mössbauer spectroscopic study on chemical changes of iron compounds with the aid of sulfate-reducing bacteria. Paper presented at International Conference on the Application of the Mossbauer Effect, Garmisch, Germany.

Mayer, K. U. 1999. A numerical model for multicomponent reactive transport in variably saturated porous media. Ph.D. Dissertation, University of Waterloo.

Mayer, K. U., D. W. Blowes, and E. O. Frind. 2001. Reactive transport modeling of an in situ reactive barrier for the treatment of hexavalent chromium and trichloroethylene in groundwater. *Water Resources Research* 37 (12): 3091-3103.

McMahon, P. B., K. F. Dennehy, and M. W. Sandstrom. 1999. Hydraulic and geochemical performance of a permeable reactive barrier containing zero-valent iron, Denver Federal Center. *Ground Water* 37 (3): 396-404.

Melitas, N., J. P. Wang, M. Conklin, P. O'Day, and J. Farrell. 2002. Understanding soluble arsenate removal kinetics by zerovalent iron media. *Environmental Science & Technology* 36 (9): 2074-2081.

Morrison, S. J., C. E. Carpenter, D. R. Metzler, T. R. Bartlett, and S. A. Morris. 2002. Design and Performance of a Permeable Reactive Barrier for Containment of Uranium, Arsenic, Selenium, Vanadium, Molybdenum, and Nitrate at Monticello, Utah. In *Handbook of Groundwater Remediation using Permeable Reactive Barriers: Applications to Radionuclides, Trace Metals, and Nutrients*, eds. David L. Naftz, Stan J. Morrison, James A. Davis and Christopher C. Fuller, 371-399. San Diego, CA: Academic Press.

Morrison, S. J., D. R. Metzler, and C. E. Carpenter. 2001. Uranium precipitation in a permeable reactive barrier by progressive irreversible dissolution of zerovalent iron. *Environmental Science & Technology* 35 (2): 385-390.

Morrison, S. J., D. R. Metzler, and B. P. Dwyer. 2002a. Collection Drain and Permeable Reactive Barrier for Treating Uranium and Metals from Mill Tailings Near Durango, Colorado. In *Handbook of Groundwater Remediation using Permeable Reactive Barriers: Applications to Radionuclides, Trace Metals, and Nutrients*, eds. David L. Naftz, Stan J. Morrison, James A. Davis and Christopher C. Fuller, 435-463. San Diego, CA: Academic Press.

Morrison, S. J., D. R. Metzler, and B. P. Dwyer. 2002b. Removal of As, Mn, Mo, Se, U, V and Zn from groundwater by zero-valent iron in a passive treatment cell: reaction progress modeling. *Journal of Contaminant Hydrology* 56 (1-2): 99-116.

Morrison, S. J., D. L. Naftz, J. A. Davis, and C. C. Fuller. 2002c. Introduction to Groundwater Remediation of Metals, Radionuclides, and Nutrients with Permeable Reactive Barriers. In *Handbook of Groundwater Remediation using Permeable Reactive Barriers: Applications to Radionuclides, Trace Metals, and Nutrients*, eds. David L. Naftz, Stan J. Morrison, James A. Davis and Christopher C. Fuller, 1-15. San Diego, CA: Academic Press.

Morse, J. W., and G. W. Luther III. 1999. Chemical influences on trace metal-sulfide interactions in anoxic sediments. *Geochimica et Cosmochimica Acta* 63 (19-20): 3373-3378.

Morse, J. W., and T. Arakaki. 1993. Adsorption and coprecipitation of divalent metals with mackinawite (FeS). *Geochimica et Cosmochimica Acta* 57 (15): 3635-3640.

Mullet, M., S. Boursiquot, and J. J. Ehrhardt. 2004. Removal of hexavalent chromium from solutions by mackinawite, tetragonal FeS. *Colloids and Surfaces A: Physicochemical and Engineering Aspects* 244 (1-3): 77-85.

Mullet, M., S. Boursiquot, M. Abdelmoula, J. R. Génin, and J. Ehrhardt. 2002. Surface chemistry and structural properties of mackinawite prepared by reaction of sulfide ions with metallic iron. *Geochimica et Cosmochimica Acta* 66 (5): 829-836.

Mushovic, P., T. R. Bartlett, and S. Morrison. 2006. Hydraulic conductivity loss at the Monticello PRB leads to trial use of ex-situ treatment cell. *Technology News and Trends* 23: 1-3.

Myers, R. H. 1990. *Classical and Modern Regression with Applications*. 2nd ed. Boston: Kent.

Naftz, D. L., C. C. Fuller, J. A. Davis, M. J. Piana, S. J. Morrison, G. W. Freethey, and R. C. Rowland. 2000. Field demonstration of permeable reactive barriers to control uranium contamination in ground water. Paper presented at Chemical Oxidation and Reactive Barriers: Remediation of Chlorinated and Recalcitrant Compounds, Monterey, CA, May 2000.

National Research Council. 1994. *Alternatives for Ground Water Cleanup*. Washington, D.C.: National Academy Press.

Nicholson, R. V., J. A. Cherry, and E. J. Reardon. 1983. Migration of contaminants in ground water at a landfill: a case study. 6. Hydrogeochemistry. *Journal of Hydrology (Amsterdam)* 63 (1/2): 131-176.

Nutting, P. G. 1930. Physical analysis of oil sands. *American Association of Petroleum Geologists Bulletin* 14 (1): 1337-1349.

O'Hannesin, S. F. 1993. Field demonstration of a permeable reaction wall for the in situ abiotic degradation of halogenated aliphatic organic compounds. Ph.D. Dissertation, University of Waterloo.

O'Hannesin, S. F., and R. W. Gillham. 1998. Long-term performance of an in situ "iron wall" for remediation of VOCs. *Ground Water* 36 (1): 164-170.

O'Hara, Suzanne. 2006. Pers. comm.

Ohfuji, H., and D. Rickard. 2006. High resolution transmission electron microscopic study of synthetic nanocrystalline mackinawite. *Earth and Planetary Science Letters* 241 (1-2): 227-233.

Oliviera, I. B., A. H. Demond, and A. Salehzadeh. 1996. Packing of sands for the production of homogeneous porous media. *Soil Science Society of America Journal* 60 (1): 49-53.

Orth, W. S., and R. W. Gillham. 1996. Dechlorination of trichloroethene in aqueous solution using Fe-0. *Environmental Science & Technology* 30 (1): 66-71.

Ott, N. 2000. *Permeable Reactive Barriers for Inorganics.* Washington, D.C.: United States Environmental Protection Agency.

Parkhurst, D. L., and C. A. J. Appelo. 1999. *User's Guide to PHREEQC (Version 2): A Computer Program for Speciation, Batch Reaction, One-Dimensional Transport, and Inverse Geochemical Calculations.* Lakewood, CO: U.S. Geological Survey, Water Resources Investigation, Report # WRI-99-4259.

Patnaik, P. 2003. *Handbook of Inorganic Chemicals*. New York: McGraw-Hill.

Patterson, R. R., S. E. Fendorf, and M. Fendorf. 1997. Reduction of hexavalent chromium by amorphous iron sulfide. *Environmental Science & Technology* 31 (7): 2039-2044.

Pedersen, H. D., D. Postma, and R. Jakobsen. 2006. Release of arsenic associated with the reduction and transformation of iron oxides. *Geochimica et Cosmochimica Acta* 70 (16): 4116-4129.

Phillips, D. H., B. Gu, D. B. Watson, and Y. Roh. 2003. Impact of sample preparation on mineralogical analysis of zero-valent iron reactive barrier materials. *Journal of Environmental Quality* 32 (4): 1299-1305.

Phillips, D. H., B. Gu, D. B. Watson, Y. Roh, L. Y. Liang, and S. Y. Lee. 2000. Performance evaluation of a zerovalent iron reactive barrier: Mineralogical characteristics. *Environmental Science & Technology* 34 (19): 4169-4176.

Phillips, D. H., D. B. Watson, Y. Roh, and B. Gu. 2003. Mineralogical characteristics and transformations during long-term operation of a zerovalent iron reactive barrier. *Journal of Environmental Quality* 32 (6): 2033-2045.

Powell, R. M., R. W. Puls, D. W. Blowes, J. L. Vogan, R. W. Gillham, P. D. Powell, D. Schultz, T. M. Sivavec, and R. Landis. 1998. *Permeable Reactive Barriers Technologies for Contaminant Remediation.* Washington, D.C.: United States Environmental Protection Agency, Report # EPA/600/R-98/125.

Puls, R. W., D. W. Blowes, and R. W. Gillham. 1999a. Long-term performance monitoring for a permeable reactive barrier at the US Coast Guard Support Center, Elizabeth City, North Carolina. *Journal of Hazardous Materials* 68 (1-2): 109-124.

Puls, R. W., C. J. Paul, and R. M. Powell. 1999b. The application of in situ permeable reactive (zero-valent iron) barrier technology for the remediation of chromate-contaminated groundwater: a field test. *Applied Geochemistry* 14 (8): 989-1000.

Purdy, C., K. Gerdes, J. Aljayoushi, D. Kaback, and T. Ivory. 2002. Examples of department of energy successes for remediation of contaminated groundwater: Permeable reactive barrier and dynamic underground stripping ASTD projects. Paper presented at 28th Annual Waste Management Conference, Tucson, AZ, 24-28 Feb 2002.

Reardon, E. J. 1995. Anaerobic corrosion of granular iron - measurement and interpretation of hydrogen evolution rate. *Environmental Science & Technology* 29 (12): 2936-2945.

Reilly, T. E., K. F. Dennehy, W. M. Alley, and W. L. Cunningham. 2008. *Ground-Water Availability in the United States.* Reston, VA: U. S. Geological Survey, Report # C 1323.

Renock, D., T. Gallegos, S. Utsunomiya, K. Hayes, R. C. Ewing, and U. Becker. 2009. Chemical and structural characterization of As immobilization by nanoparticles of mackinawite (FeS_m). *Chemical Geology* 268 (1-2): 116-125.

Reynolds, G. W., J. T. Hoff, and R. W. Gillham. 1990. Sampling bias caused by materials used to monitor halocarbons in groundwater. *Environmental Science & Technology* 24 (1): 135-142.

Rickard, D. T. 1969a. The chemistry of iron sulphide formation at low temperatures. *Stockholm Contributions in Geology* 20: 67-95.

Rickard, D. T. 1969b. The microbiological formation of iron sulphides. *Stockholm Contributions in Geology* 20: 49-66.

Rickard, D. 2006. The solubility of FeS. *Geochimica et Cosmochimica Acta* 70 (23): 5779-5789.

Ritter, K., M. S. Odziemkowski, and R. W. Gillham. 2002. An in situ study of the role of surface films on granular iron in the permeable iron wall technology. *Journal of Contaminant Hydrology* 55 (1-2): 87-111.

Roberts, L. R., W. P. Ball, P. Searson, H. Fairbrother, P. J. Vikesland, J. Klausen, H. J. Zimmermann, and D. R. Burris. 2002. *Final Report for the SERDP Project CU-*

1125: Influence of Groundwater Constituents on Longevity of Iron-Based Permeable Barriers. Baltimore, MD: John Hopkins University, Report # CU-1125.

Rochette, E. A., B. C. Bostick, G. Li, and S. E. Fendorf. 2000. Kinetics of arsenate reduction by dissolved sulfide. *Environmental Science & Technology* 34 (22): 4714-4720.

Roh, Y., S. Y. Lee, and M. P. Elless. 2000. Characterization of corrosion products in permeable reactive barriers. *Environmental Geology* 40 (1-2): 184-194.

RTDF. 2001. Permeable Reactive Barrier Installation Profiles. http://www.rtdf.org/public/permbarr/prbsumms/default.cfm (accessed March 1, 2005).

Saripalli, K. P., P. D. Meyer, D. H. Bacon, and V. L. Freedman. 2001. Changes in hydrologic properties of aquifer media due to chemical reactions: A review. *Critical Reviews in Environmental Science and Technology* 31 (4): 311-349.

Sarr, D. 2001. Zero-valent iron permeable reactive barriers - how long will they last? *Remediation: The Journal of Environmental Cleanup Costs, Technologies & Techniques* 11 (2): 1-18.

Sass, B. M., A. R. Gavaskar, N. Gupta, S. W. Yoon, J. E. Hicks, D. O'Dwyer, and C. Reeter. 1998. Evaluating the moffett field permeable barrier using groundwater monitoring and geochemical modeling. Paper presented at Designing and Applying Treatment Technologies: Remediation of Chlorinated and Recalcitrant Compounds: The First International Conference on Remediation of Chlorinated and Recalcitrant Compounds, Monterey, CA, May 18-21.

Scherer, M. M., S. Richter, R. L. Valentine, and P. J. J. Alvarez. 2000. Chemistry and microbiology of permeable reactive barriers for in situ groundwater clean up. *Critical Reviews in Environmental Science and Technology* 30 (3): 363-411.

Schippers, A., and B. B. Jørgensen. 2001. Oxidation of pyrite and iron sulfide by manganese dioxide in marine sediments. *Geochimica et Cosmochimica Acta* 65 (6): 915-922.

Schippers, A., and B. B. Jørgensen. 2002. Biogeochemistry of pyrite and iron sulfide oxidation in marine sediments. *Geochimica et Cosmochimica Acta* 66 (1): 85-92.

Schlicker, O., M. Ebert, M. Fruth, M. Weidner, W. Wüst, and A. Dahmke. 2000. Degradation of TCE with iron: The role of competing chromate and nitrate reduction. *Ground Water* 38 (3): 403-409.

Schumacher, B. A., K. C. Shines, J. V. Burton, and M. L. Papp. 1990. *A Comparison of Soil Sample Homogenization Techniques.* Las Vegas, NV: U.S. Environmental Protection Agency, Report # 600//X-90/043.

Schwertmann, U., and E. Murad. 1983. Effect of pH on the formation of goethite and hematite from ferrihydrite. *Clays and Clay Minerals* 31 (4): 277-284.

Senzaki, T. 1991. Removal of chlorinated organic compounds from wastewater by reduction process: II. Treatment of trichloroethylene with iron powder II. *Kogyo Yosui* 391: 29-35.

Senzaki, T., and Y. Kumagai. 1989. Removal of chlorinated organic compounds from wastewater by reduction process: II. Treatment of trichloroethylene with iron powder. *Kogyo Yosui* 369: 19-25.

Senzaki, T., and Y. Kumagai. 1988. Removal of chlorinated organic compounds from wastewater by reduction process: I. Treatment of 1,1,2,2-tetrachloroethane with iron powder. *Kogyo Yosui* 357: 2-7.

Shirley, D. A. 1972. High-resolution X-ray photoemission spectrum of the valence bands of gold. *Physical Review B (Solid State)* 5 (12): 4709-14.

Shoemaker, S. H., J. F. Greiner, and R. W. Gillham. 1995. Permeable Reactive Barriers. In *Assessment of Barrier Containment Technologies*, eds. R. R. Rumer, J. K. Mitchell, 301-353. Springfield, VA: National Technical Information Service.

Simon, F., T. Meggyes, T. Tunnerrneier, K. Czurda, and K. E. Roehl. 2001. Long-term behaviour of permeable reactive barriers used for the remediation of contaminated groundwater. Paper presented at 8th International Conference on Radioactive Waste Management and Environmental Remediation, Sep 30-Oct 4 2001, Bruges, Belgium.

Sivavec, T. M., and D. P. Horney. 1997. Reduction of chlorinated solvents by Fe(II) minerals. Paper presented at 213th ACS National Meeting, San Francisco, CA, April 13-17, 1997.

Sivavec, T., T. Krug, K. Berry-Spark, and R. M. Focht. 2003. Performance monitoring of a permeable reactive barrier at the Somersworth, New Hampshire, Landfill Superfund Site. *Chlorinated Solvent and DNAPL Remediation* 837: 259-277.

Smyth, D. J. A., S. G. Shikaze, and J. A. Cherry. 1997. Hydraulic performance of permeable barriers for in situ treatment of contaminated groundwater. *Land Contamination & Reclamation* 5 (3): 131-137.

Sorel, D., S. D. Warner, B. L. Longino, J. H. Honniball, and L. A. Hamilton. 2003. Performance Monitoring and Dissolved Hydrogen Measurements at a Permeable Zero Valent Iron Reactive Barrier. In *Chlorinated Solvent and DNAPL Remediation: Innovative Strategies for Subsurface Cleanup*, eds. Susan M. Henry, Scott D. Warner, 278-285. Washington, DC: American Chemical Society / Oxford University Press.

Sposito, G. 1989. *The Chemistry of Soils*. New York: Oxford University Press.

Starr, R. C., and J. A. Cherry. 1994. In-situ remediation of contaminated ground-water - the funnel-and-gate system. *Ground Water* 32 (3): 465-476.

Stumm, W., and J. J. Morgan. 1996. *Aquatic Chemistry: Chemical Equilibria and Rates in Natural Waters*. 3rd ed. New York: Wiley.

Su, C., and R. W. Puls. 2004. Significance of iron(II,III) hydroxycarbonate green rust in arsenic remediation using zerovalent iron in laboratory column tests. *Environmental Science & Technology* 38 (19): 5224-5231.

Su, C., and R. W. Puls. 2003. In situ remediation of arsenic in simulated groundwater using zerovalent iron: Laboratory column tests on combined effects of phosphate and silicate. *Environmental Science & Technology* 37 (11): 2582-2587.

Su, C., and R. W. Puls. 2001a. Arsenate and arsenite removal by zerovalent iron: Effects of phosphate, silicate, carbonate, borate, sulfate, chromate, molybdate, and nitrate, relative to chloride. *Environmental Science & Technology* 35 (22): 4562-4568.

Su, C., and R. W. Puls. 2001b. Arsenate and arsenite removal by zerovalent iron: Kinetics, redox transformation, and implications for in situ groundwater remediation. *Environmental Science & Technology* 35 (7): 1487-1492.

Sweeny, K. H. 1981a. The reductive treatment of industrial wastewaters. I. Process description. *AIChE Sypmosium Series* 77 (209): 67-71.

Sweeny, K. H. 1981b. The reductive treatment of industrial wastewaters. II. Process applications. *AIChE Sypmosium Series* 77 (209): 72-88.

Sweeny, K. H., and J. R. Fischer. 1973. *Decomposition of halogenated pesticides.* Patent 3640821, filed 1973.

Sweeny, K. H., and J. R. Fischer. 1972. *Reductive degradation of halogenated pesticides.* Patent 3640821, filed 1972, and issued February 8.

Taylor, S. W., P. C. D. Milly, and P. R. Jaffe. 1990. Biofilm growth and the related changes in the physical properties of a porous medium. 2. Permeability. *Water Resources Research* 26 (9): 2161.

Uhlig, H. H., and R. W. Revie. 1985. *Corrosion and Corrosion Control: An Introduction to Corrosion Science and Engineering*. 3rd ed. New York: Wiley.

US DOE - Subsurface Contaminants Focus Area. 2000. *Permeable Reactive Treatment (PeRT) Wall for Rads and Metals.* United States Department of Energy, Report # OST/TMS ID 2155; DOE/EM-0557.

US General Accounting Office. 1987. *Superfund: Extent of Nation's Potential Hazardous Waste Problem Still Unknown: Report to Congressional Requesters*. Washington, D.C.: US General Accounting Office.

Vandevivere, P., and P. Baveye. 1992. Relationship between transport of bacteria and their clogging efficiency in sand columns. *Applied Environmental Microbiology* 58 (8): 2523-2530.

Vannela, R., P. Adriaens, and K. F. Hayes. 2007. Reactivity studies of biogenic nanosized iron sulfide minerals for as(III) removal. Paper presented at 234th National Meeting and Exposition of the American Chemical Society, Boston, MA, August 2007.

Vaughan, D. J., and A. R. Lennie. 1991. The iron sulfide minerals - their chemistry and role in nature. *Science Progress* 75 (298): 371-388.

Vaughan, D. J., and M. S. Ridout. 1971. Mössbauer studies of some sulphide minerals. *Journal of Inorganic & Nuclear Chemistry* 33 (3): 741-&.

Vikesland, P. J., J. Klausen, H. J. Zimmermann, A. L. Roberts, and W. P. Ball. 2003. Longevity of granular iron in groundwater treatment processes: Changes in solute transport properties over time. *Journal of Contaminant Hydrology* 64 (1-2): 3-33.

Vogan, J. L., B. J. Butler, M. S. Odziemkowski, G. Friday, and R. W. Gillham. 1998. Inorganic and biological evaluation of cores from permeable iron reactive barriers. Paper presented at Designing and Applying Treatment Technologies: Remediation of Chlorinated and Recalcitrant Compounds: The First International Conference on Remediation of Chlorinated and Recalcitrant Compounds, Monterey, CA, May 18-21.

Vogan, J. L., R. M. Focht, D. K. Clark, and S. L. Graham. 1999. Performance evaluation of a permeable reactive barrier for remediation of dissolved chlorinated solvents in groundwater. *Journal of Hazardous Materials* 68 (1-2): 97-108.

Wagner, C. D., L. E. Davis, M. V. Zeller, J. A. Taylor, R. H. Raymond, and L. H. Gale. 1981. Empirical atomic sensitivity factors for quantitative analysis by electron spectroscopy for chemical analysis. *Surface and Interface Analysis* 3 (5): 211-25.

Warner, S. D., B. L. Longino, M. Zhang, P. Bennett, F. S. Szerdy, and L. A. Hamilton. 2005. The first commercial permeable reactive barrier composed of granular iron: Hydraulic and chemical performance at 10 years of operation. Paper presented at First International Symposium on Permeable Reactive Barriers, Belfast, Northern Ireland, March 2004.

Warner, S. D., and D. Sorel. 2003. Ten Years of Permeable Reactive Barriers: Lessons Learned and Future Expectations. In *Chlorinated Solvent and DNAPL Remediation: Innovative Strategies for Subsurface Cleanup*, eds. Susan M. Henry, Scott D. Warner, 36-50. Washington, DC: American Chemical Society.

Warner, S. D., C. L. Yamane, N. T. Bice, F. S. Szerdy, J. L. Vogan, D. W. Major, and D. A. Hankins. 1998. Technical update: The first commercial subsurface permeable reactive treatment zone composed of granular zero-valent iron. Paper presented at Designing and Applying Treatment Technologies: Remediation of Chlorinated and Recalcitrant Compounds: The First International Conference on Remediation of Chlorinated and Recalcitrant Compounds, Monterey, CA, May 18-21.

Watson, J. H. P., B. A. Cressey, A. P. Roberts, D. C. Ellwood, J. M. Charnock, and A. K. Soper. 2000. Structural and magnetic studies on heavy-metal-adsorbing iron sulphide nanoparticles produced by sulphate-reducing bacteria. *Journal of Magnetism and Magnetic Materials* 214 (1): 13-30.

Weber, E. J. 1996. Iron-mediated reductive transformations: Investigations of reaction mechanism. *Environmental Science & Technology* 30 (2): 716-719.

Wieckowski, A., E. Ghali, M. Szklarczyk, and J. Sobkowski. 1983. Behaviour of iron electrode in CO2-saturated neutral electrolyte - II. Radiotracer study and corrosion considerations. *Electrochimica Acta* 28 (11): 1627-1633.

Wilkin, R. T., and R. W. Puls. 2003. *Capstone Report on the Application, Monitoring, and Performance of Permeable Reactive Barriers from Ground-Water Remediation; Volume 1, Performance Evaluations at Two Sites.* Washington, DC: United States Environmental Protection Agency, Report # EPA/600/R-03/045A.

Wilkin, R. T., R. W. Puls, and G. W. Sewell. 2003. Long-term performance of permeable reactive barriers using zero-valent iron: Geochemical and microbiological effects. *Ground Water* 41 (4): 493-503.

Wilkin, R. T., C. Su, R. G. Ford, and C. J. Paul. 2005. Chromium-removal processes during groundwater remediation by a zerovalent iron permeable reactive barrier. *Environmental Science & Technology* 39 (12): 4599-4605.

Wolthers, M. R., L. Charlet, P. R. Van der Linde, D. Rickard, and C. H. Van der Weijden. 2005a. Surface chemistry of disordered mackinawite (FeS). *Geochimica et Cosmochimica Acta* 69 (14): 3469-3481.

Wolthers, M. R., L. Charlet, C. H. Van der Weijden, P. R. Van der Linde, and D. Rickard. 2005b. Arsenic mobility in the ambient sulfidic environment: Sorption of arsenic(V) and arsenic(III) onto disordered mackinawite. *Geochimica et Cosmochimica Acta* 69 (14): 3483-3492.

Wolthers, M. R., S. J. Van der Gaast, and D. Rickard. 2003. The structure of disordered mackinawite. *American Mineralogist* 88 (11-12): 2007-2015.

Wyllie, M. R. J. 1962. Relative Permeability. In *Petroleum Production Handbook, Vol. II: Reservoir Engineering*, eds. T. C. Frick, R. W. Taylor, 25.1-25.14. New York, NY: McGraw-Hill.

Yabusaki, S., K. J. Cantrell, B. M. Sass, and C. Steefel. 2001. Multicomponent reactive transport in an in situ zero-valent iron cell. *Environmental Science & Technology* 35 (7): 1493-1503.

Yoon, S. W., A. R. Gavaskar, B. M. Sass, N. Gupta, R. Janosy, E. Drescher, L. Cumming, J. E. Hicks, and A. Lightner. 2000. Innovative Construction and Performance Monitoring of a Permeable Reactive Barrier at Dover Air Force Base. In *Chemical Oxidation and Reactive Barriers: Remediation of Chlorinated and Recalcitrant Compounds*, eds. Godage B. Wickramanayake, Arun R. Gavaskar and Abraham S. C. Chen, 409-416. Columbus, Ohio: Battelle Press.

Zhang, Y., and R. W. Gillham. 2005. Effects of gas generation and precipitates on performance of Fe^0 PRBs. *Ground Water* 43 (1): 113-121.

Zimmerman, J. B., J. R. Mihelcic, and J. Smith. 2008. Global stressors on water quality and quantity. *Environmental Science & Technology* 42 (12): 4247-4254.